FREQUENCY DOUBLED CONTINUOUS WAVE DYE LASERS

Allister Ian Ferguson

A Thesis Submitted for the Degree of PhD
at the
University of St Andrews

1977

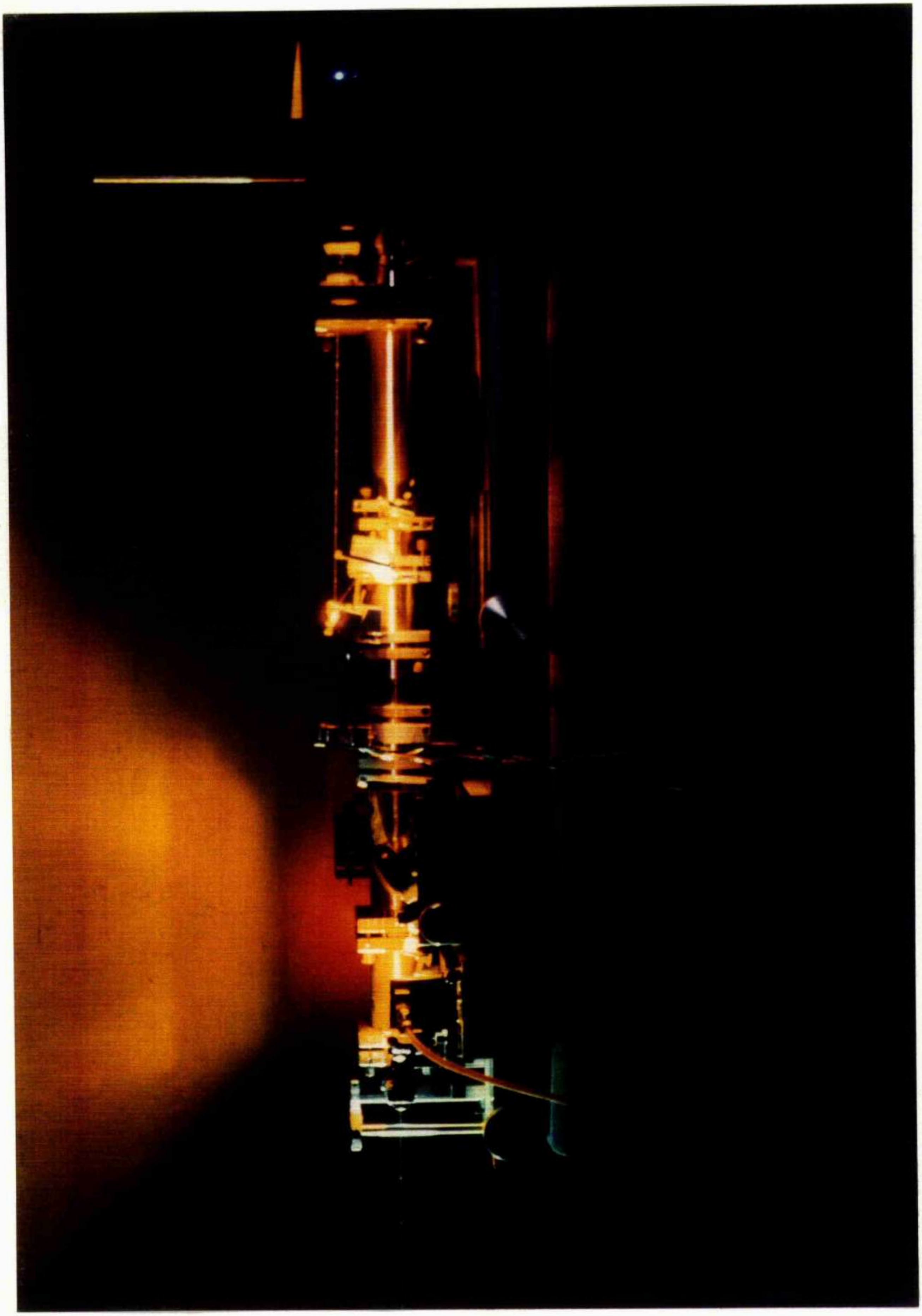

ProQuest LLC.
789 East Eisenhower Parkway
P.O. Box 1346
Ann Arbor, MI 48106 – 1346

FREQUENCY DOUBLED CONTINUOUS WAVE DYE LASERS

A thesis presented by
A. I. Ferguson, B.Sc
to the
University of St Andrews
in application for the degree of
Doctor of Philosophy
September 1977

DECLARATION

I hereby certify that this work has been composed by me, and is a record of work done by me, and has not previously been presented for a Higher Degree.

This research was carried out in the Department of Physics, in the University of St Andrews under the supervision of Dr M H Dunn.

A I Ferguson

CERTIFICATE

I certify that Allister I Ferguson, B.Sc, has spent nine terms of research work towards the Degree of Doctor of Philosophy of the University of St Andrews under my direction, that he has fulfilled the conditions of the Resolution of the University Court, 1967, No 1, and that he is qualified to submit the following thesis in application for the Degree of Doctor of Philosophy.

M H Dunn
Research Supervisor

ACKNOWLEDGEMENTS

I should like to thank Dr Malcolm H Dunn for his encouragement, enthusiasm and guidance throughout the course of this work. I also thank Dr A Maitland for allowing me to make use of the facilities developed by him. I have relied heavily on the skills and efforts of the electrical and mechanical workshops of the Physics Department and I therefore gratefully acknowledge the assistance of Mr Ron McCraw, Mr Mike Robertson and their colleagues. I thank Patricia Russell and Joyce Izatt for their accurate and expeditious typing of the manuscript. My wife, Kathleen deserves special thanks for her tolerance over the past few years and for her assistance in the final preparation of the manuscript. I would like to express my thanks to Professor J F Allen for his support and encouragement during my time at St Andrews.

CAREER

Allister I Ferguson was born in Aberdeen on the 10th December 1951 and educated at Aberdeen Academy. He obtained the degree of B.Sc at the University of St Andrews in June 1974. His post-graduate training commenced in October 1974 at Imperial College where he worked on picosecond pulses and the production of tunable ultraviolet radiation by third harmonic generation in metal vapours. Since October 1975 he has been a research student at the University of St Andrews. He has been awarded a Lindemann Fellowship to continue work on laser spectroscopy during 1977-78 at Stanford University.

LIST OF PUBLICATIONS

Publications by the author on topics discussed in this thesis.

A I Ferguson, M H Dunn and A Maitland, Tunable, continuous-wave, ultraviolet radiation around 300 nm by frequency doubling a Rhodamine 6G dye laser, Opt Comm 19, 10(1976)

M H Dunn and A I Ferguson, Coma Compensation in off-axis laser resonators, Opt Comm, 20, 214 (1976)

A I Ferguson and M H Dunn, Intracavity second-harmonic generation in continuous-wave dye lasers, IEEE J Quant Electron, QE13, 751 (1977)

A I Ferguson and M H Dunn, A tunable, frequency-doubled, continuous-wave dye laser using ADA, to be published in Optics Communications

A I Ferguson and M H Dunn, Detection of the Rydberg states of rubidium using a frequency doubled CW dye laser, to be published in Optics Communications

ABSTRACT

This thesis describes the design and development of a frequency doubled, continuous wave dye laser and its application to a study of the high Rydberg states of Rubidium.

The laser uses the dye rhodamine 6G as the active medium and is optically pumped with an argon ion laser. Frequency doubling is by an ADA (ammonium dihydrogen arsenate) or ADP (ammonium dihydrogen phosphate) crystal located within the laser cavity. Continuous output powers in the ultra-violet in excess of 30 mW and tunable over the wavelength range 285-315 nm have been produced. The linewidth can be chosen to be 0.02 nm broadband system) or 0.002 nm (narrowband system) depending on the frequency selecting elements used.

In order to keep insertion losses small the crystals have optical faces cut at Brewster's angle, and in order to increase generation efficiency the intracavity radiation field is focused into the crystal. Such an arrangement introduces the aberrations of coma and astigmatism which must be compensated by suitable cavity design. A variety of cavity and crystal configurations have been analysed for aberrations, and a novel arrangement for the simultaneous elimination of coma and astigmatism developed.

Several practical frequency doubled dye lasers have been investigated. In particular the performances of ADA and ADP as the frequency doubling crystals are compared and contrasted. ADA has the advantage that it can be non-critically phase matched at these wavelengths and this results in a higher generation efficiency and a better UV beam quality than encountered with ADP. However, since it can only be temperature tuned, the tuning range (292-302 nm for temperature range 20-80°C) is more limited than that for ADP (285-315 nm) which can also be angled tuned.

For both types of crystal, thermal phase mismatching is identified as the process limiting generation efficiency. Evidence is also presented that thermal focusing ultimately limits the UV output power by upsetting cavity stability.

A computer model of intracavity frequency doubling has been developed. Thermal phase mismatching effects in the crystal as well as excited state absorption in the dye are included. This model is used to investigate the influence of cavity losses and crystal absorption on generation efficiency. Optimization of conversion efficiency by correct choice of crystal parameters is considered.

Two systems have been developed to allow continuous scanning over an extended frequency range. One allows the broadband laser (0.02 nm) to be continuously tuned over 3 nm, the other allows the narrowband laser (0.002 nm) to be continuously tuned over 2 nm. The operation of a single frequency version of the laser and its stabilization on an external reference cavity is also described.

The excitation of high Rydberg states in Rubidium using the frequency doubled laser is described. The states are detected by a space-charge limited ionization detector. The principal series of Rb up to a principal quantum number of n = 74 has been detected. A novel triode arrangement of electrodes in the space charge detector has enabled a small electric field to be applied to the rubidium vapour. The consequent Stark mixing of n^2S, n^2P and n^2S states has allowed the n^2S and n^2D states to be excited from the 5^2S ground state. New term values of the n^2S and n^2D series are reported.

TABLE OF CONTENTS

Chapter I Introduction

Chapter II Review of the Principles of Second Harmonic Generation

Chapter III A Theory of Second Harmonic Generation in Dye Lasers

Chapter IV Coma Compensation in Off-Axis Laser Resonators

Chapter V Experimental Details of Some Prototype Second Harmonic Dye Lasers

Chapter VI Study of the Rydberg States of Rubidium using a Second Harmonic Dye Laser

Chapter VII A Single Frequency Second Harmonic Dye Laser

CHAPTER I

INTRODUCTION

Abstract

The production of tunable ultraviolet laser light by intracavity frequency doubling is considered. The continuous wave frequency doubled dye laser whose development is described in this work is compared with some pulsed frequency doubled dye lasers. Some uses of continuous wave ultraviolet laser radiation in trace element analysis, pollution monitoring, laser photochemistry and high resolution laser spectroscopy are described. Early approaches to intracavity harmonic generation are outlined and previous work on frequency doubling of continuous wave dye laser light is reviewed. A summary of the contents of the thesis are outlined at the end of the chapter.

Ever since the discovery of the laser in the early 1960's two prevailing aims of laser physicists have been to produce lasers which operate at short wavelengths and which can be tuned over extended wavelength ranges. Intensive work in recent years has led on the one hand to the development of a variety of ultraviolet lasers of fixed wavelength and on the other hand to lasers which are tunable throughout the visible and infrared regions of the spectrum. The realization of both aims in the development of a tunable ultraviolet laser source is still awaited. Dye lasers have been particularly successful in producing tunable visible and infrared radiation. However the extension of this approach into the ultraviolet is limited because photochemical decomposition competes with radiative deactivation of the molecule since, in the ultraviolet, the energy of the absorbed quantum is higher than any bond in the molecule. Over the past few years the most promising development has been discharge pumped excimer and exiplex lasers. However, a continuous wave excimer laser which is readily tunable and suitable as a general laboratory tool has yet to be proved feasible.

At present the only satisfactory method of producing tunable UV coherent radiation is by frequency doubling the radiation from a tunable dye laser. The dye laser used can either be pulsed or continuous. The commercially available systems are at present all based on pulsed lasers. Usually the dye is pumped by a pulsed nitrogen laser, but direct pumping can also be done using a flashlamp. The frequency doubling is performed using a nonlinear crystal either inside or outside the dye laser cavity. Pulsed frequency doubled dye lasers have yet to reach their full potential in laser spectroscopy although they are beginning to be used more widely.

In this thesis the production of continuous-wave (CW) tunable UV radiation by frequency doubling a CW dye laser using an intracavity crystal is considered. The output powers from CW dye lasers are much lower than those from pulsed lasers, and in view of the quadratic dependence of second harmonic power on fundamental power it is essential to place the harmonic generator in the laser cavity where there is a high circulating field. However, because the power developed in the laser cavity is very sensitive to losses care must be taken to minimize these losses. Frequency doubling a CW dye laser is more difficult than the pulsed laser approach and so some justification for this method is required. In order to develop this point some typical data on commercial pulsed frequency doubled dye lasers are first considered and then contrasted with the present findings on CW frequency doubled dye lasers.

The data on pulsed dye lasers are presented in table 1. One of the lasers is flashlamp pumped with a pulse duration in the region of 1 μsec (Chromatix CMX-4) and the other is a nitrogen pumped laser with a pulse duration of 5 nsec (Molectron DL 200). The pulse duration of the nitrogen pumped laser is so short that little advantage is gained by inserting the crystal into the cavity whereas the flashlamp pumped laser is quasi-continuous and the conversion is more efficient if the doubling crystal is inside the cavity. The flashlamp pumped system has the greater average power, this being about 10 mW at a repetition rate of 30 pps. The peak power of the nitrogen pumped dye laser is between 1 kW and 10 kW in the UV but average powers are very low due to the short pulse duration. The linewidth of both lasers can be made as small as

0.002 nm by frequency narrowing but is usually in the region of 0.02 nm.

As will be shown later we have developed a continuous wave frequency doubled dye laser which is capable of producing continuous UV powers in excess of 30 mW and is tunable over the range 285 nm to 315 nm. The broadband laser linewidth is in the region of 0.02 nm but can be readily narrowed to 0.002 nm by the inclusion of a single etalon in the cavity. A second etalon is capable of reducing laser oscillation to a single cavity mode with a linewidth in the region of 10 MHz.

The main advantage of a continuous wave laser over a pulsed laser is now apparent in that the linewidth of a continuous laser can be made very small. The linewidth of a pulsed laser is limited to approximately the inverse of its pulse duration; this is about 100 MHz for a 5 nsec nitrogen pumped dye laser. The resolution of a continuous laser is usually limited only by the cavity stability. Dye lasers with long time averaged linewidths of less than 300 Hz have been developed and are described in Chapter VII. The frequency stability of a free running CW dye laser at 10 MHz is still an order of magnitude better than that of a typical pulsed system.

A second important advantage of continuous wave lasers is their high average power. This is particularly important if their radiation is used to study processes which are linear in pump power, such as most photochemical reactions. The frequency and intensity stability of continuous wave lasers means that if signals are small,very long integration times can be used in signal recovery equipment. This has importance in applications such as Raman and Brillouin scattering and two photon absorption.

In the following section some of the important uses of tunable UV radiation are described and the advantages of continuous wave UV over pulsed UV is enlarged. Work by other investigators on the frequency doubling of dye lasers is then reviewed, and this is followed by a discussion of the approach adopted in the present work.

I.2 Some Uses of Tunable UV Radiation

In this section the importance of a tunable UV source operating in the 300 nm region of the spectrum will be demonstrated. Some of the topics discussed are laser-based trace element analysis, pollution monitoring, laser photochemistry, studies of Rydberg atoms and high resolution laser spectroscopy.

Ultraviolet atomic absorption spectroscopy is a widely used method of detecting small quantities of the elements. Typically, a liquid sample is aspirated into an air-acetylene or nitrous oxide-acetylene flame where an atomic vapour of the element is formed. The elements are then identified by their characteristic absorptions. In order that the element absorbs radiation,the radiation must be tuned to the wavelength of a transition which is radiatively connected to the ground state. Such lines are known as resonances or resonance lines. The resonance lines of most elements lie in the region of 350 nm to 200 nm making this the most important spectral region for standard atomic absorption.

The dramatic increase in sensitivity of atomic absorption spectroscopy when laser sources are used has been predicted by several authors[1-4] and Gelbwachs, Klein and Wessel[5] have recently reported the detection of Na at an atomic concentration of less than 1 part in 10^{14}. This compares with a sensitivity of about 1 part in 10^8 which can be achieved, under favourable circumstances, using standard atomic absorption techniques[6].

A list of elements accessible to a frequency doubled Rhodamine 6G dye laser is shown in appendix D. Throughout the spectral region from 285 nm to 315 nm some 34 elements are accessible to this laser. The strengths of the lines are also shown on the table indicating those transitions which would be suitable for atomic absorption spectrophotometry.

Radiation in the region of 300 nm has also assumed importance in recent years because of its influence on chemical reactions in the upper atmosphere (see for example Thrush[7]). The effect of pollution of the stratosphere on the ozone layer will only be understood when detailed chemical reactions have been studied under controlled conditions. The importance of tunable ultraviolet lasers in understanding these reactions has been recently reviewed by Pitts and Finalyson-Pitts[8] and by Johnston[9].

Of interest in atmospheric studies is the photochemistry and photokinetics of formaldehyde. Formaldehyde can be present in the atmosphere either as a primary pollutant, for example emitted by car exhausts, or as a secondary pollutant in ozone-olefin reactions[8].

Bradley Moore[10,11] and his co-workers have been conducting photochemical studies on formaldehyde for a number of years and the advent of pulsed second harmonic dye lasers has helped to reveal a considerable amount of detailed information of the primary photochemistry of this molecule. An important use of the narrow linewidth of a laser source has been to perform isotope separation in formaldehyde[11]. By tuning the laser to the relevant transition, an isotope selective photo-predissociation can be induced in formaldehyde. Bradley Moore's group have already reported the separation of carbon 12 and 13 isotopes with enrichment factors of the order of 80 and also the separation of deuterium from hydrogen using a frequency doubled dye laser at a wavelength of about 300 nm[12]. The average UV laser power was in the region of 0.3 mW with a linewidth of 0.1 cm^{-1}. The separation factors were limited by jitter on the laser frequency and by intensity fluctuations. The higher average power of a CW laser and more stable frequency make it an attractive possibility to use this laser for isotope separation. It may then be possible to separate or enrich samples in ^{14}C, ^{17}O and ^{18}O. The isotope separation of hydrogen and deuterium may have important economic consequences for the production of heavy water fission reactor or deuterium-tritium fusion reactors. A commercial plant for the production of deuterium by UV predissociation of formaldehyde has been proposed by Vanderleden[13] in connection with the Canadian atomic reactor programme.

Another chemical pollutant which is of atmospheric importance is sulphur dioxide. This chemical is produced by oil fired and coal fired power stations and pumped high into the atmosphere by giant smoke stacks. When the sulphur dioxide combines with water it forms sulphuric acid and can be very damaging to people, buildings and vegetation. This has stimulated the development of a variety of laser methods for remotely monitoring the presence of SO_2[14,15]. The strong absorption of SO_2 at around 300 nm means that pulsed frequency doubled dye lasers are widely used to monitor its presence[15]. A continuous wave laser would allow much lower concentrations to be monitored.

Tunable UV laser radiation also has application in spontaneous Raman and Brillouin studies where, because of the λ^{-4} dependence of the cross-section on the excitation wavelength, the sensitivity should be increased by a factor of about 16 over a laser working in the visible and at the same power. The long integration times made possible by a continuous wave source should open the field of resonant Raman scattering to the UV spectral region.

Tunable UV lasers are of importance in high resolution spectroscopy since they extend laser spectroscopy techniques to a new spectral region.

Such methods as Doppler-free saturated absorption[16] and Doppler-free two photon absorption[17] should be amenable to a tunable UV laser.

Some important areas of atomic physics where tunable UV laser radiation may be usefully applied is in the study of high lying atomic states (Rydberg states), the search for parity non-conservation effects in atoms[18] and in the development of a UV frequency standard[19,20].

A considerable amount of interest has arisen in recent years over the ability of dye lasers to excite very high atomic states. Atoms have been selectively excited to states with principal quantum numbers n $\geqslant$ 70. Since the radius of a Bohr orbit increases as n^2 very large geometrical cross-sections can be expected for these states. Gigantic polarizabilities and consequent Stark shifts have also been reported for Rydberg atoms. Most of the work on Rydberg atoms has been done using two step excitation; the first step from the ground state to a state of opposite parity and the second from this state up to the states close to the continuum having the same parity as the ground state. A tunable laser in the region of 300 nm can be used to excite nearly all the alkali metals to high lying states. Since a UV laser involves direct excitation from the ground state, transitions of opposite parity to the ground state can be studied. Some preliminary work on the Rydberg states of rubidium using the CW frequency doubled dye laser is reported in Chapter VI.

Another interesting application of a tunable UV laser is the possibility of detecting weak neutral currents in atoms[18]. If it is assumed that the interaction of an electron with the nucleus is affected by weak neutral currents which do not conserve parity then new effects arise which involve mixing atomic states of even and odd parity. The consequence of this is that radiation emitted from certain states will be circularly polarized and the plane of polarized light incident on an isotropic medium will be rotated[18]. A transition for which this rotation is particularly large is the $6^2P_{\frac{1}{2}} - 7^2P_{\frac{1}{2}}$ transition in atomic thallium which occurs at a wavelength of 292.7 nm[21]. This wavelength is readily obtained with a frequency doubled Rhodamine 6G dye laser. Preliminary experiments have been performed with a pulsed dye laser[21] but the expected rotation of 3×10^{-3} rad will probably only be detectable with a continuous wave laser.

Finally, and perhaps most importantly, a frequency doubled dye laser could be used in the development of a UV frequency standard which is comparable or even superior to visible frequency standards. The hydrogen 1S-2S two photon Doppler-free absorption at 243.0 nm has been proposed as a very high resolution frequency standard in the UV[19]. The natural lifetime of the 2S state of hydrogen is about 0.15 sec which could lead to an ultimate linewidth of only 1Hz. In principal,it should be possible to achieve a resolution of better than 1 part in 10^{15} and to measure the line centre to about 1 part in 10^{17}[20]. In order to obtain a resolution even remotely approaching this a continuous wave UV laser source at 243.0 nm will be necessary. The most probable method of obtaining radiation at this wavelength with sufficiently high resolution is by frequency doubling a dye laser operating at 486.0 nm. Efficient continuous wave second harmonic generation at this wavelength will be difficult but efforts towards achieving this end will be handsomely rewarded by new information on the hydrogen atom and the possibility of a superb frequency standard.

I.3 Intracavity Frequency Doubling of Laser Radiation

The enhancement of second harmonic generation when the nonlinear second harmonic generator is placed inside the laser cavity was first observed in 1963 by Wright working at the Royal Signals Research and

Development establishment[22]. He noted that by placing an 8 mm phase matched ADP crystal into the cavity of a neodymium doped calcium tungstate laser the second harmonic power generated was more than a factor of 20 greater than that generated with the same laser but with the crystal outside the cavity.

Since that time,intracavity second harmonic generation has become a widely used method of producing either visible radiation from an infrared laser or UV radiation from a visible laser. Intracavity harmonic generation is particularly advantageous for continuous-wave lasers since the low output power of these lasers leads to inefficient harmonic generation outside the cavity. The circulating power inside the laser cavity is much higher than outside and,since the second harmonic power is proportional to the fundamental power squared there is a considerable advantage in putting the crystal inside the cavity. The crystal will introduce two loss mechanisms, one of them is the linear loss due to reflection, scattering,etc, and the other is a nonlinear loss due to the conversion of fundamental radiation into second harmonic radiation. This loss depends on the intracavity power which in turn depends upon the cavity losses. It is well known that for a given laser there is an optimum coupling of radiation out of the cavity. If the coupling is too big the cavity losses will be too high and the laser power will fall. If the coupling is too small the intracavity power may be high but only a small fraction will be coupled out. There will therefore be some output coupling which maximises the usable output power. By similar arguments there is an optimum nonlinear output-coupling which maximises second harmonic power. This problem has been treated by Polloni and Svelto[23] and by Smith[24].

The important points of Smith's analysis are that the optimum nonlinear coupling coefficient is independent of pump power and that the maximum available second harmonic power is equal to the maximum fundamental power available from the laser for the same value of total linear loss. In Chapter III it will be shown that a more realistic treatment of crystal absorption and dye saturation is required if the theory of intracavity harmonic generation is to be applied to the design of a practical second harmonic dye laser.

Some possible intracavity harmonic generation systems are shown in figure 1(a) to 1(c). The arrangement shown in figure 1(a) is the simplest form of second harmonic cavity. The gain medium and second harmonic generator (SHG) are both placed within the cavity. Because there are counter-propagating beams in a cavity the second harmonic will be generated in two directions. In this arrangement both mirrors are highly reflecting at the fundamental wavelength and the mirror on the right is made transmitting at the second harmonic. Only one half of the second harmonic will be usefully coupled out of the cavity since the second beam travelling in the opposite direction will probably be absorbed by the active medium or, if the medium is transparent, by the back mirror.

Several methods have been proposed to enable the second harmonic power to be extracted in both directions[25,26,27]. An example of one such attempt is illustrated in figure 1(b). This cavity was proposed by Gonzalez, Niegh and Steier[25]. In this cavity, a prism, which may have been included for the tuning of the laser, is used as the second harmonic output coupler. The harmonic beam generated in one direction is reflected by a maximum reflector back through the second harmonic generator and out through the prism. The reflector can either be a coated mirror which is highly reflecting at the fundamental and second harmonic or, if this should prove too difficult to manufacture, a corner cube reflector. The advantage of the latter is its ease of alignment.

A difficulty associated with all methods which attempt to extract both harmonic beams is that, in order to ensure that the second harmonic radiation re-entering the crystal leads to constructive and not destructive interference, the phase of the incoming second harmonic beam must be matched to the phase of the fundamental beam[24]. The phase shift between fundamental and second harmonic due to the dispersion of air and phase shifts in the reflector must be taken into account. The result is that the spacing between the output end of the crystal and the reflector must be carefully controlled. Since the crystal effectively has its length doubled and, since the second harmonic power goes as the square of the length, an increase of up to a factor of four can be expected in the second harmonic output power. However, this is offset by the increased criticality of phase matching and the sensitivity of the harmonic generation to the crystal-to-reflector spacing.

In the arrangement shown in figure 1(b) there are considerable losses due to the Fresnel reflections of the second harmonic (polarized perpendicular to the fundamental) at the prism surfaces. A coupling system which avoids these losses is that shown in figure 1(c). This coupling arrangement which was proposed by Ross[26], is based on the use of a Glan-Taylor (GT) polarizer. The second harmonic is coupled out in one direction only by the reflector which has maximised reflectivity at the fundamental and second harmonic. The second harmonic which is perpendicularly polarized to the fundamental can then be coupled out of the cavity with very high efficiency. The drawback of this method is that the polarizer presents a fairly high loss to the fundamental which makes the method a poor one for a continuous-wave laser.

Although it has been shown that up to a factor of four in second harmonic power can be gained by coupling the harmonic in one direction, the operational difficulties associated with such methods has meant that most practical second harmonic laser systems have utilized the simplest coupling scheme 1(a) where the second harmonic radiation is extracted in one direction.

I.4 Review of Some Practical Intracavity Doubling Systems

One of the first reports of efficient intracavity frequency doubling was by Smith, Nassau and Galvin[28] who were able to frequency double the 1.06 μm radiation from a CW neodymium doped YAG laser by putting a lithium niobate crystal into the cavity. A continuous output power of only 300 μW was obtained. However, it was found that by chopping inside the laser cavity at a frequency of 1 kHz the intracavity power rose by a factor of 10^2 and the second harmonic power by 10^4. They were therefore able to obtain second harmonic powers in the region of 1W which was comparable to the output power from the optimally coupled CW neodymium doped YAG laser without the doubler in the cavity. The fall in power for the continuous laser was attributed to optically induced refractive index inhomogeneities. By using barium sodium niobate ($Ba_2\ Na\ Nb_5\ O_{15}$) as the second harmonic generator Geusic et al[29] were able to generate 1.1W of second harmonic power continuously. This corresponds to 100% conversion efficiency from the pump radiation to second harmonic power in the sense that the second harmonic power was equal to the fundamental output with optimum output coupling and without the crystal in the cavity. This remarkably high conversion was attributed to the good optical quality, low absorption and high nonlinear coefficient of $Ba_2\ Na\ Nb_5\ O_{15}$[29].

The continuous-wave conversion of visible light into UV was reported by Dowley and Hodges[30] who found that ADP and KDP could be 90° phase-matched at the 514.5 nm line of an argon laser. Because of the low gain of the argon laser it was necessary to keep the reflection loss from the crystal surfaces as low as possible. A variety of methods were tried by these authors. These included the use of antireflection (AR) coated windows applied to the crystal faces with an index matching fluid and the use of antireflection coating applied direct to the crystal. The index matching fluids used were dry glycerin ($n = 1.475$) and Dow 200 fluid ($n = 1.41$). Since the fluids were to match crystals with refractive index $n = 1.52$, glycerin would be expected to be superior to Dow 200 fluid. However, it was found that when glycerin was used, a UV power level in the region of 1 mW was attained before the argon laser stopped oscillating. This was attributed to the UV absorption of glycerin being so great that local heating took place on the crystal surface and caused damage in a very short time. If the intracavity beam was chopped at a duty cycle of 1 part 'on' to 250 parts 'off' the operation was found to be stable and UV powers in the region of 100 mW were obtained during the 'on' period.

By using Dow 200 fluid the continuous UV power was 5 mW. It was found that an initial intracavity power of 10 W fell to about 1 Watt over a 30 minute period. However, when the laser was chopped the UV power was found to be 50 mW. Again the cause was thought to be crystal damage induced by absorption in the fluid.

When crystals with anti-reflection coatings were used it was found that continuous power of up to 50 mW could be obtained but that the fundamental power was about 20% to 40% down on its value before UV generation. The fundamental power was not recovered again unless the crystal was moved.

All the indications of the Dowley and Hodges[30] work is that when significant amounts of UV power are expected, index matching fluids tend to absorb and cause damage. AR coatings appear to be more satisfactory but since they are applied to the temperature sensitive and hygroscopic crystal surfaces they must be 'soft' coatings which are susceptable to both [illegible] it would therefore appear that the best way to avoid crystal damage problems is to avoid all index matching fluids and AR coatings applied direct to the crystal. Further support for this view is given by the subsequent work of Dowley[31] who found that by using the frequency doubler at Brewster's angle and thereby eliminating any direct contact with the crystal surface, a second harmonic power of more than 400 mW was produced. This was obtained using 90° phase-matched KDP and ADP crystals in an argon laser with optimum output coupler.

I.5 Continuous Wave Frequency Doubling of Dye Lasers

The first reported use of intracavity frequency doubling to produce continuous wave tunable UV was by Gabel and Hercher[32] in 1972. A schematic diagram of their laser is shown in figure 2. The dye was Rhodamine 6G and was contained in quartz cell placed at Brewster's angle to the cavity mode. The mirrors M_2 and M_3 were used in the astigmatically compensated arrangement described by Kogelnik et al[33]. Crystals of ADP and lithium formate monohydrate (LFM) were used as harmonic generators. The reflection losses of the crystals were minimised by applying AR coated quartz slides to the crystals with a UV transparent epoxy (Epo-Tek 305). The UV was coupled through a quartz slide set at Brewster's angle. The maximum pump power available to Gabel and Hercher was 1W from an argon ion laser. At this pump power tunable UV radiation from 290 nm to 315 nm was obtained. The maximum second harmonic power generated in the cavity was estimated to be 1.1 mW at 296 nm when ADP was used. The power from LFM was found to be about five times less than this.

The only other reported work on intracavity frequency doubling of a continuous wave dye laser, besides that reported herein is that of Fröhlich, Stein, Schröder and Welling in 1976[34]. The dye laser cavity used by Fröhlich et al[34] was almost identical to that of Gabel and Hercher[32] except that the pump laser was focused directly onto a jet stream of Rhodamine 6G and that Fabry-Perot etalons were introduced into the cavity for frequency narrowing. The crystal used was ADA which can be 90° phase-matched at the lasing wavelengths of Rhodamine 6G. The crystal was 30 mm in length and antireflection coated fused silica flats were attached to the end faces using silicone oil (Bayer AG 10,000). Using the prism as a tuning element and including a 0.1 mm thickness etalon, the laser linewidth was 15 GHz. The maximum available pump power was 7 W from an argon ion laser operating at 514.5 nm. It was found that at pump powers beyond about 4W the dye laser power saturated. This was attributed to thermal lensing in the dye jet causing the laser to operate in high order modes. By changing from an ethylene glycol solution to an aqueous solution with a polyvinyl alcohol[35] added they found that powers in excess of 9 W could be used without noticeable detrimental thermal effects.

The maximum UV power generated by Fröhlich et al[34] was 140 mW generated both ways within the cavity. They were able to extract 50 mW in one direction. Single frequency operation was obtained by placing two etalons in the cavity. The measured single frequency UV output power was 4 mW (an estimated 11 mW was generated) with a linewidth of less than 50 MHz. Fröhlich et al[34] attributed much of the reduction of single mode power to thermally induced losses in the frequency selecting etalons. By going to a ring laser arrangement, they argue, the frequency selecting effort is smaller due to the reduced hole burning and so higher power would be expected. In a footnote to their paper they have reported that single mode UV powers of up to 40 mW have been measured in a ring laser.

All of the reported work on second harmonic CW dye lasers has involved the use of Rhodamine 6G as the laser dye. This has restricted the UV tuning range to the region 285 nm to 315 nm. There is no fundamental reason why frequency doubled dye lasers should not be extended to other dyes and new crystals. The reason that attention has been restricted to Rh 6G in the recent past is that this is by far the most efficient dye, it has a long lifetime and is efficiently pumped by the powerful 514.5 nm line of the argon laser. It therefore provides an ideal system for development studies. Once an efficient design has been established for this dye the extension to other wavelengths can then be entertained. Table 2 lists a range of laser dyes and crystals which can be used for generating tunable UV from about 210 nm to 350 nm. The laser dyes are given in the first column, followed by their efficient lasing wavelengths. A suitable harmonic generator for this wavelength is then listed in the third column. If it is possible to achieve 90° phase-matching over the wavelength region, the relevant crystal is listed in the fourth column and its wavelength range in the last column. It should be noted that, for unaxial crystals such as ADP, the efficiency of harmonic generation increases at shorter wavelengths as the 90° phase-matching condition is approached.

I.6 The Approach Adopted in this Work

In this work we shall be concerned with the design of an intracavity frequency doubled dye laser. The principal feature of this design is that the crystal is set at Brewster's angle inside the laser cavity to avoid the use of index matching fluids and antireflection coatings applied to the crystal. The optical aberrations introduced when focusing into a medium at Brewster's angle are minimised by use of off-axis spherical focusing mirrors in a new cavity arrangement. Methods of tuning the laser over an extended range are described and the laser is used to detect the Rydberg states of atomic rubidium as an example of its use in atomic spectroscopy. A single frequency version of the laser has been developed for high resolution spectroscopy.

Chapter II contains a review of nonlinear optics with special emphasis on second harmonic generation. Phase-matching techniques and focusing for maximum harmonic generation are described. The reduction of harmonic conversion due to a thermal phase-mismatching effect is considered.

A new analysis of intracavity second harmonic generation, necessitated by the experimental results of this work, is given in Chapter III. It is shown that the inclusion of the thermal phase-mismatching effect and crystal absorption results in conclusions which are different from previous simpler analyses[23,24]. The choice of crystal parameters which optimise the second harmonic power for a given cavity loss and crystal absorption is calculated as a function of the pump power.

In Chapter IV the optical aberrations caused by focusing into a Brewste angled crystal are calculated. It is shown that, besides the well-known aberration of astigmatism, there is considerable amount of coma. It is shown that both coma and astigmatism can be eliminated by a suitable off-axis cavity arrangement.

Two prototype second harmonic dye lasers are described in Chapter V. The first uses ADP as the frequency doubler with Rhodamine 6G as the dye. This produces a continuous output power of 35 mW at 295 nm for a pumping power of 20 W. The second uses ADA as the doubler and 30 mW at a pump power of 4.5 W has been obtained with this system. The UV linewidth could be narrowed to 0.002 nm and some tuning systems which allow the second harmonic to be continuously scanned over a range of up to 3 nm are described. A new method of scanning the second harmonic while maximising the harmonic generation is proposed.

In Chapter VI an atomic spectroscopy experiment using the second harmonic dye laser is described. The properties of Rydberg atoms and some methods of studying them are first reviewed. An experiment involving the second harmonic dye laser and a new kind of space charge limited ionization detector in which states up to a principal quantum number of about n = 74 have been selectively excited in atomic rubidium, is described. By applying a small electric field to the detector the dipole selection rules have been broken by Stark mixing of the n^2S, n^2P and n^2D states. As a consequence,new term values of the n^2S and n^2D series up to 54^2S and 52^2D have been measured. A new 'saturated ionization' technique of Doppler-free spectroscopy for high lying states based on these experiments is proposed.

Chapter VII contains a review of active frequency stabilization techniques for single frequency fundamental dye lasers. A prototype single frequency second harmonic dye laser which produces about 0.1W of tunable UV with a linewidth of better than 10 MHz at 295 nm is described. A method of fast frequency stabilization of the second harmonic dye laser which uses the harmonic generator also as a modulator is proposed.

The thesis concludes with appendices which detail some of the specialised electronics used in this work, a new method for obtaining a convenient laser frequency reference, and a description of the construction principles of degenerate interferometers for use as laser frequency analysers.

References

1. M B Denton and H V Malmstadt, Appl Phys Lett 18, 485 (1971)
2. J Kuhl and Marowsky, Opt Comm 4, 125 (1971)
3. J Kuhl and H Spitschan, Opt Comm 7, 256 (1973)
4. R D H Brown, An Assessment of Laser-Based Analytical Techniques in Flame Spectroscopy (not published)
5. J A Gelbwachs, C F Klein and J E Wessel, Appl Phys Lett 30 489 (1977)
6. R J Reynolds and K Aldous, Atomic Absorption Spectroscopy, Griffin, London (1970)
7. B A Thrush, Endeavour, New Series 1, 3 (1977)
8. J N Pitts and B J Finlayson-Pitts, Tunable Lasers and Applications, A Mooradian and T Jaeger (Eds), Springer-Verlag, Berlin (1976)
9. H S Johnston, Tunable Lasers and Applications, A Mooradian and T Jaeger (Eds), Springer-Verlag, Berlin (1976)
10. A P Baronavski et al, Tunable Lasers and Applications, A Mooradian and T Jaeger (Eds), Springer-Verlag, Berlin (1976)
11. A P Baronavski et al, Laser Spectroscopy (Haroche et al, Ed), Springer-Verlag, Berlin (1975)
12. J H Clark, Y Haas, P L Houston and C B Moore, Chem Phys Lett 35, 82 (1975)
13. J C Vanderleeden, Laser Focus p51 (June 1977)
14. R T Thompson, J M Hoell and W R Wade, J Appl Phys 46, 3040 (1975)
15. R S Adrain, D J Brassington, S Sutton and R H Varey, Lasers in Chemistry, Conference Digest,Royal Institution, London (1977)
16. V S Letokhov, High Resolution Laser Spectroscopy, Springer-Verlag, Berlin (1976)
17. N Bloembergen and M D Levenson, High Resolution Laser Spectroscopy, Springer-Verlag, Berlin (1976)
18. V A Alekseev, B Ya Zel'dovich and I I Sobel'man, Sov Phys Usp 19, 207 (1976)
19. E V Baklanov and V P Chebotaev, Opt Spectrosc 38, 215 (1975)
20. T W Hänsch, Physics Today, p34 (May 1977)

21. S Chu, E D Commins and R Conti, Phys Lett 60A, 96 (1977)

22. J K Wright, Proc IEEE 51, 1663 (1963)

23. R Polloni and O Svelto, IEEE J Quant Electron, QE-4, 528 (1968)

24. R G Smith, IEEE J Quant Electron QE-6, 215 (1970)

25. D G Gonzalez, S T K Niegh and W H Steier, IEEE J Quant Electron QE-9, 23 (1973)

26. I N Ross, Br J Appl Phys 3, 10 (1970)

27. V D Volosov and V N Krylov, Opt Spectrosc 35, 69 (1973)

28. R G Smith, K Nassau and M F Galvin, Appl Phys Lett 7, 256 (1965)

29. J E Geusic, H J Levinstein, S Singh, R G Smith and L G Van Vitert, Appl Phys Lett 12, 306 (1968)

30. M W Dowley and E B Hodges, IEEE J Quant Electron QE-4, 552 (1968)

31. M W Dowley, Appl Phys Lett 13, 395 (1968)

32. C Gabel and M Hercher, IEEE J Quant Electron, QE-8, 850 (1972)

33. H W Kogelnik, E P Ippen, A Dienes and C V Shank, IEEE J Quant Electron QE-8, 373 (1972)

34. D Fröhlich, L Stein, H W Schröder and H Welling, Appl Phys 11, 97 (1976)

35. S Leutwyler, E Schumacher and L Wöste, Opt Comm 19, 197 (1976)

	DL 200	CMX-4
Pump	Nitrogen Laser	Flashlamp
Wavelength range	258 - 360 nm	265 - 365 nm
Linewidth in UV	0.02 nm	0.1 nm
Peak UV power	10 kW	400 W
Pulse duration	5 n sec	1 μsec
Average UV power	1 mW	10 mW

Table 1 Typical characteristics of two frequency doubled pulsed dye lasers.

Laser Dye	Wavelength range (nm)	Critical phase matched crystal	Non-critical phase match crystal	Non-critical phase match wavelength range (nm)
Cresyl violet	700 - 650	ADP	RDA	700 - 670
Rhodamine B	680 - 610	ADP	RDP	640 - 630
Rhodamine 6G	650 - 570	ADP	ADA	610 - 570
Sodium Fluorescin	580 - 540	ADP	ADP	550 - 540
Coumarin 7	570 - 500	ADP	ADP	540 - 500
Coumarin 102	520 - 460	KPB	ADP	500 - 490
Coumarin 74	500 - 450	KPB		
Coumarin 2	490 - 430	KPB		
Carbostyril 165	480 - 420	KPB		

Abbreviations
ADA - Ammonium Dihydrogen Arsenate
ADP - Ammonium Dihydrogen Phosphate
KPB - Potassium Pentaborate
RDA - Rubidium Dihydrogen Arsenate
RDP - Rubidium Dihydrogen Phosphate

Note KDP can be used to replace ADP over most of the critically phase-matched range

Table 2 Some laser dyes and crystals for frequency doubling in the range 210 nm to 350 nm

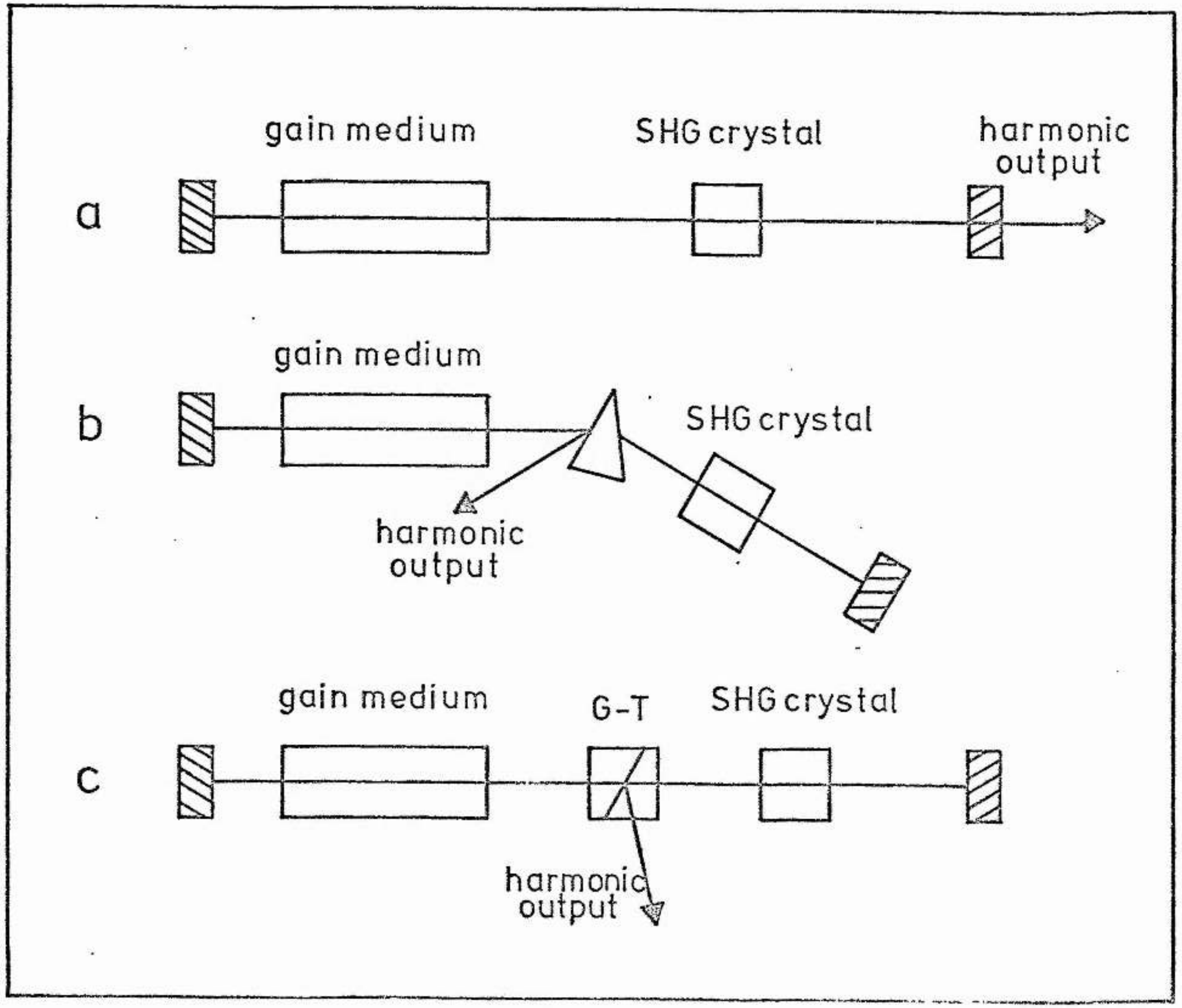

Figure 1. Some possible cavity arrangements for extracting the second harmonic output.

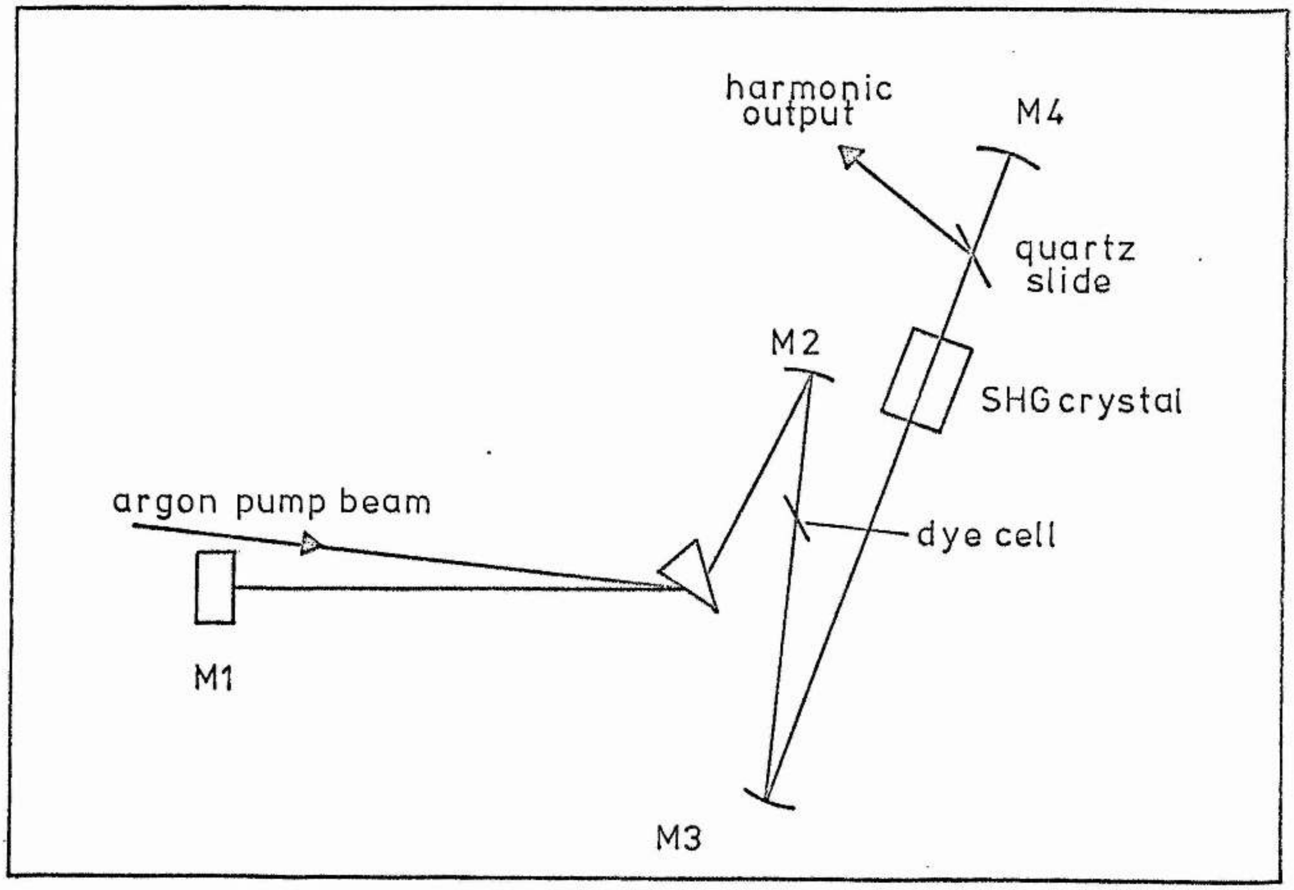

Figure 2. Schematic diagram of the cavity used by Gabel and Hercher[32].

CHAPTER II

REVIEW OF THE PRINCIPLES OF SECOND HARMONIC GENERATION

Abstract

A review of the principles of nonlinear optics with particular reference to second harmonic generation is given in this chapter. Emphasis is given to methods of phase matching and the choice of focusing for maximum conversion efficiency. Thermal effects such as thermal phase mismatching and thermal lensing which reduce the second harmonic generation efficiency are shown to be important when high power continuous wave laser beams are used.

II.1 Introduction

Second harmonic generation was the first nonlinear optical effect to result from the use of laser radiation and was discovered in 1961 shortly after the first demonstration of the ruby laser[1]. Second harmonic generation is still one of the most widely used nonlinear optical processes for the extension of laser radiation to new wavelength regions. The power density required to achieve significant harmonic generation has been dramatically reduced by the use of phase-matching processes. The interaction is made efficient by ensuring that the phase of the propagating wave and the generated nonlinear polarization are in step. For second harmonic generation, phase-matching implies that the phase velocity of the fundamental and second harmonic waves are equal in the nonlinear material. The most common method of achieving phase-matching in a crystal is by the use of natural birefringence of the material.

The second important method of increasing the efficiency of harmonic generation is to focus the fundamental beam into the nonlinear element. This problem has been thoroughly treated including the case where birefringence exists.. Also, several focusing rules have been established for designing a harmonic generation system[2].

An effect which is detrimental to phase-matched harmonic generation is the absorption of fundamental radiation within the nonlinear element[3,4]. This is particularly serious in a continuous-wave system where large average powers are involved. The absorbed radiation leads to a nonuniform heating .which destroys the phase-matching across the laser beam. This effect cannot easily be corrected and leads to a reduction of harmonic power.

In the following we shall consider some the above points with reference to harmonic generation in a crystal.

II.2 Nonlinear Phenomena

When a medium is subjected to an electric field there is an induced polarization. For a weak electric field the polarization is linearly proportional to the applied field and is given by

$$\underline{P} = \varepsilon_o \chi_1 \underline{E} \qquad (1)$$

where χ_1 is the linear susceptibility and ε_o is the permittivity of free space. The linear susceptibility is related to the refractive index of the medium n by the relationship $\chi_1 = n^2 - 1$.

In crystalline media the linear susceptibility is a tensor which follows the symmetry properties of the crystal.For isotropic media there is therefore only one value of the refractive index. For uniaxial media there are two values, n_o the ordinary and n_e the extraordinary indices and for biaxial crystals there are three values of the refractive index, n_α, n_β and n_γ.

A linear polarization is only an approximation to the complete constitutive relation which can be written as a power series in the applied field, as

$$\underline{P} = \varepsilon_o [\chi_1 \cdot \underline{E} + \chi_2 \cdot \underline{E} \cdot \underline{E} + \chi_3 \cdot \underline{E} \cdot \underline{E} \cdot \underline{E} + \dots] \qquad (2)$$

where χ_2 is the second order nonlinear susceptibility and χ_3 is the third order nonlinear susceptibility. Many interesting optical phenomena arise from the second and third order susceptibilities[5]. For example, χ_2 gives rise to second harmonic generation, dc rectification, the linear electro-optic effect, parametric oscillation,and three-frequency sum and difference mixing. The third order susceptibility gives rise to third harmonic generation, the quadratic electro-optic effect, two-photon absorption, and Raman, Brillouin and Rayleigh scattering. We shall consider only effects arising from χ_2.

As with the linear susceptibility, the second order nonlinear susceptibility must display the symmetry properties of the crystal medium. A consequence of this fact is that in centro-symmetric crystals the second order susceptibility must vanish[6]. Second order nonlinear effects can therefore only occur in anisotropic materials.

II.3 Coupled Wave Equations

In order to show how a nonlinear polarization gives rise to generated electromagnetic fields we derive a set of coupled wave equations[5]. To do this we first show how Maxwell's equations can be used to derive a wave equation where the nonlinear polarization acts as the source term responsibl for nonlinear effects.

Maxwell's equations can be written in SI units as

$$\nabla \times \underline{E} = - \dot{\underline{B}} \qquad (3)$$

$$\nabla \times \underline{H} = \dot{\underline{D}} + J \qquad (4)$$

with constituitive relations

$$\underline{D} = \varepsilon\, \underline{E} + \underline{P} \qquad (5)$$

$$\underline{J} = \sigma\, \underline{E} \qquad (6)$$

$$\underline{B} = \mu_o\, \underline{H} \qquad (7)$$

where $\underline{P}$ is the nonlinear part of the polarization. Assuming that the medium is nonmagnetic and nonconducting and taking the curl of equation (3) we obtain

$$\begin{aligned}\nabla \times \nabla \times \underline{E} &= \nabla(\nabla.\underline{E}) - \nabla^2\underline{E} - \frac{\partial}{\partial t}(\nabla \times \underline{B}) \\ &= - \mu_o \frac{\partial}{\partial t}(\nabla \times \underline{H}) \\ &= - \mu_o \frac{\partial^2}{\partial t^2}\, \underline{D} \qquad (8)\end{aligned}$$

or

$$\nabla^2\underline{E} - \mu_o\varepsilon \frac{\partial^2\underline{E}}{\partial t^2} = \mu_o \frac{\partial^2\underline{P}}{\partial t^2} . \qquad (9)$$

This wave equation describes the electric field in the medium generated by the nonlinear polarization $\underline{P}$. The fields referred to in equation (8) are instantaneous fields. We now convert these fields to their Fourier components since it is customary to define the nonlinear susceptibility in terms of frequency components. We can write the electric field and driving polarization as

$$\underline{E}(r,t) = \tfrac{1}{2} [\,\underline{E}\ (\underline{r},\omega)\ \exp i\ (\underline{k}.\underline{r} - \omega t) + c.c.\,] \qquad (10)$$

$$\underline{P}(\underline{r},t) = \tfrac{1}{2} [\,\underline{P}\ (\underline{r},\omega)\ \exp i\ (\underline{k}.\underline{r} - \omega t) + c.c.\,] \qquad (11)$$

We now reduce the problem to one dimension by assuming that the waves propagate only in the z direction. By substituting equations(10) and (11) into equation (9) we find that

$$ik \frac{\partial E}{\partial z} + i\ \omega\ \mu_o\ \varepsilon \frac{\partial E}{\partial t} = - \frac{\omega^2\mu_o}{2}\ P$$

where the slowly varying wave approximation has been made, ie

$$\omega^2 P >> \omega \frac{\partial P}{\partial t} >> \frac{\partial^2 P}{\partial t^2}$$

and $$k \frac{\partial E}{\partial z} >> \frac{\partial^2 E}{\partial z^2}$$

$$\omega E >> \frac{\partial E}{\partial t}.$$

Dividing equation (12) by ik and noting that $k = n\omega/c$ and $\mu_o\varepsilon_o = 1/c^2$ we have

$$\frac{\partial E}{\partial z} + \frac{1}{c}\frac{\partial E}{\partial t} = \frac{i\mu_o c\omega}{2n}\ P. \qquad (13)$$

This equation relates the envelopes of the electric field and nonlinear polarizations. We now go on to use this equation in deriving the coupled wave equation for the particular case of second harmonic generation.

II.4 Second Harmonic Generation

Allowing for the tensor properties of χ_2 and the frequency properties of the electric field, the complete polarization in a frequency summing process is given by a repeated summation of the components of a tensor of order two. However, because of symmetry many of the components are zero and for second harmonic generation the polarization reduces to

$$P_{2\omega} = \varepsilon_o \, d_{eff} \, E_\omega \, E_\omega \exp \left[i(2 \, \underline{k}_\omega - \underline{k}_{2\omega}) \cdot \underline{r} \right] \tag{14}$$

and

$$P_\omega = 2\varepsilon_o \, d_{eff} \, E_{2\omega} \, E_\omega \exp \left[i(\underline{k}_{2\omega} - 2\underline{k}_\omega) \cdot \underline{r} \right] \tag{15}$$

where d_{eff} is the effective nonlinear coefficient for the interaction and will be discussed in section II.5. The subscripts on P and E represent the frequency of the components.

Substituting equations (14) and (15) into equation (13) and assuming a steady state we obtain

$$\frac{dE_\omega}{dz} = i\kappa \, E_{2\omega} \, E_\omega^* \exp (i\Delta kz) \tag{16}$$

$$\frac{dE_{2\omega}}{dz} = i\kappa \, E_\omega \, E_\omega \exp (-i\Delta kz) \tag{17}$$

where

$$\Delta k = k_{2\omega} - 2k_\omega = 4\pi (n_{2\omega} - n_\omega)/\lambda \tag{18}$$

and

$$\kappa = \omega d_{eff}/nc. \tag{19}$$

We now assume that the fundamental wave is undepleted by the generating process, ie $dE_\omega/dz = 0$ and integrate equation (17) over the crystal length ℓ to obtain

$$E_{2\omega} = \int_{-\ell/2}^{\ell/2} i\kappa E_{\omega}^{\ 2} \exp\ (-i\Delta kz)\ dz$$

$$= \kappa E_{\omega}^{\ 2}\,\ell\,\frac{\sin(\Delta k\ell/2)}{(\Delta k\ell/2)}\ . \qquad (20)$$

Noting that the intensity (defined as power per unit area) is given by

$$I = nc\varepsilon_{o}|E|^{2}/2 \qquad (21)$$

the low conversion limit harmonic intensity is given by

$$I_{2\omega} = (2\kappa^{2}\ell^{2}I_{\omega}^{\ 2}/nc\varepsilon_{o})\,\mathrm{sinc}^{2}(\frac{\Delta k\ell}{2}) \qquad (22)$$

This shows how phase-matching enters the conversion process through the phase synchronism factor $\mathrm{sinc}^2\ (\Delta k\ell/2)$. When phase-matching has been accomplished ie $\Delta k\ell = 0$ the generation process is proportional to κ^2, ℓ^2 and the square of the fundamental intensity. This result holds in the plane wave focusing limit where $I = P/A$ and the beam area $A = \pi w_o^{\ 2}/2$ with w_o the gaussian beam electric field radius. The ability to obtain phase-matching is the most important factor in determining the efficiency of the harmonic process and we now discuss some methods of obtaining phase matching in uniaxial crystals.

II.5 Phase-Matching

Since most materials are positively dispersive over the frequency range of interest it is usually the case that $n_{2\omega} > n_{\omega}$ unless special steps are taken. The most common method of ensuring that phase-matching can be accomplished is to use the natural birefringence of the crystalline materials to offset the effect of dispersion.

For wave propagation in birefringent media, an incident wave of arbitrary polarization is resolved into two polarization components upon entering the medium. The polarizations are orthogonal and in uniaxial crystals are resolved into ordinary and extraordinary components. The ordinary wave propagates with an index of refraction n_o which is independent of the propagation direction. The extraordinary wave is polarized in the plane containing the optic axis and the propagation direction and has an index of refraction which is direction dependent and given by

$$1/n_e(\theta) = (\sin^2\theta/n_e{}^2 + \cos^2\theta/n_o{}^2)^{\frac{1}{2}}. \qquad (23)$$

The extraordinary refractive index may be either greater than or less than the ordinary refractive index corresponding to either a positive or negative uniaxial crystal respectively. Unless the crystal birefringence is exactly the correct size the propagation direction for phase matching in the crystal must be chosen at some angle θ such that $n_{e,2\omega}(\theta) = n_{o,\omega}$ for a negative birefringent crystal or $n_{o,2\omega} = n_{e,\omega}(\theta)$ for a positive birefringent crystal. This is referred to as type I phase-matching and, for $\theta \neq 90^o$, as critical phase-matching.

A second parameter, of importance when choosing a propagation direction in the crystal, is the effective nonlinear coefficient which we introduced earlier.

The nonlinear susceptibility used in equation (13) is a tensor and must be evaluated for each crystal symmetry and propagation direction. The parameter d_{eff} is introduced as a convenience so that the repeated summations are evaluated and a single parameter results which can be used in further calculation. The procedure for calculating d_{eff} has been extensively covered for all the acentric point groups[9]. Since we shall be concerned exclusively with ADP and its isomorphs in the point group $\bar{4}2m$ we simply quote the result for the value of d_{eff} in this case.

For a wave propagating at an angle θ to the optic axis and ϕ (see fig 1) to the crystal x-axis the only nonzero nonlinear coefficient is d_{14} (see ref 6,7,9 for a definition of the subscripts) and the effective nonlinear coefficient is

$$d_{eff} = - d_{14} \sin \theta \sin 2\phi. \qquad (24)$$

The value d_{14} can be found in the standard tables[10]. For ADP the value of d_{14} is 5×10^{-13} mV^{-1}.

Clearly, to maximise d_{eff}, ϕ should be chosen to be at 45° to the x-and y-axes. The angle θ will usually be determined by the phase-matching condition however, and d_{eff} cannot always be maximised. It is advantageous to make $\theta = 90^o$ if this is possible.

The more serious aspect of the restriction on the value of θ to allow phase-matching is the double refraction when θ is not equal to 90°. We shall now consider this.

When the extraordinary wave propagates in a crystal its power flow direction differs by the double refraction angle ρ (see fig 1) from the phase velocity direction. The effect is usually referred to as Poynting vector walk-off and leads to a walk-off of the generated beam at an angle ρ. The double refraction angle is given by

$$\rho \simeq \tan \rho = \frac{n_{o,\omega}}{2} \left[1/(n_{e,2\omega})^2 - 1/(n_{o,2\omega})^2 \right] \sin 2\theta \qquad (25)$$

For a laser beam focused into the crystal, the power flow leads to a separation of the extraordinary and ordinary waves after a distance

$$\ell_a = \pi^{\frac{1}{2}} w/\rho \qquad (26)$$

called the aperture length[2]. In equation (26), w is the radius of the focused beam. Typically, the angle ρ in ADA may be 1° and $w = 20$ μm, which gives $\ell_a = 0.2$ cm. This may be less than the total crystal length and can thus lead to a substantial reduction in second harmonic efficiency. When θ is 90° the angle ρ is 0 there is no Poynting vector walk-off and there is thus an infinite aperture length. Again 90° phase-matching is desirable when it is possible.

A further advantage of 90° phase-matching is the increased acceptance angle over a critically phase-matched crystal. (The acceptance angle is the change in angle θ which reduces the harmonic generation from its maximum at perfect phase-matching to zero. This occurs when the phase mismatch Δk goes from zero to $2\pi/\ell$ (see equation (22).)

The acceptance angle can be calculated by expanding the phase mismatch parameter Δk in a Taylor series in θ about the phase-matching condition to give

$$\Delta k(\theta) = \Delta k(\theta_m) + \frac{\partial \Delta k}{\partial \theta}\Big|_{\theta_m} (\theta - \theta_m) + \frac{\partial^2 \Delta k}{\partial^2 \theta}\Big|_{\theta_m} (\theta - \theta_m)^2/2! .$$

The first term in this expansion is zero since θ_m is the phase-matching angle. For a critically phase-matched negative uniaxial crystal the acceptance angle $\delta\theta(\theta_m)$ which gives $\Delta k(\theta) = 2\pi/\ell$ is found by using the second term in the expansion and is

$$\delta\theta(\theta_m) = \lambda / [\, \ell(n_{o,2\omega} - n_{e,2\omega}) \sin(2\theta_m) \,] . \tag{27}$$

For a noncritically phase-matched crystal with $\theta_m = 90^\circ$, the second term in the expansion is zero and the acceptance angle is given by the third term as

$$\delta\theta(90^\circ) = [\, \lambda/2\ell(n_{o,2\omega} - n_{e,2\omega}) \,]^{\frac{1}{2}} . \tag{28}$$

The ratio of acceptance angles for the same medium is

$$\delta\theta(90^\circ)/\delta\theta(\theta_m) = \sin 2\theta_m \, [\, \ell(n_{o,2\omega} - n_{e,2\omega})/2\lambda \,]^{\frac{1}{2}} . \tag{29}$$

Typical values for the above parameters are $\sin 2\theta_m \simeq 1$, $\ell \simeq 1$ cm,

$(n_{o,2\omega} - n_{e,2\omega}) \approx 10^{-2}$, $\lambda \approx 6 \times 10^{-5}$ cm. This gives a ratio of acceptance angles, $\delta\theta(90^{\circ})/\delta\theta(\theta_m) \approx 10$.

This means that when 90° phase-matching is not possible the angular tolerance on harmonic generation is more critical. This can have its effects when strong focusing is attempted or when a highly divergent laser beam(such as is found in a multimode laser)is used to perform harmonic generation in a critically phase-matched crystal.

II.6 Focusing

In order to perform efficient harmonic generation it is important that the fundamental beam shall be focused into the crystal. This is particularly important when a relatively low power continuous-wave source is used. In this section we consider the effects of focusing on the harmonic generation process. The gaussian nature of laser beams is also taken into account in the analysis.

The fundamental mode electric field is described by

$$\underline{E}(r,z) = \underline{E}_o \frac{w_o}{w(z)} \exp\left[-i(kz-\phi)\right] \exp\{-r^2[\frac{1}{w^2(z)} + \frac{ik}{2R}]\} \qquad (30)$$

where

$$\phi = \tan^{-1}(z/z_R) \qquad (31)$$

and

$$2z_R = b = w_o{}^2 k. \qquad (32)$$

In the above, ϕ is the phase factor for a TEM_{oo} mode, b is the confocal parameter of the beam, z_R is the Rayleigh range, R is the wavefront curvature, w_o is the electric field radius at the focal point $z = 0$ and k is the wavevector, $k = 2\pi n/\lambda$.

The beam radius is, in general, a function of the distance z along the beam propagation direction given by

$$w^2(z) = w^2_o\,[\,1 + (z/z_R)^2\,] \tag{33}$$

and the wavefront curvature is

$$R(z) = z\,[\,1 + (z_R/z)^2\,]\,. \tag{34}$$

The far field beam diffraction angle is

$$\theta = \lambda/\pi w_o\,. \tag{35}$$

The z dependent electric field leads to complications in solving the coupled nonlinear equations and only an integral solution is possible. The solution of the coupled wave equations including beam diffraction and the effects of Poynting vector walk-off have been considered by Boyd and Kleinman[2]. We shall discuss the results of their analysis.

According to Boyd and Kleinman[2] the second harmonic power can be written in terms of a reduction factor $h(B,\xi)$ as

$$P_{2\omega} = \left(\frac{2\omega^2\, d_{eff}^{\,2}}{\pi n_\omega^{\,2} n_{2\omega}\varepsilon_o c^3}\right) P_\omega^{\,2}\,\ell k_\omega h(B,\xi) = K h(B,\xi)\,\ell P_\omega^{\,2} \tag{36}$$

where B is the walk-off parameter

$$B = \tfrac{1}{2}\,\rho\,(\ell k_\omega)^{\frac{1}{2}} \tag{37}$$

and ξ is the focusing parameter

$$\xi = \ell/b. \tag{38}$$

The factor $h(B,\xi)$ determines the reduction of the second harmonic power due to Poynting vector walk-off and to focusing. The factor $h(B,\xi)$ is plotted in figure 2 as a function of walk-off B. In this it has been assumed that ξ has been chosen to maximise $h(B,\xi)$. It is often important to determine how much second harmonic power will be generated in the fundamental mode. Boyd and Kleinman have calculated a second reduction factor $\overline{h}(B,\xi)$ which determines the power in the second harmonic generated in the fundamental mode and it is also shown in figure 2. It can be seen in figure 2 that for small B ie small walk-off angles, or for crystal lengths much smaller than the aperture length, the factor $\overline{h}(B,\xi) \rightarrow h(B,\xi)$. This corresponds to the total second harmonic output becoming less multimode due to walk-off and becoming more fundamental mode in nature.

The reduction factor $\overline{h}(B,\xi)$ is shown as a function of ξ for various values of the walk-off parameter B in figure 3. The maximum value of $\overline{h}(B,\xi)$ is 1.068 and occurs when there is no walk-off at $\xi = 2.84$ $(B = 0)$. For small values of ξ, $\overline{h}(B,\xi)$ decreases approximately linearly with ξ as is predicted by a calculation based on a near field assumption that the beam spot size is approximately constant throughout the crystal.

In the presence of strong focusing $(\xi \gg 1)$ the divergence of the focused beam approaches the acceptance angle of the crystal and the harmonic power is reduced.

In the intermediate region $(\xi \sim 1)$ the crystal walk-off is the principal factor determining the reduction of the harmonic power. In this region the reduction factor can be approximately written

$$\overline{h}(B,\xi) \rightarrow \pi/4B^2 \qquad (B^2/4 > \xi > 2/B^2). \qquad (39)$$

In addition to seriously reducing the harmonic power crystal walk-off also flattens the reduction factor over a wide range of focusing parameters.

In order to keep the intensity on the crystal surface as small as possible, ξ should be chosen such that $\xi \gtrsim 2/B^2$. This condition corresponds to a focal spot size w given by

$$w \lesssim \rho \ell / (2\sqrt{2}). \tag{40}$$

For larger spot sizes the harmonic efficiency is reduced and for smaller spot sizes the second harmonic conversion is practically constant but the laser intensity on the crystal increases.

A series of limiting forms has been evolved which enables us to choose parameters for practical designs. Introducing an effective length due to focusing

$$\ell_f = 2b/\pi \tag{41}$$

and using the aperture length ℓ_a defined in equation (26), the limiting forms can be summarized as follows[2]:

$$P(2\omega) = \frac{KP\omega^2}{w^2} \begin{cases} \ell^2 & (\ell_a,\ \ell_f \gg \ell) & (42) \\ \ell\ell_a & (\ell_f \gg \ell \gg \ell_a) & (43) \\ \ell_f\ell_a & (\ell \gg \ell_f \gg \ell_a) & (44) \\ 4\ell_f{}^2 & (\ell \gg \ell_a \gg \ell_f) & (45) \\ 4.76\ell_f{}^2 & (\ell_a \gg \ell \gg \ell_f). & (46) \end{cases}$$

The first limit corresponds to plane wave focusing where $h(\xi, B) \simeq \ell/b$ and the harmonic conversion efficiency is optimised at $\ell/b = 2.84$ where $h = 1.068$.

When $\rho \neq 0$ the aperture length will limit the interaction length to the second and third cases. In general, the last two cases are not encountered experimentally.

Hitherto, crystal absorption has been neglected. Absorption in the crystal can clearly have the effect of reducing the fundamental and harmonic field. However, we shall be particularly concerned by the thermal heating which the absorption of radiation creates. This has a detrimental effect on the harmonic efficiency and will be discussed in the next section.

II.7 Thermal Effects

When a laser beam with a Gaussian intensity profile is partially absorbed in going through a crystal the deposited energy gives rise to a temperature variation across the beam. This nonuniform heating of the crystal causes a nonuniform variation of refractive index of the crystal and results in a phase change across the beam. Nonuniform phase mismatching, thermal self-focusing and self-defocusing can be the result of these variations.

For a heat source of Gaussian form and assuming cylindrical symmetry with propagation direction along the z-axis the temperature distribution over the crystal is given by the heat diffusion equation for a steady state as[8]

$$d^2\, T/dr^2 + (dT/dr)/r + (q/\kappa_T)\exp(-2r^2/w_o^2) = 0 \qquad (47)$$

where q is the averaged absorbed power per unit volume and is given by

$$q = P_\omega(0)\{1-\exp(-\delta_1 \ell)\}/2\pi\ell \int_0^\infty r dr\ \exp(-2r^2/w_o^2)$$

$$\simeq 2P_\omega(0)\ \delta_1/\pi w_o^2 \qquad (48)$$

where the approximation in equation (48) is valid for small $\delta_1\ell$ and where κ_T is the thermal conductivity of the crystal and δ_1 is the absorption coefficient at the fundamental wavelength. Absorption of the second harmonic is assumed to have a negligible effect. Provided that when r = 0, dT/dr is not infinite the solution to equation (47) is

$$dT/dr = (P_\omega\delta_1/2\pi\kappa_T)\{1 - \exp(-2r^2/w_o^2)\}/r. \qquad (49)$$

A good approximation to this temperature profile is[4]

$$T(r) = (P_\omega \delta_1 / 2\pi\kappa_T) \exp(-r^2/w_o{}^2) \qquad (50)$$

in that the first three terms of the Taylor expansion of equation (50) are equal to the corresponding ones in the expression that is obtained by expanding equation (49) in a series and integrating term by term. Close to the axis, the temperature distribution can be further approximated by a quadratic dependence[3],

$$T(r) = T(0) - (P_\omega \delta_1 / 2\pi\kappa_T)(r^2/w_o{}^2). \qquad (51)$$

The deflection of the part of the beam at a distance r from the axis of the beam is approximately given by

$$\theta = \left| \frac{\partial}{\partial r} \int_o^\ell [\, n_\omega(r,z)/n_\omega(0) \,] \; dz \right|. \qquad (52)$$

The deflection of the beam at its waist is thus

$$\theta = (P_\omega \delta_1 \ell / P_T)\theta_d \qquad (53)$$

where θ_d is the angle of beam divergence given by

$$\theta_d = 2/k_1 w_o \qquad (54)$$

The critical dissipated power is given by

$$P_\ell = \lambda_1 \kappa_T (\partial n_\omega / \partial T)^{-1} \qquad (55)$$

and determines when thermal lensing has a signficiant effect. If the total power absorbed in the crystal exceeds the critical value P_L, the divergence due to the thermal lensing effect becomes comparable to the divergence of the focused beam. The thermal lensing effect may not have a very serious effect on the harmonic power generated since, as shown by Boyd and Kleinman[2], the generated power is not a strong function of the focusing parameter over the region where this parameter is optimum (see figure 3). However, if the crystal is inside a laser cavity the lensing effect can seriously upset the cavity stability and eventually lead to a completely unstable cavity.

Inserting values typical of ADP into equation(55) ($\lambda_1 = 6 \times 10^{-5}$ cm, $\kappa_T = 2 \times 10^{-2}$ W cm^{-1} K^{-1}, $(\partial n_\omega/\partial T) = 3 \times 10^{-5}$ K^{-1}) the critical dissipated power obtained is $P_L \approx 40$ mW. For crystals with low absorption coefficients in the region of $\delta_1 \approx 10^{-3}$ cm^{-1}, the thermal lensing effect should not be significant except for fundamental powers greater than about 20W or for long crystals.

We now consider the reduction of harmonic power due to the nonuniform phase change across the beam profile. In the near field limit the expression (30) for the TEM$_{oo}$ Gaussian mode reduces to

$$E(r) = E(0)\ \exp(-r^2/w_o^2). \tag{56}$$

The second harmonic field amplitude generated by such a wave amplitude at the fundamental wavelength is given by

$$\begin{aligned} E_{2\omega}(r) &= \kappa \ell E_\omega^{\,2}(r)\ \mathrm{sinc}^2(\Delta k\ell/2) \\ &= \kappa \ell E_\omega^{\,2}(0)\ \exp(-2r^2/w_o^2)\ \mathrm{sinc}^2(\Delta k\ell/2). \end{aligned} \tag{57}$$

The second harmonic power is therefore given by

$$P_{2\omega} = \frac{n_\omega c\varepsilon_o}{2} \int_0^{2\pi} \int_0^{\infty} |\ E_{2\omega}(r)\ |^2 r\,dr\,d\phi \tag{58}$$

and the fundamental power is

$$\begin{aligned} P_\omega &= \frac{n_\omega c\varepsilon_o}{2} \int_0^{2\pi} \int_0^{\infty} |\ E_\omega(r)\ |^2 r\,dr\,d\phi \\ &= \frac{n_\omega c\varepsilon_o}{2} \left(\frac{\pi w_o^{\,2}}{2}\right) |\ E_\omega(0)\ |^2 . \end{aligned} \tag{59}$$

The total second harmonic power generated by the fundamental wave is

$$P_{2\omega} = (\kappa^2 \ell^2 P_\omega^{\,2}/n_\omega c\pi\varepsilon_o w_o^{\,4}) \int_0^\infty e^{(-4r^2/w_o^{\,2})} \mathrm{sinc}^2(\Delta k\ell/2)\,r\,dr \qquad (60)$$

Under phase-matching conditions the second harmonic power reduces to

$$P_{2\omega}^{\,o} = (\kappa^2\ell^2/8n_\omega c\varepsilon_o \pi w_o^{\,2})P_\omega^{\,2} \qquad (61)$$

The effect of phase-mismatching across the beam can be obtained by expanding the momentum mismatch parameter Δk about the phase-matched condition. For a negative uniaxial crystal which is type I, critically phase-matched the expansion gives

$$\begin{aligned}\Delta k &= (4\pi/\lambda)\{n_{o,\omega} - n_{2\omega}(\theta_m)\}_{T=T_m} \\ &+ (4\pi/\lambda)\{\partial[n_{o,\omega} - n_{2\omega}(\theta_m)]/\partial T\}_{T=T_m}(T-T_m). \end{aligned} \qquad (62)$$

Since θ_m and T_m are the phase-matched angle and temperature respectively, the first term on the right hand side of equation (62) is zero. The second term expresses the phase mismatch caused by the nonuniform heating.

If it is assumed that the crystal is adjusted such that phase-matching is achieved in the centre of the beam, $(T - T_m)$ in equation (62) will be given as $(P_\omega\delta_1/2\pi\kappa_T)\ \{1 - \exp(-r^2/w_o^{\,2})\}$. The second harmonic power is therefore given by

$$P_{2\omega} = (\kappa^2\ell^2 P_\omega^{\,2}/n_\omega c\pi\varepsilon_o w_o^{\,4}) \int_0^\infty \exp(-4r^2/w_o^{\,2})\ \frac{4\sin^2[a\{1-\exp(-r^2/w_o^{\,2})\}/2]}{a^2\{1-\exp(-r^2/w_o^{\,2})\}^2}\ r\,dr \qquad (63)$$

where $$a = 2\beta P_\omega\delta_1\ell/\lambda\kappa_T \equiv P_\omega/P_T \qquad (64)$$

and $$\beta = (\partial n_{o,\omega}^{\;o}/\partial T - \partial n_{2\omega}(\theta_m)/\partial T)\ \Big|_{T-T_m} \qquad (65)$$

The reduction of harmonic power from that expected when there are no thermal effects is

$$h_T = P_{2\omega}/P_{2\omega}^{o} = (8/w_o^{\,2}) \int_0^\infty \exp(-4r^2/w_o^{\,2})\ \frac{4\sin^2[a\{1-\exp(-r^2/w_o^{\,2})\}/2]}{a^2\{1-\exp(-r^2/w_o^{\,2})\}^2}\ r\,dr \qquad (66)$$

Evaluating the integral, the following result is obtained

$$h_T = (8/a^2)\,[\,a\mathrm{Si}(a) - (1 \cos a) - 3(\gamma - \mathrm{Ci}(a) + \ln a) + 3(a - \sin a)/a$$
$$-(a/2 - \sin a)/a - (1 - \cos a)/a^2\,] \qquad (67)$$

where

$$\mathrm{Si}(a) = \int_o^a (\sin x/x)dx$$

$$\mathrm{Ci}(a) = \int_o^a (\cos x/x)dx$$

γ = Euler's constant = 0.57721.

This is the result obtained by Okada and Ieiri[4*]. In the approximation of equation (51) the reduction factor becomes

$$h_T = (8/w_o{}^2)\int_o^\infty \exp\,(-4r^2/w_o{}^2)\mathrm{sinc}^2\,[\,ar^2/2\omega_o{}^2\,]\ rdr$$

$$= (8/a)\,[\,\arctan\,(a/4) - (2/a) - \ln(1 + a^2/16)] \qquad (68)$$

This is the result obtained by Mikhina et al[3] and corresponds to a quadratic phase variation across the beam.

When the parameter a becomes very large both of the equations (67) and (68) reduce to

$$h_T \to (4\pi/a) \qquad (69)$$

The parameter h_T is plotted as a function of a in figure 4 using the results of Okada and Ieiri[4] and those of Mikhina et al[3]. The results agree within a tolerance of about 10% and both predict a behaviour in which the second harmonic power is quadratic in fundamental power at low powers and saturates to being linearly dependent at high power. We shall show in Chapter III how this can considerably modify the design of an intracavity second harmonic laser.

---

*Notice that there is a misprint in their equation (10).

II References

1. P A Franken, A Hill, C Peters and G Weinreich, Phys Rev Lett 7 118 (1961)
2. G D Boyd and D A Kleinman, J Appl Phys 39, 3597 (1968)
3. T V Mikhina, A P Sukhorukov and I V Tomov, Zh Prikl Spectrosk 15, 1001 (1971)
4. M Okada and S Ieiri, IEEE J Quant Electron 7, 469 (1971)
5. R W Minck, R W Terhune and C C Wang, Appl Opt 5, 1595 (1966)
6. N Bloembergen, Nonlinear Optics, Benjamin, New York (1965)
7. F Zernike and J E Midwinter, Applied Nonlinear Optics, Wiley, New York (1973)
8. H S Carslaw, Mathematical Theory of the Conduction of Heat in Solids, MacMillan, London (1921)
9. C Flytzanis, Theory of Nonlinear Susceptibilities, Quantum Electronic Vol I, Nonlinear Optics Part A, H Rabin and C L Tang (Eds), Academic Press, New York (1975)
10. S Singh, Handbook of Lasers p497, R J Pressley (Ed), The Chemical Rubber Co, Cleveland, Ohio (1971)

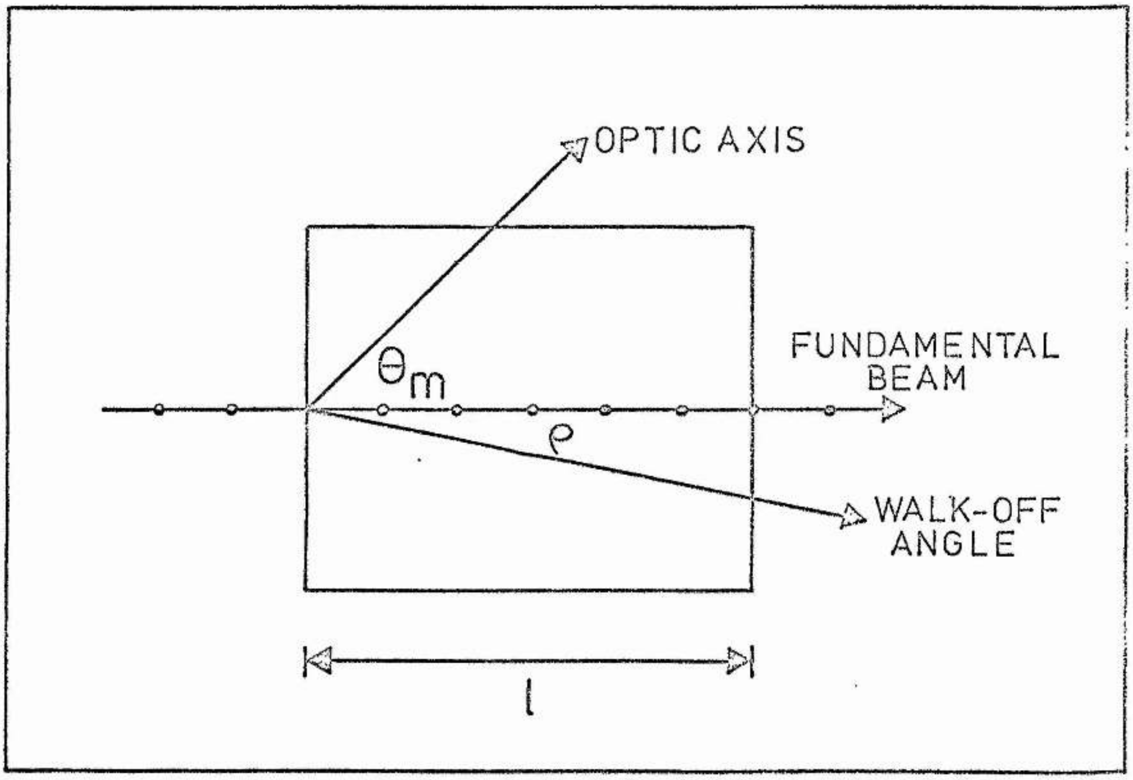

Figure 1. A schematic diagram of a second harmonic crystal of length ℓ. The phase matching angle θ_m and walk-off angle ρ are indicated. The electric field vector of the fundamental beam is polarized perpendicular to the plane of the page for type I phase-matching.

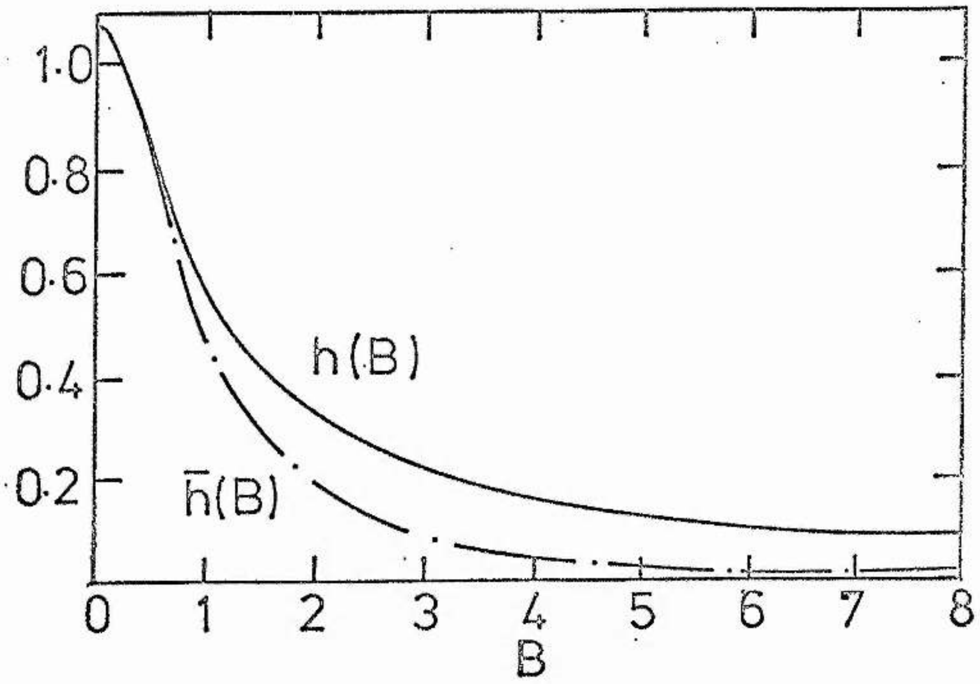

Figure 2. The reduction of second harmonic conversion at optimum focusing due to the Poynting vector walk-off parameter B.

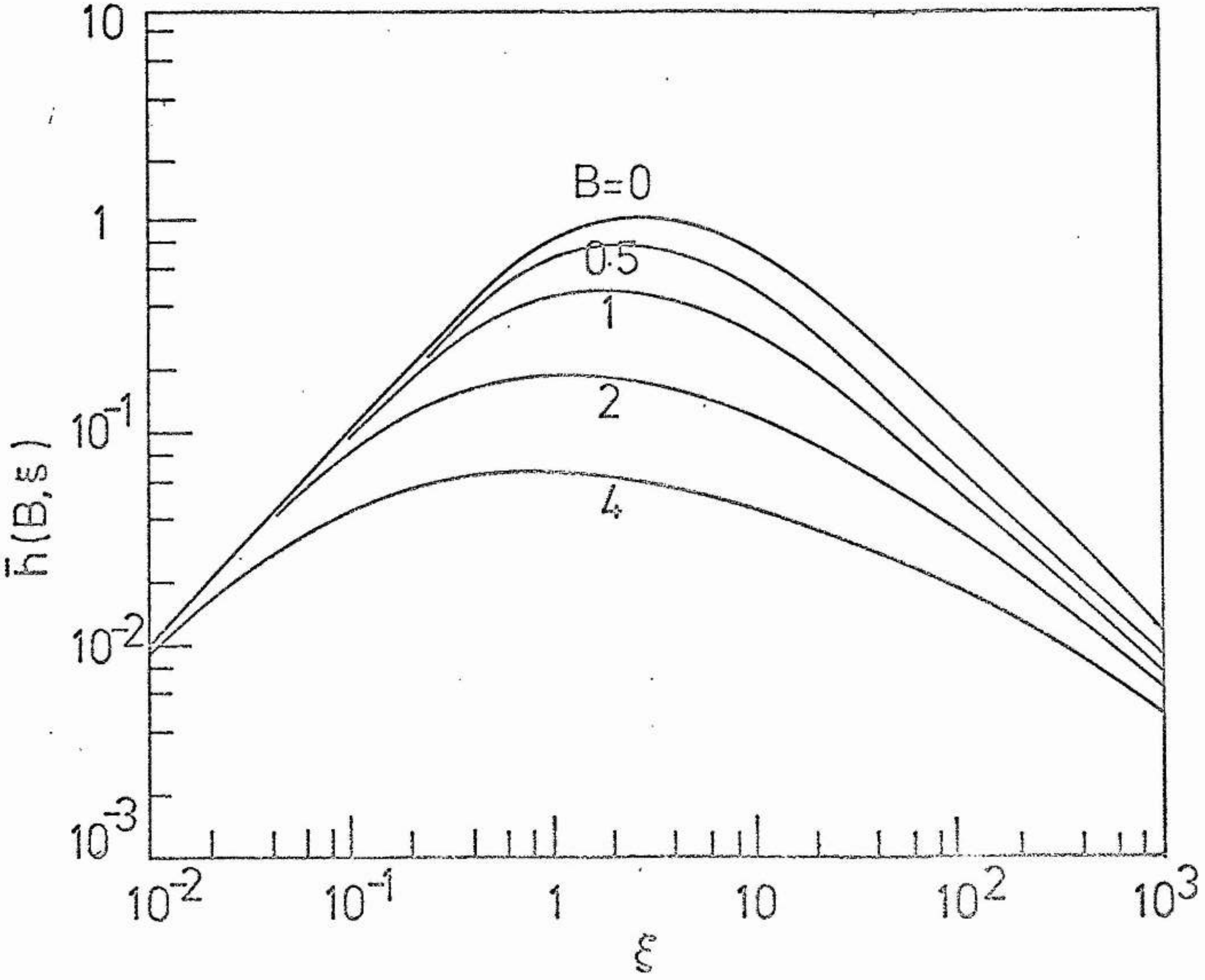

Figure 3. The second harmonic reduction factor $\overline{h}$ (B,ξ) as a function of the focusing parameter for various values of the walk-off parameter B.

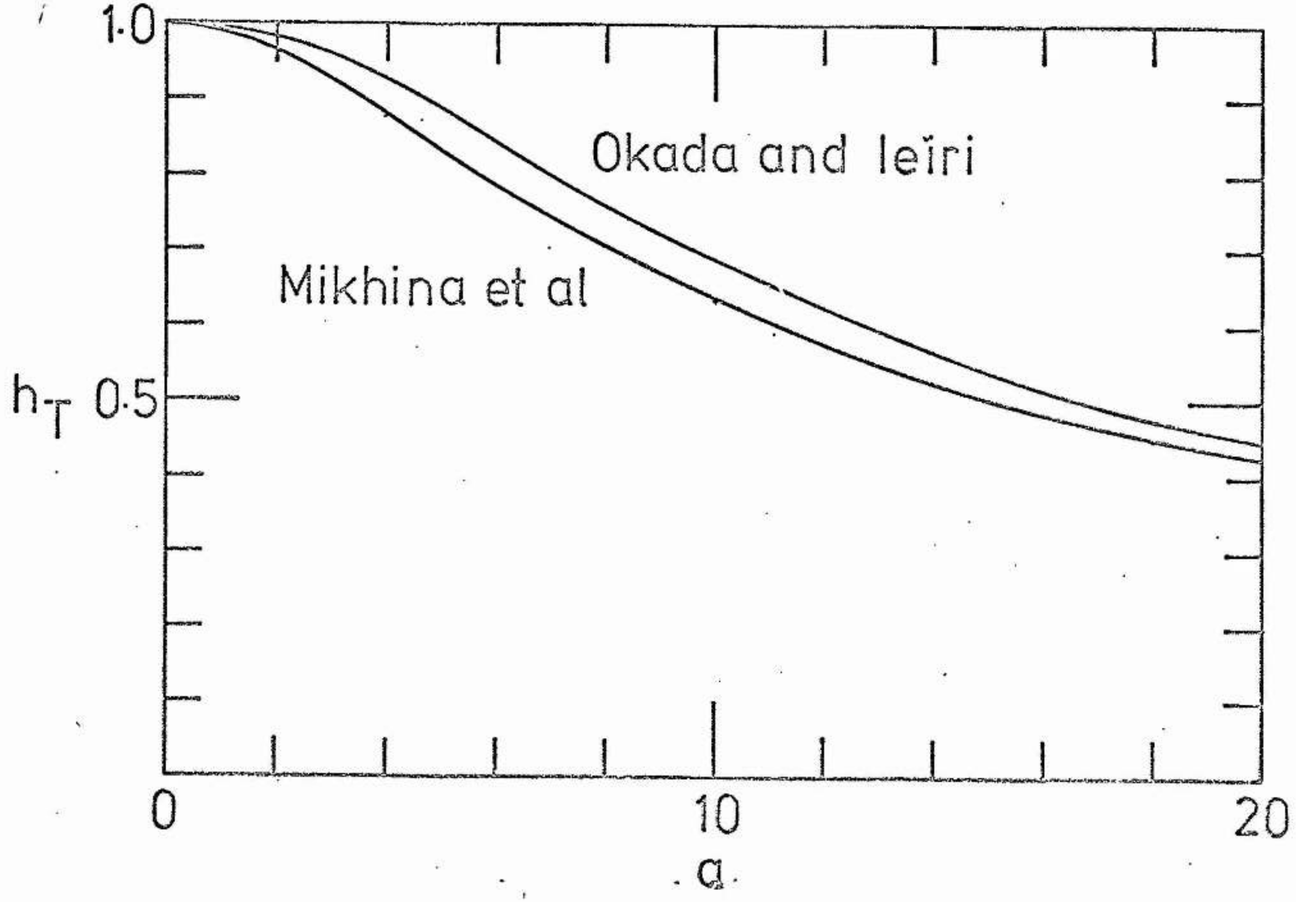

Figure 4. The reduction of second harmonic conversion as a function of the normalised fundamental power. The upper line is a plot of the results of Okada and Ieiri[4] and the lower is that of Mikhina et al[3].

CHAPTER III

A THEORY OF SECOND HARMONIC GENERATION IN DYE LASERS

Abstract

A new theoretical analysis of intracavity second harmonic generation in a dye laser is developed. The model includes absorption and its associated thermal phase mismatching effect in the crystal and excited state absorption in the dye. The resulting coupled nonlinear equations are solved by computer. The results are shown to be quite different from the conclusions of more simple analyses where thermal effects and absorption in the crystal are neglected. Optimum conversion efficiency and choice of crystal lengths are given for a range of pumping powers, crystal absorption and linear losses from the cavity.

III.1 Introduction

The generation of second harmonic radiation by locating the doubling element inside the laser cavity has been extensively treated[1-5]. Most analyses have dealt specifically with the case of harmonic generation with solid state lasers. The simplest model of intracavity second harmonic generation is that proposed by Smith[2]. This model has been described in Chapter I and the main results are quoted here. In Smith's model the lasing transition is assumed to be homogeneously broadened and the laser cavity is assumed to have mirrors which are totally reflecting at the fundamental wavelength. The effect of the nonlinear harmonic generator in the cavity is accounted for by introducing a power-dependent reflection coefficient which corresponds to the output coupling via second harmonic generation. This coupling is assumed linear in intracavity power. The fundamental power within the laser cavity is found by equating the saturated laser gain to the sum of the linear (parasitic) and nonlinear (useful) losses. On solving the resulting equation two interesting points arise. The first is that there is an optimum nonlinear coupling coefficient which is dependent upon the linear loss of the cavity but independent of the pumping power. The linear loss in the cavity directly increases the amount of nonlinearity required to extract the maximum second harmonic power but once the nonlinearity has been chosen to maximise the second harmonic power this will be the optimum coupling for all pump powers. This is in contrast to the case of a normal homogeneously broadened laser where the optimum output coupling is dependent on pump power. The second interesting point to arise from the solution of the 'gain equals loss' equation is that the second harmonic power output at optimum coupling is exactly equal to the power available from the laser operating at the fundamental wavelength when the optimum transmission mirror has been chosen.

Subsequent analyses of the problem of intracavity second harmonic generation have been slightly more sophisticated than Smith's approach but the basic models have been similar. Volosov et al[3] have introduced more complex gain equations which are applicable to three and four level lasers and have allowed for saturation of second harmonic generation at high harmonic conversion efficiencies. They also allowed for absorption in the nonlinear medium and in a subsequent paper considered the effect of wave mismatch conditions[5].

In our approach to the problem of harmonic generation in the cavity of a dye laser we use the model of Teschke et al[6] for high power continuous-wave dye lasers and allow for crystal absorption and its associated thermal effects in the harmonic generation process[7,8].

III.2 Dye Laser Model

An energy level diagram of a typical laser dye is shown in Figure 1. The photophysical properties of dyes have been extensively discussed in the literature and no detailed description is given here. The very fast thermalization time within the vibrational - rotational continuum of a given electronic level allows the dye to be considered as homogeneously broadened. As a consequence, the population of each electronic level is considered *in toto*, and emission and absorption from and to a given band influences the entire population regardless of the wavelength of the radiation. A change in wavelength only changes the relative magnitude of the interaction and is described by a wavelength dependent cross-section.

Stimulated emission takes place at the laser wavelength with cross-section σ_e given by

$$\sigma_e = E(\lambda)\lambda^4/8\,\pi\,\tau_1\,c\,n^2 \qquad (1)$$

where n is the index of refraction of the dye medium, τ_1 is the fluorescence decay time and $E(\lambda)$ is the fluorescence line shape normalized such that

$$\int_0^\infty E(\lambda)d\lambda = \phi \qquad (2)$$

where ϕ is the quantum efficiency. The total fluorescence lifetime is given by

$$\tau_1^{-1} = \tau_{1r}^{-1} + k_{ss} + k_{st} \qquad (3)$$

where τ_{1r} is the radiative lifetime of S_1, k_{ss} is the nonradiative singlet ($S_1 \rightarrow S_0$) relaxation rate and k_{st} is the singlet-triplet cross-over rate. The fluorescence quantum efficiency ϕ is related to these quantities by

$$\phi = \frac{\tau_{1r}^{-1}}{\tau_{1r}^{-1}+k_{ss}+k_{st}} = \frac{\tau_1}{\tau_{1r}} . \qquad (4)$$

A schematic diagram of the dye laser geometry used, is shown in figure 2. The pump beam (I_p) propagates in one direction only, while the laser beam consists of two oppositely running waves (I_ℓ^+, I_ℓ^-), assumed to have uniform area. The quantities I_p, I_ℓ^+ and I_ℓ^- are the intensities of the respective beams (photons sec^{-1} cm^{-2}). The steady state photon transport equation for the pump is

$$\frac{dI_p}{dx} = I_p \left[\sigma_{ap}^{0} N_0 + \sigma_{ap}^{1} N_1 \right] \qquad (5)$$

where σ_{ap}^{0} is the ground state absorption cross-section of pump radiation and σ_{ap}^{1} is the excited S_1 state absorption cross-section of the pump radiation. The populations of the ground and excited states are N_0 and N_1 respectively. The second term on the right hand side of this expression represents excited state absorption which will be detrimental to laser action and is the first departure of the Teschke et al[6] model from other simple dye laser models. For one of the laser beams the steady state photon transport equation becomes

$$\frac{dI_\ell^{+}}{dx} = I_\ell^{+} [\sigma_e N_1 - \sigma_{a\ell}^{1} N_1 - \sigma_{a\ell}^{0} N_0 - \sigma_{a\ell}^{t} N_t] \qquad (6)$$

where $\sigma_{a\ell}^{1}$, $\sigma_{a\ell}^{0}$ and $\sigma_{a\ell}^{t}$ are the cross-sections for absorption of the laser beam radiation by the excited state, ground state and triplet state, respectively. The population of the triplet state is N_t.

The population rate equation for S_1 is

$$\frac{dN_1}{dt} = \sigma_{ap}^{0} N_0 I_p - N_1 \frac{1}{\tau_1} - N_1 \sigma_e I_\ell + N_0 \sigma_{a\ell}^{0} I_\ell \qquad (7)$$

where $I_\ell = I_\ell^{+} + I_\ell^{-}$. This equation neglects the effect of population change of the S_1 state due to $S_1 \to S_2$ transitions because the molecules in the S_2 states rapidly return to S_1[6]. The rate equation for the triplet state is

$$\frac{dN_t}{dt} = k_{st} N_1 - \frac{1}{\tau_t} N_t \qquad (8)$$

where τ_t is the lifetime of the triplet state.

The final rate equation is

$$N_0 + N_1 + N_t = N_{tot} = \text{constant}. \qquad (9)$$

The photon transport equations (5,6) and the population rate equations (7,8,9) constitute the basic equations of the dye laser medium.

We now consider a laser cavity with a nonlinear element, such as a harmonic generator, within the cavity. The output coupling is given by

$$T_2 = I_2^{+}/I_\ell^{+} \qquad (10)$$

where I_2^{+} is the one way second harmonic power generated after the fundamental radiation of power I_ℓ^{+} passes through the crystal. The fundamental power is assumed to be constant throughout the crystal in calculating the generated harmonic power but the power generated at the harmonic frequency is lost to the cavity. The nonlinear crystal is assumed to present bulk absorption to the fundamental laser beam with an absorption coefficient δ_1. Absorption at the second harmonic is neglected. In addition to the loss presented by crystal absorption there will be residual loss ℓ_o which includes mirror diffraction losses, scattering in the dye and from mirrors, windows etc. The fractional attenuation in a one-way pass which includes both linear and nonlinear losses is

$$\Lambda = \frac{I_{\ell\,f}^{+}}{I_{\ell\,i}^{+}} = 1 - T_2 - \ell_o - \delta_1 L \qquad (11)$$

The gain of the laser medium in a one-pass in the absence of losses is defined as

$$G = \frac{I_{\ell\,f}^{+}}{I_{\ell\,i}^{+}} \qquad (12)$$

where i and f in equations indicate initial and final values. Under steady-state conditions we have

$$G = 1/\Lambda = (1 - T_2 - \ell_o - \delta_1 L)^{-1}. \qquad (13)$$

The equations (5 - 9) can now be solved to obtain the steady state intracavity power and consequently the harmonic output power. The solution of these equations can be greatly simplified if it is assumed that the ground state absorption of the laser radiation is neglected ($\sigma_{a\ell}^{0} = 0$). This is a reasonable assumption for most laser dyes over the wavelength range of laser operation. In this case the equations (5 - 9) reduce to

$$N_0\, \sigma_{ap}^{0}\, I_p = N_1\ (1/\tau_1 + \sigma_e\, I_\ell) \qquad (14)$$

$$dI_p/dx = -I_p\ (\sigma_{ap}^{0}\, N_0 + \sigma_{ap}^{1}\, N_1) \qquad (15)$$

$$dI_\ell^{+}/dx = I_\ell^{+}\, N_1\, \sigma_{ef} \qquad (16)$$

where

$$\sigma_{ef} = \sigma_e - \sigma_{a\ell}^{1} - \sigma_{a\ell}^{t} k_{st} \tau_t \tag{17}$$

and the solution to equation (8), $N_t = N_1 k_{st} \tau_t$, has been used. Equation (16) can be solved by rewriting it as

$$\frac{1}{I_\ell^+} dI_\ell^+ = N_1 \sigma_{ef} \frac{dx}{dI_p} dI_p \tag{18}$$

Combining this with (15) and integrating through the length of the dye t, we obtain

$$\ell n \frac{I_{\ell f}^+}{I_{\ell i}^+} = - \int_{I_{pi}}^{I_{pf}} \frac{dI_p}{I_p} \cdot \frac{\sigma_{ef} N_1/N_o}{\sigma_{ap}^{o} + \sigma_{ap}^{1} N_1/N_o} \tag{19}$$

On substituting for N_1/N_o from equation (14) this reduces to

$$\ell n\ G = - \int_{I_{pi}}^{I_{pf}} \frac{dI_p}{I_p} \frac{\sigma_{ef} \sigma_{ap}^{o} I_p}{\sigma_{ap}^{1} (\sigma_{ap}^{o} I_p + \sigma_{a\ell}^{o} I_\ell)} \tag{20}$$

The quantity I_ℓ can be shown to be fairly constant throughout the thickness t[9] and so this equation gives

$$\ell n\ G = - \frac{\sigma_{ef}}{\sigma_{ap}^{1}} \ \ell n \left[\frac{1 + I_\ell/I_s + I_p/I_1}{1 + I_\ell/I_s + TI_p/I_1} \right] \tag{21}$$

where

$$I_s^{-1} = \sigma_e \tau_1 \tag{22}$$

$$I_1^{-1} = \sigma_{ap}^{1} \tau_1 \tag{23}$$

and $T = I_{pf}/I_{pi}$ is the transmission of the dye at the pump wavelength. The transmission of the pump beam can be found by first integrating equations (15) and (16) to give

$$\ell n\ T = -t\ \overline{N}_o\ \sigma_{ap}^{\ o} - t\ \overline{N}_1\ \sigma_{ap}^{\ 1} \tag{24}$$

$$\ell n\ G = t\ \overline{N}_1\ \sigma_{ef} \tag{25}$$

where

$$\overline{N}_i = \frac{1}{t} \int_o^t N_i\ dx \tag{26}$$

is the average population of the i'th state over the length of the active medium. The equations (24) and (25) can be used to obtain

$$\ell n T = -t\ N_{tot}\ \sigma_{ap}^{\ o} + \frac{\sigma_{ap}^{\ 1}}{\sigma_{ef}}\ (\gamma - 1)\ \ \ell n\ \frac{1}{(1 - T_2 - \ell_o - \delta_1 \cdot L)} \tag{27}$$

where

$$\gamma = (1 + k_{st}\ \tau_t)\ \sigma_{ap}^{\ 0}/\sigma_{ap}^{\ 1} \tag{28}$$

The first term on the right hand side of equation (27) is the small signal transmission of the pump beam assumed in most simple dye laser models. The other term is a correction term due to the pumping of molecules into the excited singlet states and has the effect of reducing the dye transmission. However, this increased pump absorption does not result in gain, but only in a rapid circulation of the dye molecules between the S_1 and S_2 states. Since the nonlinear coupling T_2 is a function of the intracavity laser power the transmission is also dependent on the laser power.

Using the expression for the laser gain (21) and dye transmission (27) we can now calculate the intracavity power and hence the second harmonic power. The equation (21) can be rewritten as

$$(1 + I_\ell/I_s + TI_p/I_1)G^{\sigma_{ap}^{\ 1}/\sigma_{ef}} = 1 + I_\ell/I_s + I_p/I_1 \tag{29}$$

Solving this equation for I_ℓ and using equation (13) we have

$$I_\ell = I_p \frac{\sigma_{ap}^{1}}{\sigma_e} \frac{1 - TQ}{Q - 1} - \frac{1}{\sigma_e \tau_1} \qquad (30)$$

where

$$Q = [1 - T_2 - \ell_o - \delta_1 L]^{-\sigma_{ap}^{1}/\sigma_{ef}} = G^{\sigma_{ap}^{1}/\sigma_{ef}} \qquad (31)$$

In equation (30) the first term gives the slope efficiency while the second term indicates threshold. When the above equations are expanded for $\sigma_{ap}^{1}/\sigma_{ef} << 1$, $T_2 - \ell_o - \delta_1 L << 1$ and $\sigma_{a\ell}^{1} = 0$ they reduce to the well known results presented by Snavely[10], ie

$$I_\ell = I_p \frac{\sigma_{ef}/\sigma_e}{(T_2 + \ell_o + \delta_1 L)} (1 - T) - \frac{1}{\sigma_e \tau_1} \qquad (32)$$

Although the results (27, 30, 31) of the above model are somewhat more complex than standard theoretical models of dye lasers there are various ways in which the model can be improved. The major modification which can be included is the extension to include the Gaussian beam nature of the pump and laser light. Pike[10] has considered this problem for a simpler dye laser model and when the active region is confined within a distance less than confocal parameters of the beam waists Pike's result is

$$P_\ell = \frac{\mu}{(1 + \mu^2)^{\frac{1}{2}}} \left[\frac{\sigma_{ef}/\sigma_e}{T_2 + \ell_o + \delta_1 L} (1 - T) P_\phi - \frac{1 + \mu}{2} \frac{hc\pi w_p^{\,2}}{\lambda_1 \sigma_e \tau_1} \right] \qquad (33)$$

where μ is the ratio of the areas of the dye laser and pump beams

$$\mu = \frac{\pi w_\ell^{\,2}}{\pi w_p^{\,2}} \qquad (34)$$

The equations no longer contain intensities (I_e, I_p) but now include the corresponding powers (P_ℓ, P_p) measured in Watts. We follow Teschke et al[6] in assuming that the results of Pike can be simply included in the equation (30). Although there is no proof that this approach is valid in the model including excited states, the limiting forms suggest that the expressions are reasonable assumptions in view of the difficulty of including them in a rigorous manner. The intracavity power can be written

$$P_\ell = \eta \; (P_p - P_{th}) \tag{35}$$

where

$$\eta = \frac{\mu}{\sqrt{(1 + \mu^2)}} \, \frac{\sigma^1_{ap}}{\sigma_e} \, \frac{1 - TQ}{Q - 1} \tag{36}$$

and the threshold pump power is

$$P_{th} = \beta/\eta \tag{37}$$

where

$$\beta = \frac{1 + \mu}{2} \, \frac{\pi \, w_p^{\;2} \, hc}{\sigma_e \, \tau_1 \, \lambda_1} \tag{38}$$

The equations (35 - 38) constitute the basic results of the dye laser model. We now solve them for the particular case of intracavity harmonic generation.

The second harmonic power generated by a fundamental power P_ℓ is given by

$$P_2 = K \;\; h \, h_T \; L \; P_\ell^{\;2} \tag{39}$$

where the parameters have been defined in Chapter II. This expression includes thermal phase mismatching effects through the parameter h_T. The nonlinear coupling $T_2 = P_2/P_\ell$ is inserted into the equation (27) to give the transmission of the dye and equation (31) to give the laser gain. These equations are finally substituted into equation (35) to determine the intracavity power. Now both T and Q are dependent on the intracavity power through T_2 and so the steady state value of the intracavity power has to be determined by an iterative approach. When the intracavity power has been calculated it is easy to calculate the generated second harmonic power using equation (39). A simple computer programme was devised to perform this procedure and the results are presented in section III.3.

Our theoretical model of the dye laser includes linear absorption in the crystal which gives rise to severely reduced second harmonic generation due to a thermal effect. The nonradiative processes in the laser dye can also give rise to thermal effects which can affect the performance of the laser.

More than 90% of the pump radiation is absorbed by the dye. Of this approximately 25% goes into nonradiative processes which generate heat[11,12]. This gives rise to refractive index inhomogeneities in the dye solvent which can seriously affect the operation of the dye laser. Even when the dye is swept out of the pump beam rapidly as in the case of jet stream dye laser, the absorption can cause astigmatism and other deleterious effects[11,12]. However, by suitable choice of dye solvent[13], flow rate, and cavity parameters, the thermal effects in the dye jet stream can be minimised. We therefore do not consider jet stream thermal effects in our analysis of cavity parameters and assume that they can be eliminated by suitable design of laser and choice of dye solvent[13].

Since there are two counter propagating beams in the laser cavity the harmonic radiation will be generated in both directions. It is possible to enhance the second harmonic output by reflecting the generated radiation back into the cavity and through the crystal so that harmonic radiation propagates in one direction and all the radiation can, in principle be extracted as described in Chapter I. However, apart from the practical difficulties of obtaining mirror coatings which reflect both the fundamental and its second harmonic this method suffers from the fact that if a cancellation of the harmonic is not to occur the phase of the generated harmonic must be carefully controlled. This results in the separation between the harmonic reflecting mirror and the nonlinear crystal being a critical quantity. We therefore assume that the resonator mirrors are transparent to the harmonic radiation and that it is extracted in one direction only.

The thermal effects in the crystal which were discussed earlier are insensitive to the direction of propagation of radiation and when evaluating the generated harmonic power the total intracavity power propagating in both directions must be used in the calculations.

III.3 Results

The results of the above analysis are now presented. Attention is restricted to the case of a rhodamine 6G dye laser with non-critically phase-matched ADA (ammonium dihydrogen arsenate) crystal inserted into the cavity. The extension to other crystals and dyes is a simple matter provided sufficient information on the relevant parameters is available. The analysis can also incorporate the case of critically phase-matched crystals although the dependence of harmonic generation on crystal length is quite different from the non-critically phase-matched case due to walk-off between the fundamental and generated harmonic radiation. The result in such a case is likely to differ significantly from those on the assumption of non-critical phase-matching.

Our final assumption is that the laser cavity can be constructed to provide a focus in the crystal which is close to the optimum calculated by Boyd and Kleinman ($\xi = 2.84$, $h = 1.068$) the details of which have been discussed earlier (Chapter II). The parameter h is not a strong function of ξ and in most cases of interest the focusing will be close to optimum.

The value of the computed second harmonic efficiency ($E = P_2/P_p$) as a function of crystal length is shown in figure 3(a). A pump power of 10W from a TEM_{oo} argon ion laser operating at a wavelength of 514 nm has been assumed. The values of the various parameters used are as shown in the figure caption. The effect of neglecting thermal degradation of harmonic generation is shown in figure 3(c). It can be seen very clearly that thermal effects must be considered when calculating the harmonic output and that discrepancies become increasingly large at the longer crystal lengths. Also shown in figure 3 is the harmonic efficiency when excited state absorption by the dye is not taken into account; the results when thermal effects are included are shown in figure 3(b) and when not included are shown in figure 3(d). By comparing figures 3(c) and 3(d) it can be seen that the inclusion of excited state absorption is important in determining the harmonic efficiency especially at longer crystal lengths where the coupling is increased. The inclusion of thermal effects in the crystal renders the harmonic efficiency somewhat less sensitive to excited state absorption (cf figures 3(a,b) and 3(c,d)).

Some physical insight into the results of figures 3(a) and 3(b) can be gained by realising that when the thermal effects become serious, ie for long crystals or a high power, the harmonic power saturates and becomes linear in intracavity power. This leads to an effectively fixed output coupling given by

$$T_2 = (\pi/2)KhLP_T \tag{40}$$

This simplifies the analysis considerably. When the laser is well above the threshold the harmonic efficiency when excited state absorption is neglected is obtained from equation (33) as

$$E = P_2/P_p = \frac{\mu}{\sqrt{(1 + \mu^2)}} \frac{(\sigma_{ef}/\sigma_e)T_2}{T_2+\ell_o+\delta_1 L} (1-T) \qquad (41)$$

Using the value for T_2 given by equation (40) and the same parameters as before, the efficiency as a function of crystal length is shown in figure 3(f). A similar process can be used in determining the harmonic efficiency when excited state absorption is included, and the result is shown in figure 3(e). For long crystal lengths the thermal effects become more serious and the constant coupling indicated by equation (40) becomes a better approximation. As can be seen by comparing figures 3(e) with 3(a) and 3(f) with 3(b), the behaviour predicted by a constant harmonic coupling (40) closely approximates the more rigorous treatment of thermal effects given earlier.

For a given pump power there is a maximum in the second harmonic power with respect to crystal length. The length at which the harmonic power is maximised is designated L_{opt} and is plotted in figure 4 as a function of the pump power when the linear loss is $\ell_o = 5\%$ and $\delta_1 = 0.005\ \text{cm}^{-1}$ as before. In figure 4(a) the thermal effects on the crystal and excited state absorption of the dye have been included. As can be seen in the figure, the optimum crystal length is strongly dependent on pumping power and increases rapidly in the region of laser threshold. As the pump power increases, the thermal effects begin to strongly effect the harmonic power and it soon becomes necessary to reduce the crystal length to offset the thermal effects and maintain optimum coupling. The results of the model when excited state absorption is neglected is shown in figure 4(b). As in figure 3, the difference between the results when excited state absorption is included and when neglected is not very great and thermal effects are mainly responsible in determining the optimum crystal length. When the thermal effects in the crystal are neglected the result is shown in figures 4(c)and 4(d) which are based on the inclusion of excited state absorption and its neglect, respectively. As before, there is again a significant difference in the predicted performance of the laser between the two cases.

If excited state absorption and thermal effects in the nonlinear crystal are neglected and it is assumed that the laser is operated well above threshold,the harmonic efficiency is given by equation (41) and the output coupling is given by

$$T_2 = KhLP_\ell \qquad (42)$$

On inserting this value for T_2 into equation (41) and then solving the resulting equation simultaneously with equation (39), a value for P_2 can be determined.

On differentiating the expression for P_2 with respect to the crystal length L and setting the differential to zero one finds that the maximum harmonic output is given at an optimum crystal length L_{opt} where

$$L_{opt} = \frac{\ell_o}{\delta_1 + 2\beta Kh} \qquad (43)$$

If δ_1 is set equal to zero in this equation the result reduces to that of Smith[2]. When the values appropriate to a Rhodamine 6G dye and ADA crystal combination, (ie $\beta = 2.5W$ and $Kh = 1.6 \times 10^{-4}$ cm^{-1} W^{-1}(are inserted into equation (43), it appears that the value of δ_1 dominates $2\beta Kh$ unless the crystal absorption, δ_1 is much less than 10^{-3}cm^{-1}. Values of δ_1 are typically in the range 10^{-3} - 10^{-2} cm^{-1} and it is therefore clear that, in an intracavity frequency doubled dye laser the crystal absorption plays a major role in determining the optimum output coupling quite apart from the thermal effects which crystal absorption invariably introduces. The optimum length deduced using equation (43) is indicated in figure 4(e).

As may be expected, the optimum length predicted by equation (43) is always greater than the optimum length when thermal effects are included.

This is the crux of the results of this analysis. The allowance for crystal absorption greatly reduces the optimum output coupling of a second harmonic dye laser even when thermal effects are not included. When thermal effects are included, the reduction in optimum coupling is severe and, at pump powers barely in excess of threshold, the optimum coupling actually decreases with pumping power. When thermal effects in the crystal are included the output coupling is reduced to such a level that excited state absorption in the dye does not have a particularly serious effect.

We now explore the optimum crystal length and maximum harmonic power as a function of pump power for a range of cavity linear losses and crystal absorptions. The results presented are based on the model including both thermal effects and excited state absorption. In figure 5(a) the optimum crystal length is plotted as a function of pump power for a variety of linear losses ℓ_o between 1 and 9 per cent but with a fixed crystal absorption of δ_1 of 0.005 cm^{-1}. In figure 5(b) the corresponding efficiencies of harmonic generation E_{opt} are plotted.

From figures 5(a,b) it can be seen that linear loss manifests itself in two important ways. Firstly, the optimum crystal length is sensitive to linear loss. This is because a decreasing loss leads to a higher circulating field and the onset of thermal effects takes place at shorter crystal lengths. Secondly, as can be seen in figure 5(b), even at these shorter crystal lengths, the efficiency of conversion increases rapidly with decreasing linear loss. The saturation of optimum conversion efficiency with increasing pump power shown in figure 5(b) is due to the onset of thermal effects changing the output coupling from being linearly dependent on circulating field to being independent of circulating field.

In figure 6(a) the optimum crystal length is plotted as a function of pump power for a variety of crystal absorptions δ_1 between 2.5×10^{-3} cm^{-1} and 10^{-2} cm^{-1} but at a fixed linear loss of $\ell_o = 0.05$. The corresponding harmonic efficiency E_{opt} is plotted in figure 6(b). The choice of optimum crystal length is very sensitive to the pumping power especially at low crystal absorptions and the harmonic efficiency is greatly reduced by the absorption.

III.4 Conclusion

In this chapter we have shown the importance of using a realistic model in designing a harmonic laser for maximum efficiency. By including thermal phase mismatching effects in the crystal and excited state absorption of the dye in the model the behaviour predicted is quite different to that based on simpler models. In order to choose a length of crystal for optimum conversion efficiency it is necessary to measure or estimate its absorption at the fundamental wavelength and also to know the linear loss of the laser cavity. In many cases this information will not be available but the results do show that it is not always desirable to use a crystal which is as long as possible and that the expected efficiency may be much lower than that predicted by previous models. However, in all models it is clear that crystals with very low absorption and cavities with very low losses are necessary to obtain high harmonic efficiency.

References

1. R Polloni and O Svelto, IEEE J Quant Electron QE4, 528 (1968)
2. R G Smith,IEEE J Quant Electron QE6, 215 (1970)
3. V D Volosov, S G Karpenko, V N Krylov, A A Man'ko and V L Strizhevskii, Sov J Quant Electron 5, 500 (1975)
4. V G Dimitriev and I Ya Itskhoki, Sov J Quant Electron 5, 735 (1975)
5. V G Dimitriev, N E Kornienko, A I Ryzhkov, V L Shizhevskii and E A Shalaev, Sov J Quant Electron 6, 209 (1976)
6. O Teschke, A Dienes and J R Whinney, IEEE J Quant Electron QE12, 383 (1976)
7. M Okada and S Ieiri, IEEE J Quant Electron QE7, 469 (1971)
8. T V Mikhina, A P Sukhorukov and I V Tomov, Zh Prikl Spectrosk 15, 1001 (1971)
9. V Ganiel, A Hardy, G Neumann and D Treves, IEEE J Quant Electron QE11, 881 (1975)
10. B B Snavely, Dye Lasers, F P Schafer (Ed) Springer-Verlag, Berlin (1973)
11. B Wellegehausen, L Laepple and H Welling, Appl Phys 6, 335 (1975)
12. O Teschke, J R Whinnery and A Dienes, IEEE J Quant Electron QE12, 513 (1976)
13. S Leutwyler, E Schumacher and L Wöste, Opt Comm 19, 197 (1976)

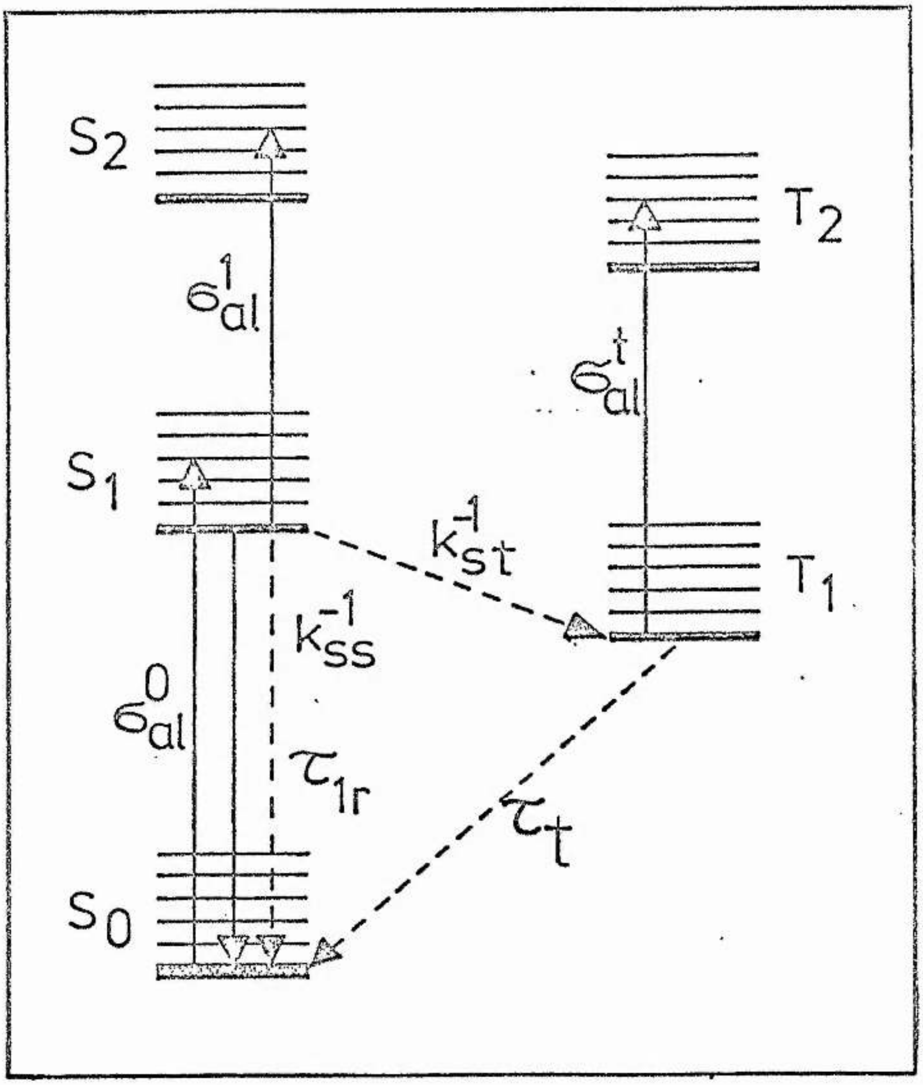

Figure 1. Schematic energy level diagram of a dye molecule. Solid lines indicate radiative processes,broken lines indicate nonradiative processes. Stimulated emission, represented by cross-section θ_e occurs between the S_1 and S_0 manifolds.

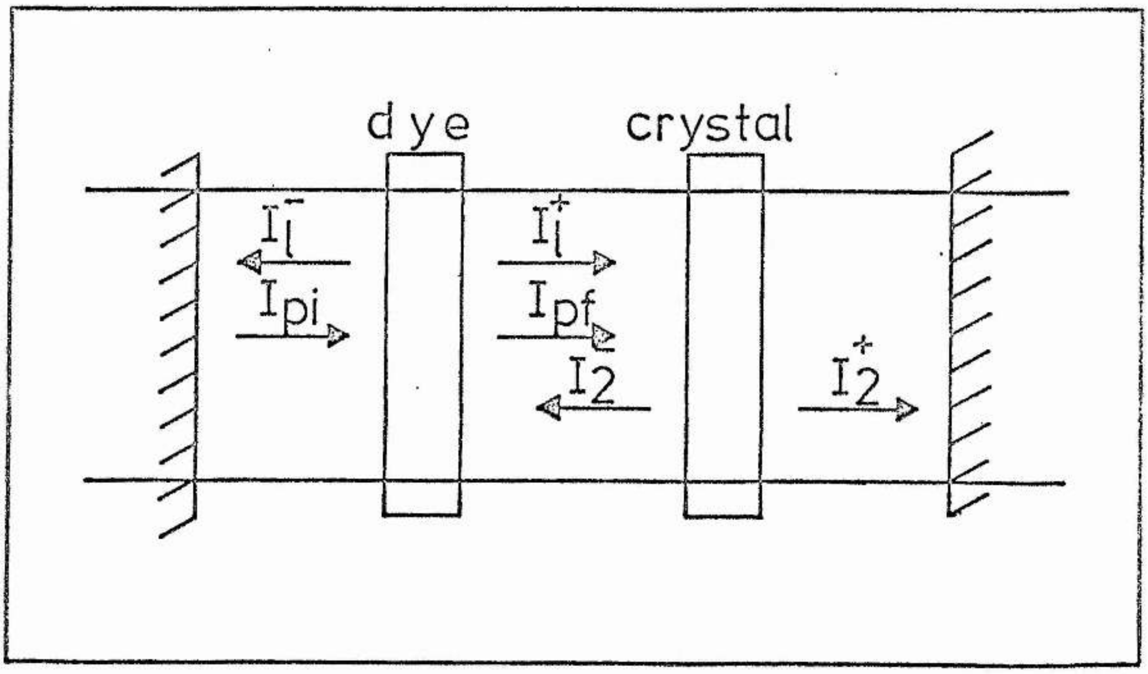

Figure 2. Geometry of the laser cavity used in the calculations.

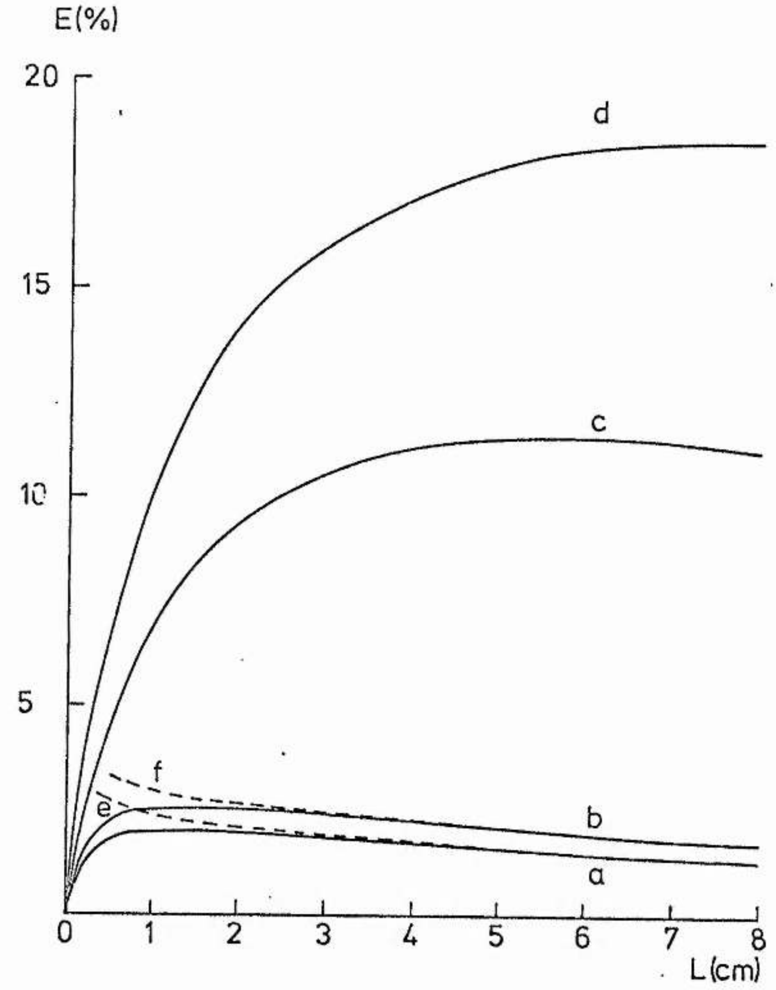

Fig. 3. Variation of second harmonic efficiency E with crystal length. Linear loss of the cavity l_0 is 5 percent and absorption coefficient of crystal is 0.005 cm^{-1}. A pump power of 10 W from a 5145 A Ar^+ laser is assumed. Curve *a* is based on the assumption of excited-state absorption cross section to pump radiation of $\sigma_{ap}^{1} = 1.75 \times 10^{-16}$ cm^2. Curve *b* is based on the assumption that $\sigma_{ap} = 0$. Curves *c* and *d* are similar to *a* and *b*, respectively, except that thermal effects in crystal have been neglected. Curves *e* and *f* are based on assumption of fixed output coupling given by (6). Other parameters are: $\sigma_{ap}^{0} = 1.53 \times 10^{-16}$ cm^2, $\sigma_e = 2.1 \times 10^{-16}$ cm^2, $\sigma_{al}^{f} = 0.45 \times 10^{-16}$ cm^2, $\tau_1 = 5 \times 10^{-9}$ s, $k_{st}\tau_f = 0.08$, $\mu = 1$, $\omega_p = 20$ μm, $t = 0.05$ cm, $\lambda = 610$ nm, $N = 4.2 \times 10^{17}$ cm^{-3}. Parameters of the crystal are, $\kappa_T = 2 \times 10^{-2}$ $W\,cm^{-1}\,K^{-1}$, $[|dn_2/dt - dn_1/dT|] = 4 \times 10^{-5}$ K^{-1}, $Kh = 1.6 \times 10^{-4}$ $W^{-1}\,cm^{-1}$.

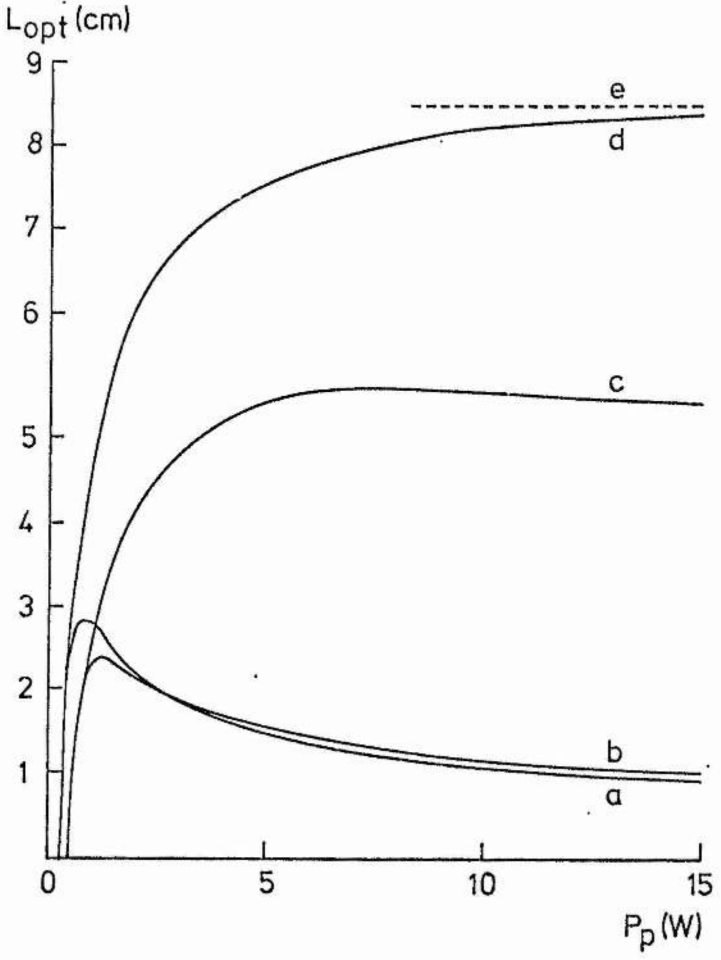

Fig. 4. Variation of optimum length L_{opt} with pump power. Curve *a* is based on model including thermal effects but neglecting excited-state absorption. Curve *d* neglects both excited-state absorption and thermal effects in the crystal. Curve *c* includes excited-state absorption but neglects thermal effects whereas curve *b* includes both excited states and thermal effects. The dotted line *e* indicates the optimum length calculated using (7). The parameters of the dye, crystal, and cavity are the same as those used in Fig. 3.

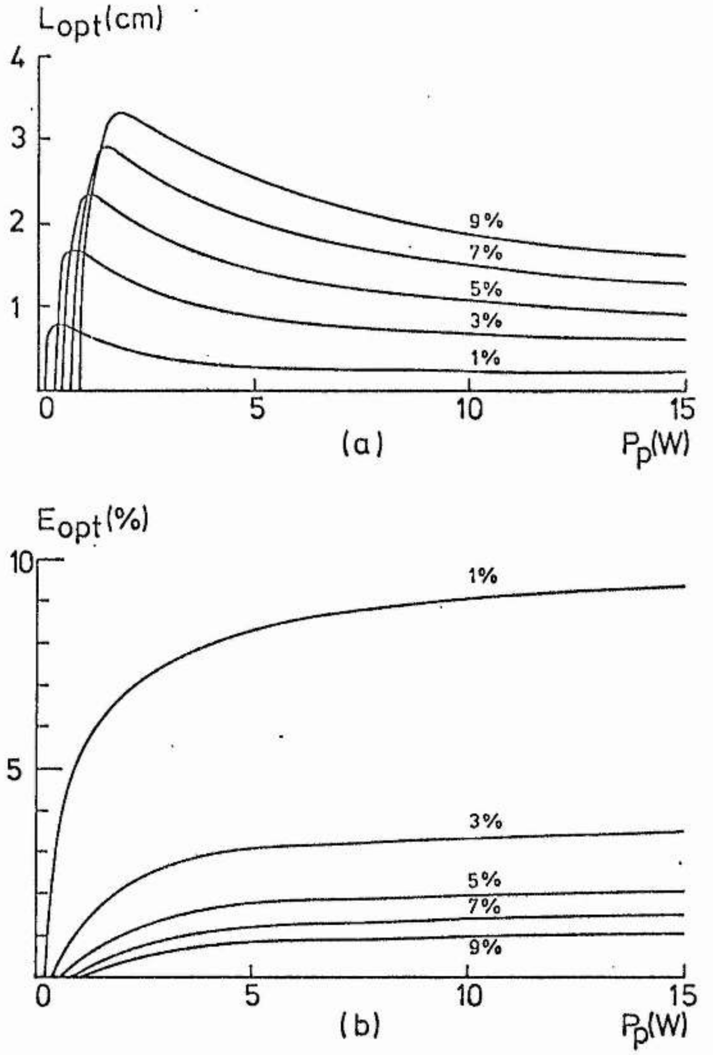

Fig. 5. (a) Variation of optimum crystal length with pump power for model including thermal effects and excited states. Percentage linear loss of cavity for each curve shown in figure. Other parameters are the same as in Fig. 1. (b) Optimum second-harmonic efficiency ($L = L_{opt}$) as a function of pump power at various values of linear loss indicated in the figure. Other parameters are same as in Fig. 3.

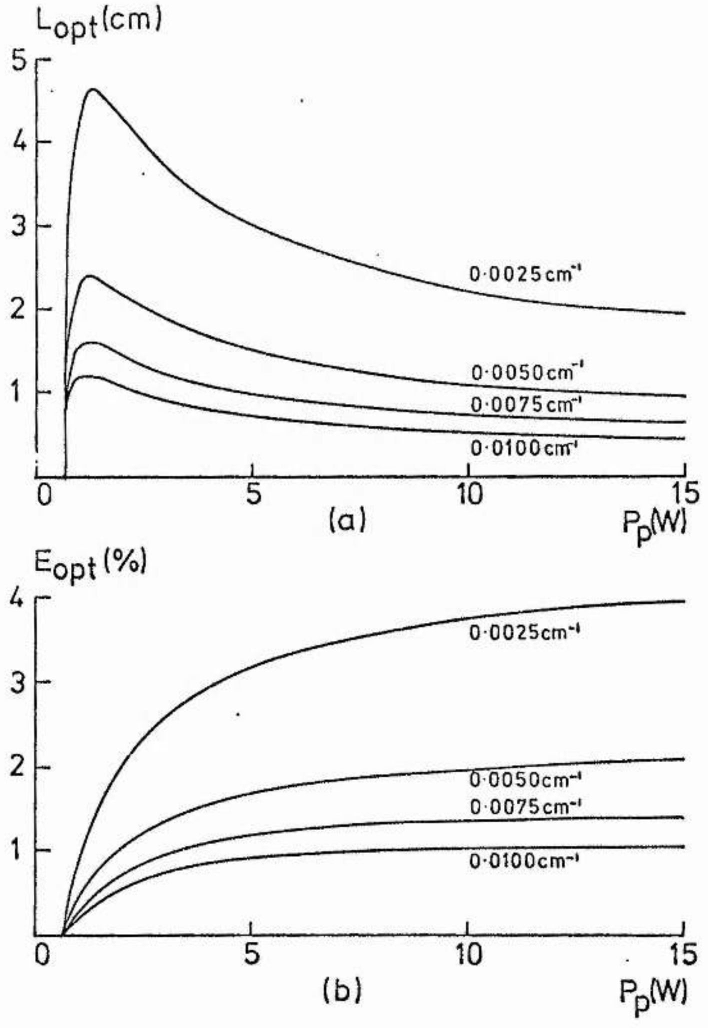

Fig. 6. (a) Variation of optimum crystal length with pump power at various values of crystal absorption δ_1 indicated in figure. This model includes thermal effects and excited state absorption. Other parameters are the same as those used in Fig. 3. (b) Corresponding variation in optimum second harmonic efficiency ($L = L_{opt}$) at indicated values of crystal absorption.

CHAPTER IV

COMA COMPENSATION IN OFF-AXIS LASER RESONATORS

Abstract

The optical aberrations of coma and astigmatism introduced on focusing into a Brewster angled crystal are calculated. An original calculation of the coma of a tilted interface and off-axis mirror is given. It is demonstrated that it is possible to compensate for both coma and astigmatism if the Brewster angled crystal and off-axis mirror are orientated in a particular manner. With this arrangement both aberrations can be eliminated for a unique off-axis angle which depends only on the refractive index of the crystal. Some cavity designs for the compensation of coma and astigmatism are discussed.

IV.1 Introduction

We have shown in Chapter III that linear losses of the laser cavity must be kept to a minimum to extract the maximum second harmonic power. Clearly precautions must be taken to eliminate the Fresnel reflection losses which occur when a crystal is inserted into a laser cavity. Several methods exist for doing this. The most common method of reducing the reflection losses is to anti-reflection coat the surface of a pair of windows set against the crystal. Reflection losses between the crystal surface and the inside surface of the window are reduced by putting an index-matching fluid between them. This method works very successfully when low average powers are incident on the crystal such as in a pulsed laser system. However, over a period of several days exposure to high power laser radiation,the index-matching fluid becomes opaque to the generated ultraviolet. This results in increased heating on the crystal surface and eventually to crystal damage. Another technique for reducing the reflection losses is to directly anti-reflection coat the crystal. This can be quite difficult to perform in practice since most nonlinear crystals are water based, are very sensitive to rapid temperature changes and have to be kept at temperatures less than about 100°C. When anti-reflection coatings are applied under such conditions they tend to be rather soft, absorbant and susceptible to optical damage.

The final technique for reducing the reflection losses is to set the crystal surfaces at Brewster's angle to the incident laser beam. This enables the crystal to be used in a completely uncoated state and fairly high intensities can be withstood if the crystal surface is kept in good condition.

All of the methods mentioned above have their disadvantages and we decided that setting the crystal at Brewster's angle was the most satisfacgory arrangement where high intracavity powers were expected. Having made this choice several problems arise from focusing into a Brewster angled optical element. The most serious of these problems is the optical aberrations of astigmatism and coma. We shall describe these aberrations and show how they can be eliminated by suitable optical design. Some practical laser cavities for eliminating these aberrations are then discussed; in particular,a novel cavity arrangement has been developed to eliminate both coma and astigmatism.

IV.2 Astigmatic Compensation

Astigmatic compensation of laser cavities has been discussed by Kogelnik, Ippen, Dienes and Shank.[1] They have shown that when a Gaussian beam is focused into a Brewster angled optical element the astigmatism introduced can be offset by the astigmatism of an off-axis spherical mirror.

The astigmatism of an inclined plane has been calculated by Hanna[5] using a Huygens' construction to find the discontinuous change in wavefront curvature on inserting the inclined interface. He has shown that the effect of an inclined plate on the wavefront curvature can be treated separately in two planes; the tangential plane which contains the optical axis and the off-axis object point,and the sagittal plane which contains the principal ray and is perpendicular to the tangential plane. Effective distance which represents the distance that a wave would have to travel in air to experience the same change wavefront curvature as in going through the medium can be calculated for each plane. To within the paraxial approximation these effective distances when the plate is at Brewsters angle can be written

$$d_s = t\ (\mu'^2 + 1)^{\frac{1}{2}}\ /\mu'^2 \qquad (1)$$

$$d_t = t\ (\mu'^2 + 1)^{\frac{1}{2}}\ /\mu'^4 \qquad (2)$$

where d_s and d_t are the effective distances in the sagittal and tangential planes respectively, t is the thickness of the plate measured perpendicular to its surface and μ' is the refractive index of the plate. It is the difference between the effective distances d_s and d_t which gives rise to the astigmatism of an inclined plate.

If an off-axis mirror is used to focus into the element the effective focal length can be ascribed to the tangential and sagittal planes, given by the well known result

$$f_s = f/\cos I \qquad (3)$$

$$f_t = f\ \cos I \qquad (4)$$

where f is the actual focal length of the mirror and I is the angle of incidence of the incoming beam on the mirror.[2]

If a beam is focused through a plate at Brewster's angle with an off-axis mirror and both the plate and the mirror are tilted in the same plane, the focus can be made free of astigmatism provided that the path length in the sagittal plane is equal to that in the tangential plane. This condition will be satisfied if

$$d_s - d_t = f_s - f_t \qquad (5)$$

The condition (3) will be satisfied when the mirror angle is tilted such that the following relationship is satisfied

$$t(\mu'^2 - 1)(\mu'^2 + 1)^{\frac{1}{2}}/\mu'^4 = f\ \sin I\ \tan I \qquad (6)$$

This is the condition for astigmatic compensation in the overall optical system.[1] In most systems of interest, the focal spot will be in the centre of the optical element and, even if the above condition (6) is satisfied there will still be some residual astigmatism at the focus. It is possible to eliminate astigmatism at the focus by the use of a second off-axis mirror after the Brewster angled element. The first mirror compensates the astigmatism introduced in the first half of the element and the second mirror compensates the astigmatism of the other half. The system will therefore be astigmatically compensated both within the focal region and in the complete optical system. Suitable laser arrangements for accomplishing this condition will be discussed in section IV.7

IV.3 Calculation of Comatic Aberration

Little regard has been paid to coma compensation in laser cavities. In cavities where focusing is required in a fairly long Brewster angled optical element coma can be large and give rise to a degraded focus and increased linear loss of the cavity. We calculate the coma introduced by focusing into a tilted optical element in the geometrical optics limit and show how it can be eliminated by suitable choice of off-axis spherical mirror.

The approach to calculating the comatic aberration is to first calculate the characteristic function (or optical path length) by use of Fermat's principle. Deviations of this function from the paraxial limit are interpreted as optical aberrations,and coma can be identified as the most significant of them for the cases we consider.

The analysis is limited to a two-dimensional treatment by considering only tangential rays. It is well known that to first order the elimination of tangential coma implies the elimination of sagittal coma.[3] For the large angles considered here this approximation may not be strictly valid and higher order terms have to be considered. However, the added complexity involved in such an approach was considered to be not rewarding at this stage. It is likely that the results obtained will describe a minimisation of coma and that the higher order terms will only indicate how far the minimum coma is from being identically zero.

IV.4 Comatic Aberration of an Inclined Plane Interface

A schematic diagram of a focused beam incident on a plane dielectric interface between air ($\mu = 1$) and a medium of refractive index μ' is shown in figure 1. The plane is tilted at an angle θ to the optical axis. The angle θ is taken to be positive when the direction of the normal is obtained by a clockwise rotation from the optical axis for beam propagating from left to right. In going into the medium, the optical axis is transferred to an angle θ' to the normal to the interface where θ' is given by

$$\mu' \sin\theta' = \sin\theta \qquad (7)$$

This transfer of axes simplifies subsequent manipulation as the characteristic function can be expanded about the conjugate points in the paraxial approximation.

We consider only rays propagating in the single plane perpendicular to the normal to the interface. A general ray can be defined by its point of origin on the X-axis which is at a distance S to the left of the interface (S is then positive), and by the point x_1 at which it crosses the X_1-axis, where the X_1-axis is a normal drawn perpendicular to the optical axis at its point of intersection with the interface. Within the interface a ray is located at a distance x' along the X'-axis, where the X'-axis is a normal drawn at a distance S' from the interface. The distance S' is measured along the optical axis and is taken as a positive quantity.

The path length W measured from the point P to P' is given by

$$W = PP_1P' = (PP_1 + \mu' P_1P') \qquad (8)$$

or
$$W = [\,(x_1 - x)^2 + (S + K\,x_1)^2]^{\frac{1}{2}}$$
$$+ \mu'\,[(M\,x_1 - x')^2 + (S' - L\,x_1)^2]^{\frac{1}{2}} \qquad (9)$$

where

$$K = \tan\theta \qquad (10)$$

$$L = \sin\theta'/\cos\theta \qquad (11)$$

$$M = \cos\theta'/\cos\theta \qquad (12)$$

The path length can now be expanded to terms of the order $(x/S)^3$ where it has been assumed that x, x_1, $x' << S$, S', to give

$$\begin{aligned} W = {} & S + \mu'S' + (K - \mu'L)\,x_1 + (1/2S + M^2\mu'/2S')\,x_1{}^2 \\ & + x^2/2S + \mu'x'^2/2S' - xx_1S - \mu'Mx'x_1/S' \\ & + (M^2\mu'L/2S'^2 - K/2S^2)\,x_1{}^3 \\ & - (K/2S^2)\,x_1x^2 + (\mu'L/2S'^2)\,x_1x'^2 \\ & + (K/S^2)\,xx_1{}^2 - (\mu'ML/S'^2)\,x_1{}^1\,x_1{}^2 \qquad (13) \end{aligned}$$

The optical ray PP_1P' can now be determined by the application of Fermat's Principle, namely

$$(\partial W/\partial x_1)_{x,x',S,S'} = 0 \qquad (14)$$

to give

$$\begin{aligned} \partial W/\partial x_1 = {} & (K - \mu'L) + (1/S + M^2\mu'/S')\,x_1 \\ & - [\,x/S + (\mu'M/S')\,x'] + 3[\,(M^2\mu'L)2S'^2 - K/2S^2]\,x_1{}^2 \\ & - (K/2S^2)\,x^2 + (\mu'L/2S'^2)\,x'^2 + (2K/S^2)\,xx_1 \\ & - (2\mu'ML/S'^2)\,x'x_1 \qquad (15) \end{aligned}$$

The zero order term in equation (15) is identically zero because of equation (7) and arises as a result of the suitable choice of axes. By ensuring that the first order term in (x/S) is zero and that $(\partial W/\partial x_1)$ is independent of x_1 the paraxial imaging condition will be satisfied. These two conditions for paraxial imaging are satisfied if

$${}^{(1)}S' = -M^2\mu'S = -\mu'\,(\frac{\cos\theta'}{\cos\theta})^2 S \qquad (16)$$

and
$${}^{(1)}x' = M\,x = (\frac{\cos\theta'}{\cos\theta})\,x \qquad (17)$$

and identifies the conjugate points $P\,(x, S)$ and $P'(x', S')$.

The expansion to third order in (x/S) about this paraxial solution gives the aberration $\delta x'$, which is the displacement from the point ${}^{(1)}x'$ given by equation (17) and measured at the plane ${}^{(1)}S'$ given by equation (16). Thus, the image point corresponding to an initial ray originating at $P(x,S)$ can, to second order, be written

$$
\begin{aligned}
& {}^{(2)}x' = {}^{(1)}x' + \delta x' \\
\text{where} \quad & \delta x' \ll {}^{(1)}x' .
\end{aligned} \tag{18}
$$

If it is assumed that the initial ray is on axis $(x=0)$ and that it passes through x_1, then on substituting equation (18) into equation (15) and ensuring that Fermat's Principle is satisfied to second order gives a value for the aberration of

$$
\begin{aligned}
\delta x' = - (3/2)(x_1{}^2/S) \, [\, (1 - \sin^2\theta/\mu'^2)^{\frac{1}{2}}/\cos\theta \,] \\
[\, \sin\theta \cos\theta/(\mu'^2 - \sin^2\theta) - \tan\theta \,]
\end{aligned} \tag{19}
$$

For this ray the characteristic function is then

$$
\begin{aligned}
W = S(1 - \mu'^2)/\cos^2\theta + (1/2S^2)[\, \sin\theta \, \cos\theta/(\mu'^2 - \sin^2\theta) - \tan\theta \,] \\
(x x_1{}^2 + x_1 x^2 - 2x_1{}^3)
\end{aligned} \tag{20}
$$

This describes a coma type aberration with the displacement from the paraxial condition, $\delta x'$, being quadratic in x_1.

When the plate is inclined at Brewster's angle equation (19) reduces to

$$\delta x' = (3/2)(x_1{}^2/S) \, \mu'^2 \, (1 - \mu'^{-4}) \tag{21}$$

We now consider the case of the coma introduced by an off-axis spherical mirror.

IV.5 Comatic Aberration of an Off-axis Spherical Mirror

A schematic diagram of parallel light incident at an angle I on a spherical mirror of radius of curvature R is shown in figure 2. The angle I is defined as being positive when, for light incident from left to right, the direction of the normal is obtained by clockwise rotation from the incident ray. A particular ray can be defined by the angle δ, which is the half angle between the normal to the ray at the mirror and the normal to the principal ray at the mirror. The general path length from a point on the wavefront of the incoming beam to a point P' on the X'-axis which is at a distance S' from the mirror is first calculated.

The line PO' in figure 2 defines a wavefront of the incident rays and the optical paths from this wavefront to the point P', relative to that for the axial ray, is hence the distance PP' − OO'. Now the distance OO' is given by

$$OO' = 2R \sin\delta \sin(I + \delta) \qquad (22)$$

and

$$(PP')^2 = (2 R \sin\delta \sin(I - \delta) + S') + (2 R \sin\delta \cos(I - \delta) - x') \qquad (23)$$

or

$$(PP')^2 = 4 R^2 \sin^2\delta + S' + x' + 4 R \sin\delta \, [S' \sin(I - \delta) - x' \cos(I - \delta)] \qquad (24)$$

Combining equations (22) and (24) we find that

$$W = (PP' - OO') = (4 R^2 \sin^2\delta + S'^2 + x'^2 + 4 R \sin\delta \, [S' \sin(I - \delta) - x' \cos(I - \delta)])^{\frac{1}{2}} - 2 R \sin\delta \sin(I + \delta) \qquad (25)$$

This expression is now expanded to third order in δ and x' (ie δ^3, $x'\delta^2$ etc) to give

$$W = S'^2 + x'^2/2S' + 2R \cos I \, [\,(R/s') \cos I - 2]\,\delta^2 - (2R/s') \cos I \, x'\delta - (4R^2/S') \sin I \cos I \, [\,(R/S') \cos I - 1]\,\delta^3 - (2R/S') \sin I \, [1 - (2R/S') \cos I]\, x'\delta^2 - (R/S'^2) \sin I \, x'^2\delta \qquad (26)$$

The optical ray is now determined by application of Fermat's Principle, namely

$$(\partial W/\partial\delta)_{S',x'} = 0 \qquad (27)$$

Differentiating equation (26) we obtain

$$\begin{aligned}(\partial W/\partial\delta) = {} & 4\ R \cos I\ [\ (R/S') \cos I - 2\ ]\ \delta \\ & - (2R/S') \cos I\ x' \\ & - (12R^2/S') \sin I \cos I\ [\ (R/S') \cos I - 1]\ \delta^2 \\ & - (4R/S') \sin I\ [\ 1 - (2R/S') \cos I]\ x'\delta \\ & - (R/S'^2) \sin I\ x'^2 \end{aligned} \qquad (28)$$

Fermat's Principle is satisfied to first order in δ if the following conditions are satisfied

$$^{(1)}S = (R/2) \cos I \qquad (29)$$

$$^{(1)}x' = 0 \qquad (30)$$

These conditions define the paraxial image point of a tilted mirror. As was done earlier in the case of a plane tilted interface, the deviation from the paraxial image condition can be obtained by substitution of $^{(2)}x' = {}^{(1)}x' + \delta x'$ into equation (28). The deviation is given by

$$\delta x' = -6R \sin I\ \delta^2 \qquad (31)$$

where $\delta x'$ is measured along the x'-axis at a distance S' defined by equation (29). The characteristic function then becomes

$$W = (R/2) \cos I + 16R \sin I\ \delta^3 \qquad (32)$$

Again, this describes a coma type of aberration. We now go on to show how aberrations of an inclined interface and off-axis spherical mirror are combined and to show how the comatic aberration can be eliminated.

IV.6 Combining Optical Aberrations

A schematic diagram of parallel light incident on an off-axis spherical mirror and then through a tilted interface is shown in figure 3. The interface is assumed to have a thickness t measured normal to the inclined face of the medium. It is further assumed that the paraxial focus is located in the centre of the medium giving the value of S' to be

$$S' = t/(2 \cos \theta') \tag{33}$$

If a ray is traced through the system in the paraxial approximation we find from (16) and (17) that

$$S = - t \cos^2\theta/(2\ \mu' \cos^3\theta') \tag{34}$$

$$x_1 = 4S\delta \quad = [\ 2\ t \cos^2\theta/(\mu' \cos^3\theta')]\ \delta \tag{35}$$

The total coma $\delta x'$ in the paraxial focal plane within the crystal is determined by combining the contribution due to the off-axis mirror (31), magnified by the passage through the interface (17), with that due to the interface (19). By using equations (34) and (35) above to eliminate x_1 and S this gives a total aberration of

$$\delta x' = [\ 6(1 - \sin^2\theta/\mu'^2)^{\frac{1}{2}}/\cos\theta\ ]\ \{\ [R \sin I + 2t \cos^2\theta/\mu' (1 - \sin^2\theta/\mu'^2)^{3/2}\ ]\ [\sin\theta \cos\theta/(\mu'^2 - \sin^2\theta) - \tan\theta\ ]\ \}\ \delta^2 \tag{36}$$

In a similar way, the aberration in the optical path length can be determined from (20) and (32) to give

$$\delta W = - 16\ \ \{R \sin I + 2t \cos^2\theta/\mu(1 - \cos^2\theta/\mu'^2)^{3/2}\ [\sin\theta \cos\theta/(\mu'^2 - \sin^2\theta - \tan\theta)]\ \}\ \delta^3 \tag{37}$$

When the interface is tilted at Brewster's angle the above equations reduce to

$$\delta x' = -6\mu'\ [R \sin I + 2t\ (1 + \mu'^2)^{\frac{1}{2}}(\mu'^4 - 1)/\mu'^7]\ \delta^2 \tag{38}$$

and

$$\delta W = 16\ [R \sin I + 2t\ (\mu'^4 - 1)(\mu'^2 + 1)^{\frac{1}{2}}/\mu'^7]\ \delta^3 \tag{39}$$

From these equations it can be seen that the aberrations can be eliminated provided

$$R \sin I = - 2t\ (\mu'^4 - 1)(\mu'^2 + 1)^{\frac{1}{2}}/\mu'^7 \tag{40}$$

The negative sign appearing in this equation describes the fact that coma can only be eliminated when the angles θ and I are chosen to be of opposite sense. As drawn in figure 3 the angles I and θ are both positive and so coma would not be eliminated.

In the above we have shown that it is possible to arrange an optical system of a tilted plane interface and off-axis spherical mirror such that a focus can be provided within the medium which is free of tangential coma. We shall go on to show how this can be used in a laser cavity and in addition show how astigmatism can be eliminated.

IV.7 Some Cavity Designs for Eliminating Aberrations

We now consider a number of laser cavities and show how the results of the previous sections can be used in designs which eliminate aberrations. We need consider only the case of a single intracavity element with the laser mode focused into this element. Schematic diagrams of arrangements for achieving an intracavity focus are shown in figure 4. In each case it is assumed that a parallel faced element is centred on the focus and that the faces are orientated at Brewster's angle. For each of the arrangements shown, the element can satisfy these conditions for two different orientations which we designate A and B. The two orientations are shown in figure 5.

The arrangement shown in figure 4(a) is the standard arrangement described in Kogelnik et al[1] and is widely used in continuous-wave dye lasers. The mirrors 2 and 3 produce the focus of the laser mode and mirror 1 is either a single mirror or an effective mirror representing more complex optical structures. In order that the theory presented earlier be accurate it must be assumed that the radii of curvature of mirrors 2 and 3 are much smaller than that of mirror 1 so that a quasi-collimated beam exists in the horizontal arm of the cavity. Figure 4(b) is a similar arrangement to figure 4(a) except that an extra arm has been introduced which makes the cavity symmetrical about the centre of the element. Figure 4(c) is another arrangement, similar to the previous arrangements except that the symmetry axis has been changed compared to that of figure 4 (b). The cavity arrangements shown in figures 4 (b) and 4 (c) have been suggested by Johnston and Runge[4] who were concerned with reducing the aberrations in off-axis resonators. They suggest that the astigmatic compensation in figures 4 (b) and 4 (c) are an improvement on figure 4 (a) but that the arrangement shown in figure 4 (c) is compensated for comatic aberration. However they did not explicitly consider the coma introduced by focusing into a Brewster angled interface. When this aberration is included in the analysis we contend that arrangement of figure 4 (c) is not coma compensated and that the arrangement of figure 4 (b) is the only cavity of these three for which it is possible to simultaneously eliminate both coma and astigmatism for the overall cavity and within the element. We now look at the cavities in more detail.

In their paper describing the properties of the cavity shown in Figure 4 (a), Kogelnik et al[1] show how it is possible to render the whole cavity free of astigmatism in the sense that a ray leaving mirror 1 will have no symptom of astigmatism after having performed a round trip of the cavity. However, there will be residual astigmatism within the element since astigmatic compensation has not been fully accomplished until the ray has propagated from mirror 2, through the element and back to the mirror 2 after reflection from mirror 3. Coma compensation in the complete cavity can also be accomplished in this arrangement in the same sense as astigmatism can be compensated.

Kognelnik et al[1] have shown that the condition for the elimination of astigmatism in the overall cavity is

$$R \sin I \tan I = 2t(\mu'^2 - 1)(\mu'^2 + 1)^{\frac{1}{2}}/\mu'^4 \qquad (41)$$

This cavity is also compensated for coma in the overall cavity if

$$R \sin I = 4t(\mu'^4 - 1)(\mu'^2 + 1)^{\frac{1}{2}}/\mu'^7 \qquad (42)$$

Here, the coma introduced by the passage through the whole Brewster angled element is compensated by a reflection at a single off-axis mirror. Although the overall cavity is coma compensated, the focal region within the element will still be degraded by the residual coma in this region. Coma can only be compensated when the element is oriented as in A of figure 5. In the arrangement B the coma of the element and the off-axis mirror will add.

The cavity arrangement shown in figure 4 (b) is an improvement on the previous arrangement since it is possible to achieve the elimination of astigmatism both for the overall cavity and within the element. The astigmatism of off-axis mirror 2 acts to compensate the astigmatism introduced at the tilted interface at the focus in the centre of the element. The mirror 3 is used to eliminate the astigmatism of the second half of the element. The astigmatism is therefore compensated both overall and within the element irrespective of whether the crystal orientation is as shown in A or B.

The condition for astigmatic compensation of this arrangement is given by Kogelnik et al[1] as

$$R \sin I \tan I = t(\mu'^2 - 1)(\mu'^2 + 1)^{\frac{1}{2}}/\mu'^4 \qquad (43)$$

When the element is orientated as in A, the coma introduced by off-axis mirror 2 is offset by coma introduced at the focus of the beam in the centre of the element. In a similar manner the coma introduced by mirror 3 and the second half of the element are in opposite directions and can therefore be eliminated. This cavity can therefore be compensated for coma and astigmatism both within the element and throughout the complete cavity. If the orientation of the element is as shown in B, the coma introduced by the mirror 2 and 3 adds to the coma of the crystal. There is therefore a significant improvement in the cavity aberrations if the crystal is oriented as in A as opposed to B.

The condition for coma compensation in overall cavity is given by

$$R \sin I = 2t(\mu'^4 - 1)(\mu'^2 + 1)^{\frac{1}{2}}/\mu'^7 \qquad (44)$$

where it has been assumed that the radius of curvature of mirrors 2 and 3 are both equal to R. When the element is centred on the focal spot within the cavity this condition also ensures that coma will be eliminated within the element.

The cavity arrangement shown in Figure 5(c) can be used to eliminate both coma and astigmatism only when there is no element in the focus between mirrors 2 and 3. If the element is centred on the focus, astigmatism can be eliminated both within the element and in the overall cavity. However, the coma introduced by the crystal cannot be eliminated either within the element or in the overall cavity.

The aberration properties of the cavity arrangements discussed above are summarized in table 1. From the table it is clear that when the element is correctly orientated the arrangement shown in figure 4(b) is superior to the other arrangements discussed here. We now go on to consider the conditions for elimination of both coma and astigmatism in this arrangement.

From equations (43) and (44) it can be seen that for the arrangement shown in figure 4(b) coma and astigmatism can be simultaneously eliminated for a unique angle of incidence on the off-axis mirror given by

$$\tan I_o = \mu'^3/2(\mu'^2 + 1) \qquad (45)$$

Provided that the angle I_o is chosen in accordance with equation (45), then the subsequent choice of remaining parameters to eliminate one of the aberrations will ensure that the other is eliminated. The variation of I_o with the refractive index of the intracavity element is tabulated in table 2.

For angles of incidence as large as those indicated in table 2 there is no assurance that sagittal coma will be eliminated. However, a full account of tangential and sagittal coma is too complex to go into here. The angle I_o is likely to be the angle at which the aberrations are minimised although they may not be completely eliminated.

We now indicate the improvement in focusing which can be gained by choosing the angles and orientation correctly. Suppose that the cavity is set up such that the element is in orientation A, of figure 5, the angle of incidence on the off-axis mirror is I_o and other parameters are chosen so that astigmatism is eliminated. To a first degree of approximation $\delta x'$ will be zero at the beam focus. If the element is in orientation B the coma introduced by the tilted interface and the off-axis mirror will be equal in size but will add. The comatic displacement in this case will be

$$\delta x' = 12\mu' \sin I_o \delta^2 \qquad (46)$$

For a small spot size cavity of the type shown in figure 4(b) the confocal parameter of the focused beam will be[1]

$$b \sim (R/2)^2/d \qquad (47)$$

where d is the separation between mirrors 1 and 2. The far field diffraction angle is given by 4δ and may be written in terms of the confocal parameter as

$$\delta = \tfrac{1}{4}\left(\frac{2\lambda}{\pi b}\right)^{\frac{1}{2}} \qquad (48)$$

This gives the coma as

$$\delta x' = (3/\pi)\ \mu\ \lambda\ (d/b)^{\frac{1}{2}} \sin I_o \qquad (49)$$

Now the beam waist in the focus is given by

$$w_o = (b\lambda/2\pi)^{\frac{1}{2}} \qquad (50)$$

Comparing the coma with the focal spot size we have

$$(\delta x'/w_o) = 3\mu'(2\lambda d/\pi b^2)^{\frac{1}{2}} \sin I_o \qquad (51)$$

Using typical values for the parameters (d = 50 cm, b = 1 cm, $\mu' = 1.5$,

$\lambda = 6 \times 10^{-5}$cm) equation (51) gives a value for the ratio $(\delta x'/w_o)$ of 6×10^{-2}. A deviation of this magnitude is likely to introduce a distortion of the focal spot and to introduce a considerable linear loss into the overall cavity. It is therefore important to design the cavity to minimise the aberrations.

In the foregoing analysis a geometrical ray tracing treatment was employed. This approximation is likely to be valid when the beam confocal parameter is much smaller than the crystal thickness or mirror radii. In many cases of practical interest optical elements of a thickness comparable to the confocal parameter are used. When this is so, the geometrical approach is no longer valid and a full Gaussian beam treatment is required in determining the aberrations.

Some indication of the kind of result which could be expected in a full analysis can be obtained by considering the focused Gaussian beam. The far field diffraction angle is δ and for a general point z from the beam waist the diffraction angle is

$$\delta(z) = w(z)/R(z) \qquad (52)$$

where w(z) is the spot size and R is the radius of curvature of the wavefront measured at a distance z and are given by

$$w^2(z) = w_o^2 \, [\, 1 + (\lambda z/\pi w_o^2)^2 \,] \qquad (53)$$

$$R(z) = z \, [\, \pi w_o/\lambda z)^2] \qquad (54)$$

The angle of diffraction is therefore given by

$$\delta(z) = (2w_o/b) \, [\, 1 + (b/2z)^2]^{\frac{1}{2}} [\, 1 + b/2z)^2]^{-1} \qquad (55)$$

where $b = 2\pi w_o/\lambda$. The first term on the right hand side of equation (55) is the far field diffraction angle and the other terms describe the Gaussian beam modifications. For distances of the order of the beam waist the angle becomes a function of distance and is reduced from its far field value. When z = b the value of δ is reduced to $\delta(b) = 0.9\delta$. This suggests that the coma in the vicinity of the focus will be somewhat reduced when the beam is incident on an element whose thickness is comparable to the confocal parameter of the beam. The overall problem is quite difficult since the angle δ does vary with distance through the element. However, the variation from the geometrical treatment will not be very large until an extreme Gaussian region is encountered.

IV.8 Conclusion

We have shown how to deal with the comatic aberration introduced when light is focused into a tilted interface in the geometrical optics approximation. An off-axis focusing mirror is also treated in the same approximation. The result shows that comatic aberration can be eliminated by suitable choice of angles and thickness of inclined plate. The application of such a design to the case of a laser cavity with focusing into a Brewster angled element is treated. A particular cavity design is described which eliminates both coma and astigmatism.

References

1 H Kogelnik, E P Ippen, A Dienes and C V Shank, IEEE J Quant Electron QE8, 373 (1972).

2 R S Longhurst, Geometrical and Physical Optics, Longmans, London (1957).

3. A E Conrady, Applied Optics and Optical Design, Oxford University Press, London (1929).

4 W D Johnston and P K Runge, IEEE J Quant Electron QE8, 724 (1972).

5 D C Hanna, IEEE J Quant Electron QE5, 483 (1969)

Cavity	Astigmatic Compensation		Coma Compensation	
	At focus	Overall	At focus	Overall
a	x	✓	x	✓
b	✓	✓	✓	✓
c	✓	✓	x	x

Table 1: Aberration compensations possible with various cavity designs illustrated in figure 5. (✓) indicates that compensation is possible, (x) indicates that compensation is not possible.

μ'	1.1	1.3	1.5	1.7	1.9	2.1
I_{corr} (degrees)	16.7	22.2	27.4	32.2	36.6	40.6

Table 2: Variation with refractive index (μ') of the off-axis angle which allows simultaneous compensation of astigmatism and coma.

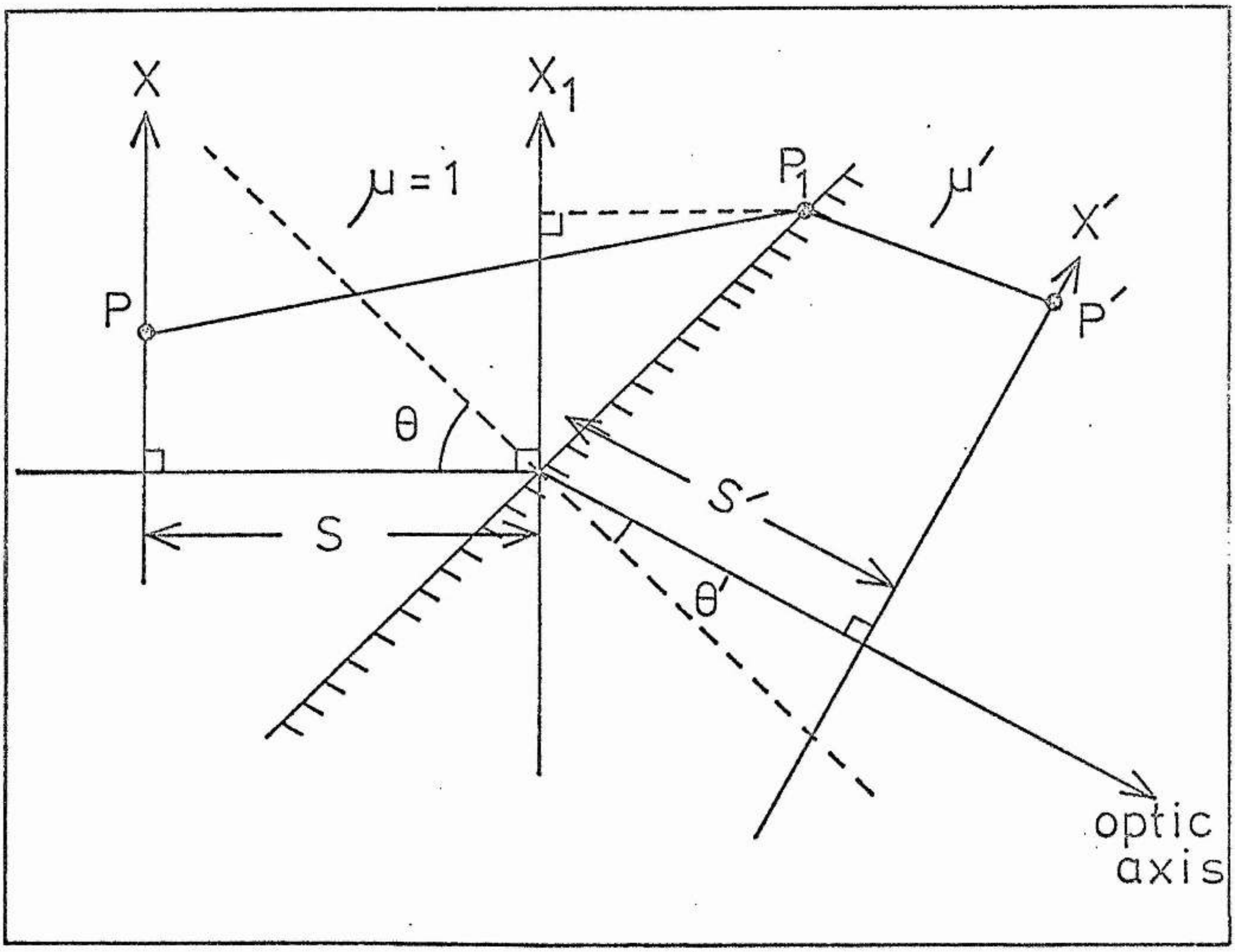

Figure 1. Geometry for ray tracing in the case of a tilted interface.

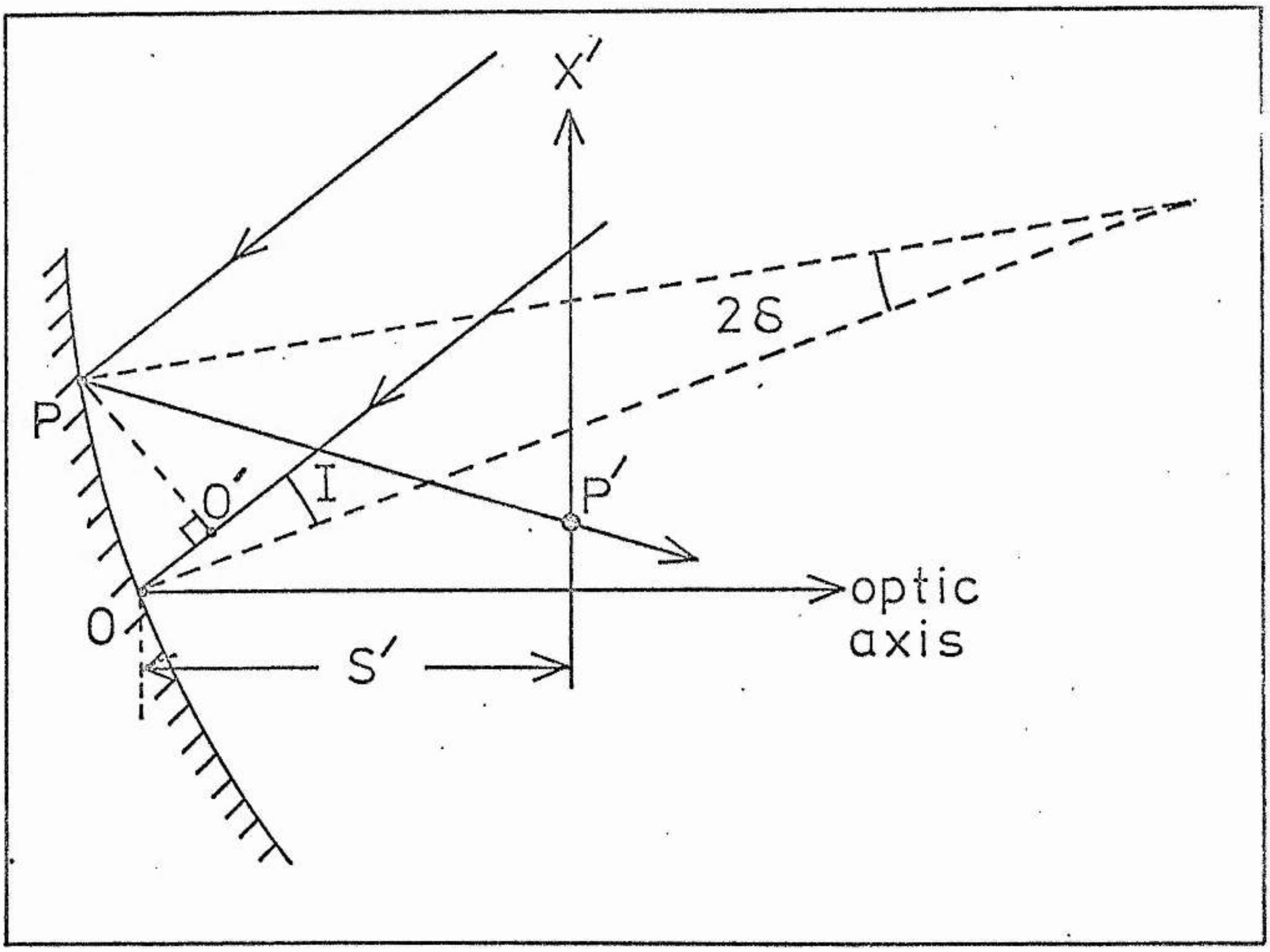

Figure 2. Geometry for ray tracing in the case of a tilted concave mirror.

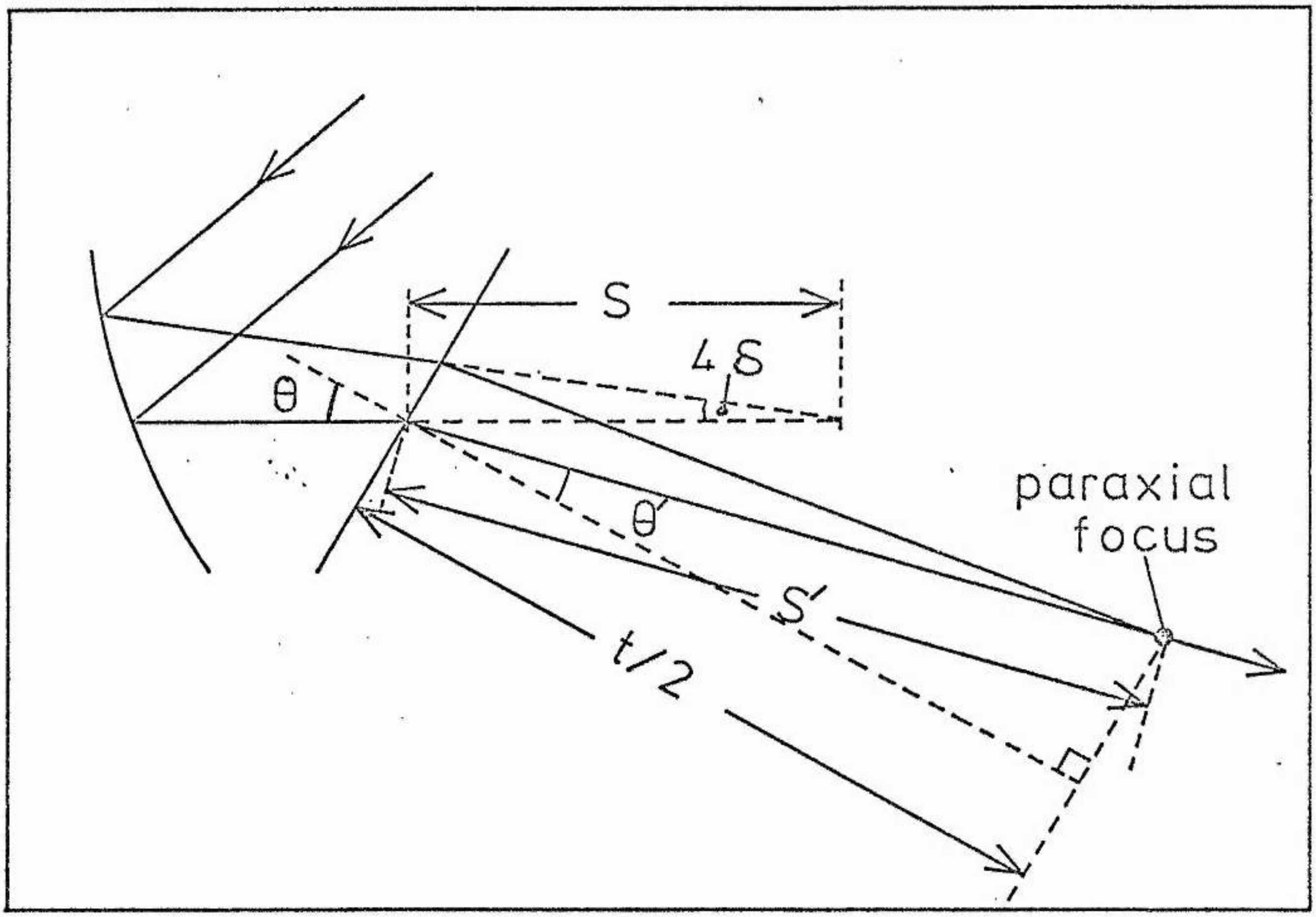

Figure 3. Geometry for combining tilted interface and tilted concave mirror.

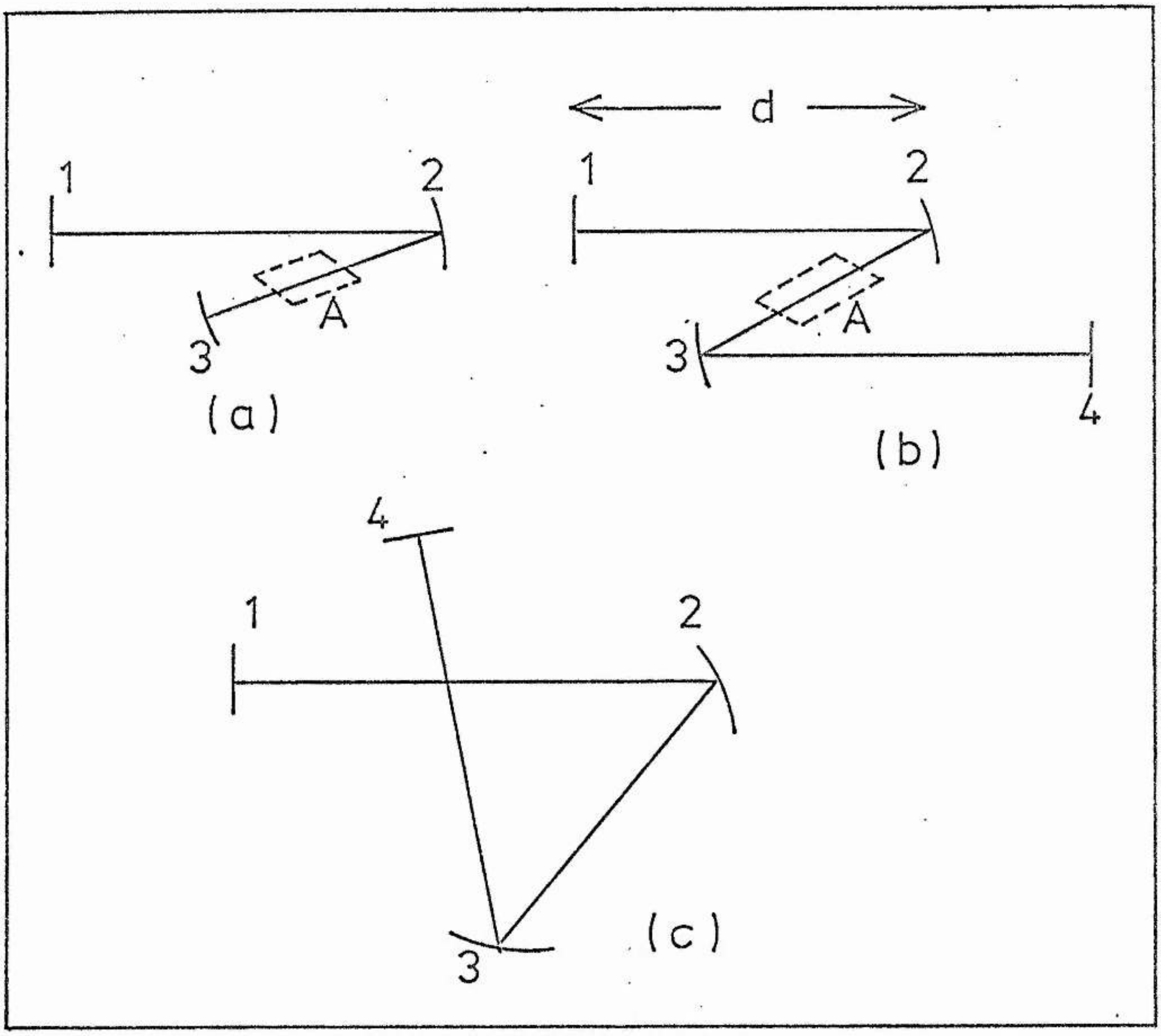

Figure 4. Cavity designs for aberration compensation.
(a) three mirror cavity with off-axis focusing.
(b) four mirror cavity with off-axis focusing.
(c) four mirror cavity with asymetrical focusing.

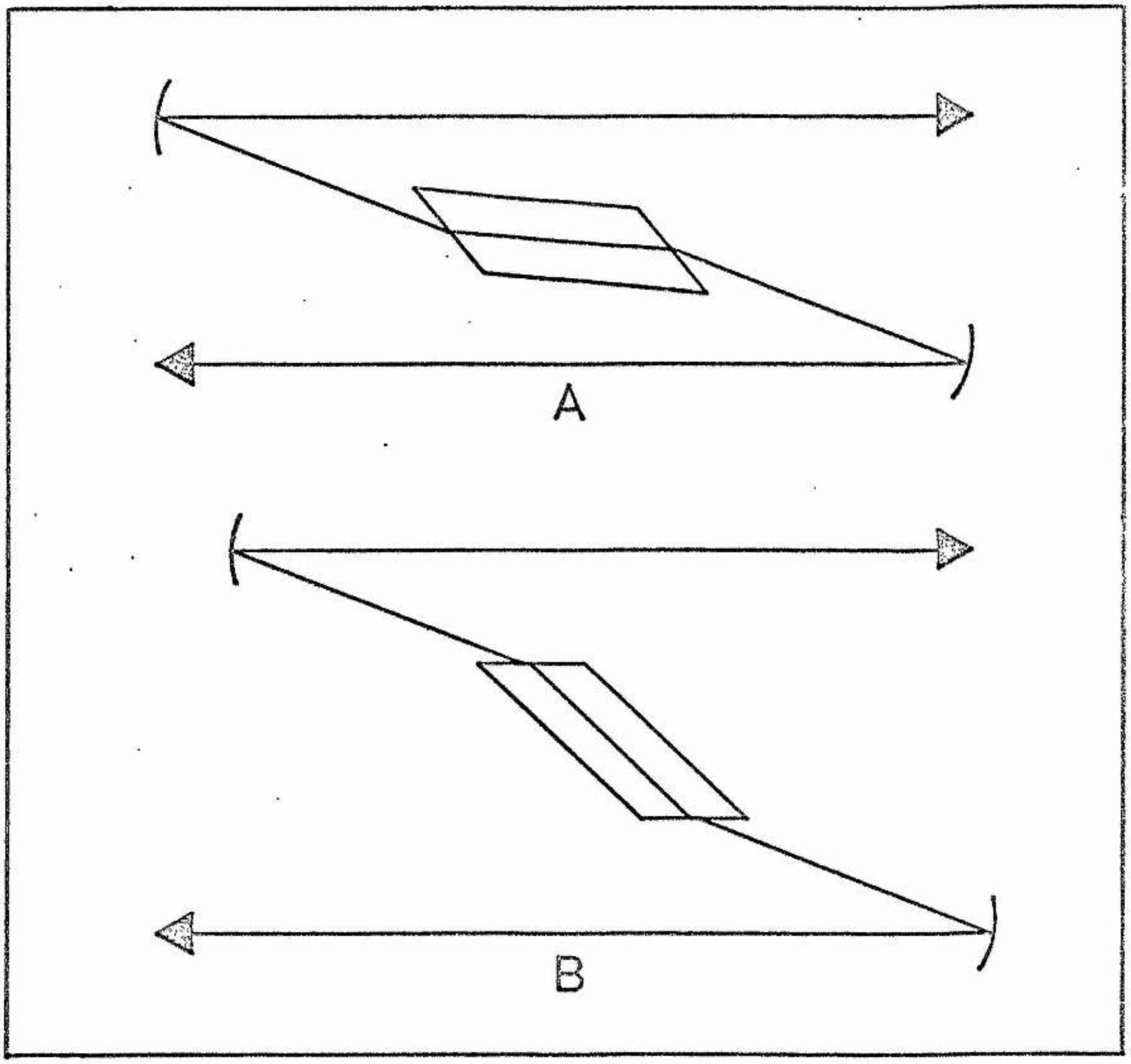

Figure 5. Two possible orientations of a Brewster angled plate.

CHAPTER V

EXPERIMENTAL DETAILS OF SOME PROTOTYPE SECOND HARMONIC DYE LASERS

Abstract

Two prototype second harmonic dye lasers are described. In the first ADP was used as the frequency doubler and was placed at the focus of the 'loop' shaped cavity described in Chapter IV. With a multiline, multimode argon laser pumping power of up to 20W the continuous UV generated power was 35mW. The conversion efficiency was limited by the onset of thermally induced phase mismatching in accordance with the theory outlined in Chapter II. The peak UV generated power can be increased to 85mW by chopping the pump radiation with a low duty cycle. The laser could be stepwise tuned from 285nm to 315nm with a linewidth of 0.02nm.

In the second system, a crystal of ADA was used as the frequency doubler. ADA can be 90° phase matched at rhodamine 6G wavelengths giving rise to a UV beam of Gaussian intensity distribution and increased efficiency over the ADP crystal. The cavity arrangement was the Z-shaped cavity with the crystal oriented appropriately for astigmatic and coma compensation as described in Chapter IV. Generated continuous UV powers of up to 30mW over the range 292nm to 302nm have been obtained with a 4.5W singe line TEM_{oo} argon pump laser. The output power was found to be limited by thermal lensing effects in either the dye jet or the crystal as well as by thermal phase mismatching. The UV laser linewidth was 0.02nm but could be reduced to 0.002nm by the inclusion of a thin etalon in the cavity.

The generation bandwidth at fixed crystal temperature and orientation was found to be about an order of magnitude less for ADA than for ADP being only 0.1nm FWHM for ADA. A variety of methods of extending this tuning range which have been developed are then described. Tuning ranges of up to 3nm at a linewidth of 0.02nm and 2 nm at a linewidth of 0.002 nm in a continuous scan have been obtained with these methods.

Proposed improvements to the experimental systems are described. A method of using the second harmonic crystal as a modulator which can then be used to lock to laser frequency to maximise UV generation is described. This should allow an even larger continuous tuning range.

V.1 Introduction

In previous chapters we have dealt with the background to the production of tunable UV by intracavity frequency doubling. We now describe some experimental arrangements which have been used. The results divide into two categories. The first involves ADP as the frequency doubler in a 'loop' shaped cavity similar to that described by Johnson and Runge^{1}. The pump laser was an argon ion laser with highly multimode spatial output operating on all lines. In the second category ADA is used as the frequency doubler and the cavity has been altered so that coma and astigmatism are reduced. A single line, TEM$_{00}$ argon ion laser was used to test this arrangement. Finally, methods of tuning the laser over an extended range are described.

V.2 The Dye Laser

In the experimental set-up one basic dye laser was used. This was a 490 laser produced by Coherent Radiation. In this laser all the components are mounted on a 2" invar rod making the system sufficiently versatile to incorporate frequency doubling crystals. The laser cavity com rised of two spherical mirrors, M_4 and M_5, fig 3, which focused the laser mode into the flowing dye jet stream. The mirrors were of radius of curvature M_5 = 5 cm and M_4 = 7.5 cm and were set at the angle which compensated the astigmatism introduced when focusing into the jet at Brewster's angle. The dye was Rhodamine 6G dissolved in ethylene glycol to about 10^{-3} molar solution. The pump laser was focused onto the jet through a 6 cm focal length lens which was anti-reflection coated for green light produced by the argon laser. The tuning element was a set of three birefringent quartz plates set at Brewster's angle as described by Bloom^{2}. With a 4% transmitting output coupler the dye laser could be tuned over the range 570 nm to 630 nm with a linewidth of approximately 0.05 nm.

The majority of experiments were performed using an argon ion laser which was developed in this laboratory. The laser was of the segmented metal discharge tube type described by Cornish and Maitland[3] and used a plasma jet cathode[4]. The discharge length was 2.5 m and the tube bore was 4 mm. The discharge current was normally in the region of 100A. Although this laser has been shown to be capable of up to 50W output (all lines) the normal maximum laser output power used in this work was about 20W. The laser output contained many transverse modes due to the relatively large bore of the tube. The output could be reduced to the TEM_{00} mode by inclusion of an aperture inside the cavity but only at the expense of considerably reduced output power.

The laser was powered by a current stabilized power supply which was also designed and developed in this laboratory. The main current control on the supply was maintained by a thyristor bridge. The spikes introduced when the thyristors switch was partially smothered by inductors and large capacitors. The fine current control was obtained using a bank of transistors in series with the laser discharge. Although the current was stable to about 1% for time scales longer than 1 sec there was considerable residual ripple due to the three phase mains and current spikes due to thyristor switching. These current fluctuations and modulations, directly affected the laser output power and intensity modulations in the region of 5% were quite common. For most experiments this output was quite adequate. However, for experiments where high stability and good mode control were important it was necessary to use an argon laser designed for lower power operation, with stability features in mind. This was particularly true when single frequency operation of the dye laser was required. For this reason a commercial argon ion laser was used to pump the dye laser (Spectra-Physics 171). The laser was capable of producing 6.5W at 514.5 nm in a single transverse mode. It also incorporated a light stabilization feature which stabilized the laser intensity to within 0.5% from DC up to 20 kHz. This is achieved by sampling the laser power output on a photo-voltaic cell and comparing it with a reference voltage to obtain an error signal. This error signal is then amplified and used to control the laser plasma current. The laser was primarily used in single frequency experiments although it has been used to investigate the overall efficiency of the second harmonic laser.

V.3 The First Prototype Frequency Doubled Dye Laser (ADP crystal; multiline multimode pump)

In the first attempt to produce an intracavity frequency doubled dye laser ADP was used as the frequency doubler. Although ADP is not 90° phase-matchable at Rhodamine 6G wavelengths it was chosen because it is the most readily available and cheapest of the nonlinear crystals suitable for frequency doubling the dye laser. The first important choice in the design of a frequency doubled dye laser is the choice of crystal length. This part of the work was done before the importance of thermal phase mismatching effects was realised. In fact, it was the results of these early experiments which led us to the conclusion that thermal effects are very important in a successful laser design. The choice of crystal length was based primarily on the need to keep astigmatic compensation angles small since higher order aberrations may become important at large angles. Referring to the asymptotic forms (42-44) in Chapter II it can be seen that the second harmonic power generated by a focused laser beam is approximately given by

$$P_{2\omega} \propto P_\omega^2 \ell^2/b \qquad \ell_a, \ell_f >> \ell \qquad (1)$$

$$P_{2\omega} \propto P_\omega^2 \ell/b^{\frac{1}{2}} \qquad \ell_f >> \ell >> \ell_a \qquad (2)$$

$$P_{2\omega} \propto P_\omega^2 b^{\frac{1}{2}} \qquad \ell >> \ell_f >> \ell_a \qquad (3)$$

where we have used the expressions (41), (32) and (26) for the aperture length ℓ_a and the effective length of focus ℓ_f to give

$$\ell_a = (\frac{b\lambda}{2\rho^2})^{\frac{1}{2}}$$

$$\ell_f = 2b/\pi$$

in terms of the confocal parameter b of the focused beam.

For a given confocal parameter it may be seen from equation (3) that there is nothing to be gained in harmonic conversion by making the crystal length greater than the effective length of focus ℓ_f since under these conditions the conversion becomes independent of crystal length. If the crystal length is made equal to ℓ_f then, as may be seen from equations (2) and (3), the conversions vary approximately as $b^{\frac{1}{2}}$. However, as b and hence ℓ are increased to attain higher conversion efficiencies, larger compensation angles are required. In view of the uncertainty regarding higher order aberrations at that time, the crystal length was chosen to be 1.6 cm so as to keep the compensation angle less than 15°. For an ADP crystal of this length the expected nonlinear coupling coefficient C defined as $C = P_{2\omega}/P_\omega^2$ is approximately 6×10^{-5} W^{-1}.

A schematic diagram of the crystal is shown in figure 1. The crystal was supplied by Electro-Optic Developments Ltd. The angle marked ϕ is cut such that a beam entering the crystal at Brewster's angle will propagate as the ordinary ray. This angle is given by

$$\phi = \tan^{-1} n(\lambda) \qquad (4)$$

where $n(\lambda)$ is the refractive index of the ordinary ray at the phase matched wavelength λ. For ADP at 590 nm this angle is 56.7°. The crystal z-axis is orientated at the phase match angle θ_m to the direction of propagation of the light beam within the crystal. For ADP at 25°C and at a wavelength of 590 nm the phase matching angle is 63°. The x and y axes were orientated at an angle of 45° to the plane containing the optic axis in order to maximise the second harmonic interaction. The crystal surfaces were polished flat and parallel to $\lambda/4$.

The crystal was housed in a simple oven and the temperature was controlled using a temperature controller by (Electro Optic Developments Ltd, Type TC15). The circuit diagram of the temperature controller is shown in Appendix A. The controller was capable of maintaining the crystal temperature to an accuracy of 0.01°C over the range 20°C to 90°C.

The crystal surfaces were open to the atmosphere and in order to prevent the condensation of moisture on to the hygroscopic crystal surfaces the oven was at all times maintained at a temperature in excess of 25°C. This was found to be quite satisfactory and the crystal was used for months without serious signs of degradation. However, the crystal was stored in a dessicator overnight.

The refractive index of ADP has been accurately determined and is well-approximated by the following dispersion relation,[14]

$$n^2 = A + B\nu^2/(1 - \nu^2/C) + D/(E - \nu^2) \tag{5}$$

where

$$\nu = 1/\lambda \ (\mathrm{cm}^{-1}) \tag{6}$$

and the other parameters, A, B, C, D and E for the ordinary and extra-ordinary ray are as indicated in table 1. The temperature variations of the refractive indices are given by the expression

$$[n - n\ (300K)\ ] \times 10^4 = F + GT + HT^2 \qquad (7)$$

when F, G and H for ADP are as indicated in table 1.

Using the above equations, the phase-matching temperature of ADP is plotted as a function of the fundamental wavelength for various values of the angle θ_m in figure 2. As can be seen from this figure the ADP crystal can be phase-matched over the entire lasing wavelength range of Rhodamine 6G by either changing the phase-matching angle or by changing the crystal temperature. Notice that in the orientation chosen, the angle which is critical for phase-matching is θ_m. A change in this angle over a limited region does not affect the orientation of the Brewster angled surfaces. The ADP crystal can therefore be angle tilted over a considerable range without increasing the reflection loss at the crystal surfaces. The major effect of tilting the crystal is to walk the beam through the cavity until lasing eventually ceases. Lasing can usually be recovered by realigning one of the laser mirrors. The walk-off of the fundamental beam can be compensated by introducing another refracting medium identical to the crystal into the cavity and tilting both elements together as has been proposed[5,6].

The laser cavity was of a type suggested by Johnson and Runge[1]. A diagram of the cavity is shown in figure 3. The dye jet stream end of the cavity and the tuning element were as described earlier. The mirrors M_2 and M_3 were both of 10 cm radius of curvature and the mirror M_1 was plane. The radius of curvature M_2 and M_3 were chosen to provide a focused beam with a confocal parameter of approximately 1 cm in the region between them.

The mirrors M_1, M_2 and M_3 all had the same dielectric coating. The coating was produced by Technical Optics Ltd and was 99.4% reflecting at

590 nm (0.5% transmitting) and 60% transmitting at 295 nm. The ultraviolet output could be coupled through any one of the mirrors although it was greatest through M_2 or M_3.

The Johnson and Runge[1] cavity was originally chosen since it was stated by the authors that the symmetry of the arrangement eliminated coma. However, it was shown in Chapter IV that their statement is only true in the absence of any element introducing coma between the mirrors. As was shown in Chapter IV there is coma introduced on focusing into a Brewster angled interface and so this cavity does not eliminate the coma created in the crystal.

The angle θ was chosen using the expression (6) in Chapter IV to evaluate the angle required for astigmatic compensation. For a 1.6 cm crystal this angle is 14.7°. At this angle the coma introduced by the crystal is only about 30% of that introduced by the off axis mirror. The cavity arrangement is therefore reasonably well corrected for coma.

Results

The dye laser was pumped with the plasma jet argon ion laser and threshold was found to be in the region of 1W. This is not very different from the value of threshold obtained with the same dye laser and pump when operated in the visible mode. The intracavity power was found to be linear with pump power up to a pumping power of at least 20W. At this pumping power the intracavity power was estimated to be 40W in one direction. This was estimated by measuring the power transmitted from one of the cavity mirrors with known transmission. The linearity of intracavity power with pump power is a reasonable indication that there are no gross losses due to nonlinear absorption, or thermal self-focusing in the crystal. There was no detectable change in intracavity power as the crystal was tuned away from the phase-matching conditions. This indicates that the cavity was undercoupled and that a higher conversion efficiency is required for optimum second harmonic output.

The second harmonic power was measured through mirror M_4 using a solar blind vacuum photodiode (Hamamatsu R404). The second harmonic power generated in one direction was then estimated by using the mirror UV transmission. The second harmonic power generated in one direction at 295 nm as a function of intracavity power is plotted in figure 4. At low power the second harmonic power increases as the square of the fundamental power, as expected. At fundamental powers in excess of a few watts the second harmonic power begins to saturate. Also shown in the figure is the effect of chopping in the cavity of the argon ion laser at various duty cycles. A duty cycle of 1:2 corresponds to 1 part 'on' for every two parts. With this definition no chopping corresponds to 1:1. The powers plotted are those measured during the 'on' part of the cycle which had a duration of about 1 ms in each case. Saturation can be postponed to higher powers by this method although it is at the expense of reduced average UV power. At an intracavity power of about 40W the measured peak power generated was 85 mW at a duty cycle of 1:50. This was reduced to 30 mW in the absence of chopping.

The reduction in harmonic power can be explained in terms of the self-induced thermal phase-mismatching effect which was discussed in Chapter II. The data for the 'no chopping' curve in figure 5 have been transformed into the form of the thermal reduction factor h_T which is given by

$$h_T = (P_{2\omega}/P_{\omega}^{2})/Kh\ell \tag{8}$$

where K, h and ℓ are defined in Chapter II.

The parameter h_T is plotted as a function of $P_\omega/P_T = a$ in figure 5 . where P_T has been defined in equation (65) of Chapter II and is

$$P_T = \lambda\kappa_T/2\beta\delta_1\ell \qquad (9)$$

where δ_1 is the absorption coefficient of the crystal at the fundamental wavelength and the other parameters are as defined in Chapter II. A value of $P_T = 2W$ has been chosen to fit the data. From equation (9) it is possible to estimate the implied value of the absorption coefficient of the ADP crystal. Using the value of the parameters $\lambda = 6 \times 10^{-5}$ cm, $\kappa_T = 2 \times 10^{-2}$ W cm^{-1} K^{-1} and $\beta = 4 \times 10^{-5}$ K^{-1} the absorption coefficient of the crystal used was 0.5% cm^{-1}. This value is about what one would expect for a reasonably good ADP crystal.

The straight line of gradiant 2 drawn in figure 4 was drawn on the basis that $Kh\ell = 6.3 \times 10^{-5}$ W^{-1} which is in good agreement with the value obtained when the parameters of equation (39) of Chapter II are evaluated for ADP.

V.3.1 Use of a Xenon Laser as Pump

The second harmonic dye laser has been pumped by a pulsed xenon ion laser. The xenon laser is attractive for this purpose since it has a relatively long pulse duration of 1 μ sec and so is capable of producing a high resolution laser while at the same time providing fairly high power.

The xenon laser was constructed in this laboratory. It consisted of a 2 m quartz tube of 3 mm bore. The excitation energy was supplied by a 1μF capacitor charged to 20 kV. The tube was pumped out to a pressure of less than 10^{-4} torr. The optimum xenon pressure was found to be in the region of 15 mtorr. The xenon laser produces many lines over the green region of the spectrum and, with argon ion laser mirrors, the total output power was about 750W.

The second harmonic dye laser was pumped with the xenon laser. The peak second harmonic power was in excess of 1W but was not optimised. The main difficulty in using this system was that the birefringent tuning element has insufficient discrimination against the laser hopping to subsiduary maxima of the filter transmission. This could be overcome by a change in design of the birefringent filter to that described by Holtom and Teschke[7], suitable for high power lasers or by using a tuning wedge of the kind used in some commercial dye lasers.

A limited amount of work was done on xenon laser pumping of the harmonic dye laser. It has been included here to record what may well be a very useful device. The compactness, cheapness and power of the xenon laser make it attractive as a pump and the possibility of using it to produce a long pulse narrow linewidth second harmonic dye laser would appear to be an idea worth persuing.

V.4 Stage Two in Dye Laser Development (ADA crystal, single line single mode pump)

After the realisation that thermal effects in crystals could be an important design consideration in second harmonic dye lasers and that coma could be improved by a change in cavity design it was decided to redesign the harmonic laser. In the new laser cavity, ADA was used as the frequency doubling element and the cavity was changed to the Z-shape described in Chapter IV.

A schematic diagram of the revised cavity is shown in figure 6. As before, the dye jet and tuning element were taken from the standard Coherent Radiation 490 cavity. The mirrors R_3 and R_4 were of 10 cm radius of curvature and had a reflectivity of 99.6% at 590 nm and a reflectivity of 80% at 295 nm. The mirror R_5 was plane and had a visible reflectivity of 99.6% and a UV transmission of 80%. All three mirrors were produced by CVI Laser Corporation. The new mirrors gave a reduced linear loss at the fundamental wavelength and an enhanced UV output coupling over the earlier mirrors supplied by Technical Optics.

An ADA crystal was chosen because it is possible to maintain 90° phase-matching of this crystal throughout the wavelength range of a Rhodamine 6G dye laser. The crystal was a 45° Z-cut as illustrated in figure 1. The crystal length was chosen to be 1.5 cm so that it could be directly compared with the ADP crystal. The aperture length of the ADP crystal was approximately 0.2 cm and so an improvement in the region of a factor of seven would be expected by going to ADA.

As can be seen from the figure 3 of Chapter II it is possible to gain some advantage in going to stronger focusing for a 90° phase-matched crystal ($B = 0$) over that of a non-critically phase-matched crystal because of the lack of walk-off in the former. However, the second harmonic power is not a strong function of focusing in the region close to optimum focusing and so a cavity focusing arrangement giving a beam with the same confocal parameter as before was used. From the theory of Chapter IV, it can be seen that for a medium with refractive index 1.57, an angle of 29° is required for both astigmatic and coma compensation. If the radius of curvature of the focusing mirror is to remain the same as in the previous section, the crystal length required for coma and astigmatic compensation is then 6.0 cm. Returning to the results of Chapter III it can be seen that this crystal length would only be an optimum either for cavities with high loss (> 10%) where the thermal effect would have a small effect on the laser performance or in the case of crystal with very low absorption coefficients (< 0.25% cm^{-1} for pump powers in excess of 3W) where again thermal effects would be small. From figures 5 and 6 of Chapter III, it can be seen that at pump powers of about 5W or greater, the maximum second harmonic power for a crystal with an absorption coefficient of 0.5% cm^{-1} placed in a cavity with a linear loss of 5% occurs at a crystal length of between 1 cm and 2 cm. It would therefore appear, on this basis, that a choice of crystal length of 1.5 cm is not unreasonable.

There may be some advantage to be gained by going to larger compensation angles and correspondingly longer crystal lengths so that coma and astigmatism can be simultaneously corrected. However, in these experiments the cavity arrangement was retained at that used in earlier experiments on ADP. Thus the angle marked θ in figure 6 was chosen as 15^{o}.

In some early experiments on the ADA, the crystal was housed in an oven similar to the one used for ADP with the end surfaces open to the atmosphere. After about a week operating under these conditions the ADA crystal surfaces were found to be very poor. This was ascribed to the absorption of water vapour and other gases which may have been present in the laboratory. This behaviour contrasts markedly to that of ADP which was found to last for many months without sign of degradation.

The ADA crystal was therefore housed in a hermetically sealed cell, a diagram of which is shown in figure 7. The crystal was orientated along the axis by two milled channels down the bore and fixed by a rubber bung. The end windows were made of spectrosil B, polished flat and parallel to $\lambda/10$ and were set at Brewster's angle for light at 590 nm. Seals were provided by Dowty bonded seals on the inside of the windows and GACO rings on the outside. The crystal was inserted into the cell and sealed under dry air conditions.

Although the addition of windows should have a small influence on the linear loss at the fundamental wavelength, apart from scattering losses and residual reflection losses, they have a more serious effect on the generated harmonic radiation. This is because the second harmonic radiation is generated with a polarization perpendicular to that of the fundamental radiation. The windows will therefore be set at a large angle in the plane perpendicular to the Brewster angle plane. The reflection coefficient for a beam whose electric vector is polarized perpendicular to the Brewster plane for an interface set at Brewster's angle between air and a medium of refractive index n is given by

$$R_{pB} = [\frac{n^2 - 1}{n^2 + 1}]^2 \qquad (9)$$

For a medium with refractive index n = 1.5 the reflection coefficient is 14.8%.

In leaving the crystal, the generated second harmonic must go through three interfaces; the crystal-air interface, air-window interface and the window-air interface. At each of these faces the transmission will only be 85% because of the high value of reflection coefficient. Therefore only 61.5% of the generated harmonic will actually be transmitted out of the cell. Such a loss of power is inevitable if fluids or coatings on the crystal are to be avoided.

An improvement in the transmission of the UV from the crystal will be obtained if an index matching fluid is inserted between the window and crystal. Normal index matching fluids are usually of the Freon type and suffer from the disadvantage that at high incidence powers they become partially opaque to UV and so lead to heating and crystal damage[8]. Also the low viscosity of most fluids used for index matching means that convective currents set up on heating. This can have a serious effect on the operation of the laser cavity. Some of these problems appear to have been overcome by Welling's group who have been using silicone oil as an index matching fluid[9]. The advantage of silicone oil is that the window can be optically contacted to the crystal with a very thin layer of oil and so very little of the fundamental beam will be absorbed to cause heating. The transmission of silicone oil is good in the visible and in the UV. Welling's group have not reported any crystal damage problems and our preliminary experiments conducted by focusing a 20W argon laser into a fused silica-silicone oil interface suggest that this approach may be quite successful.

Results

The revised second harmonic dye laser was pumped by the plasma jet argon ion laser and by a Spectra Physics 171 argon ion laser. The performance of the frequency doubling crystal was found to be similar with both pump lasers but the efficiency of coupling into the dye laser was greatly increased by the TEM_{00} mode single line output of the commercial laser. However it was found that with single mode pumping of the dye laser, the intracavity power saturated with pump power and eventually decreased with increasing pump power.

One of the first observations made when the crystal was changed from ADP to ADA was that phase-matching in ADA was considerably more critical than in ADP. The phase-matching bandwidth for fixed temperature and angle for ADP was approximately 1 nm FWHM at the fundamental but in the case of ADA this was reduced to 0.1 nm. The probable explanation for this is that in the case of the 90° phase-matched ADA crystal the phase-match must be maintained throughout the length of the 1.5 cm crystal, whereas, in the case of ADP, where Poynting vector walk-off between fundamental and second harmonic occurs, the match need only be maintained over an effective aperture length of about 0.2 cm. A given wave vector mismatch therefore is of greater consequence in a noncritically phase-matched crystal. The penalty in the case of ADP is, of course, a lower maximum generation efficiency for comparable crystal parameters. Generated UV power in ADA was insensitive to angular changes in the direction of the fundamental, as expected for 90° phase-matching, whereas ADP could be readily tuned by changing the incidence angle. Because of its narrow tuning range at fixed angle and temperature, the ADA crystal is very sensitive to temperature changes; a change of 0.1°C was sufficient to halve the generated power. In fact as the pump power was increased, the phase-matching wavelength changed due to increased heating through absorption of fundamental within the crystal. This point is illustrated in figure 8 where measured harmonic power is plotted as a function of laser wavelength for various values of the fundamental power, the oven temperature being fixed throughout. The experimentally determined phase-matched wavelength as a function of temperature for the 90° phase matched ADA crystal at a fixed intracavity power is plotted in figure 9. The limits indicate the tuning range over which the crystal has been successfully operated.

Using the Spectra-Physics 171 argon ion laser operating in the TEM_{oo} mode at 514.5 nm as the pump laser the useful UV output power at 295 nm monitored through mirror R_5 is plotted as a function of pump power in figure 10. THis curve was obtained by adjusting the dye laser wavelength to optimise the UV output for each value of the intracavity power. This ensures that the crystal is always phase-matched along the axis of the Gaussian beam. The phase-matching wave-length was found to change at a rate of 0.05 nmW^{-1} of intracavity power.

The straight line of gradient 2 in figure 10 was drawn for a value of $Kh\ell = 3.0 \times 10^{-4}\ W^{-1}$ allowing for Fresnel losses in the windows and mirror losses. The agreement between this value and the calculated value of $2.4 \times 10^{-4}\ W^{-1}$ is quite good although it should be noted that an extra factor of two should be included in the calculated value because of the many longitudinal modes of the laser. The probable reason for the good agreement is that the second harmonic power generated by the broadband system is less than would be expected because the laser linewidth is approaching that of the generation bandwidth of ADA at fixed temperature and orientation. The fundamental power is therefore not fully utilized in the harmonic generation process.

The progressive departure of the generated harmonic from a quadratic dependance on the intracavity power is similar to that observed when ADP was used as the doubler. This fall-off in power is again attributed to thermally induced phase-mismatching. The thermal reduction factor h_T defined in Chapter II is plotted as a function of the intracavity power parameter a in figure 11. The solid line is an experimental fit of the expression for h_T calculated by Okada and Ieiri[10] and given in Chapter II. The parameter P_T was varied to fit the data. Good agreement is obtained when $P_T = 1.7W$.

The intracavity power as a function of pump power is shown in figure 12. The threshold for the second harmonic dye laser was in the region of 500 mW. From the figure it can be seen that the intracavity power tends to saturate and eventually go through a maximum with pump power at a pump power of about 4W.

At even higher powers the laser eventually stopped oscillating. This observation is in contrast to the behaviour when the laser was pumped with the high power multimode plasma jet argon ion laser. In this case the intracavity power was observed to be linear in pump power up to pump powers in excess of 10W. The behaviour was also linear when this argon laser was used to pump the original ADP cavity. In this case more than 20W argon ion power was used and up to 50W intracavity power was generated. A probable explanation for this is that when TEM_{oo} mode pumping was used a very small spot was focused onto the jet and strong thermal effects resulted. However when the multimode beam was focused with the same lens the focused spot size was much larger and so thermal effects would only become serious at much higher pump powers.

The above cannot be the complete explanation since it was observed that when pumping a fundamental dye laser with a TEM_{oo} mode argon ion laser the output power was linear in pump power up to powers of at least 6.5W. It was only when the crystal was in the cavity that the dye laser power saturated with pump power. This may be explained by a possible overall reduction in the stability of the cavity when the crystal was incorporated, the combined effect of thermal lensing in the dye jet and thermal lensing in the crystal limiting the maximum pump power.

It is possible to estimate the absorption coefficient of the ADA crystal used in these experiments by comparing the shift in phase-matching wavelength at changing intracavity power with the temperature rise expected when a given amount of intracavity power is absorbed. The rise in temperature can be estimated by knowledge of the phase-matching wavelength against phase-matching temperature characteristics.

The rise in temperature on the axis of a Gaussian beam when a power of $P_\omega \delta_1$ per unit length is absorbed is given by equation (55) of Chapter II as

$$\Delta T = T\ (0) - T\ (\infty) = P_\omega \delta_1 / 2\pi\kappa_T \qquad (10)$$

and since this can be written

$$\frac{\Delta T}{P_\omega} = \left(\frac{\Delta T}{\Delta\lambda}\right)\left(\frac{\Delta\lambda}{P_\omega}\right) = \frac{\delta_1}{2\pi\kappa_T} \qquad (11)$$

it is possible to estimate δ_1 knowing only the thermal conductivity κ_T, and the ratios $(\frac{\Delta T}{\Delta\lambda})$ and $(\frac{\Delta\lambda}{P_\omega})$. The change in phase-matching wavelength as a function of intracavity power was found to be linear and changed at a rate of about 0.05 nmW^{-1}. This rate of change was found to be independant of the bulk crystal temperature. It has also been found that the change in phase-matching wavelength with crystal temperature is a linear function and changes at a rate of 0.37 nmK^{-1}. The value of κ_T for ADP is 0.02 W cm^{-1} K^{-1} and is unlikely to be very different for ADA and so the absorption coefficient is estimated to be 0.015 cm^{-1} for this sample of ADA.

With a knowledge of the crystal absorption coefficient and P_T,it is possible to estimate β,the rate of change of the difference in ordinary and extraordinary refractive indices with temperature as defined in equation (66) of Chapter II. It can be expressed as

$$\beta = (\partial n_{o,\omega}/\partial T - \partial n_{e,2\omega}/\partial T)_{T=T_m} = \frac{\lambda\kappa_T}{2P_T\delta_1\ell} \qquad (12)$$

Therefore at a fundamental wavelength λ = 600 nm,the factor β is estimated to be 1.6×10^{-5} K^{-1}.

The critical dissipated power which determines when the divergence due to thermal lensing becomes comparable to the divergence of the focused Gaussian beam can now be estimated. This power is given in equation (56) of Chapter II as

$$P_L = \lambda\kappa_T(\partial n_\omega/\partial T)^{-1} \qquad (13)$$

The value of $(\partial n_\omega/\partial T)$ is not known for ADA but,if it is assumed that the measured value of β is approximately equal to $(\partial n_\omega/\partial T)$,an order of magnitude estimate for P_L is $P_L = 80$ mW. For a 1.5 cm long crystal of 1.5% cm^{-1} absorption this critical dissipated power corresponds to two way intracavity power of 3W. The experimental evidence indicates that powers in the region of 20W can be reached before thermal lensing becomes really serious. This lack of agreement is probably due to the assumption that the crystal acts as a thin lens, and to uncertainties in the effect that such a lens has on the intracavity power and cavity stability.

The saturation of the intracavity power with pump power when single mode pumping is used is clearly a severe limit to the ultimate efficiency of the second harmonic laser. More effort will have to go into establishing whether the thermal lens effect in the jet or the thermal lens in the crystal is the more important. If it is the jet which is the more serious, steps such as using new solvents can be taken but if it is the crystal the only way of ameliorating the effect is to redesign cavity so that a thermal lens has less influence on the power.

The UV linewidth was estimated by measuring the linewidth of the visible dye laser. An upper limit on the UV linewidth is obtained by assuming that the UV linewidth (cm^{-1}) is twice that of the fundamental linewidth (cm^{-1}). The visible linewidth was measured using a Fabry Perot scanning interferometer with an adjustable plate separation. A typical scan of the visible laser linewidth is shown in figure 13. The plate separation was 1.5 mm which corresponds to a free spectral range of approximately 3.5 cm^{-1} and the measured visible linewidth was 1.3 cm^{-1}. The UV linewidth was therefore estimated to be less than 2.6 cm^{-1} or less than 0.02 nm at a wavelength of 300 nm. When the laser was subsequently used in the study of the high lying states of Rb, the UV linewidth corresponded to 0.015 nm confirming that the estimated linewidth is an upper limit. The linewidth of the laser depended weakly on the laser power, increasing slightly at higher powers, so a reasonable estimate of the UV laser linewidth is 0.02 nm.

The laser linewidth could be substantially reduced by including a Fabry Perot etalon in the cavity. A fused silica etalon of 0.5 mm thickness dielectrically coated to 30% reflectivity at 590 nm was inserted in the cavity. The resulting linewidth was measured in a manner similar to the broadband laser and was estimated to be 0.2 cm^{-1} or 0.002 nm at a wavelength of 300 nm. The intracavity power was reduced by a factor of about two when the etalon was introduced. However it was found that the UV power did not drop by the expected factor of four but nearer to a factor of two. This was attributed to the linewidth of the broadband visible laser being comparable to the second harmonic generation bandwidth of the ADA crystal at fixed temperature and orientation. When the narrowband laser was used it was possible to centre the laser wavelength to the maximum of the harmonic generation curve and hence extract relatively more UV power. The maximum extracted second harmonic power with the narrowband system was 10 mW.

V.5 Tuning the Frequency Doubled Dye Laser

Because of the narrow wavelength range over which phase-matching can be maintained in ADA at constant temperature, the temperature of the crystal must be changed progressively with the laser wavelength if the laser is to be scanned over more than about 0.1 nm. Two tuning systems have been devloped to allow the second harmonic laser to be tuned over an extended range. The first is a system suitable for tuning the broadband 0.02 mm laser and the second is suitable for scanning the narrowband laser with linewidth 0.002 nm. The broadband system has been tuned over a range of 2 nm and the narrowband system has been tuned over a range of 1 nm around 295 nm, both in a single scan.

In the broadband tuning system, the laser wavelength is tuned by rotating the birefringent filter while at the same time ramping the crystal temperature. The simplest method of doing this is to devise a method whereby the crystal temperature and the birefringent filter's angular setting are both made to respond to an input voltage. They can then be ramped together and kept in step by a preset proportional division of the voltage.

The crystal temperature was made voltage sensitive by modifying the temperature controller as shown in appendix A. Basically, the input voltage after going through a buffer stage is added to one arm of the potentiometric bridge and so changes the balance point.

The birefringent filter's angular position was made voltage sensitive by the potentiometric bridge arrangement shown in appendix A. The filter drive mechanism was directly coupled to a potentiometer which sensed the filter position. If the bridge is off-balance the zero error voltage is applied to an amplifier which drives a DC motor. The filter could be set with an angular accuracy corresponding to less than 0.02 nm in the UV and had a response time of about 1 sec.

A linear ramp voltage was provided by a motorized potentiometer. The output voltage was apportioned between the laser wavelength controller and the temperature controller so that phase-matching was maintained at the laser wavelength. Because of the thermal capacity of the crystal holder, the maximum linear temperature rise was 1°C per minute. This is equivalent to a maximum UV scanning rate of 0.2 nm per minute. The laser could be scanned over a range of 2 nm before the filter and crystal temperature went out of step and harmonic generation ceased.

An alternative approach to proportional control that has been used was to lock the fundamental wavelength to maximise UV power output. In this way the tuning of the birefringent filter automatically follows the crystal temperature. The UV power is maximised by modulating the birefringent filter, and locking onto the zero in the amplitude of the resulting modulation of UV power. (This occurs at the peak of the second harmonic tuning curve.) The signal from a detector monitoring the UV power is fed through a phase sensitive detector and then through a double integrator. The latter gives a 12 dB per octave roll-off well below the modulation frequency falling to a 6 dB per octave roll-off close to the modulation frequency. The phase sensitive detector and first integrator were a lock-in amplifier (Brookdeal 401) and the second integrator was built to the NPL design which is described in appendix A. The output from the double integrator is fed to the voltage sensitive drive mechanism on the birefringent filter. The response time of the mechanical tuning system was less than one second. The modulation frequency was therefore chosen to be 1 Hz and the integration time of the first integrator either 3 sec or 10 sec depending on the tightness of lock required. The amplitude of the wavelength modulation corresponded to 0.02 nm peak to peak, and was necessary to overcome the noise due to intensity fluctuations at this frequency. This tuning system had a range of 3 nm in the UV (limited only by the integrator output voltage) at a rate of 0.4 nm per min. However, the slowness of the tuning element and the intensity fluctuations in the laser meant that the lock could be easily lost. It will eventually be interesting to use this system with electro-optical modulation so that higher modulation amplitude and consequently a tighter lock can be maintained. A proposed method of doing this will be described later.

The narrowband tuning was accomplished by tilting a thin etalon inside the laser cavity. In order to avoid jumps in the laser oscillation frequency every free spectral range of the etalon (0.2 nm) the birefringent filter must be tuned with the etalon.

If the oscillation frequency is ν_o when the etalon is set normal to the laser beam, the change in oscillation frequency in tilting the etalon through an angle θ is

$$\Delta\nu = \nu_o - \nu = \frac{c}{2tn}(1 - \cos\theta) = \nu_o (1 - \cos\theta) \qquad (14)$$

where t is the thickness of the etalon and n is its refractive index. Provided that θ is small the change in oscillation frequency is approximately given by

$$\Delta\nu/\nu_o = \theta^2/2 \qquad (15)$$

The loss introduced by tilting an etalon due to internal beam walk-off can be written as[11]

$$\ell = [R/(1 - R^2)^2]\ (2t\theta/nw_o)^2 \qquad (16)$$

where R is the reflectivity of the etalon and w_o is the spot size of the Gaussian mode on the etalon. This equation is valid provided the value of the loss is small ($\ell \lesssim 10\%$) and that the reflectivity is reasonably large ($R \gtrsim 15\%$). The thin etalon used was made of fused silica and was 0.5 mm thick and dielectrically coated to about 30% reflectivity at 590 nm. Assuming a spot size of 1 mm on the etalon, the laser can be tuned through about 10 nm at 300 nm for an increase in linear loss of only 1%. This would require an angular tilt of about 15°.

The etalon was tilted using a torsion galvanometer (General Scanning, type 308). This scanner could be tilted up to 6° either side of zero and could be set to an accuracy of about 1% of its total excursion. In order that the laser frequency be scanned linearly with the input voltage,it is necessary to electronically take the square root of the input voltage. The circuit which was used to do this is shown in appendix A along with the power amplifier circuit to the galvanometer. The square root circuit is fairly simple but suffers from the disadvantage that at low input voltages,dc off-sets can give rise to large errors in the output. The laser frequency was therefore not completely linear over the tuning range.

When tuning the narrowband UV system it is necessary to gang together the tilting etalon, the birefringent filter and the crystal temperature. This was done by suitably apportioning the ramp voltage to the inputs of the drive amplifiers of the three different elements in a similar way to the method described for the broadband system (see figure 14). A tuning range of 1 nm in the UV has been obtained with this arrangement and was limited mainly by the maximum excursion of the scanning galvanometer.

V.6 Proposed Improvements

Although the design of a frequency doubled dye laser has been quite successful in producing tunable UV radiation and is capable of producing about 50 mW at 295 nm with a linewidth of 0.02 nm for a pump power of about 5W there are several ways in which the design may be improved in the future.

The first of these improvements involves extracting more of the generated second harmonic power from the cavity by adding an index matching oil between the crystal and window. The second improvement would be to increase the crystal length so that coma and astigmatism can be simultaneously corrected. Both of these improvements are fairly speculative in the sense that they will only be shown to be improvements by experiment. The final improvement that is to be discussed is the use of servo locking techniques to improve the tuning range of the broadband second harmonic system.

It has already been mentioned that about 40% of the UV radiation is lost by reflection in going from the crystal to outside the crystal cell. If the crystal is to be sealed in a hermetic cell, and if phase-matching fluids are to be avoided, this loss is inevitable. One of the major features of this laser design is that phase-matching fluids are avoided since it has been reported that crystal damage is the factor which limits the efficiency and lifetime of the crystals[12]. This design appears to have been successful in this regard since crystals have been operated in cavities with one-way powers in excess of 40W without signs of damage over periods of many months. However a 40% UV loss is quite significant and it may be that, for some low power applications, it is desirable to extract the maximum UV. Welling[9] has reported that when silicone oil is used as a matching fluid, crystal damage is avoided. It is certainly worth experimental investigation in this system to see if a thin layer of silicone oil between the crystal and window would lead to any damage problems.

The refractive index of ADA at 590 nm is 1.57, the refractive index of fused quartz is 1.46 and the refractive index of Bayer silicone oil is 1.40. The slight differences in refractive index between the surfaces will give rise to residual reflection losses at fundamental even if one of the surfaces is set at Brewster's angle. A small reflection loss for the fundamental could severely reduce the intracavity power and it is therefore important to know the reflection coefficient between a medium of refractive index n set at Brewster's angle and a medium of refractive index n + δn where δn is small compared to n.

The reflection coefficient for an s-polarised wave(ie a wave for which there is a Brewster angle)is given by

$$R_s = \left[\frac{\{n/(n + \delta n)\}\cos\theta_i - \cos\theta_t}{\{n/(n + \delta n)\}\cos\theta_i - \cos\theta_t}\right]^2 \qquad (17)$$

and the corresponding p-polarised reflection coefficient is

$$R_p = \left[\frac{-\cos\theta_i + \{n/(n + \delta n)\}\cos\theta_t}{\cos\theta_i + \{n/(n + \delta n)\}\cos\theta_t}\right]^2 \qquad (18)$$

where θ_i and θ_t are the incidence angle and the angle of the transmitted beam respectively. Making the assumption that n >> δn these reduce to

$$R_s = \left[\frac{\delta n(1 - 2\cos^2\theta_i)}{2n\cos^2\theta_i - \delta n}\right]^2 \qquad (19)$$

$$R_p = \left[\frac{\delta n\,(1 - 2\cos^2\theta_i)}{2\,n\cos^2\theta_i + \delta n(1 - 2\cos^2\theta_i)}\right]^2 \qquad (20)$$

At Brewster's angle $\tan\theta_i = n$ and $\cos\theta_i = (n^2 + 1)^{-1}$ and so these reduce to

$$R_s = \left[\frac{\delta n(n^2 - 1)}{2n - \delta n(n^2 + 1)}\right]^2$$

$$R_p = \left[\frac{\delta n(n^2 - 1)}{2n + \delta n(n^2 - 1)}\right]^2$$

If it is assumed that $\delta n = 0.1$ and $n = 1.5$, then $R_s = 0.22\%$ and $R_p = 0.16\%$.

In going through a cell with two windows the total loss at the fundamental wavelength will be 4 x 0.22% which is almost 1%. This loss is higher than is desirable but the gain in UV output efficiency may well compensate the reduced intracavity power.

The theory of coma and astigmatic compensation discussed in Chapter IV indicates that, if coma and astigmatism are to be simultaneously compensated, a compensation angle of 29.1° is required. This means that a crystal of 6.0 cm will be required for mirrors of 10 cm radius of curvature if the theory is to be fully tested. For a crystal of this length, the thermal phase mismatching and lensing effects will be more apparent than in the 1.5 cm crystal used so far. However, the improvement in the cavity beam quality and linear loss may well make the compensated cavity with a long crystal an efficient device. This, like the index matching oil can only really be tested by experiment.

The final improvement discussed here is the use of the Pockels effect to provide a modulation in the UV intensity so that a servo system can be used to lock the laser frequency to the maximum UV output. This would be similar to the method of locking which was described earlier when a UV modulation was provided by changing the laser frequency. The advantage of this method is that a high modulation frequency can be used where the laser intensity noise is small. A second advantage is that the frequency of the laser does not have to be modulated.

If a crystal is cut so that $\theta_m = 90^\circ$ and the fundamental beam propagates at 45° to both the x and y-axis with an electric field applied along the z-axis, as in the case of a transverse electro-optic modulator, only the ordinary refractive index will be changed by the electric field. The magnitude of the change of the ordinary refractive index is given by[13]

$$\Delta n_o = r_{63}\, n_o^3\, E/2 \qquad (23)$$

where r_{63} is the electro-optic constant ($r_{63} = 9 \times 10^{-12}$ m V^{-1} for ADA), ℓ is the crystal length and E is the applied electric field. If the phase-matching condition is satisfied in the absence of an electric field the phase-mismatch on application of a field becomes

$$\Delta k = \frac{2\omega\Delta n_o}{c} = \omega\, r_{63}\, n_o^{\,3}\, E/c. \tag{24}$$

The effect of a small mismatch on second harmonic generation can be obtained by expanding the phase synchronism factor introduced in Chapter II about the phase-matched condition. This gives

$$\frac{\sin^2(\Delta k\ell/2)}{(\Delta k\ell/2)^2} \simeq 1 - \frac{2(\Delta k\ell)^2}{4!}. \tag{25}$$

Inserting the expression for Δk of (24) into (25) gives the fractional change in second harmonic power due to an applied voltage V across a crystal of thickness t as

$$\Delta P_{2\omega}/P_{2\omega} = \left(\frac{\pi r_{63}{}^2 n_o{}^6 \ell^2}{3\, \lambda^2\, t^2}\right) V^2 \tag{26}$$

where λ is the wavelength of the fundamental. For an ADA crystal of length 1.5 cm and thickness 0.5 cm the fractional change in UV power is

$$\Delta P_{2\omega}/P_{2\omega} = 2.3 \times 10^{-8}\ V^2. \tag{27}$$

Thus an applied voltage of 660 V will reduce the harmonic output by 1%.

An oscillating voltage between 0V and 660V should be more than adequate to provide a detectable modulation on the second harmonic output. The modulation can be detected by a phase sensitive detector which will provide a zero crossing signal when the UV intensity is a maximum. The zero error can be applied to the tuning element to lock the laser frequency on to the maximum second harmonic. Tuning is then accomplished by changing the crystal temperature. Servo circuits suitable for doing this will be described in Appendix A.

This tuning system should be superior to the earlier system where the laser frequency was modulated since the response of the system is much faster and the modulation can be applied at a frequency where the laser amplitude noise is low.

References

1. W D Johnson and P K Runge IEEE J Quant Electron QE8, 724 (1972)
2. A L Bloom, J Opt Soc Am 64, 447 (1974)
3. J C L Cornish and A Maitland, J Phys E, 6, 880 (1973)
4. A Maitland, Brit J of Appl Phy (J Phys D) 2, 535 (1969)
5. J Kuhl and H Spitschan, Opt Comm 13, 6 (1975)
6. S Saikan, Opt Comm 18, 439 (1976)
7. G Holtom and O Teschke, IEEE J Quant Electron QE10, 577 (1974)
8. J S Mitchell, Electro-Optic Developments, Private Communication
9. D Frölich, L Stein, H W Schröder and H Welling, Appl Phys 11, 97 (1976)
10. M Okada and S Ieiri, IEEE J Quant Electron QE7, 469 (1971)
11. W R Leeb, Appl Phys 6, 267 (1975)
12. M W Dowley and E B Hodges, IEEE J Quant Electron QE1, 552 (1968)
13. A Yariv, Introduction to Optical Electronics, Holt, Rinehart and Winston, New York (1971)
14. F Zernike, J Opt Soc Am 54, 1215 (1964)

Table 1 Parameters used to calculate the refractive indices of ADP from the data of Zernike[14]

	n_e	n_o
A	2.163077	2.302484
B	9.670312×10^{-11}	1.117089×10^{-10}
C	7.785289×10^{9}	7.605372×10^{9}
D	1.451540×10^{6}	3.751806×10^{6}
E	2.5×10^{5}	2.5×10^{5}
F	153.0	143.3
G	−0.969	−0.618
H	1.57×10^{-3}	4.81×10^{-4}

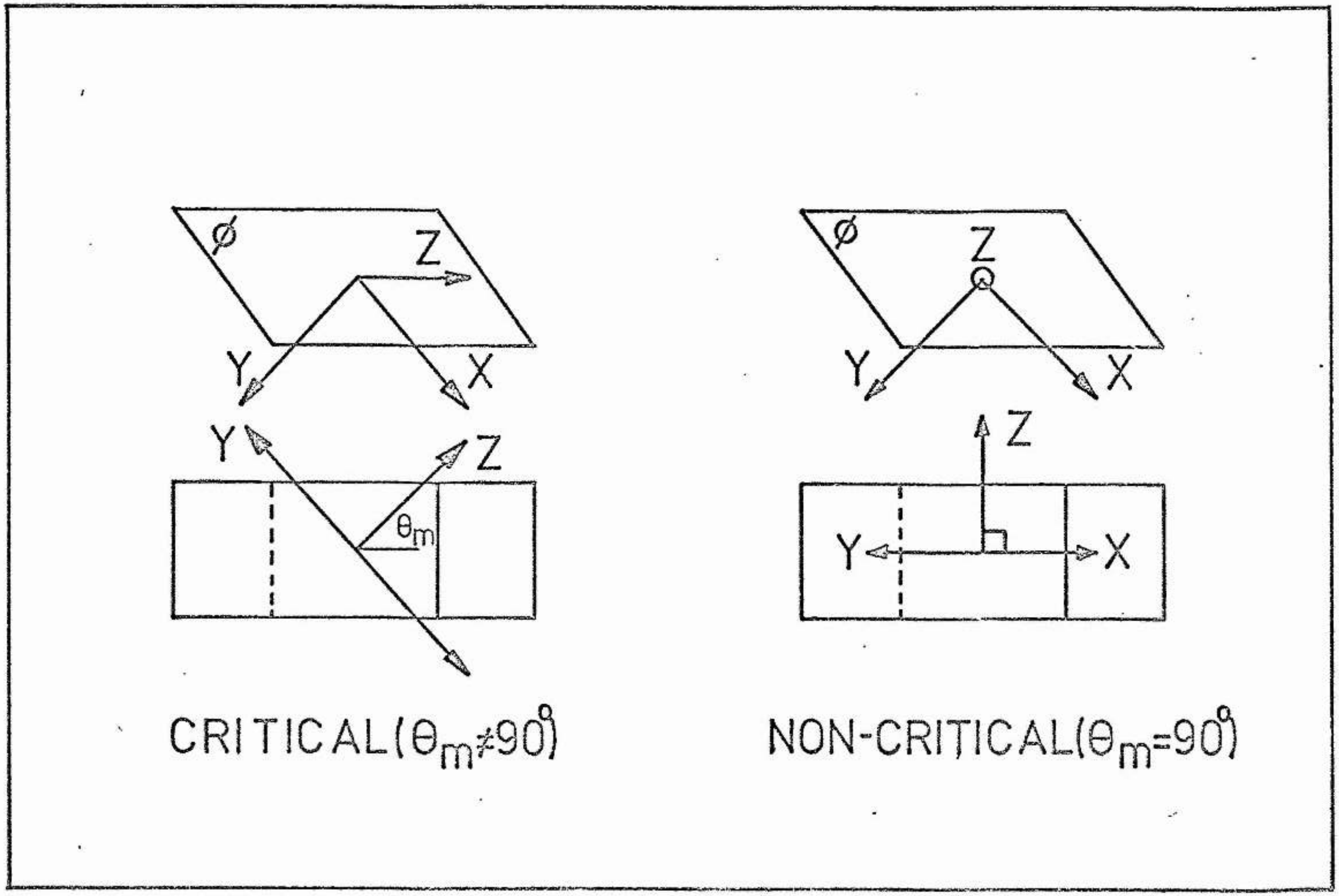

Figure 1. Orientation and cut of crystals for critical and noncritical phase matching.

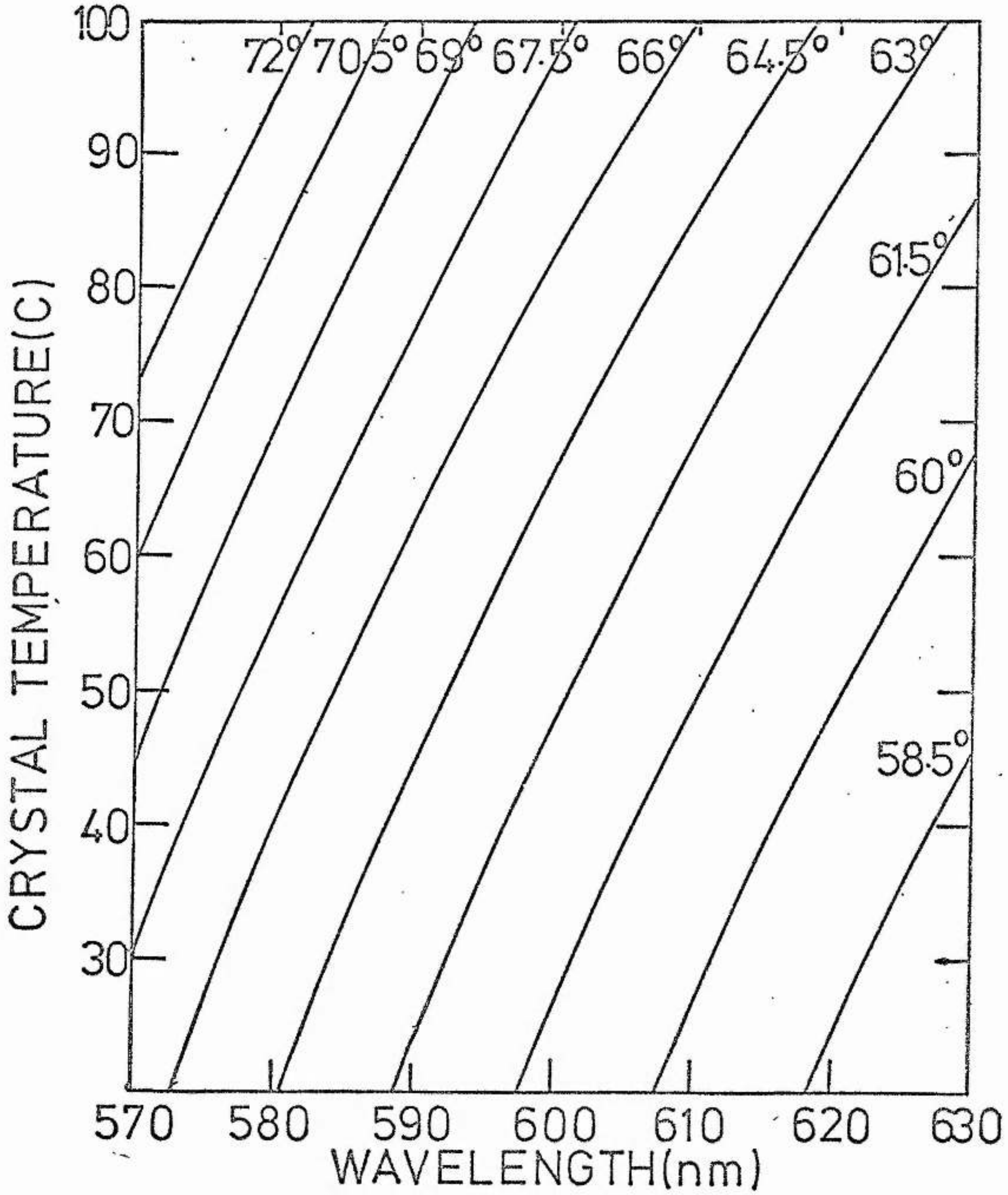

Figure 2. Phase matching temperature of ADP as a function of wavelength at various values of the angle θm.

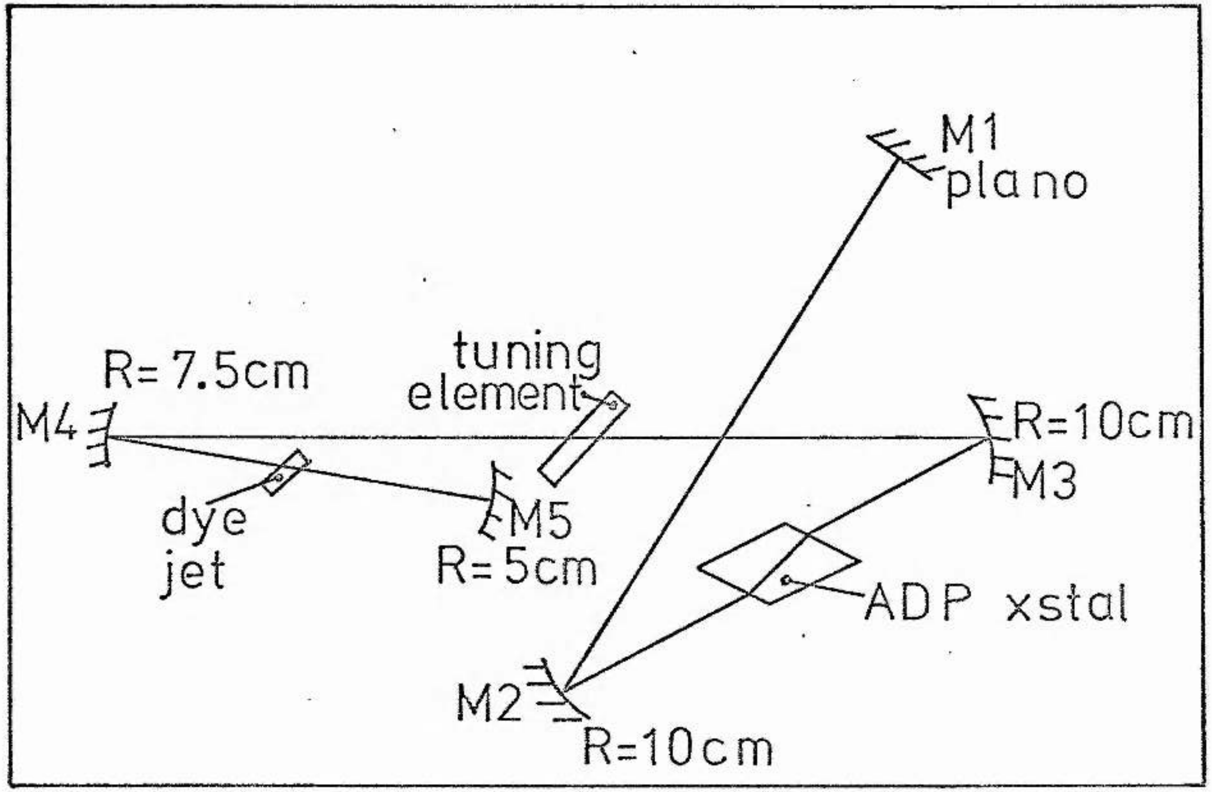

Figure 3. Schematic diagram of the dye laser cavity.

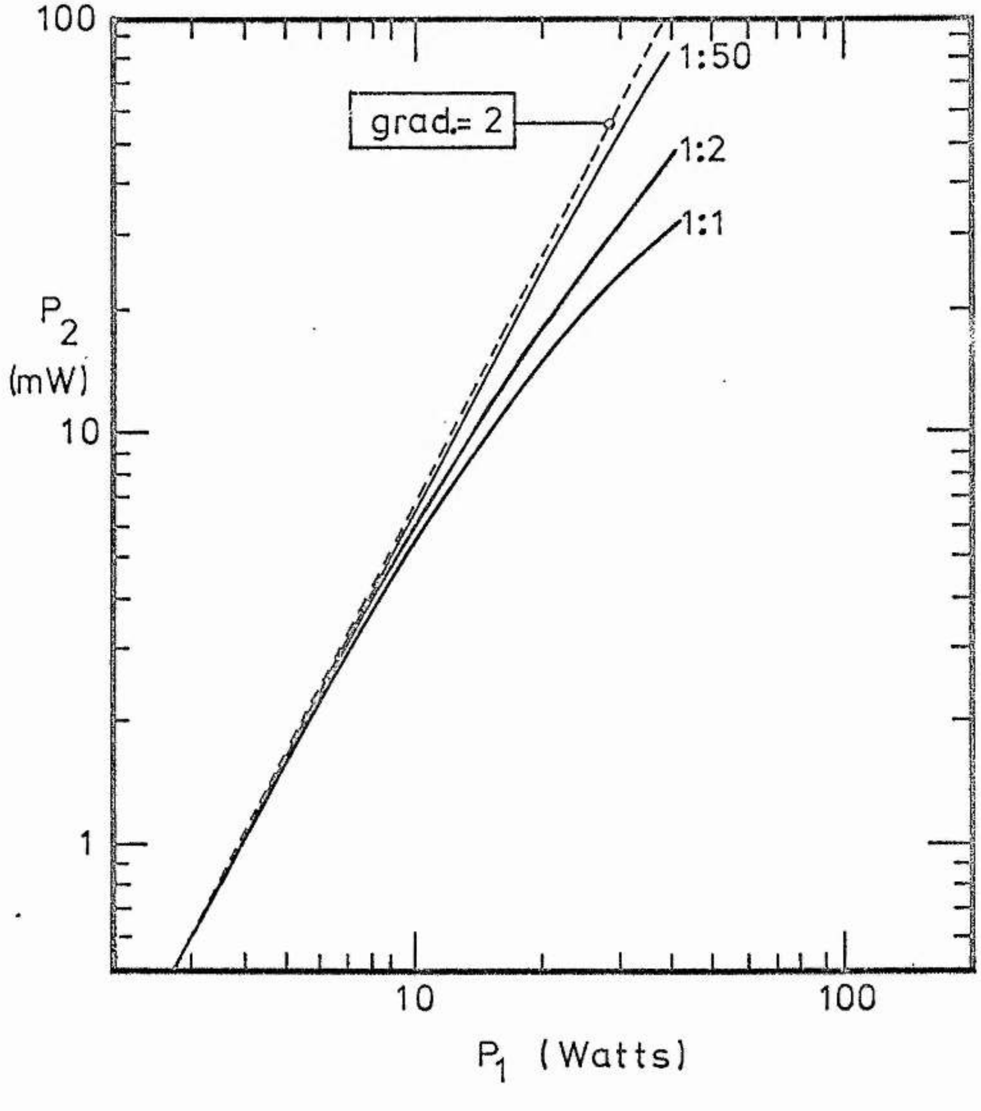

Figure 4. Generated second harmonic power as a function of intracavity power at various chopping duty cycles.

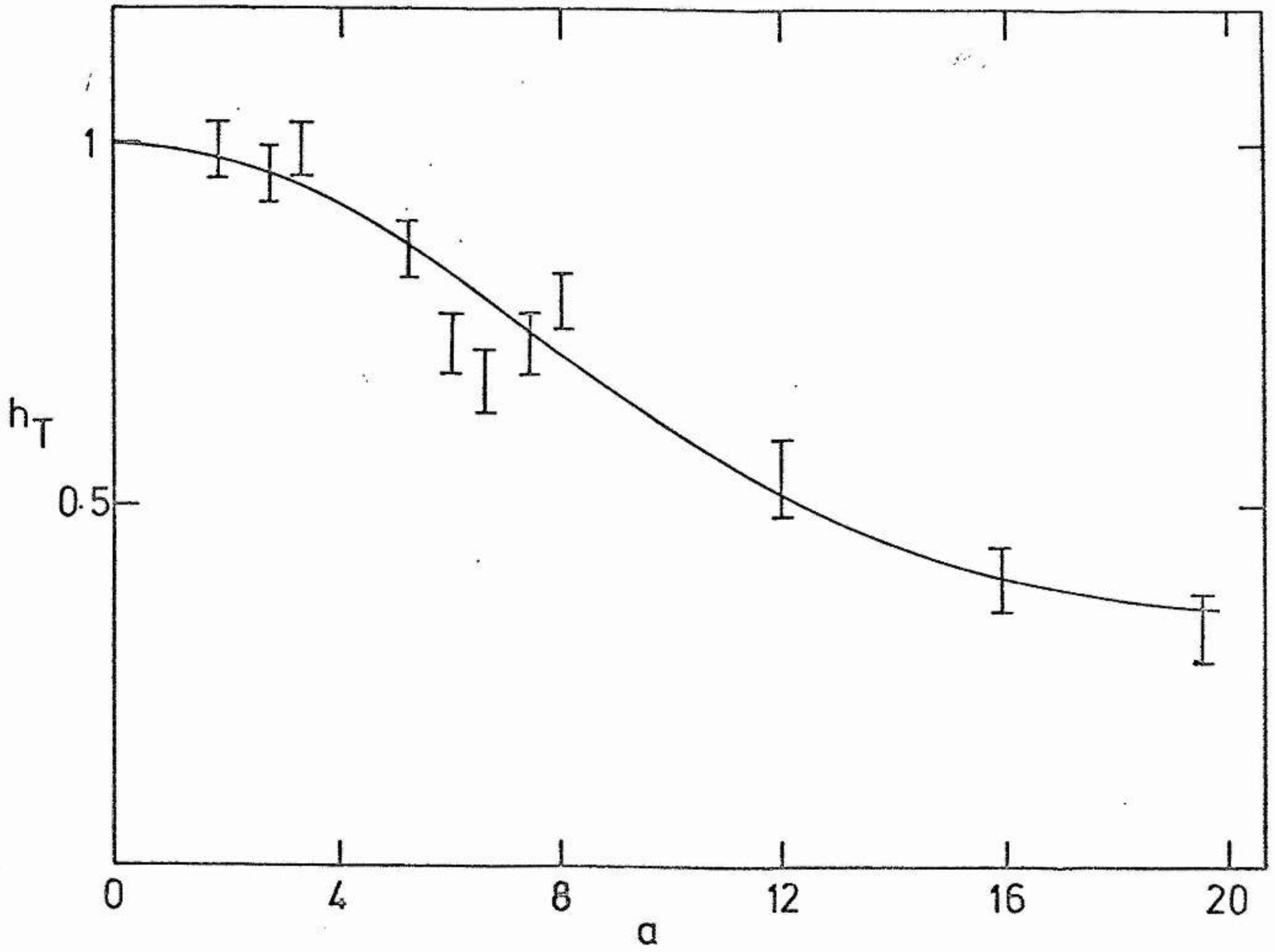

Figure 5. Reduction in second harmonic conversion as a function of intracavity power with no chopping.

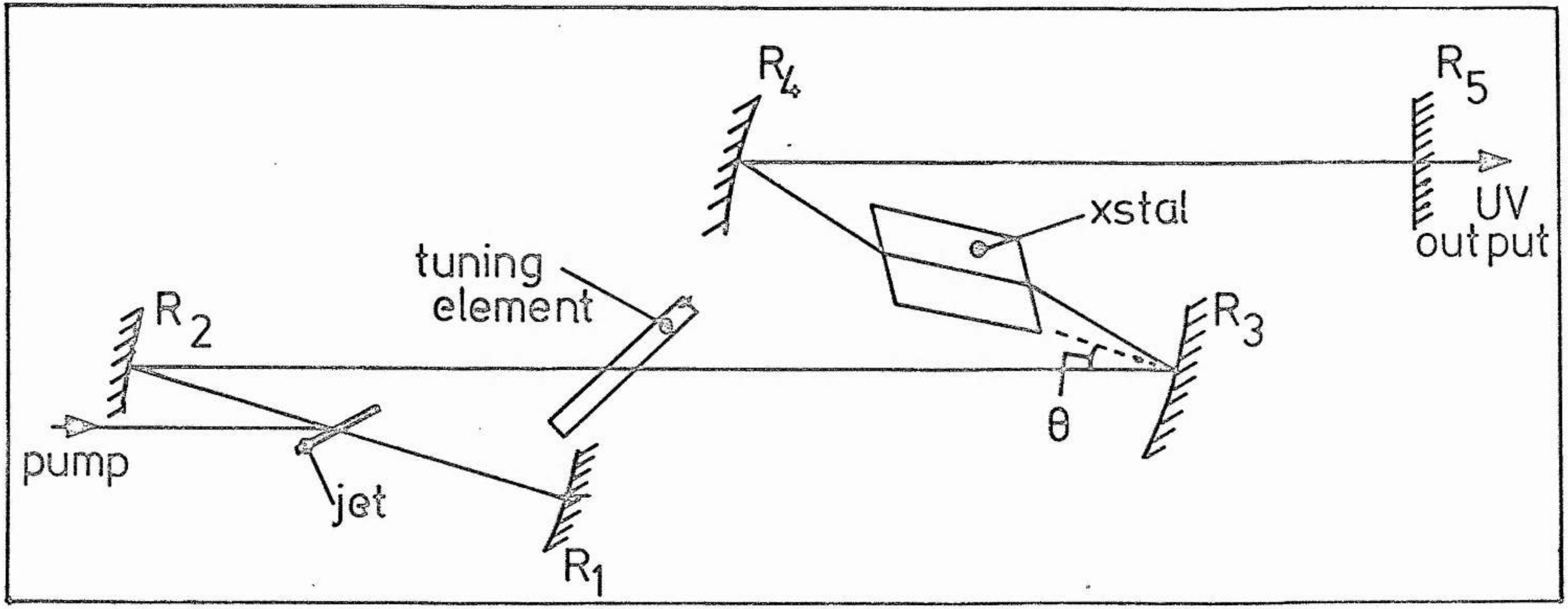

Figure 6. Schematic diagram of laser cavity using ADA as the doubler.

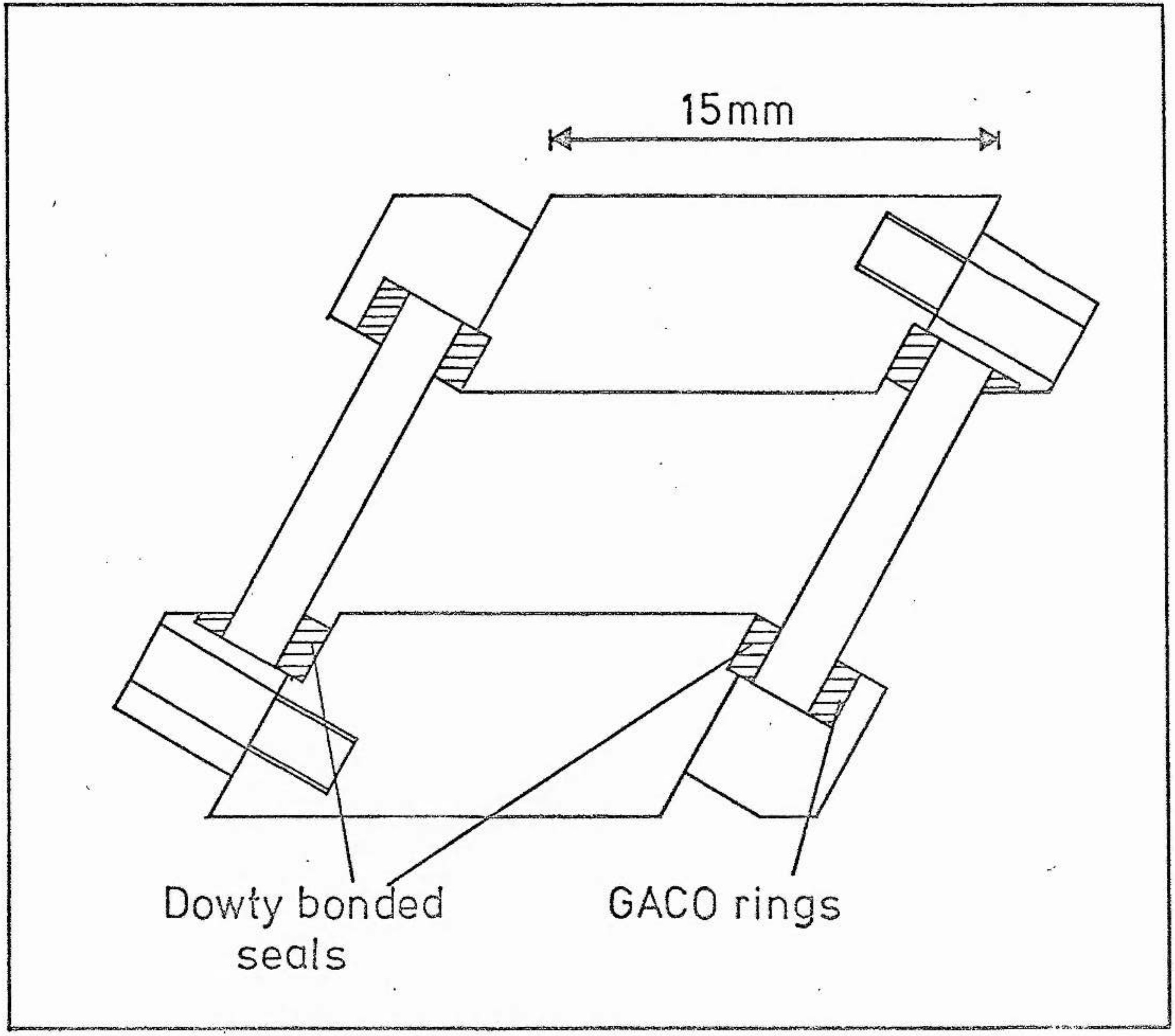

Figure 7. Diagram of the hermetically sealed cell for containing the ADA crystal.

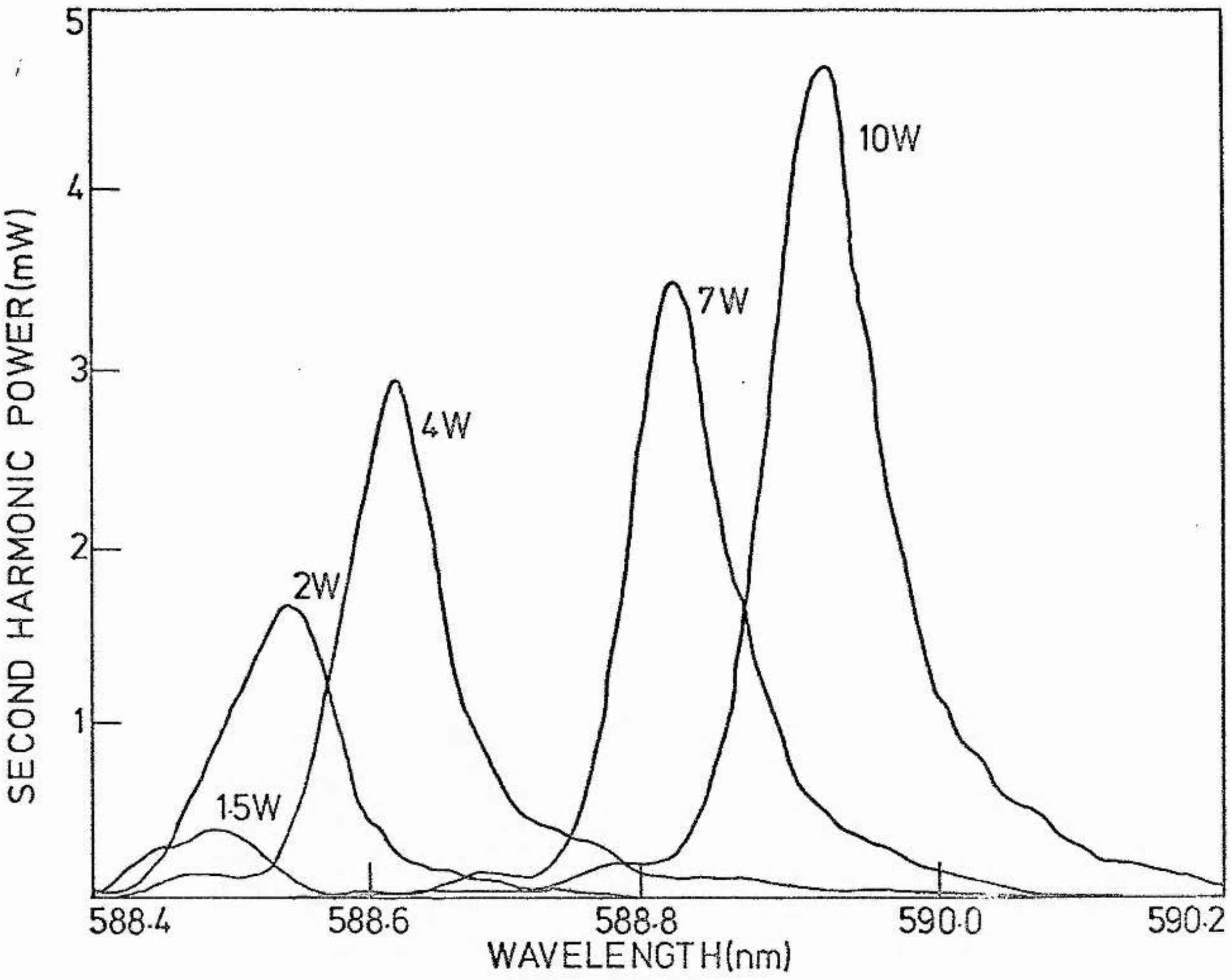

Figure 8. The second harmonic power as the laser wavelength is changed at fixed crystal temperature and orientation for various values of intracavity power.

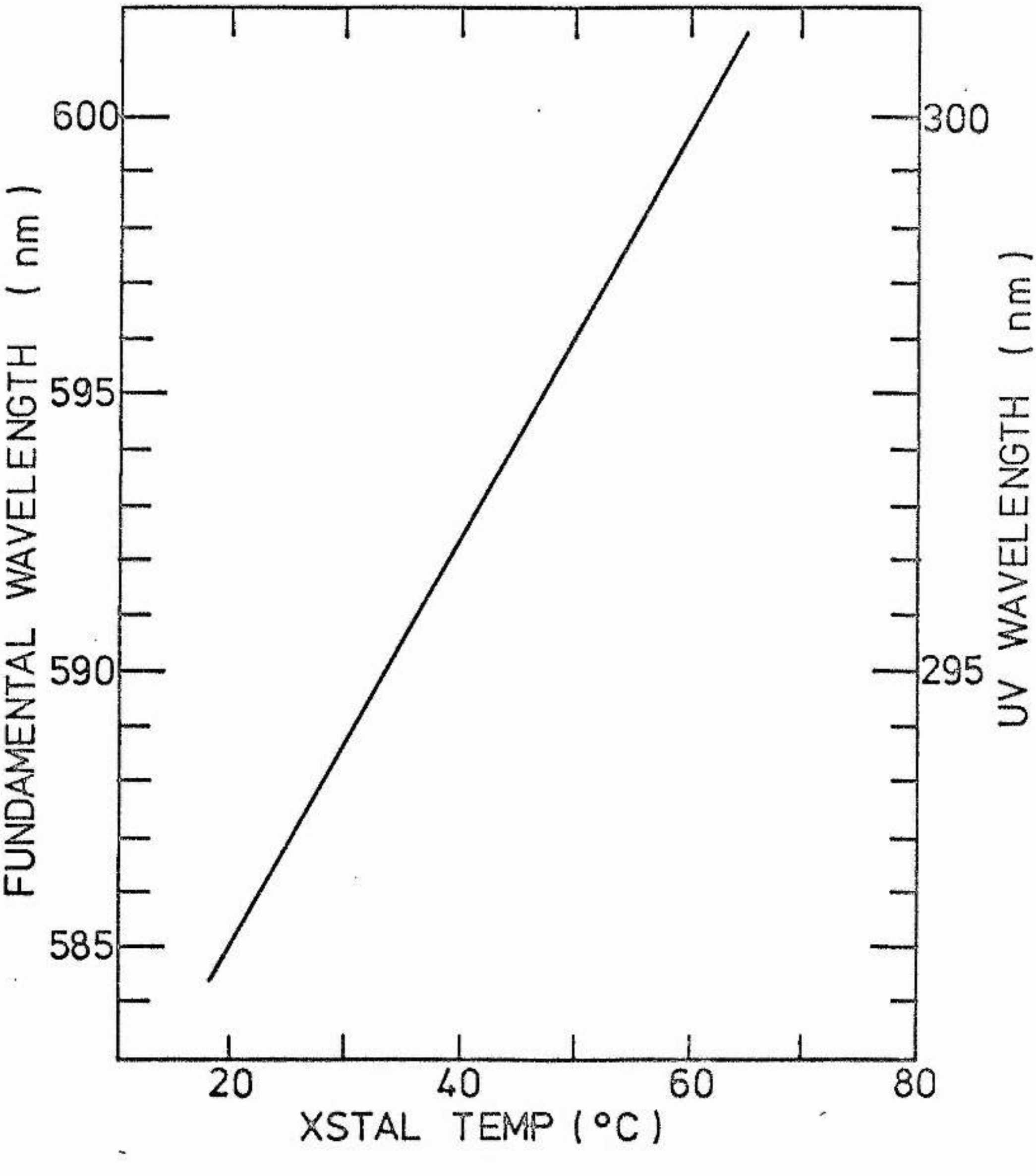

Figure 9. Experimental plot of phase matching wavelength as a function of crystal temperature for ADA.

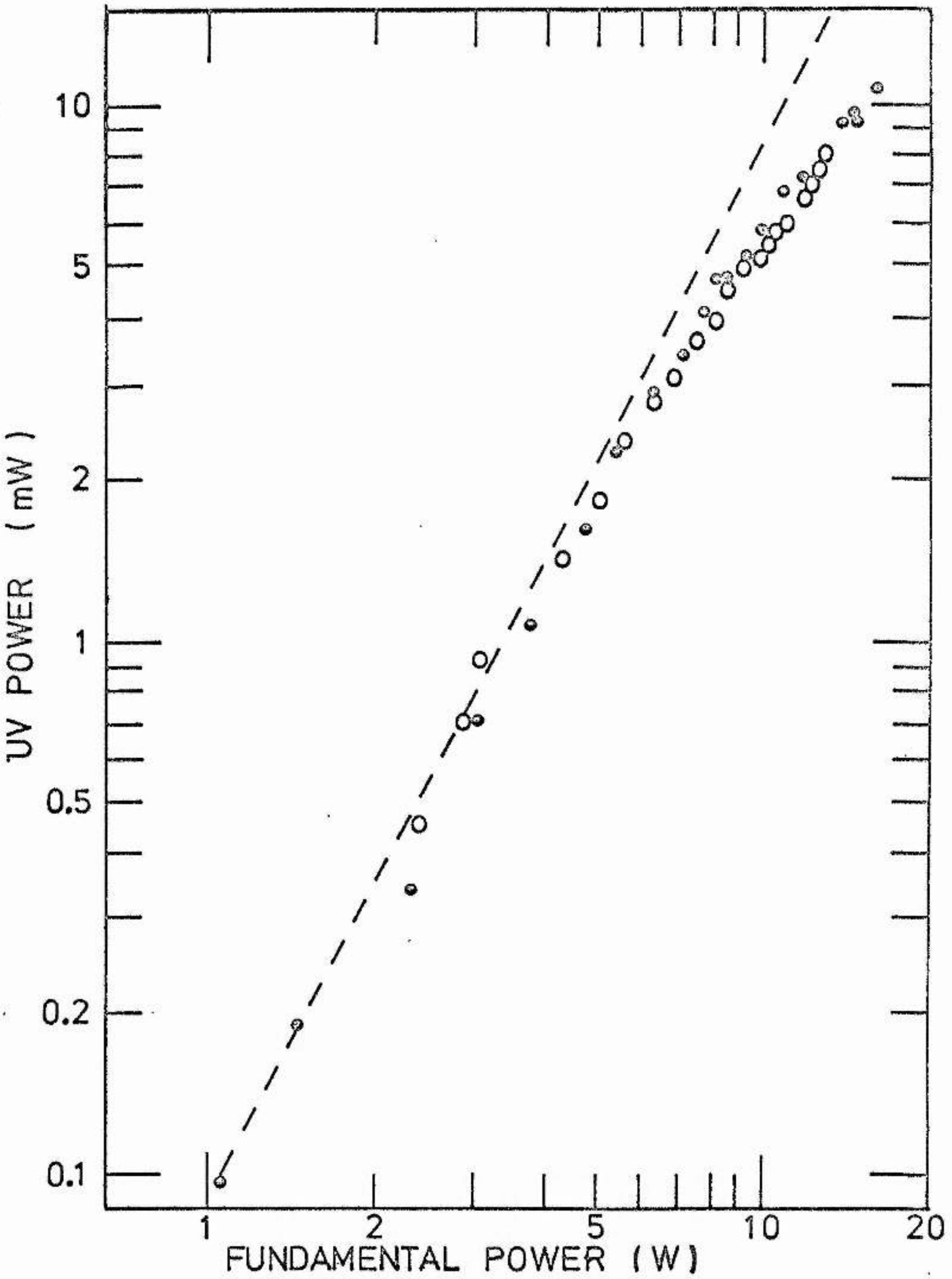

Figure 10. Second harmonic output power as a function of intracavity power.

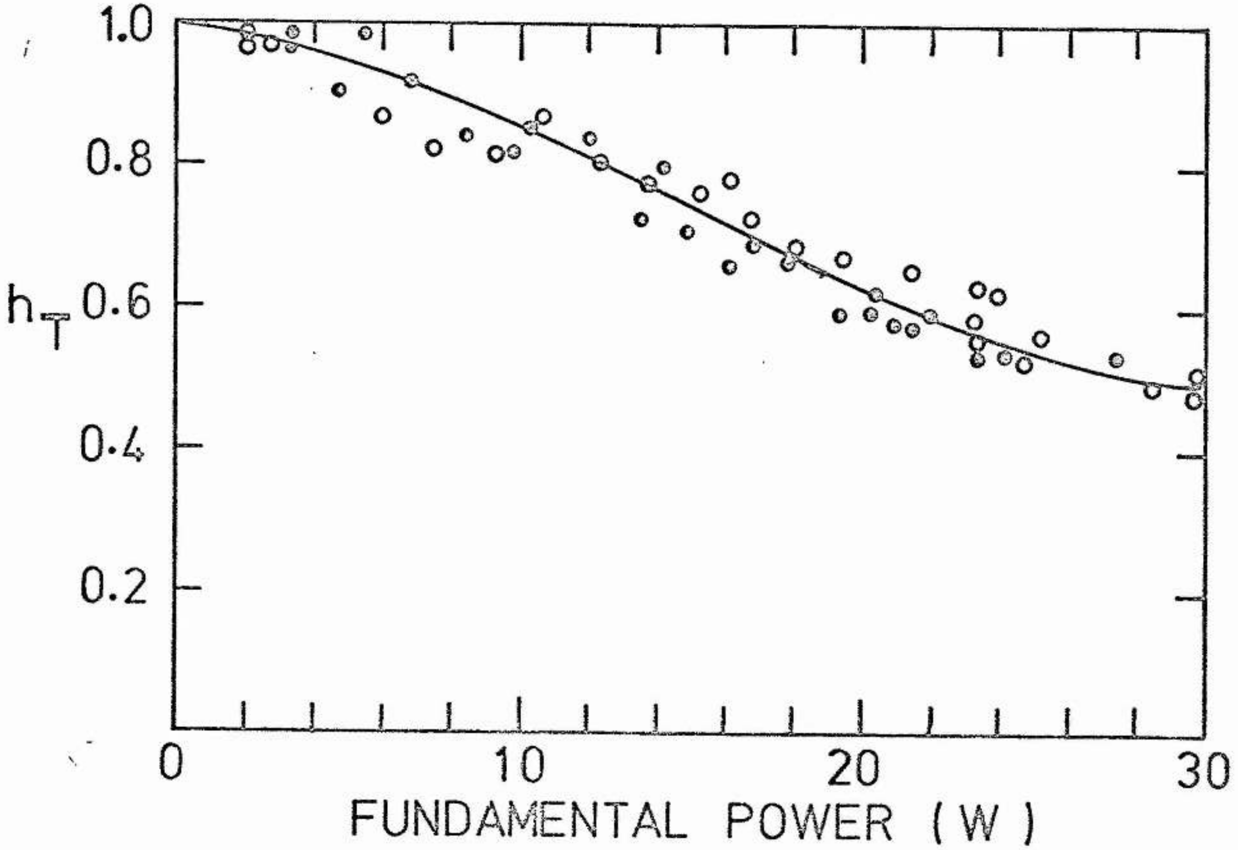

Figure 11. The second harmonic thermal reduction factor h_T as a function of intracavity power.

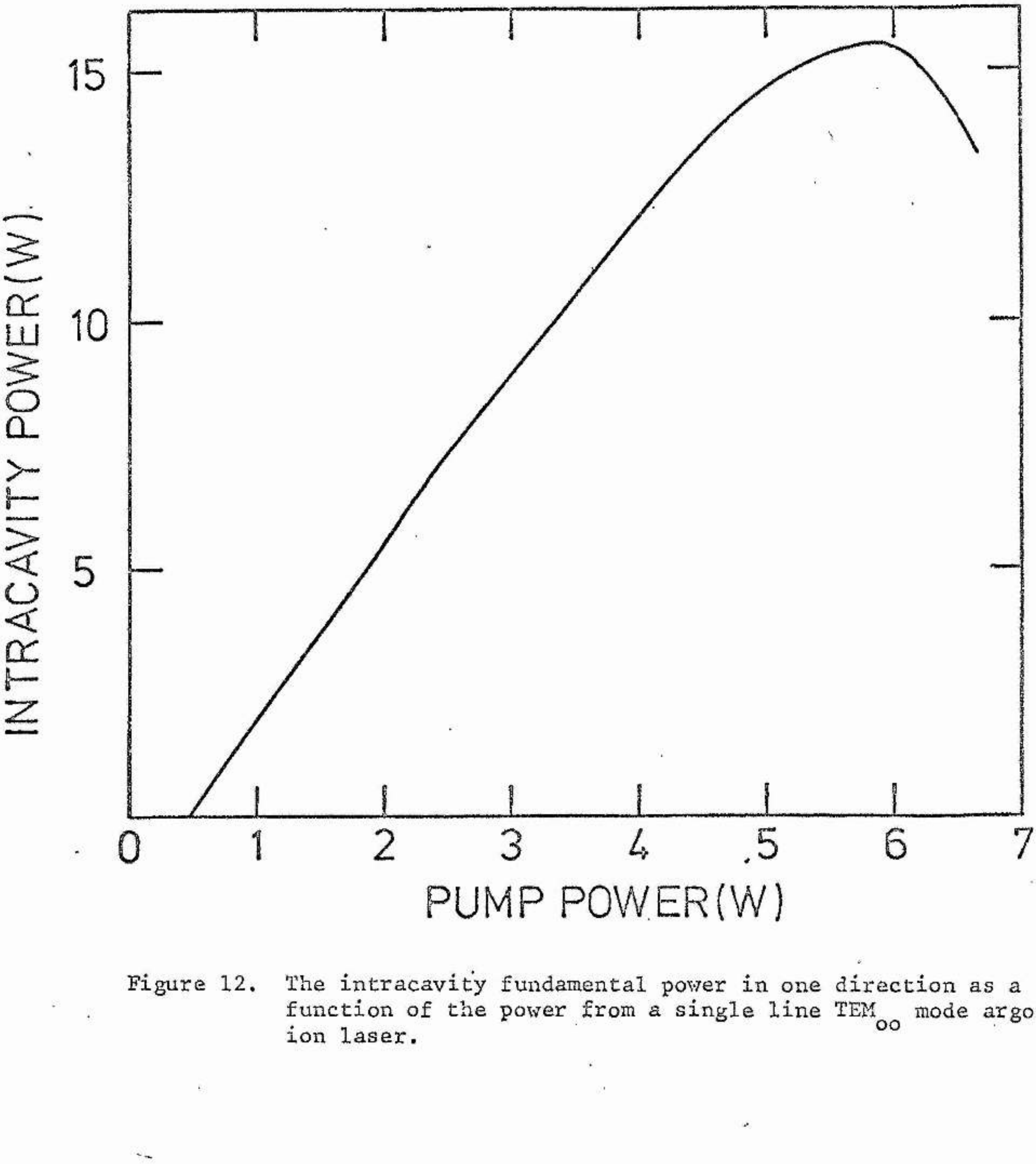

Figure 12. The intracavity fundamental power in one direction as a function of the power from a single line TEM_{oo} mode argon ion laser.

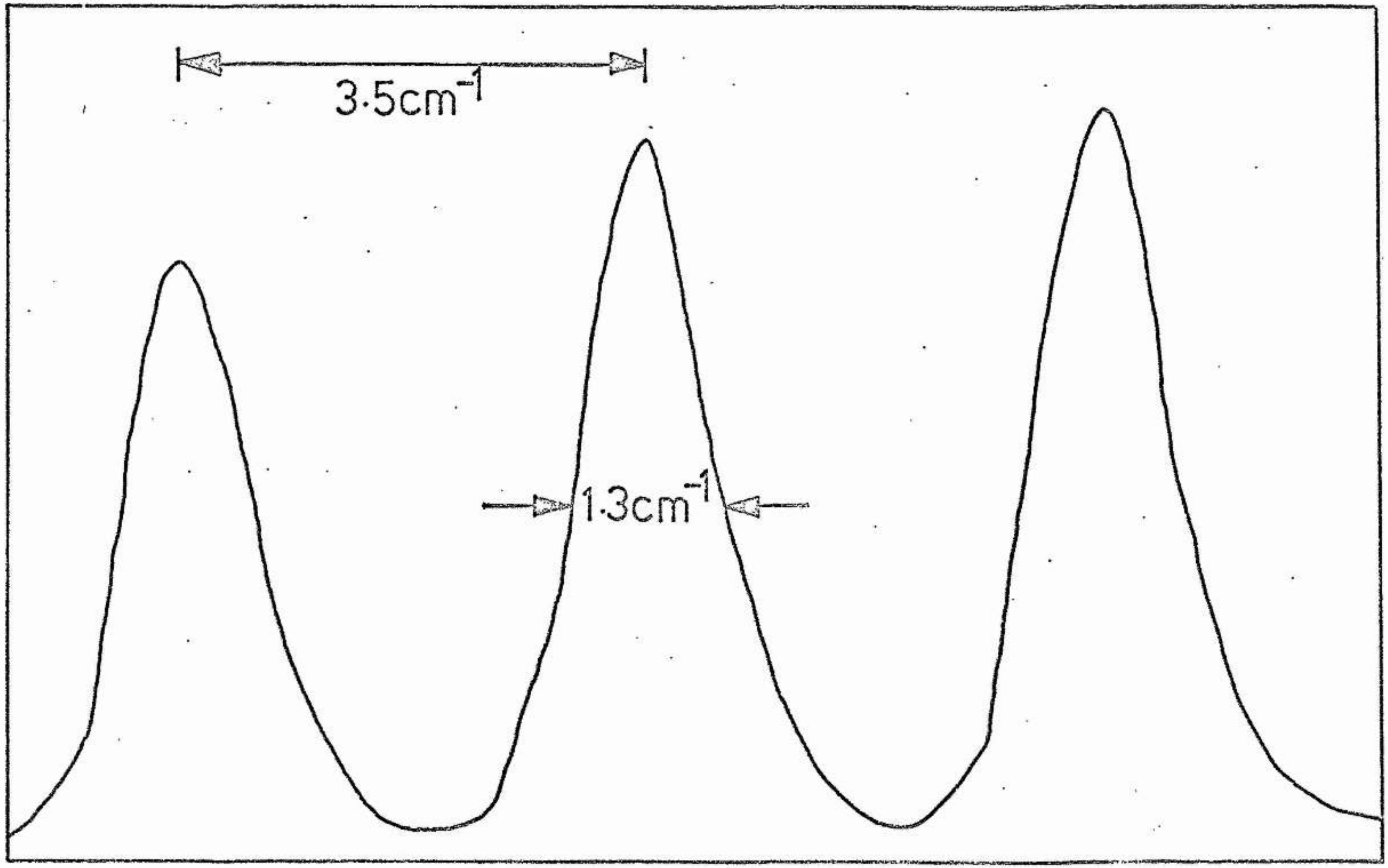

Figure 13. The transmission of the broadband laser through a scanning Fabry-Perot interferometer to measure the laser linewidth.

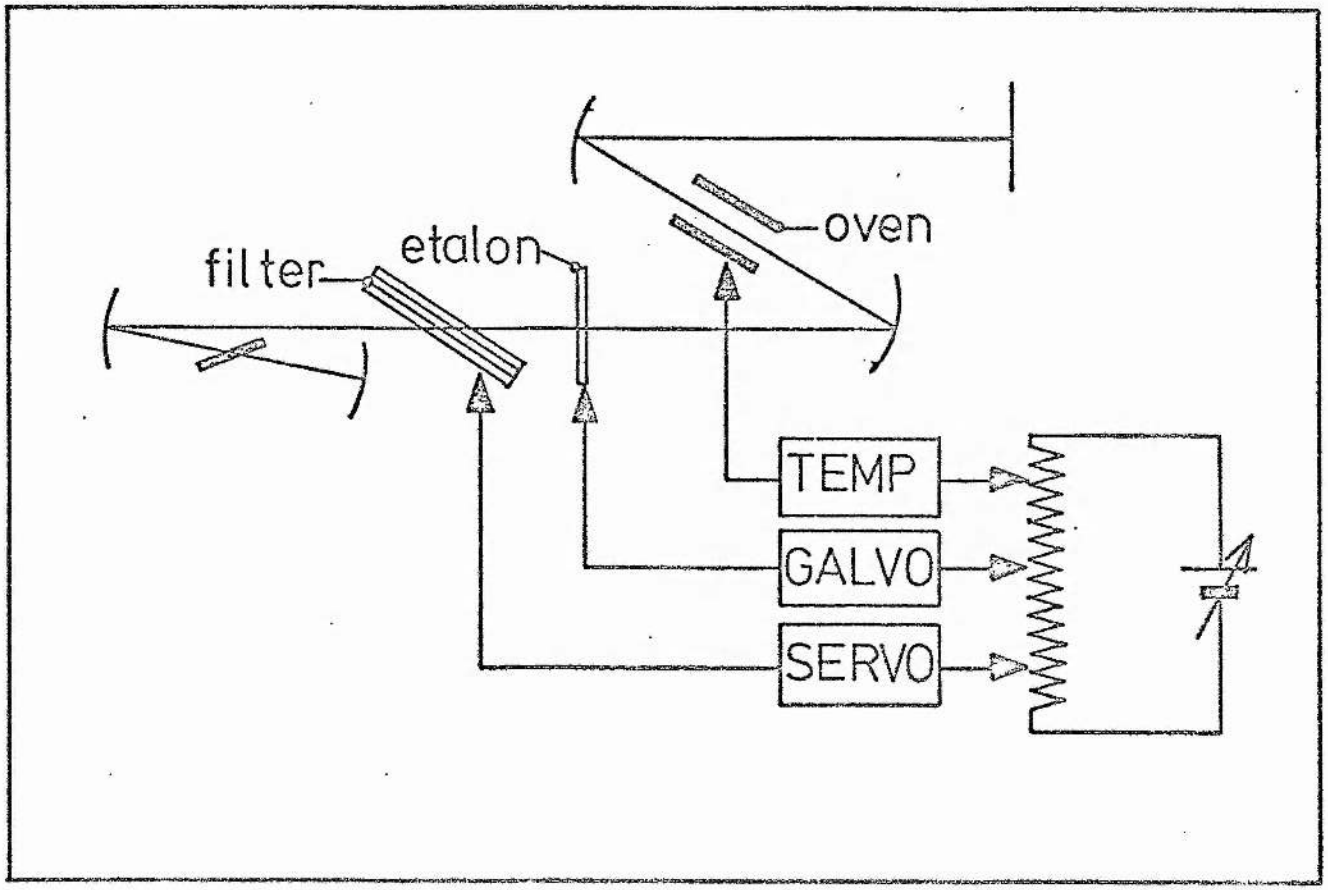

Figure 14. Schematic of proportional control system used to scan the wavelength of the narrowband laser.

CHAPTER VI

STUDY OF THE RYDBERG STATES OF RUBIDIUM USING A SECOND HARMONIC DYE LASER

Abstract

Some of the basic properties of alkali metal atoms in high lying Rydberg states are outlined. A review of current experimental methods of exciting and detecting Rydberg atoms is then given.

The creation and detection of the rubidium Rydberg states using the frequency doubled dye laser and a novel space charge limited thermionic ionization detector is described. The new feature of the space charge limited detector is that it is in the form of a stainless steel oven with a simple ionization probe insert as opposed to previous glass cells. A triode arrangement of probes allows the ions to be created in a field controlled region and detected in a space charge limited region.

Using this detector it has been possible to detect the principal series of Rb for states of principal quantum number ranging from n = 23 to n = 50 using the broadband (0.02nm) version of the frequency doubled dye laser. By going to the narrowband (0.002nm) version of the laser, states up to a principal quantum number of n = 74 have been detected. By applying a small electric field in the field controlled zone it has been possible to Stark mix the ^2S, ^2P and ^2D series and break the dipole selection rules. New term values of the n^2S and n^2D series up to 54^2S and 52^2D have been measured to an accuracy of 0.3 cm^{-1} by using the accurately known n^2P series term values as references.

A new 'saturated ionization' technique of Doppler free

(Chapter VI Abstract continued)

spectroscopy for high lying states is described. The feasibility of the method is assessed for the case of the Rydberg states of rubidium excited by a single frequency second harmonic dye laser. More accurate data on fine structure splittings and Stark shifts are obtainable with the method.

VI.1 Introduction

In this chapter we demonstrate the resolution and tunability of the CW frequency doubled dye laser as a source for ultraviolet spectroscopy by describing its use in a study of the high Rydberg states of rubidium.

The Rydberg states are essentially hydrogenic and are characterised by very long lifetimes, large polarizabilities and Stark shifts, low binding energies, and large orbital radii. Despite their similarities to the hydrogen atom in some of their properties, the Rydberg states of the alkali atoms show very pronounced differences. Foremost among these differences has been the inverted nature of the fine structure of the n^2D states in the sense that the $n^2D_{3/2}$ state is more energetic than the $n^2D_{5/2}$ state[1,2]. Some anomalies in the hyperfine structure have also been observed[2]. The fine structure of the ^2D states of the alkalis is in complete contrast to that of hydrogen and has been one of the more puzzling features of the alkali Rydberg atoms. Recent theoretical[3] and improved experimental studies[4] have helped to resolve some of the differences.

In this chapter we briefly review some of the properties of high lying Rydberg states with particular reference to the alkali metals. We then describe some of the current methods of producing and detecting Rydberg states. The development of a novel space charge limited ionization detector for monitoring Rydberg states is described. The detector allows a small electric field to be applied in a field controlled zone.

The use of this detector in conjunction with the frequency doubled dye laser allows the high lying states of Rb to be observed. The n^2P

series up to n = 74 has been excited using the narrow band version of the dye laser. By applying a small electric field the ^2S, ^2P and ^2D series have been excited directly from the ground state. The term values of the ^2S and ^2D series up to 54^2S and 52^2D have been measured using the n^2P states as references.

We conclude by proposing a new Doppler-free experiment which it should be possible to perform with modified forms of the existing apparatus.

VI.2 Properties of Rydberg Atoms

The energy levels of an alkali metal atom can be fairly accurately expressed in a series of the form

$$E_{n\ell} = -\frac{1}{2n^{*2}_{\ell}} = -\frac{1}{2(n-\delta_{\ell})^2} \qquad (1)$$

where n is the principal quantum number, δ_ℓ is the quantum defect and n^*_ℓ is the effective quantum number of the series with angular momentum quantum number ℓ. The units used are atomic units which means that energy is measured in units of twice the ionization potential of hydrogen. The quantum defect is approximately independent of n and is different for each of the ℓ series. It is a measure of the effect that penetration of the valence electron into the inner electron core has on the energy of the atomic state. The measured quantum defects of the alkali metals are given in table 1[5].

From the table it can be seen that the quantum defect is large only for those series whose angular momentum quantum number ℓ is less than the ℓ-value for the outer closed shell of the atom. It should also be noted that for the heavier alkali metals the quantum defects of some of the series can be larger than 1. This has the effect that the nearest energy level in an adjacent series does not necessarily have the same value of principal quantum number. The case of the ordering of the energy levels of rubidium is shown in figure 1. The level adjacent to the n^2P level in the n^2S series is $(n + 1)^2S$ and in the n^2D series $(n - 1)^2D$.

We now look at the influence of a small external electric field on an atom. The Hamiltonian for the atom in a small field E is given by

$$H = H_o - \underline{E}.\underline{p} \qquad (2)$$

where H_o is the Hamiltonian in the absence of the field and $\underline{p} = - \Sigma_i e\, \underline{r}_i$ is the electronic dipole moment (-e is the charge on the electron). If it is assumed that the eigenfunctions of H_o have definite parity then the expectation value of the perturbing term $< n\ell \mid \underline{E}.\underline{p} \mid n\ell >$ vanishes since $\underline{E}.\underline{p}$ has odd parity. The first order perturbation in E is therefore zero. The change in energy of a state $\mid n\ell >$ to lowest order in E is given by second order perturbation theory as

$$\Delta E = \Sigma_i \frac{\mid < n\ell \mid \underline{E}.\underline{p} \mid n'\ell' > \mid^2}{E(n\ell) - E(n'\ell')} \qquad (3)$$

where Σ_i represents the summation over all intermediate states $\mid n'\ell' >$. This is the second order Stark energy shift of the state $\mid n\ell >$.

A rough estimate of the magnitude of the Stark energy shift of the alkali metal Rydberg atoms can be obtained by neglecting the sum over states implied in equation (3) and restricting the sum to an interaction between the nearest neighbours only. Using the quantum defect model for the unperturbed states, the energy difference in the denominator of equation (3) can be written

$$E(n\ell) - E(n'\ell') = \frac{(\delta_{n'\ell'} - \delta_{n\ell})}{n^3} \qquad (4)$$

where it has been assumed that $n \simeq n' >> \delta_{n\ell}, \delta_{n'\ell'}$. As was mentioned earlier,some of the alkali metals have quantum defects in excess of 1 which corresponds to nearest neighbours being states with different principal quantum number. It can be ensured that the interaction between nearest neighbours is considered if only the fractional part of the quantum defect is used in equation (5) and if the difference between quantum defects is greater than 0.5 then the compliment of this number is taken. The difference is denoted as $\min(\delta_{n'\ell'} - \delta_{n\ell})$. Because of the dipole selection rules there are two series accessible for any given energy level except those levels belonging to the sharp series. The maximum influence will be exerted by the adjacent series whose fractional part of the quantum defect is nearest to that of the series in question. If $\min(\delta_{n'\ell'} - \delta_{n\ell})$ is close to 0.5 for a series, the perturbing states will be approximately mid-way between the states of the series in question and the effect of the Stark interaction due to that series will be very small.

In order to evaluate the dipole matrix elements in the numerator of equation (3) it is necessary to know the excited state wavefunctions of the alkali atoms. When the alkali atoms are in very high lying states the wavefunctions can be well approximated by hydrogen wavefunctions. Further, for hydrogen states with large principal quantum number the form of the wavefunctions changes little with n and an average orbital radius can be ascribed to each state. The average orbital radius for hydrogen wavefunctions is[5]

$$\bar{r} = a_o n^2 \left[1 + \tfrac{1}{2} \left(1 - \frac{\ell(\ell + 1)}{n^2}\right) \right] \qquad (5)$$

where a_o is the Bohr radius. The influence of the electric field on the atom can be estimated by expressing $\underline{E}.\underline{p}$ as $e\,\bar{r}\,E$. For states with $n \gg \ell$ the Stark energy shift in practical units is given by combining (4) and (5) in (3) to give

$$\Delta E(n\ell) = 1.8 \times 10^{-14}\ n^7\ E^2/\min(\delta_{n'\ell'} - \delta_{n\ell}) \qquad (6)$$

where $\Delta E(n\ell)$ is the Stark shift measured in cm^{-1} and E is measured in V cm^{-1}. This formula is similar to that given by Unsöld[6] provided that $n \gg \ell$. The n^7 dependence of the Stark shift on principal quantum number is common to more rigorous treatments of the Stark effect of the alkali metals in Rydberg states[7]. This very strong dependence of the Stark shift on principal quantum number means that high lying Rydberg states can be considerably perturbed by even a small electric field.

The application of an electric field to an atom not only affects the energy of the atomic states,but also the wavefunctions and, consequently,the selection rules. If $\psi_{n,\ell}$ is the wavefunction of a particular state in a field free region,the equivalent eigenfunction in a weak field contains a small admixture of two wavefunctions $\psi_{n,\ell\pm 1}$ which can be calculated by first order perturbation theory. For a transition in a field-free region the selection rule on the orbital quantum number is $\Delta\ell = \pm 1$. The mixture of states increases with principal quantum number and so normally only affects the upper states. In the presence of a field, therefore, the excited state wavefunctions can combine optically with lower levels or orbital quantum number ℓ, $\ell \pm 2$ and so transitions which obey the selection rule $\Delta\ell = 0, \pm 2$ are allowed.

The strength of these transitions can be calculated using first order perturbation theory. The result of perturbation calculations are given by Bethe and Salpeter[8]. They find that in general the intensities of the forbidden lines are quadratic in the field strength and are smaller than those of the allowed lines by approximately the ratio of the Stark energy shift of the upper level to its energy separation from the nearest energy level for which $\Delta\ell = \pm 1$.

In strong fields, the Stark energy shift becomes comparable to the energy separation between terms in adjacent series and there are no rules on ℓ. The Stark energy shift then becomes linear in electric field.

When a large electric field is applied to an atom the field is capable of removing an electron from the atom. The potential energy of an electron in a field E is given by (in atomic units)

$$V = 1/r - Ez \qquad (7)$$

where z is the distance of the electron from the atom in the direction of the applied field and r is the radial distance of the electron from the nucleus which is assumed to have unit charge. The potential can be seen to go through a maximum of $V_{max} = -2E^{\frac{1}{2}}$. It is evident that it is possible for the electron to tunnel through this potential barrier and be completely stripped from the atom. There is a sharp increase in the electron ionization for an electron in a state of principal quantum number n when the potential maximum is equal to the term energy of the electron. If the Stark energy shift is neglected the term energy is given by $E(n,\ell) = -[2\, n_{\ell}^{*2}]^{-1}$. Equating this value for the term energy to the maximum value of the potential barrier, a threshold field for ionization is

$$E_c = [16\, n_{\ell}^{*4}]^{-1}. \qquad (8)$$

This is the classical value for the threshold field given by Bethe and Salpeter[8]. Although based on very crude assumptions this expression is in good agreement with recent experimental results[9,10].

VI.3 The Excitation and Detection of Rydberg States

Until recently the only data on atoms in pure Rydberg states came from radioastronomical observations of the recombination lines in interstellar hydrogen[11]. The first modern work on highly excited atoms was reported by Riviere and Sweetman in 1963[12] when they were able to investigate Rydberg states in hydrogen up to $n = 28$. Highly excited atoms were formed by electron capture of protons accelerated to 25 - 100 keV. The excited atoms were detected by Stark field ionization. An ionizing voltage of up to 10^5 V cm^{-1} was sufficient to ionize atoms with n greater than 9. Subsequent work on beam excitation of Rydberg states has been reported by Bayfield and Koch[13] who have excited a beam of hydrogen to states of $n = 63 - 69$ by charge exchange with xenon.

With the advent of tunable dye lasers,Rydberg atoms have received increasing attention. One of the earliest laser-based experiments on Rydberg states was performed by Gallagher, Edelstein and Hill[14]. In their experiment,Na atoms, contained in a pyrex cell, were excited to high-lying states by two step excitation from two dye lasers. The population of the states was monitored by detecting the fluorescence of high-lying n^2S and n^2D states as they decayed back to the 3^2P state. States up to $n = 13$ were detected in this way. The lifetime of the excited states were found to vary as n^{*3} in accordance with the hydrogenic theory of the alkali atoms.

The fine structure intervals and polarizabilities for the high lying states of Na were measured by Fabre, Gross and Haroche[15] and Fabre and Haroche[16] using quantum beats. The experimental apparatus used was similar to that used by Gallagher, Edelstein and Hill[14] but the time dependence of the fluorescence was monitored. A small electric field in the Na cell allowed the polarizability of the $n = 10, 11, 12$ states to be measured[16].

The fine structure intervals of nD states from n = 9 to n = 16 have also been measured using quantum beats[15].

The detection of Rydberg states using fluorescence detection is limited because of the low oscillator strength of the transitions and the long lifetime of the excited states. The oscillator strength of high lying levels falls as n^{*-3} and the lifetime increases as n^{*3}. A loss of fluorescence signal occurs when the radiative lifetime becomes longer than the time for an atom to pass out of the observation region. Ducas, Littman, Freeman and Kleppner[9] have been able to detect Na Rydberg states with principal quantum numbers up to n = 30 by fluorescence detection but have been able to extend this to n = 38 by field ionization techniques[9]. The laser linewidth was insufficient to resolve the n^2S and $(n - 1)^2D$ states beyond this but pairs up to n = 50 were detected. In these experiments Na atoms were excited by two step pulsed laser excitation as previously but the Na was in the form of an atomic beam. After the atoms had been excited by the pulsed dye lasers a pulsed ionizing field was applied and the resulting ions were observed with a channel electron multiplier. The critical ionizing field is found to be in good agreement with the classical expression given in equation (8). The field ionizing technique was also used by Stebbings, Latimer, West, Dunning and Cook[17] who detected the Rydberg states of Xe in an atomic beam apparatus up to a principal quantum number of n = 40.

In more recent work by Gallagher et al[18], Fabre et al[19], and Littman et al[20], alkali atoms have been excited to high lying states by two step laser excitation from the ground states and the detection has been with selective field ionization of an atomic beam. In the work of Gallagher et al[18], fine structure intervals and polarizations of high lying n^2P and n^2D states have been measured by inducing rf transitions between the fine structure levels. The work of Fabre et al[19] has been concerned with microwave transitions between fine structure levels from high lying ^2D levels to nearby ^2D, ^2F, ^2G levels. Littman et al[20] have looked at the Stark effect in high lying states of Na in weak to strong electric fields.

Atomic Rydberg states have been directly excited in experiments performed by Goundand, Fournier, Cavellier and Berlande[21]. In these experiments a cell of Rb atoms was excited by a nitrogen pumped Rhodamine B dye laser which was externally frequency doubled with a KDP crystal. The excitation of the n^2P series was detected by observing direct fluorescence of the n^2P to 4^2D transitions. With a laser linewidth of 0.03 nm,states from n = 12 to 22 could be detected provided that sensitive high-speed photon counting was employed.

Direct excitation using a pulsed frequency doubled dye laser has also been reported by Tuan, Liberman and Pinard[10]. In this case a nitrogen pumped dye laser was externally frequency doubled using an ADA crystal and the Rb was in the form of an atomic beam. The population of the Rydberg states was monitored by applying a pulsed field after the laser excitation pulse to produce field ionization. The ions were then accelerated and collected on the cathode of an electron multiplier. Using this technique Tuan et al[10] have been able to detect the n^2P Rydberg states of Rb from n = 28 to n = 78. They have also verified the classical field ionizing $E_c = [16 n^{*4}]^{-1}$ law.

A different approach to the detection of Rydberg states is the use of a thermionic space charge limited diode detector. The thermionic diode combines the advantages of ionization detection with the simplicity of an atomic cell. There is no need for an atomic beam apparatus and no field ionization voltages are required. The diode detector in its simplest form is an evacuated cell containing the alkali metal vapour with an anode and filamentary cathode. When the cathode is heated, thermionic emission will ensue and provided the anode voltage is small, the diode current will be limited by a build up of a space charge around the cathode. Atoms in high lying states can be detected with this device, provided the states are within a few meV of the ionization limit, since collisions with ground state atoms are sufficient to ionize the excited atoms. Positive ions are then attracted towards the electron barrier and partially neutralise it, thereby allowing an increased electron current to flow until the ions recombine or discharge to the cathode. Gains in the region of 10^5 to 10^6 have been claimed for this device[22-27].

The earliest use of a thermionic diode for the detection of ionization was by Kingdon[22] and Hertz[23] in 1923. It was subsequently used by Mohler and Boeckner[24], Lawrence and Edlefsen[25] and Freudenberg[26] around 1930. The first modern use of this detector was reported by Popescu et al[27]; by using a lock-in technique they achieved detectabilities approaching one ion per second.

The advantage of the space charge limited detector over fluorescence detection of high lying states is that, whereas fluorescence efficiency falls rapidly with increasing principal quantum number, the ionization efficiency is high, reaching almost 100% for states close to the continuum. An ionization detector is also insensitive to nonresonant laser light and other ambient illumination. The high gain and low noise of a space charge limited detector make it more sensitive than field ionization detection.

In early work on the detection of high lying states using a space charge limited diode, the excitation source was a high pressure xenon or mercury arc lamp filtered through a monochromator. Linewidths were typically of the order of 0.1 nm. The principal series of Cs has been detected by Marr and Wherrett[28] up to n = 24 and by Popescu et al[29,30] up to n = 35 using this kind of arrangement.

Popescu, Collins, Johnson and Popescu[31] have used a nitrogen pumped dye laser to excite the Cs Rydberg states by multiphoton ionization. However, they were only able to detect ^2D and ^2S states up to n = 13 and n = 14 respectively due to the low strength of the multiphoton processes.

Collins et al[32] found that the two photon ionization probability was greatly enhanced by use of continuum molecular intermediate states. They found that single-and two-photon resonances occurred at wavelengths corresponding to the line spectra from excited atomic states. This was attributed to the dissociation of the resonant intermediate molecular states in a time short compared to the photo-excitation. Thus, for example, the intermediate $d\pi(^3\Pi_g)$ molecular states would dissociate to give an excited 5^2D atom and the resulting resonances would correspond to the fundamental 5^2D to n^2F series of Cs. Notice that, in this process, the frequency of the incident light does not correspond to half the energy separation between the initial and final state of the two photon resonance, but to the energy separation between the intermediate atomic state to which the molecules dissociate, and the final state, the energy difference being taken up by the dissociating molecule. In this way they have determined the term values of the Cs n^2F states up to a principal quantum number of n = 50. Other series such as the $6^2P_{3/2} \rightarrow n^2D_{3/2,5/2}$ were also observed. Collins et al[33] have extended this technique to the detection of multiphoton ionization of Rb and found a similar behaviour to that of Cs.

The most recent published work on the detection of Rydberg states using a space charge limited diode is that of Harvey and Stoicheff[4]. In this work a single mode CW dye laser is used to excite high lying states of Rb in a process of Doppler-free two-photon absorption[34]. The cell used to contain the Rb was similar to that used by previous workers except that a grid was included to shield the atoms in the excitation region from stray electric fields. This was necessary since at the 10 MHz resolution of this experiment even very small fields (< 1 V cm^{-1}) could broaden, shift and split the resonances. Harvey and Stoicheff[34] have been able to detect Rydberg states up to a principal quantum number of $n = 85$, only 16 cm^{-1} from the ionization limit. They were also able to measure the fine structure splitting of the n^2D series up to $n = 65$. It was found that for states of high n value ($n > 25$) the fine structure splitting was well represented by

$$\Delta_{fs}\ (\mathrm{GHz}) = 10800\ n^{*-3}.$$

This can be compared with the earlier work of Kato and Stoicheff[35] who found that for values $n = 4$ to $n = 25$ an n^{*-5} contribution had to be included in the fine structure splitting. Furthermore, the n^2D series was found to be inverted for low n values but normal for large n values. The crossover takes place at approximately $n = 25$. This is the first time that such a crossover has been seen to take place and confirms that at sufficiently high n value the alkali atoms are essentially hydrogenic in nature. It will be interesting eventually to see if Na follows this behaviour, since, up to about $n = 16$, the n^2D states remain inverted and appear to extrapolate to an inverted fine structure[16].

In section VI.5 we shall show how the frequency doubled dye laser has been used to excite the principal series of Rb up to a principal quantum number of $n = 74$. The application of a small electric field to produce

Stark mixing has allowed the n^2D and n^2S series, as well as the n^2P series, to be excited directly from the ground state. By using a single frequency version of the CW frequency doubled dye laser, measurement of the fine structure intervals, term values and polarizabilities of the n^2S, n^2P and n^2D series should be possible by a means of 'saturated ionization' as proposed in section VI.6.

VI.4 The Space Charge Limited Thermionic Diode

The use of a space charge thermionic diode for the detection of ions has been briefly described in the previous section. In this section a fuller description of the operation of these devices is given.

It is well known that the maximum current which can be drawn from a thermionic diode is limited by a space charge region which surrounds the cathode and presents a barrier to electrons[36]. The value of the current then becomes independent of the properties of the cathode provided that there is enough thermionic emission.

In a space charge limited ionization detector, positive ions are trapped within the electron space charge which acts as a potential well, provided that the trap depth exceeds the kinetic energy of the ion at formation[37]. The containment of ions within this potential well reduces the potential barrier to the flow of electrons and increases the current by an amount directly related to the time spent by the ion within the space charge[22].

An order of magnitude calculation is sufficient to indicate the effect that an ion has on the space charge limited current. The effectiveness of a single ion in reducing the space charge can be estimated by comparing the ratio of the time taken for an ion to cross the anode to cathode region compared to the time taken by an electron. A rough kinetic theory value of this ratio is just the square root of the ion mass to the electron mass. Therefore an ion of mass 10^4 m_e will have the effect of releasing the charge of about 100 electrons. However, the ion will move repeatedly between anode and cathode until its orbit is disturbed[22]. Experimental evidence suggests that the life of the ions is determined by collisions with gas molecules in the cell[22,28]. An ion will traverse the anode to cathode distance (R) approximately L/R times before discharging to the cathode, where L is the ion mean free path. The mean free path of an ion is roughly given by

$$L \simeq 1/p \qquad (9)$$

where L is measured in cm and p is the vapour pressure in torr. For a typical vapour pressure of 10^{-3} torr and a cathode-to-anode spacing of 1 cm, an ion can make about 10^3 traverses of the diode before discharging to the cathode. The resulting electron current amplification factor α is in the region of 10^5. This kind of amplification factor is usually realised in practice[22] and is the principal reason for the great sensitivity of the space charge detector. The inverse dependence of the amplification factor on vapour pressure has been verified by Marr and Wherrett[28].

A remarkable property of space charge limited diodes used with the alkali metals is the high thermionic current available. The thermionic emission of pure tungsten can be approximately written in the form of the Richardson-Dushman equation[36]

$$J = AT^2 \, e^{-W/kT} \qquad (10)$$

where J is the thermionic current emitted per cm^2 of the cathode, T is the temperature of the cathode in degrees Kelvin and k is the Boltzman constant. The factor W is the work function of the material and A is approximately a constant for pure metals. For pure tungsten the work function is 4.5 eV[36].

The expression (10) is plotted as a function of T^{-1} in figure 2 together with the measured thermionic current density from a tungsten filament in the presence of Rb[38]. The Rb on tungsten data are plotted at a variety of cell temperatures, corresponding to different vapour pressures. For filament temperatures in the region of 1000 K or less, it can be seen that the thermionic emission of a Rb activated tungsten cathode is many orders of magnitude greater than thermionic emission from pure tungsten. This kind of behaviour has been exhibited by all of the alkali metals.

The probable explanation for this behaviour is that the tungsten filament becomes coated with a monolayer of alkali metal ions held by an image force. The work function of the cathode is reduced, thereby allowing much greater thermionic emission[38,39].

Provided that the tungsten surface remains fully covered, the thermionic emission follows the Richardson-Dushman equation of the form of equation (10) but with a greatly reduced work function. As the filament temperature is raised, a point is reached where the alkali metal ions begin to evaporate and the thermionic emission will be reduced. If the temperature is increased still further, all of the alkali metals ions will be evaporated from the surface and the emission will correspond to that of pure tungsten. For most combinations of alkali metals and tungsten the thermionic emission peaks in the region of 1000 K. The rather large values of thermionic current emitted in the presence of alkali metals ensures that, even at low cathode temperatures, there is adequate emission in hand when an ion arrives to reduce the space charge.

Despite the fact that the thermionic emission from pure tungsten at high temperatures (> 1000 K) can be greater than that of tungsten coated with an alkali metal, the detector is best used at low temperatures where the probability of surface ionization is low.

VI.5 The Rydberg States of Rubidium

The basic design of a space charge limited thermionic diode has changed little since its first use as a photo-ionization detector[24,25,26]. A basic design which has been used in this work is shown in figure 3. The cell was made of pyrex and has an extension arm to contain the liquid alkali metal. Two fused silica windows were sealed to the main body of the cell by graded seals. The anode was formed by a 5 mm x 25 mm silver plate and the cathode was a 0.15 mm diameter tungsten wire of about 25 mm in length. The cell was attached to a vacuum system and evacuated to about 10^{-5} torr while baking for several hours. The Rb was distilled into the side arm and the whole cell sealed.

The cell was housed in an oven where a temperature difference existed between the side arm and the cell. This was to ensure that Rb was not deposited on the windows or electrodes.

The thermionic current was measured by heating the tungsten filament with a stabilized current supply while applying a positive voltage to the anode and measuring the current. The maximum thermionic current is given when the voltage-ampere characteristic of the diode saturates at a steady current independent of applied voltage. A plot of the maximum thermionic current as a function of cathode current is shown in figure 4. The absolute cathode temperature was difficult to measure but is expected to be directly related to the cathode current at a fixed vapour pressure. The cell temperature was 40°C, corresponding to a Rb pressure of 2×10^{-6} torr[40]. This curve is in good agreement with the form of the curves given by Langmuir and Kingdon[39] and Killian[38]. This was taken as an indication that the diode was operating satisfactorily.

The broadband output (0.02 nm) from the second harmonic dye laser was chopped and directed into the cell. The filament was operated at a current in the region of the maximum in figure 4. A load resistor of 180 kΩ was connected between the filament and anode and served to detect the current between anode and cathode. The voltage across the load resistor was applied to a lock-in amplifier (Brookdeal 401). The chopping frequency was about 20 Hz. No voltage was applied between anode and cathode. Strong signals were obtained with this arrangement while the cell was in good condition. However, after a few hours it was found that the Rb had attacked the fused silica windows and that the pyrex was also slightly discoloured. In the experiments which we now describe an alternative approach was adopted in which a stainless steel oven (with buffer gas to protect the windows) was used. However we record the development of a pyrex cell here since a cell of similar design will probably be required in the high resolution Doppler-free experiments proposed in Section VI.6

The main problem with a stainless steel oven is that windows must be sealed to the main body of the cell. Now if this is to be done with rubber O rings the windows must be kept at temperatures well below 100°C. Oven temperatures in the region of about 200°C are required for a Rb vapour pressure of 10^{-2} torr[40] and so the windows must be cooled. If the windows are cooler than the main body of the oven the metal vapour can diffuse onto the window. The normal method of overcoming this diffusion is to add an inert buffer gas to the oven which helps to contain the vapour. A more recent extension of this is the heat pipe where the addition of a wick allows an equilibrium situation to develop with pure vapour contained in the hot region and buffer gas on the outside[41]. At the outset of these experiments it was not clear whether the addition of a buffer gas would destroy the sensitivity of the space charge limited detector or whether the high vapour pressure required for operation as a heat pipe would destroy the sensitivity.

The oven used in these experiments was designed so that if necessary it could be used in a heat-pipe mode. A schematic diagram of the oven is shown in figure 5. It consisted of a cylinder of type 316 stainless steel to which had been welded stainless steel flanges at each end. The flanges were water-cooled and could be attached to a vacuum system. Fused silica windows were held on each end by rubber O rings. A fine stainless mesh was spot-welded to the inside of the tube to provide a 'wick' should the oven be required to operate as a heat pipe. Rubidium is highly reactive and will ignite spontaneously in dry air, consequently, the 1g breakseal ampoules were inserted under flowing argon. The oven was then evacuated to about 10^{-3} torr and heated to above the melting point of Rb. When the contents of the ampoule had trickled out, the empty ampoule was removed under argon and the system was again evacuated.

The cylindrical part of the oven was heated by passing a current through kanthal resistance wire. This was wound on to asbestos paper and then covered with aluminium oxide cement. The oven could be raised to a temperature of greater than $900^{\circ}C$ with this arrangement. However, a temperature of $180^{\circ}C$ was more usual when Rb was in the oven.

The ionization detector was in the form of an electrode insert which could replace one of the windows. The first insert is shown in figure 6(a). The anode was formed by a 10 mm x 60 mm stainless steel plate hard soldered to a 2 mm diameter stainless steel rod. The cathode was made of 0.15 mm diameter tungsten wire and was suspended between two 2 mm diameter stainless steel rods. The three stainless steel rods made electrical contact by use of vacuum feed-through. In the arrangement used the laser beam could not pass through the oven.

A schematic diagram of an experimental arrangement is shown in figure 7. The output from the frequency doubled dye laser was fed into the region between the anode and cathode of the ionization detector; the exact position was not critical. The cathode was heated to about 1000 K using a current stabilized power supply and a load resistor of 180 kΩ was connected between the anode to cathode. The voltage developed across this resistor was fed to a lock-in amplifier (Brookdeal 401). Part of the UV laser beam was directed onto a photodiode and used as an intensity monitor. This intensity signal was fed to a ratiometer which normalised the output from the lock-in amplifier to the laser intensity. The ratiometer circuit is a slow device and any intensity flucuations at frequencies of 10Hz or higher was not be properly normalised. ratiometer circuit is shown in appendix A. The chopping rate was maintained at a frequency of 20 Hz to allow enough time for the diffusion of the ions through the space charge.

The dye laser wavelength was calibrated using a neon hollow cathode discharge lamp as described more fully in appendix B. Once calibrated, the changing wavelength was monitored by observing the transmissions of a fused silica Fabry-Perot etalon.

A typical experimental ionization spectrum of Rb obtained using the broadband (0.02 nm) version of the dye laser is shown in figure 8. This shows the n^2P series of Rb from n = 23 to n = 50 over the approximate wavelength range 297 nm to 299 nm. UV powers were typically less than 1 mW. To obtain this spectrum the birefringent tuning element and crystal phase-matching temperature were ganged together as described in Chapter V. The oven temperature was about 180°C and the buffer gas pressure was about 1 torr. A typical ionization signal was found to change with buffer gas pressure; being reduced at higher pressures as expected, but good signal to noise ratios were still obtained at pressures in the region of 10 torr. The lock-in amplifier integration time was

1 sec. Despite the use of a ratiometer, differerences in peak heights in figure 8 are due mainly to fast changes in the dye laser intensity.

More spectra are shown in figures 9, 10. These were taken with the laser linewidth reduced to 0.002 nm and scanned over the range close to the Rb ionization limit. The experimental details are similar to those relating to figure 8. With the reduced laser linewidth, states up to n = 64 are shown in figure 9. A slower scan of the short wavelength region is shown in figure 10. Here it is possible to resolve n^2P states up to n = 74. In this region the splitting between the lines of the principal series is comparable to the Doppler width, so if significantly higher states are to be observed, Doppler-free spectroscopy will have to be employed.

By observing figure 10, it can be seen that near the base of the principal series resonances, there appears to be some unresolved structure which eventually becomes comparable in height to the resonances. This is attributed to the Stark mixing of these high lying states with the n^2P and n^2D series neighbours caused by the small voltage developed by the heater current along the cathode. As the principal quantum number increases, the Stark energy shift becomes larger and the mixing stronger in accordance with the increase in height of the unresolved lines. This is perhaps better illustrated in figure 11. This is a scan similar to that of figure 9 except that the vertical scale has been expanded by about a factor of ten. The principal series members around n = 40 can be clearly seen but between them there is evidence of two other resonances. We shall show that these weak lines are Stark induced transitions to the n^2S and n^2D series.

The voltage applied between the ends of the cathode was in the region of 1V and, since the cathode-to-anode spacing is about 1 cm, a field of up to 1 V cm^{-1} exists at some points along the cathode. This stray voltage was eliminated by the inclusion of a grid between the anode and cathode. This grid was made of a 60 mm x 10 mm piece of stainless steel mesh and located with a fourth stainless steel rod (see figure 6(b)). There were now two regions in the detector; a field controlled region where the ions were created and a space charge limited region where they were detected. The field controlled region could be made field-free by shorting the grid to the anode. The Rb atoms were then completely unperturbed by stay fields. This mode of operation is useful if precision measurements of the Rb Rydberg states are required. If, on the other hand, it is desired to study the Stark effect a field can be applied between the grid and anode. Provided that the anode is made positive with respect to the grid the created ions will drift, under the influence of the field, through the grid and into the space charge limited region where they will be detected.

A spectrum taken with the thermionic triode is shown in figure 12. The bottom trace is taken with no field applied and the upper with a field of 5 V cm^{-1} applied. The laser used was the narrow band system and the Rb states around 40^2P were excited. As can be seen in the bottom trace there is no sign of any intermediate states between the n^2P states. This was true even with the vertical sensitivity increased by a factor of 100. This is in contrast to the previous diode where intermediate states could clearly be seen. When a field of 5 V cm^{-1} is applied, as in the upper trace, the n^2S and n^2D series are readily excited.

The sensitivity of the triode was somewhat reduced over the diode arrangement, presumably because the anode to cathode spacing was larger in the triode and because some ions will be lost in going through the grid. The sensitivity of the triode was dependent on the applied voltage, falling to about 10% of its field-free value at a field of about 20 V cm^{-1}. This was probably due to the inefficient shielding of the grid allowing the Stark voltage to upset the space charge region.

Even for the high lying states, the resolution of the laser was insufficient to detect Stark energy shifts at the applied fields allowed by the detector. For example the Stark energy shift of the 50^2D state of Rb will be in the region of 0.2 cm^{-1} for an applied field of 5 V cm^{-1} according to equation (6). This Stark shift is too small to be easily detected with the laser since its linewidth is comparable to the estimated Stark shift. This is confirmed by observing the intensity of the forbidden lines. Very roughly, the intensity of the allowed lines is equal to the ratio of the Stark energy shift to the separation between the lines[8]. Intensity ratios were of the order of 0.1 and so the ratios of the shifts is expected to be about the same size. The separation between the high lying states was about 0.5 cm^{-1} and shifts an order of magnitude down on this would not be detected.

By inducing forbidden transitions with a small electric field ($\sim$ 5 V cm^{-1}) it is possible to excite the n^2S, n^2P and n^2D series in the same run. The term values of the Rb principal series have been determined to within 0.01 cm^{-1} by Kratz[42] up to a principal quantum number of $n = 77$ by observing the absorption of a continuum source in traversing a 40 m to 50 m absorption length. We have determined term values of the n^2S and n^2D series by linear interpolation between the n^2P states.

The measured term values of the ^2S and ^2D series determined in our experiment are tabulated in Table 2. The expected accuracy of the term values is about 0.3 cm^{-1}. Also shown in the table is the effective principal quantum number and the quantum defects of each of the levels calculated using the series limit given by Moore[1]. The mean value of the quantum defect for the n^2S series is 3.14 ± 0.04 and for the n^2D series is 1.35 ± 0.03. This agrees with the tabulated values of 3.13 and 1.34 given by Pauling and Goudsmit[5] for lower lying levels. We take this to indicate that to within the resolution of the experiment the Stark energy shifts are not significant.

Throughout the course of these experiments the stainless steel triode arrangement was found to be a very reliable detector of Rydberg states and to be extremely sensitive. A stainless steel oven will allow much higher vapour pressures to be used than with a glass cell since it is much more corrosion resistant to the alkali metals. This should allow studies of pressure broadening effects on the high lying levels and also of the possible effects on the Rb_2 molecule.

VI.6 A Proposed Doppler Free Experiment

In this section,a proposed experiment based on Doppler free saturated absorption is described. Using the method described,it should be possible to observe the very high lying n^2P states of Rb without the Doppler effect masking the features such as the fine structure and Stark energy shifts. The absolute measurement of the Stark energy shift for these high lying levels will then give both the tensor and scalar polarizability[43]. This should be interesting since only the tensor polarizability, which affects the splitting between Stark sublevels, can be measured using rf or quantum beat techniques. The fine structure measurements would compliment those of Harvey and Stoicheff[4] for the n^2D states using two photon Doppler-free spectroscopy.

Saturated absorption has become a widely used technique for the elimination of the Doppler effect[44]. A typical experimental set-up is shown in figure 13. The output from a single mode tunable laser is split into a weak probe beam and a strong saturating beam. The strong beam is then modulated by a chopper. The two beams are directed into the absorption cell in opposite directions with as much overlap as possible. The probe beam is monitored by a photodetector. When the laser is tuned to within the Doppler width of a transition each beam will interact with a different velocity group of atoms and the two beams will behave independantly of each other. However,if the laser is tuned to within the natural linewidth of the transition both beams will interact with the same group of atoms. The saturating beam is assumed to be sufficiently intense that it significantly changes the populations of the ground and excited states. When the saturating beam is 'on',the ground state population will be reduced and the sample will become more transparent to the probe beam. Therefore the probe beam will be modulated at the same frequency as the saturating beam when the laser is tuned within the natural linewidth. This modulation can be picked out with a lock-in amplifier and a resonance which is free of the Doppler effect will be obtained. The maximum sensitivity of this method is limited by the minimum detectable modulation on top of a large probe beam background. The maximum sensitivity of a saturation spectrometer has been reviewed by Shimoda[45]. He has shown that saturated absorption spectroscopy is about 3 times less sensitive than linear absorption spectroscopy. The minimum detactable absorption is usually taken to be about 1%. Clearly, standard saturated absorption cannot be used for the weak transitions involved in detecting Rydberg states.

The sensitivity of saturated absorption can be increased by monitoring the fluorescence intensity from the sample when atoms are excited by the standing wave field. This method was proposed by Basov and Letokhov[46] and has been demonstrated by Freed and Javan[47]. In this method a small change in the fluorescence intensity is monitored as the laser is tuned to within the natural linewidth. A sensitive method of isolating this small dip in fluorescence has been used by Sorem and Schawlow[48]. A schematic diagram of a typical experimental set-up is shown in figure 14. The arrangement is similar to that for saturated absorption except that the two beams are usually of equal intensity and that one is chopped at a frequency f_1 and the other at a frequency f_2. When the laser is tuned to within the natural linewidth of the resonance for sationary atoms the fluorescence will be modulated at frequencies $f_1 + f_2$, $f_1 - f_2$ as well as f_1 and f_2. However the modulations at$f_1 + f_2$ and $f_1 - f_2$ will only appear on resonance,unlike the signal at modulation frequencies f_1 and f_2 which will be present throughout the Doppler profile. Therefore, if a lock-in amplifier is tuned to $f_1 + f_2$ this resonance will appear with virtually no background.

Detection of the Rydberg states of Rb with a space charge limited detector is very similar to fluorescence detection except that an ion is responsible for the signal instead of a photon. For high lying states the quantum efficiency for ionization is almost unity and the collection solid angle can be made almost 4π. Provided that modulation at the difference frequency $f_1 - f_2$ or at f_1 and f_1 is sufficiently well discriminated by the electronics,the sensitivity of detection should be limited solely by the space charge limited detector. Popescu et al[27] have reported detection sensitivities as low as one ion per second and it would therefore appear possible that the Rydberg states could be investigated without Doppler broadening in this way. Further support for this view is given by the work of Harvey and Stoicheff[4] who,with a single mode CW dye laser beam of 50 mW have been able to detect two photon resonances with good signal-to-noise ratios. The current modulation expected in the case of the detection of Rb is now estimated to establish the required sensitivity of the detector.

The absorption coefficient at a laser frequency ω for a Doppler broadened transition in the presence of a standing wave of intensity I is given by[48]

$$\begin{aligned}\Gamma(\omega) &= \Gamma_1 + \Delta\Gamma \\ &= (\Gamma_o/\Delta\omega\pi^{\frac{1}{2}})\{\exp\left[-(\omega-\Omega_o)^2/\Delta\omega^2\right] - (\frac{I}{2I_s})\frac{\gamma^2}{(\omega-\Omega_o)^2+\gamma^2}\}\end{aligned} \tag{11}$$

where Ω_o is the resonance frequency and γ is the natural linewidth,or laser linewidth,whichever is the larger. The other parameters are Γ_o,the low intens attenuation coefficient for a homogeneously broadened transition,given by

$$\Gamma_o = N|\mu|^2\omega/\varepsilon_o \hbar c \tag{12}$$

and N is the ground state population number density, μ is the dipole matrix element of the transition and other symbols have their usual meaning. The saturation intensity I_s is given by

$$I_s = \varepsilon_o c \hbar^2/2|\mu|^2\gamma^2 \tag{13}$$

where we have assumed equal transverse and longitudinal relaxation times. The linewidth $\Delta\omega$ is related to the Doppler width and is given by

$$\Delta\omega^2 = \frac{2kT\Omega_o{}^2}{Mc^2} \tag{14}$$

where M is the atomic mass, k is Boltzman's constant and T is the temperature.

The rate of production of ions is proportional to the absorbed power and for low absorption is given by

$$n(\omega) = \eta \, ALI \, \Gamma(\omega)/\hbar\omega \tag{15}$$

where η is the quantum efficiency for the collection of ions, A is the area of the laser beam and L is the absorption length.

Assuming that the laser is tuned to near the centre of the Doppler width, the first part in the brackets of equation (11) is equal to unity and the rate of ion detection can be written

$$n(\omega) = \frac{\eta\ AL\ \Gamma_1}{\hbar\omega} \left[I - \left(\frac{I^2}{2I_s}\right) \frac{\gamma^2}{(\omega-\Omega_o)^2+\gamma^2} \right]. \qquad (16)$$

The laser intensity is given by two contributions, I_1 and I_2 where $I = I_1 + I_2$. It is assumed that I_1 is modulated at frequency f_1 and I_2 is modulated at frequency f_2 and that

$$I_1 = (I_o/2)(1 + \cos f_1\ t),\ I_2 = (I_o/2)(1 + \cos f_2\ t). \qquad (17)$$

The component of ion current modulated at frequency $f_1 + f_2$ on resonance is given by

$$n(\Omega_o,\ f_1 + f_2) = -\frac{1}{8}\ \eta\ AL\ \Gamma_1\ I_o{}^2/I_s\ \hbar\omega. \qquad (18)$$

This can be compared with the ion signal expected at frequency f_1 in a standard ionization detection system given by

$$n(\Omega_o, f_1) = \frac{1}{2}\ \eta\ AL\ \Gamma_1\ I_o. \qquad (19)$$

Therefore the saturated ionization signal at modulation frequency $f_1 + f_2$ is a factor $(1/4)I_o/I_s$ down on the modulation signal expected by straightforward ionization detection.

In order to evaluate the expressions for the relative sensitivity of 'saturated' ionization to 'linear' ionization it is necessary to know the dipole matrix elements of the high lying Rb states. It is well known that the oscillator strength of hydrogen and the alkali metals falls off as $f \sim n^{-3}$. This is used to give an order of magnitude estimate of the matrix element. The relationship between oscillator strength and dipole matrix element (neglecting statistical weights) is approximately given in atomic units as[49]

$$|\mu|^2 \simeq 3.3 \times 10^{-13}\ \lambda\ f \tag{20}$$

where λ is the wavelength of the transition measured in metres. The high lying states of Rb are at a wavelength of about 300 nm and the dipole matrix elements can therefore be approximated by

$$|\mu|^2 \simeq 7 \times 10^{-78}\ n^{-3} \tag{21}$$

where μ is measured in metre Coulombs.

In order to evaluate the saturation intensity I_s the natural linewidth γ must be estimated. The natural lifetime of the high lying states is very long and the natural linewidth will be dominated by pressure broadening. Using a laser of 10 MHz linewidth, Harvey and Stoicheff[4] have not been able to detect pressure broadening of states up to at least $n = 85$ at pressures in the region of 10^{-2} torr. The factor γ will therefore be approximately given by the laser linewidth which is taken to be 10 MHz. Thus, the saturation intensity for a state of principal quantum number n on evaluating equation (13) is

$$I_s(\mathrm{Wm}^{-2}) \simeq 2\ n^3. \tag{22}$$

The Doppler width for Rb at 200°C is 1 GHz and hence Γ_1 is approximately

$$\Gamma_1(\mathrm{m}^{-1}) \simeq 30\ p/n^3 \tag{23}$$

where we have used the fact that the density of atoms can be written

$$N(\mathrm{m}^{-3}) = 9.66 \times 10^{24}\ p(\mathrm{torr})/T. \tag{24}$$

Using these values of I_s given in equation (22), the ratio of 'saturated ionization' to 'linear ionization' at a UV laser power of 1 mW in a 1 mm diameter beam is roughly $10^2\ n^{-3}$. This ratio varies between about 8×10^{-4} and 2×10^{-4} for states of principal quantum number between n = 50 and n = 80. The signal to noise ratio in the ionization experiments where a buffer gas was included was between 10^2 and 10^3. By using a cell with no buffer gas the sensitivity and signal to noise ratio would be increased. The saturated ionization signal should easily be observable although this would probably mean resorting to a pyrex cell where the evidence was that higher signal to noise ratios were possible.

The minimum detectable ion current reported by Popescu et al[27] was between 1 and 10 ions per second. It is therefore interesting to calculate the ion production rate expected in this experiment. Assuming that ions can be detected with 100% quantum efficiency and that the absorption length is 1 cm the ion rate for a 1 mW beam of 1 mm diameter is approximately given as

$$n(\Omega_0, f_1 + f_2)(\mathrm{sec}^{-1}) = 2 \times 10^{19}\ n^{-6}.$$

Even at the very highest lying Rydberg levels this equation predicts a comfortably large ion current (eg approximately $8 \times 10^7\ \mathrm{sec}^{-1}$ at n = 80).

It is therefore concluded that the technique of saturated ionization proposed for the detection of Doppler free resonances may be successfully applied to high lying states of Rb. The reduction in sensitivity and decrease in natural lifetime in the presence of a buffer gas may mean that the experiment has to be conducted using a pyrex vacuum cell. Apart from the increase in sensitivity of these cells, the high vacuum usually associated with them will probably be necessary if careful Doppler free measurements are to be made.

References

1. C E Moore, Atomic Energy Levels, NBS Circ No 467 (US GPO Washington, DC, 1952)
2. K H Liao, L K Lam, R Gupta and W Happer, Phys Rev Lett 32, 1340 (1974)
3. T Lee, J E Rodgers and T P Das, Phys Rev A 14, 51 (1976)
4. K C Harvey and B P Stoicheff, Phys Rev Lett 38, 537 (1977)
5. L Pauling and S Goudsmit, The Structure of Line Spectra, McGraw-Hill, New York (1930)
6. A Unsöld, Ann der Phys 82, 355 (1927)
7. C Fabre and S Haroche, Opt Comm 15, 254 (1975)
8. H Bethe and B Salpeter, Quantum Mechanics of One- and Two-Electron Systems, Handb Phys, S Flügge (Ed), Springer, Berlin (1957)
9. T W Ducas, M G Littman, R R Freeman and D Kleppner, Phys Rev Lett 35, 366 (1975)
10. D H Tuan, S Liberman and J Pinard, Opt Comm 18, 533 (1976)
11. A K Dupree and L Goldberg, Annu Rev Astron Astrophys 8, 231 (1970)
12. A C Riviere and D R Sweetman, Atomic Collision Processes, M R C McDowell (Ed), North-Holland, Amsterdam (1964)
13. J E Bayfield and P M Koch, Phys Rev Lett 33, 258 (1974)
14. T F Gallagher, S A Edelstein and R M Hill, Phys Rev A 11, 1504 (1975)
15. C Fabre, M Gross and S Haroche, Opt Comm 13, 393 (1975)
16. C Fabre and S Haroche, Opt Comm 15, 254 (1975)
17. R F Stebbings, C J Latimer, W P West, F B Dunning and T B Cook, Phys Rev A 12, 1453 (1975)
18. T F Gallagher, L M Humphrey, R M Hill, W E Cook and S A Edelstein, Phys Rev A 15, 1937 (1977)
19. C Fabre, P Goy and S Haroche, J Phys B 10, L183 (1977)
20. M G Littman, M L Zimmerman, T W Ducas, R R Freeman and D Kleppner, Phys Rev Lett 35, 366 (1975)
21. F Gounand, P R Fournier, J Cuvellier and J Berlande, Phys Lett 59A, 23 (1976)
22. K H Kingdon, Phys Rev 21, 408 (1923)

23. G Z Hertz, Z Phys 18, 307 (1923)

24. F L Mohler and C Boeckner, J Res Natl Bur Std 3, 303 (1929), 5, 51 (1930), 5, 399 (1930), 5, 831 (1930)

25. E O Lawrence and N E Edlefsen, Phys Rev 34, 233 (1929)

26. K Freudenberg, Z Physik 67, 417 (1931)

27. I Popescu, C Ghita, A Popescu and G Musa, Ann Phys 18, 103 (1966)

28. G V Marr and S R Wherrett, J Phys B 5, 1735 (1972)

29. D Popescu, I Popescu and J Richter, Z Physik 226, 160 (1969)

30. D Popescu, M L Pascu, C B Collins, B W Johnson and I Popescu, Phys Rev A 8, 1666 (1973)

31. D Popescu, C B Collins, B W Johnson and I Popescu, Phys Rev A 9, 1182 (1974)

32. C B Collins, B W Johnson, M Y Mirza, D Popescu and I Popescu, Phys Rev A 10, 813 (1974)

33. C B Collins, S M Curry, B W Johnson, M Y Mirza, M A Chellehmalzadeh, J A Anderson, D Popescu and I Popescu, Phys Rev A 14, 1662 (1976)

34. B Cagnac, G Grynberg and F Biraben, J Phys (Paris) 34, 845 (1973)

35. Y Kato and B P Stoicheff, J Opt Soc Am 66, 490 (1976)

36. L R Koller, The Physics of Electron Tubes, McGraw-Hill, New York (1934)

37. F A Baker and J B Hasted, Phil Trans Roy Soc A 261, 33 (1966)

38. T J Killian, Phys Rev 27, 578 (1926)

39. I Langmuir and K H Kingdon, Proc Roy Soc A 107, 61 (1925)

40. R E Honig and D A Kramer, R C A Review 30, 285 (1969)

41. C R Vidal and J Cooper, J Appl Phys 40, 3370 (1968)

42. H R Kratz, Phys Rev 75, 1844 (1949)

43. A Khadjavi, A Lurio and W Happer, Phys Rev 167, 128 (1968)

44. V S Letokhov, High-Resolution Laser Spectroscopy, K Shimoda (Ed), Springer-Verlag, Berlin (1976)

45. K Shimoda, High-Resolution Laser Spectroscopy, K Shimoda (Ed), Springer-Verlag, Berlin (1976)
K Shimoda, Appl Phys 1, 77 (1973)

46. N G Basov and V S Letokhov, Electron Tech 2, 15 (1969)

47. C Freed and A Javan, Appl Phys Lett 17, 53 (1970)

48. M S Sorem and A L Schawlow, Opt Comm 5, 148 (1972)

49. W L Wiese, M W Smith and B M Miles, Atomic Transition Probabilities, NBS Circ no 22 (US GPO Washington, DC, 1969)

Element	s	p	d	f	g
Li	0.40	0.04	0.00	0.00	0.00
Na	1.35	0.85	0.01	0.00	0.00
K	2.19	1.71	0.25	0.00	0.00
Rb	3.13	2.66	1.34	0.01	0.00
Cs	4.06	3.59	2.46	0.02	0.00

Table 1 Quantum defects for the alkali metals (taken from reference 5).

Table 2 Experimental term values of the ^2S and ^2D series of Rb.

^2S				^2D		
n	E(cm^{-1})	n*	δ	E(cm^{-1})	n*	δ
37	33604.6	35.64	1.36			
38	33609.5	36.69	1.31			
39	33613.7	37.68	1.32	33605.7	35.87	3.13
40	33617.5	38.64	1.36	33610.4	36.89	3.11
41	33621.3	39.68	1.32	33614.5	37.87	3.13
42	33624.5	40.62	1.38	33618.4	38.88	3.12
43	33627.7	41.64	1.36	33621.9	39.84	3.16
44	33630.5	42.58	1.32	33625.4	40.89	3.11
45	33633.5	43.68	1.32	33628.4	41.87	3.13
46	33635.9	44.62	1.38	33631.3	42.87	3.13
47	33638.3	45.63	1.37	33633.9	43.84	3.16
48	33640.7	46.70	1.30	33636.4	44.83	3.17
49	33642.5	47.56	1.44	33638.8	46.80	3.20
50	33644.7	48.68	1.32	33643.1	47.86	3.16
51	33641.5	49.66	1.34	33645.0	48.84	3.16
52	33648.3	50.67	1.33	33646.8	49.82	3.18
53	33649.7	51.60	1.27			
54	33651.5	52.70	1.30			

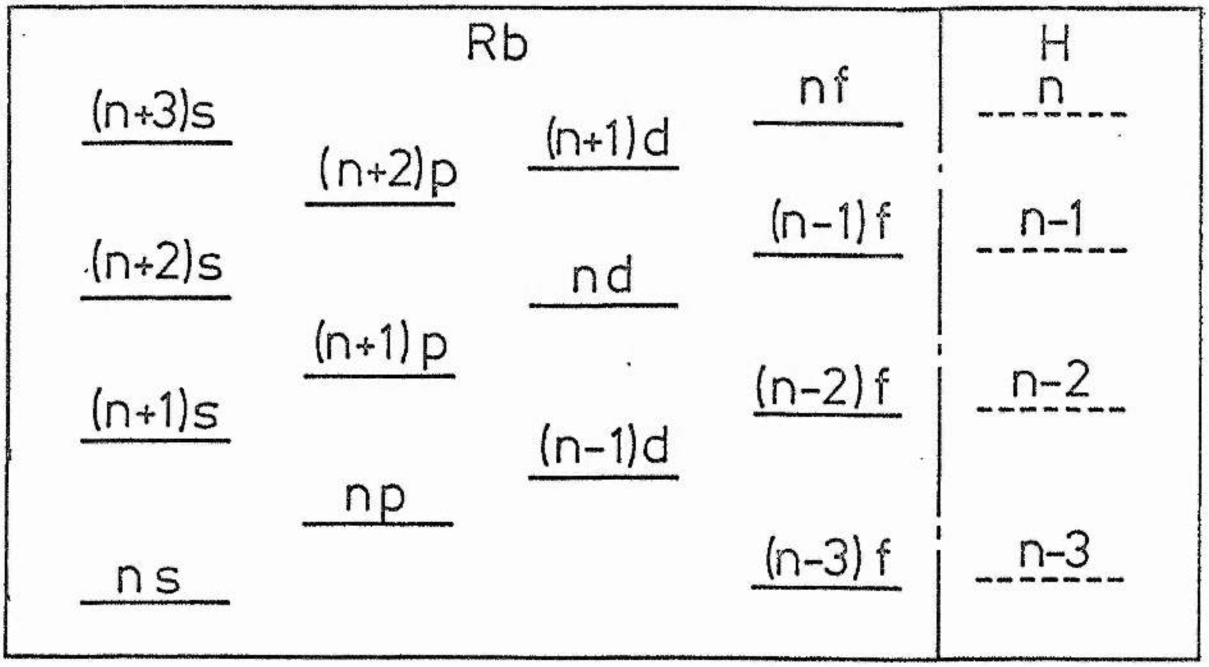

Figure 1. Ordering of the energy levels of rubidium. The energy levels of hydrygen are shown for comparison.

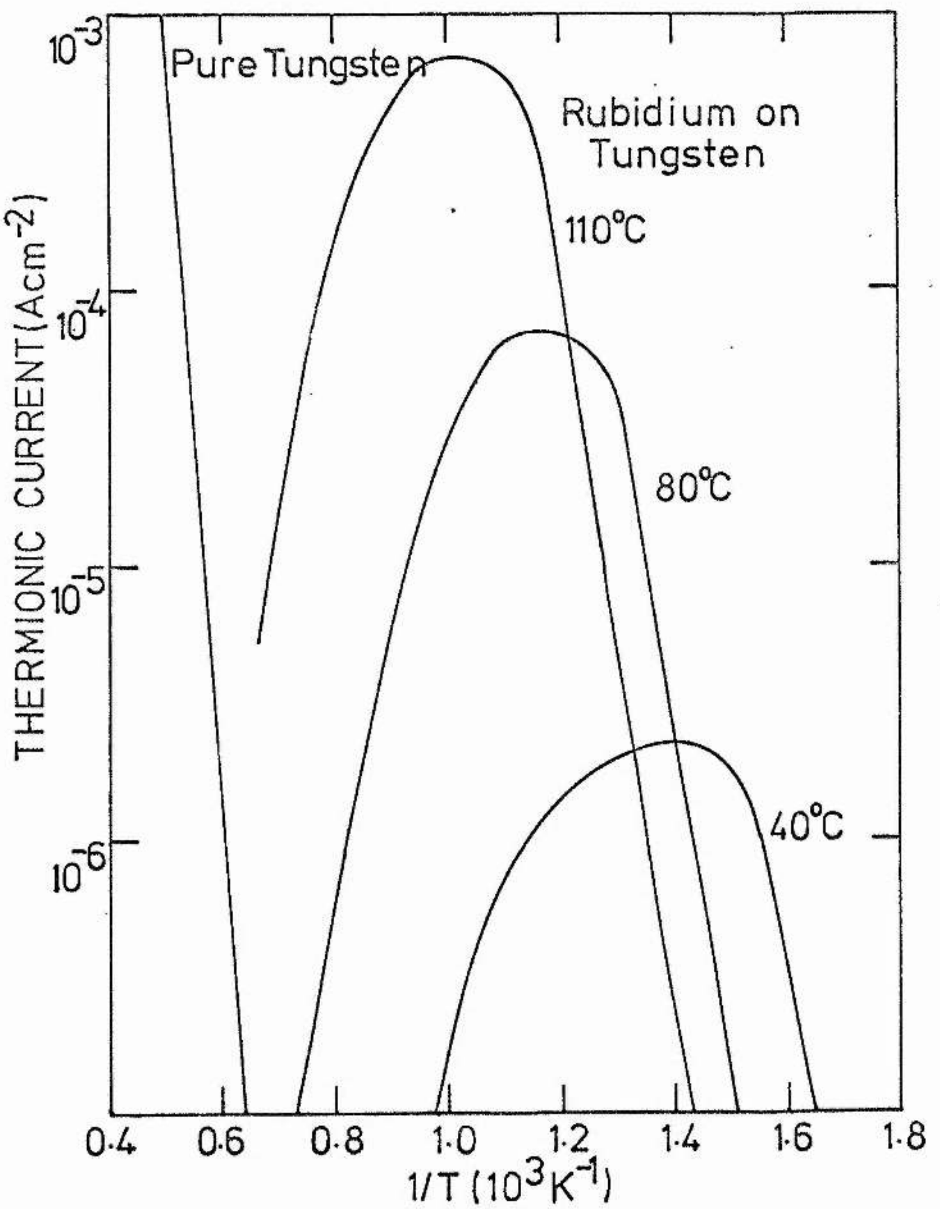

Figure 2. The thermionic emission current density as function of the inverse of the filament temperature for a tungsten filament in the presence of rubidium vapour compared with the emission from pure tungsten. The cell temperature determining the rubidium vapour pressure is indicated.

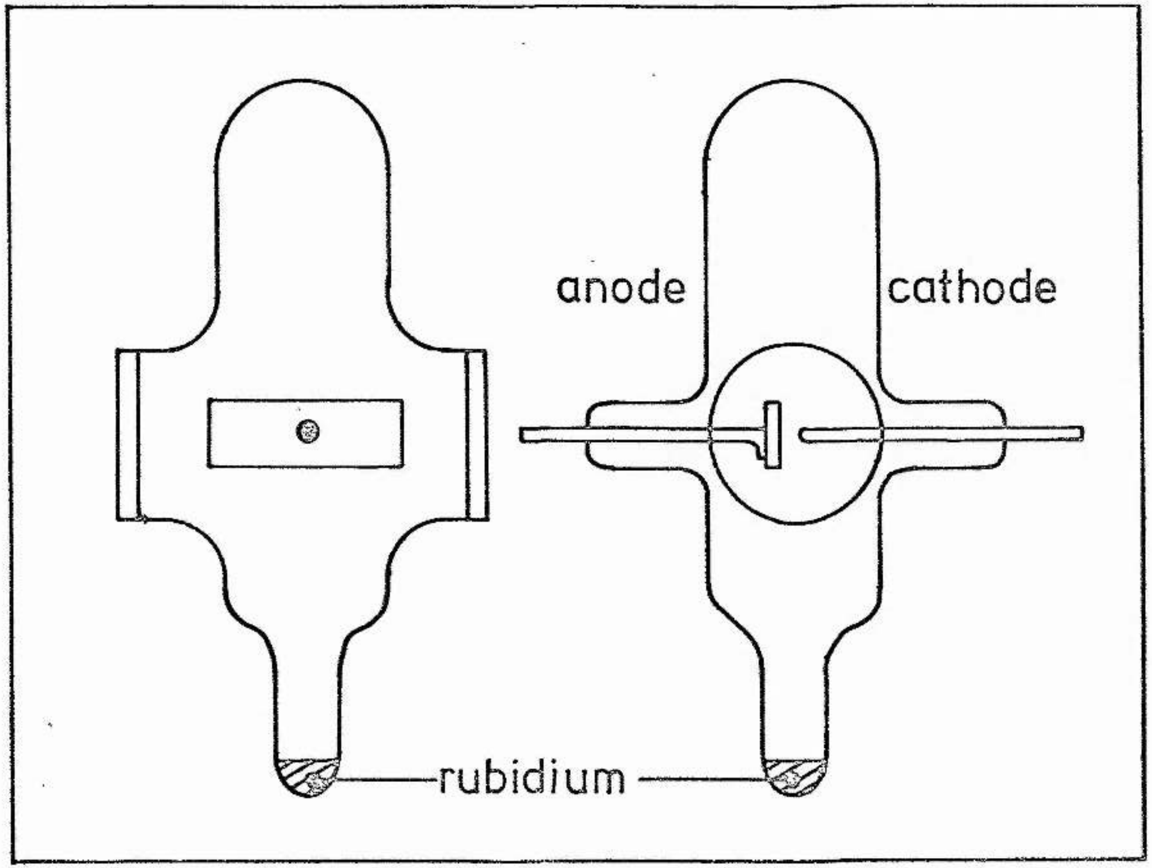

Figure 3. Design of the original pyrex detector used in this work.

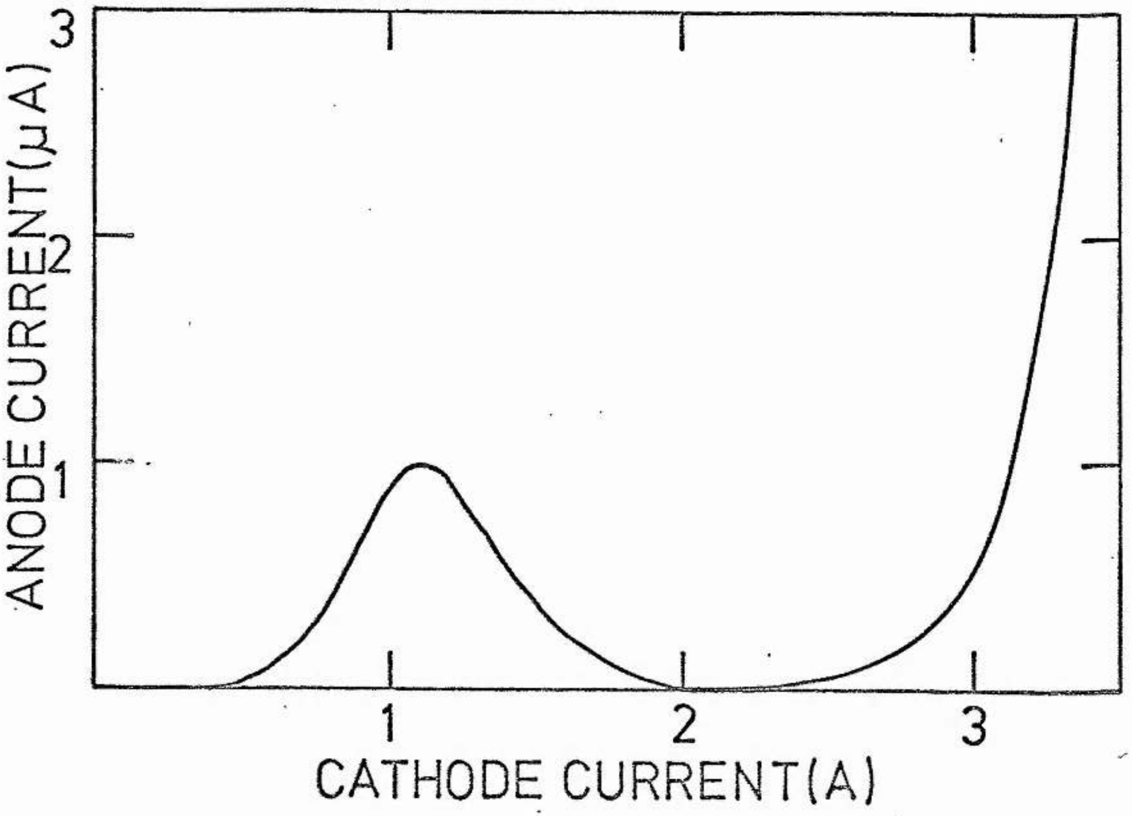

Figure 4. Behaviour of the thermionic emission as the cathode filament temperature is increased in the presence of a saturated vapour pressure of rubidium at 40°C.

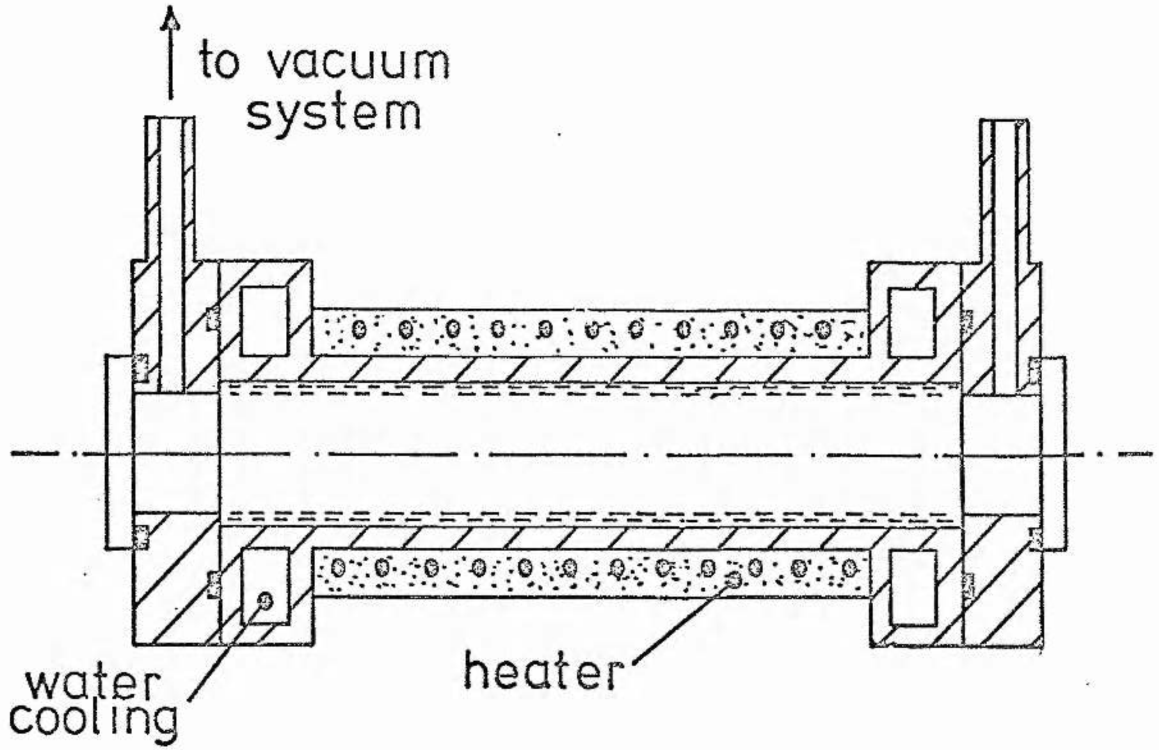

Figure 5. Schematic diagram of the oven used in the experiments described.

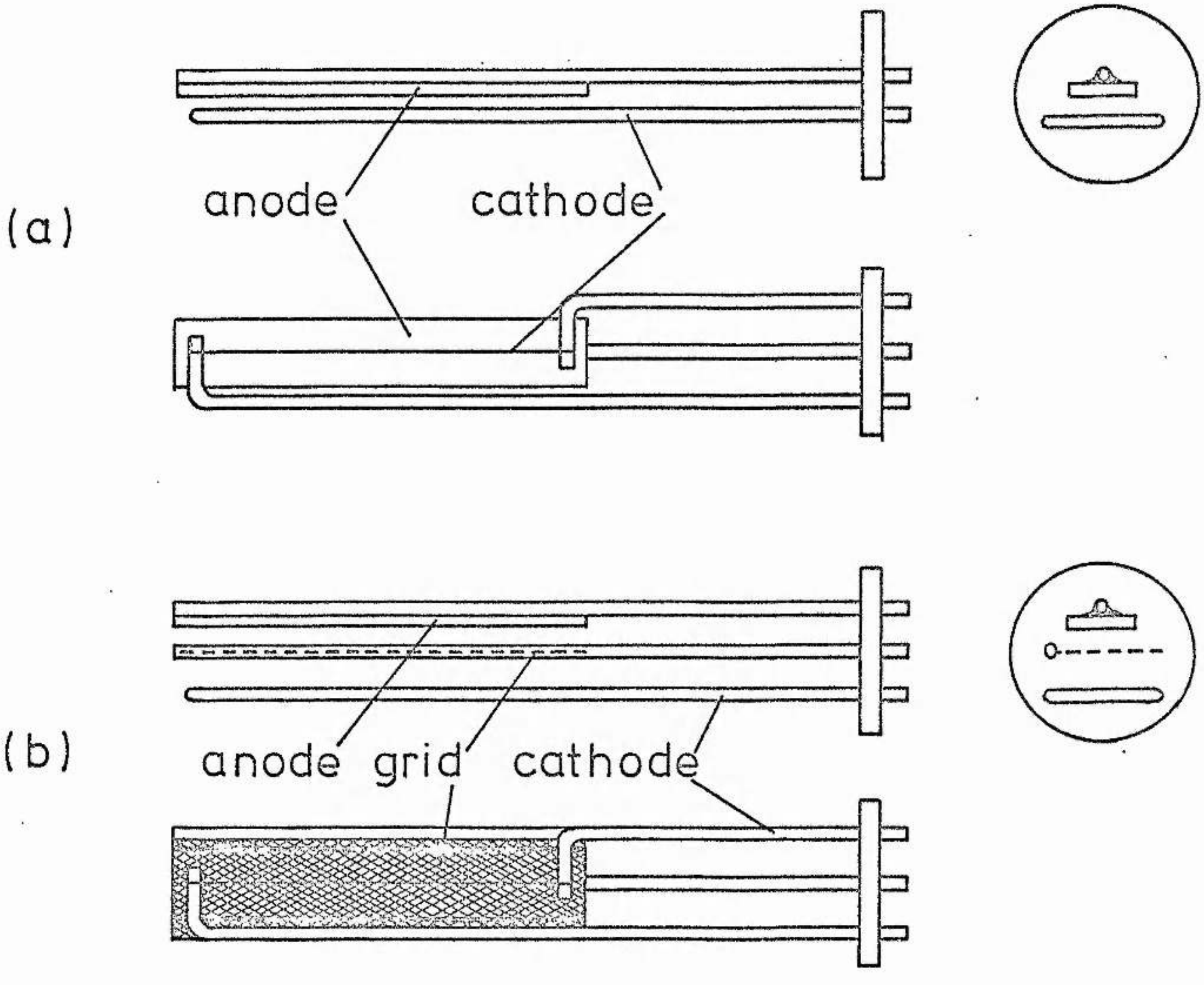

Figure 6. Sketches of the ionization probes used for the detection of Rb Rydberg states. (a) simple diode arrangement. (b) A triode arrangement enabling a field controlled zone to be used.

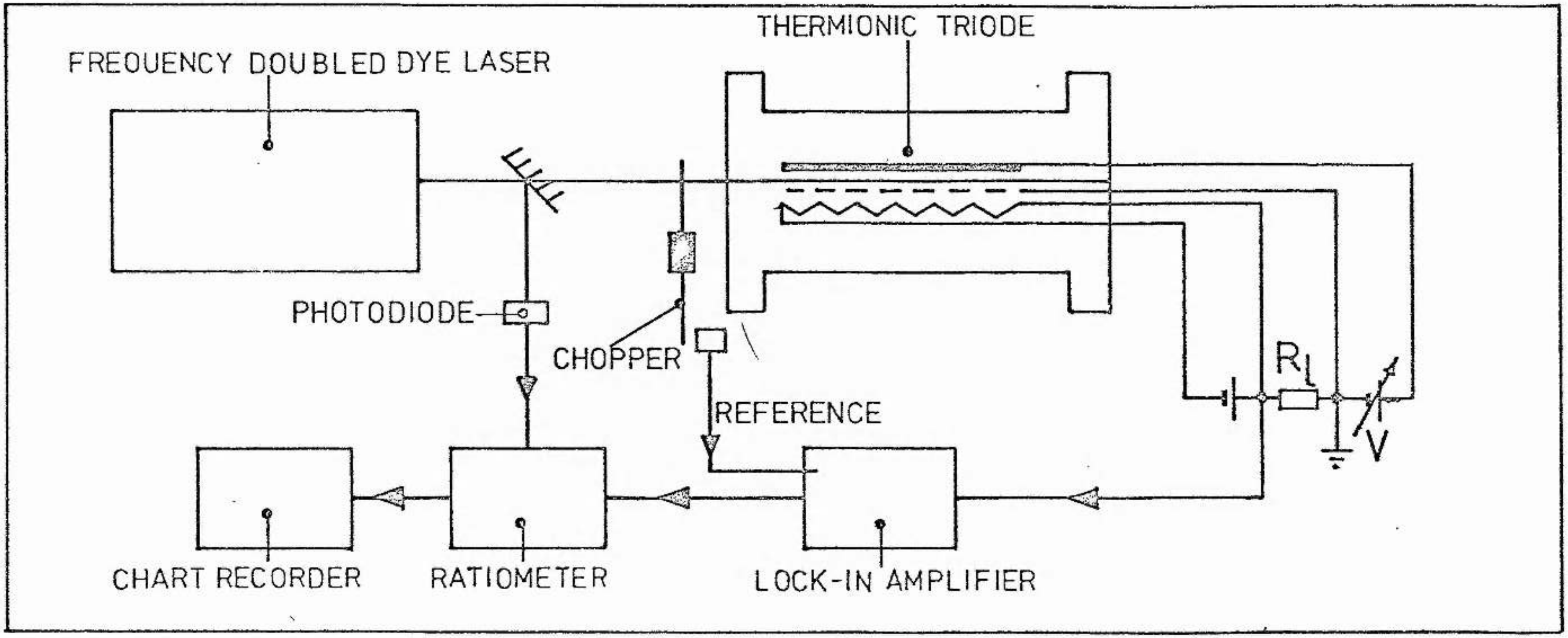

Figure 7. Schematic diagram of apparatus used in the detection of Rydberg states. Light from the frequency doubled laser traverses the zone between grid and anode. The variable voltage V controls the electric field in this region.

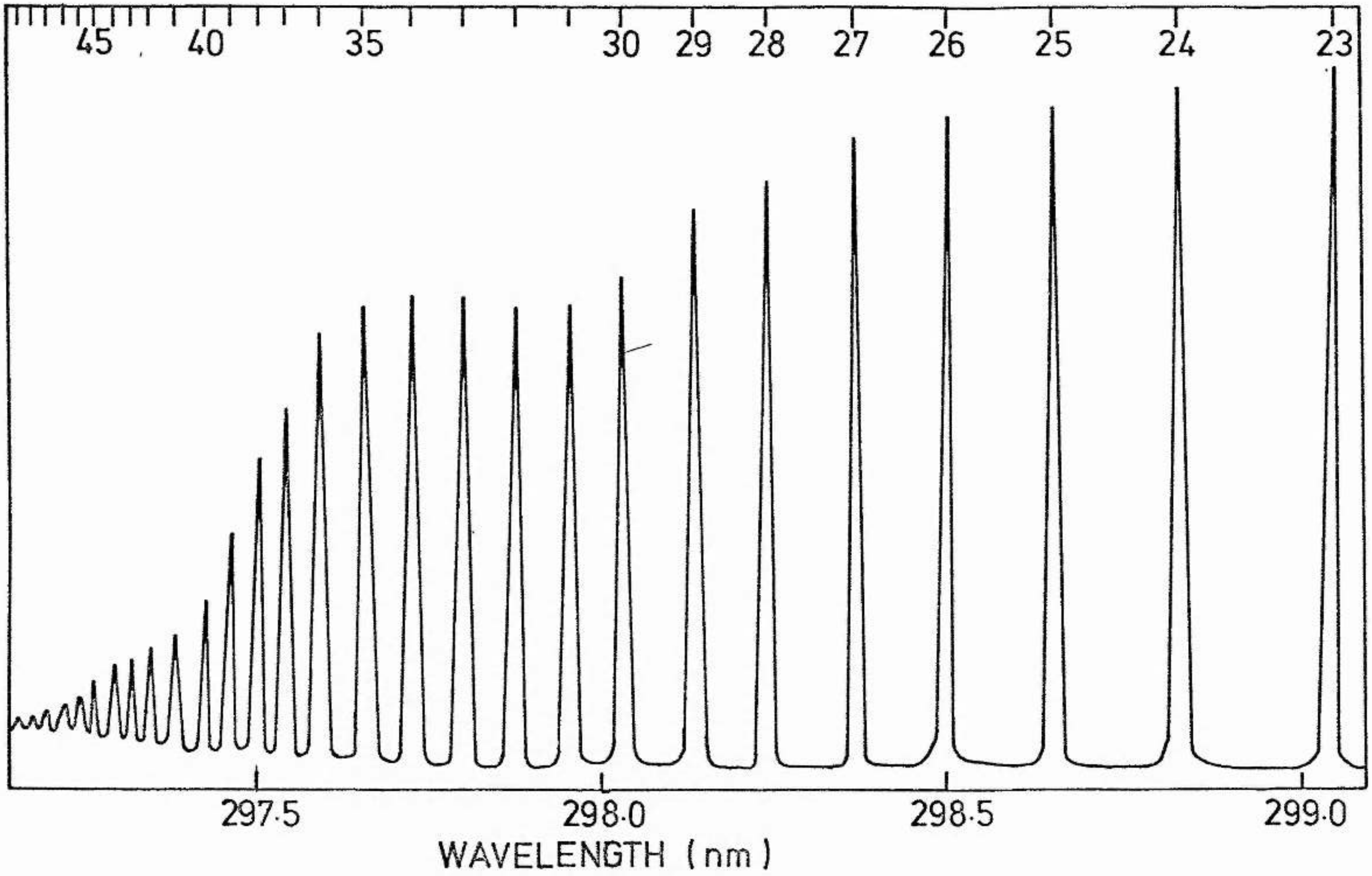

Figure 8. The Rydberg states of rubidium for a principal quantum number n = 23 to n = 50. The states were excited with radiation of 0.02 nm linewidth tuned over the range 297 nm to 299 nm.

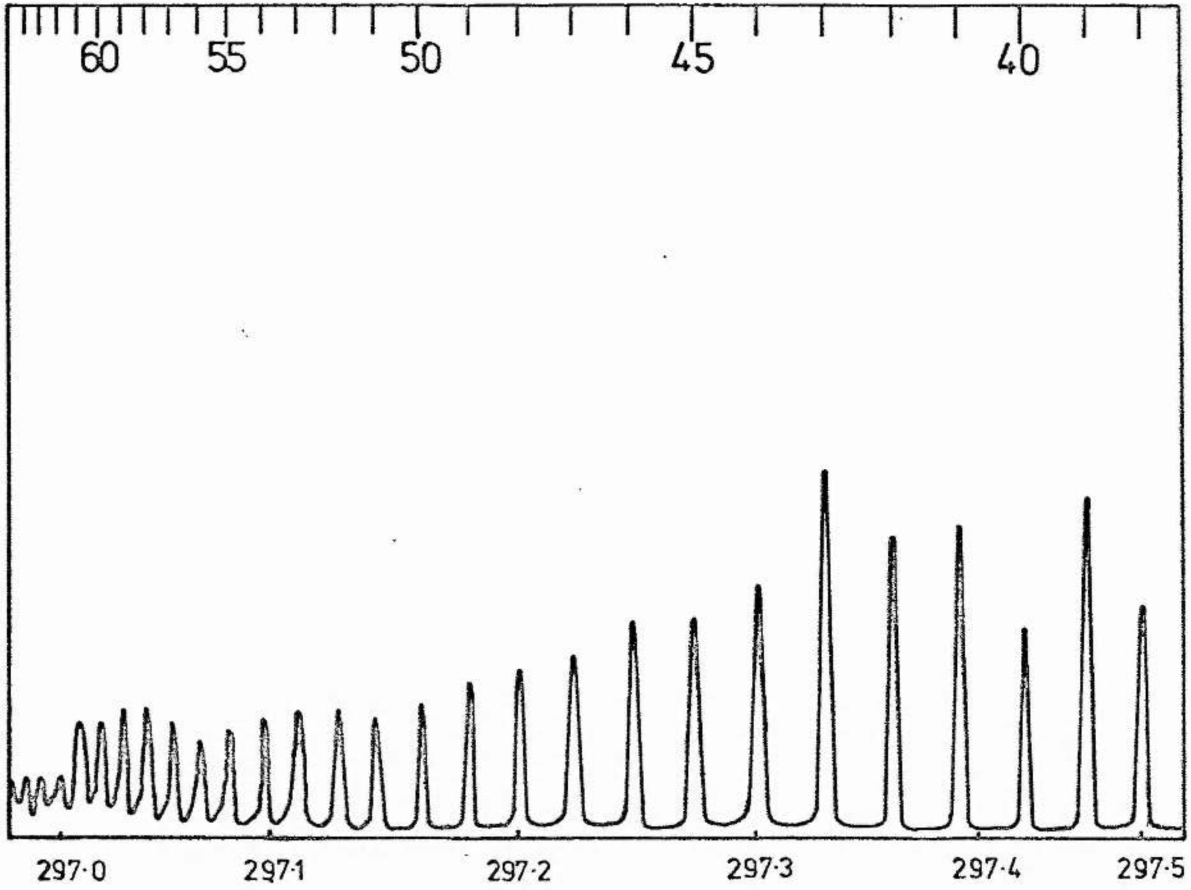

Figure 9. Rydberg states of Rb from states of principal quantum number $n = 38$ to $n = 64$. The laser linewidth was 0.002 nm.

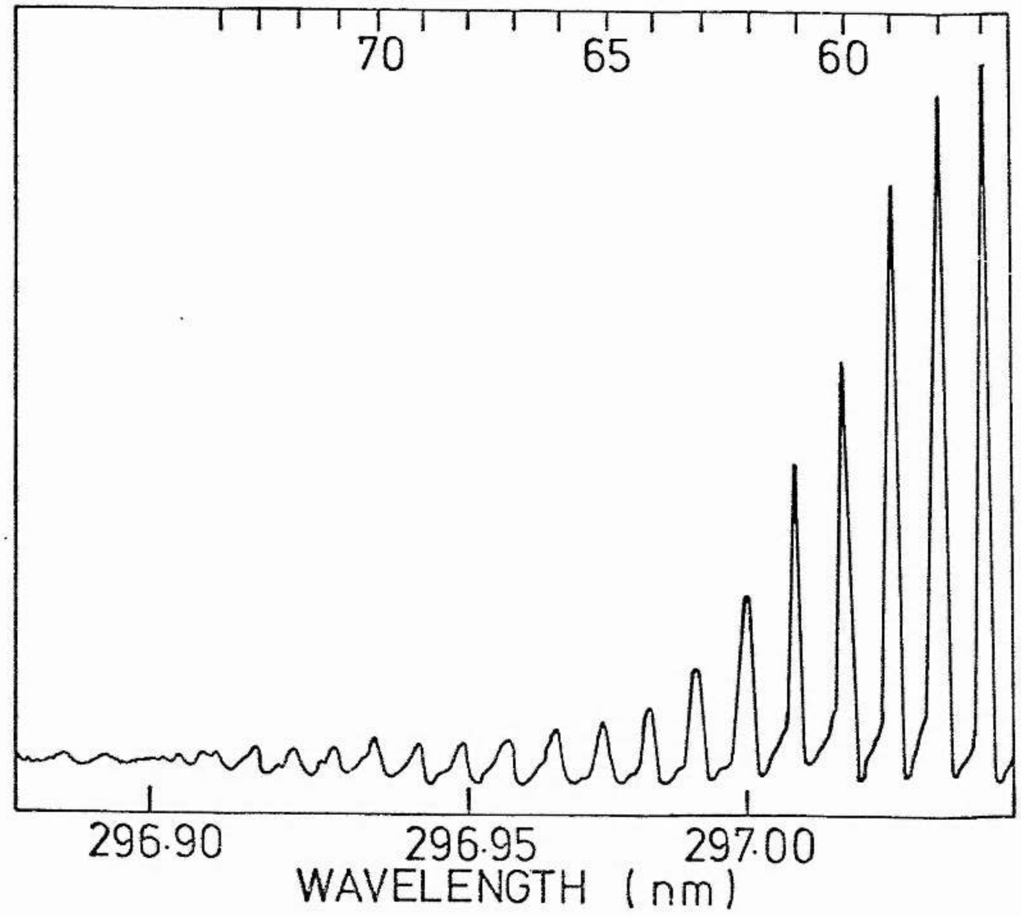

Figure 10. Rydberg states of Rb. The frequency doubled laser of linewidth 0.002 nm can resolve states up to n = 74.

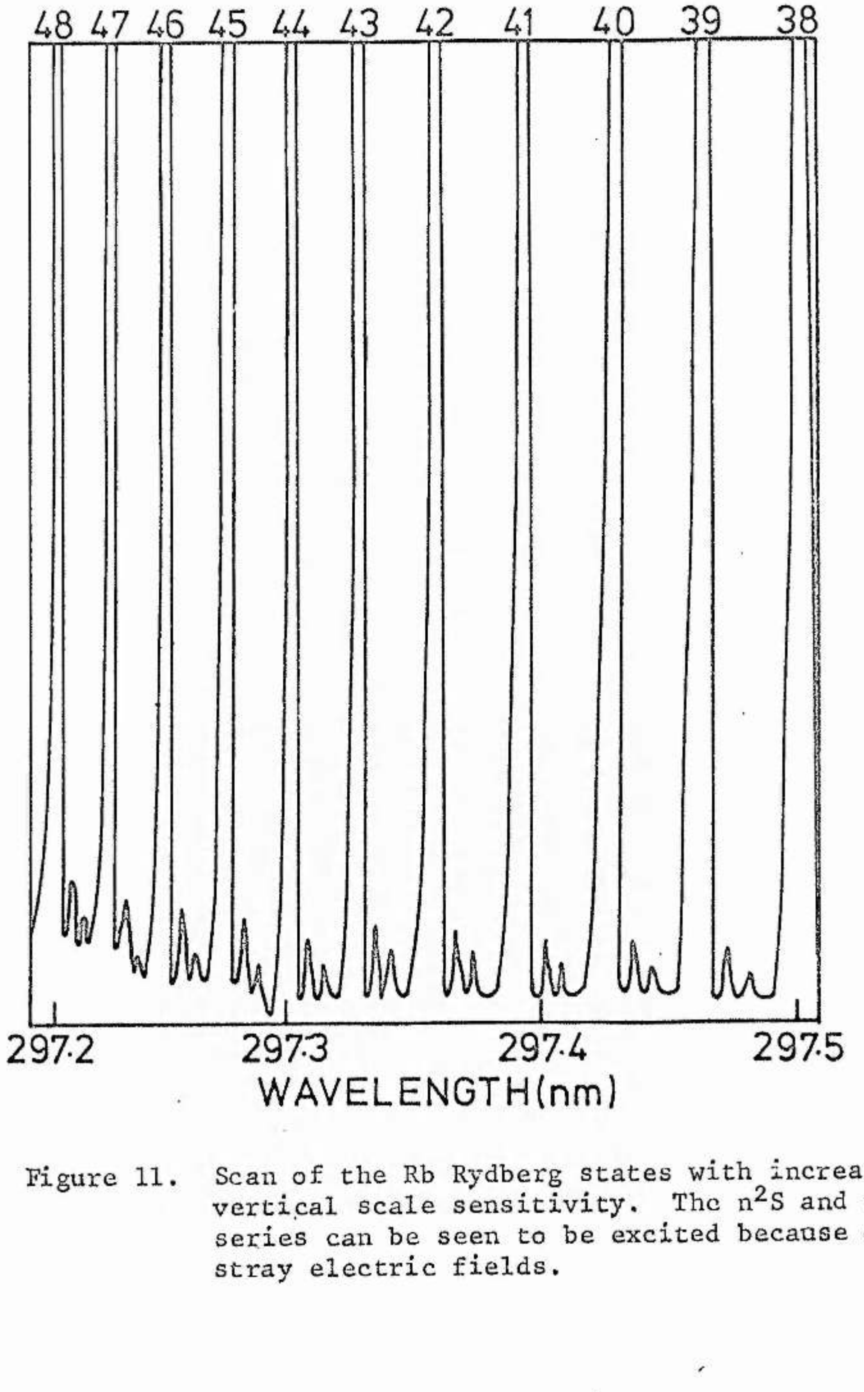

Figure 11. Scan of the Rb Rydberg states with increased vertical scale sensitivity. The n^2S and n^2D series can be seen to be excited because of the stray electric fields.

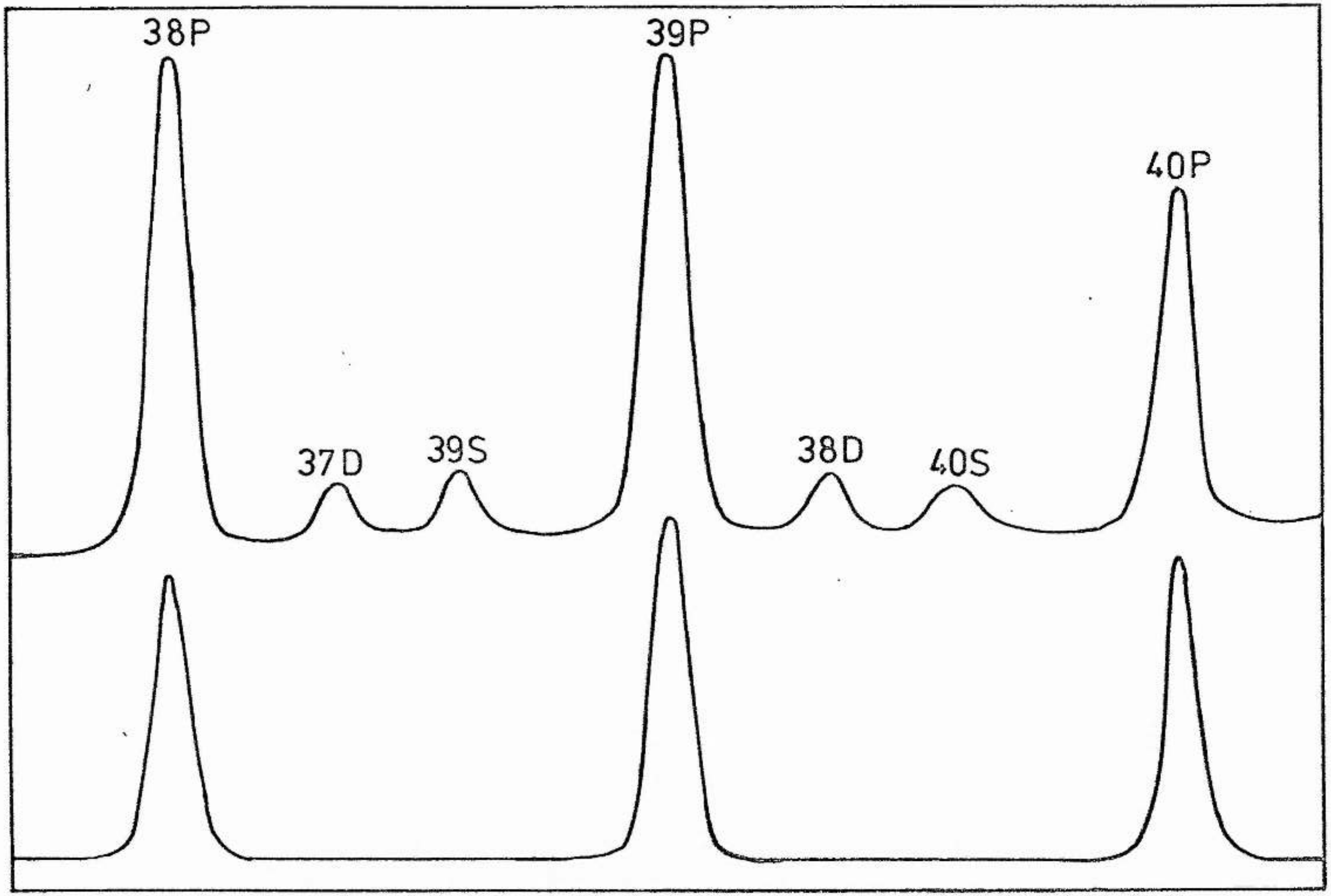

Figure 12. Signal from thermionic triode as a function of laser wavelength. The lower trace is for the case of zero field between grid and anode when only P states are excited. The upper trace is when an electric field of 5V cm^{-1} is applied resulting in excitation of D and S states as well.

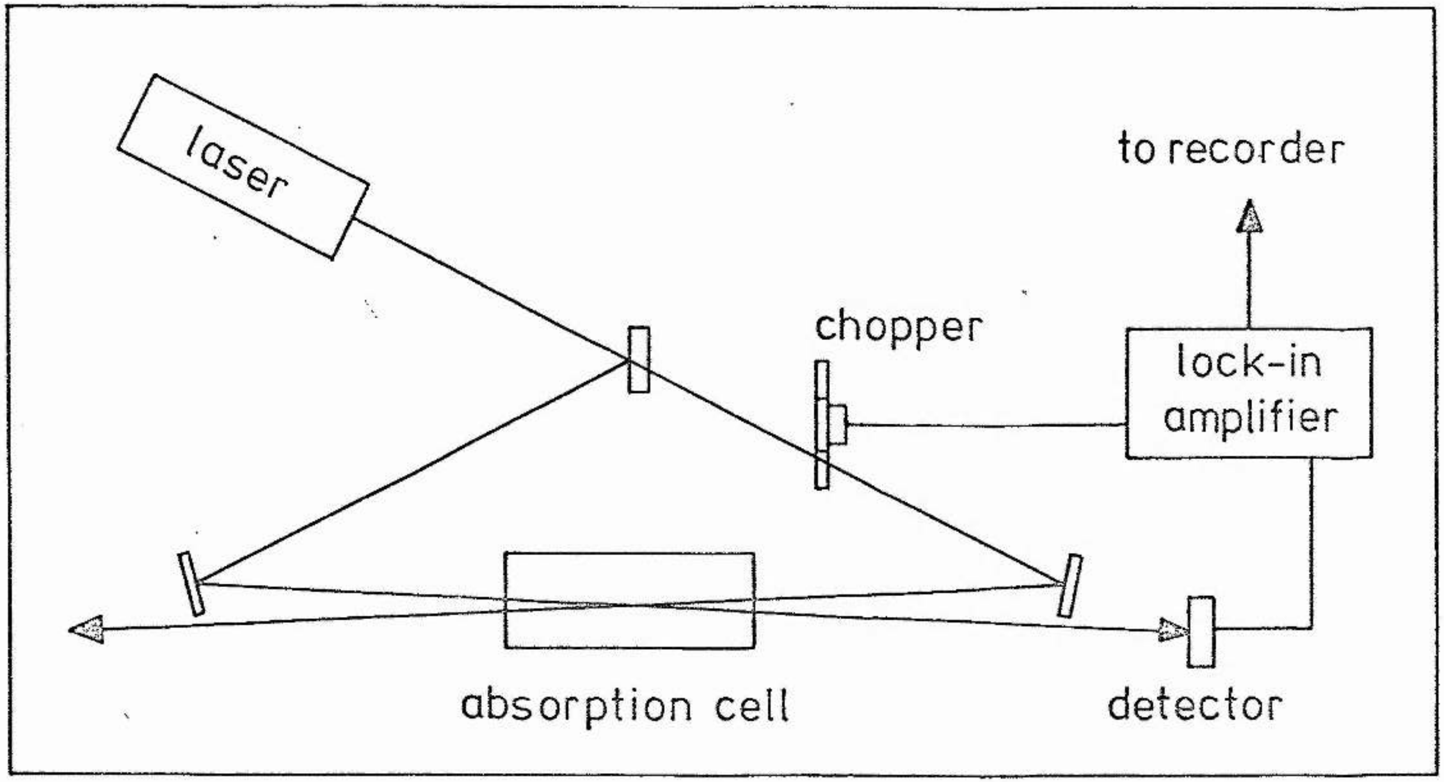

Figure 13. A typical experimental arrangement for saturation absorption spectroscopy.

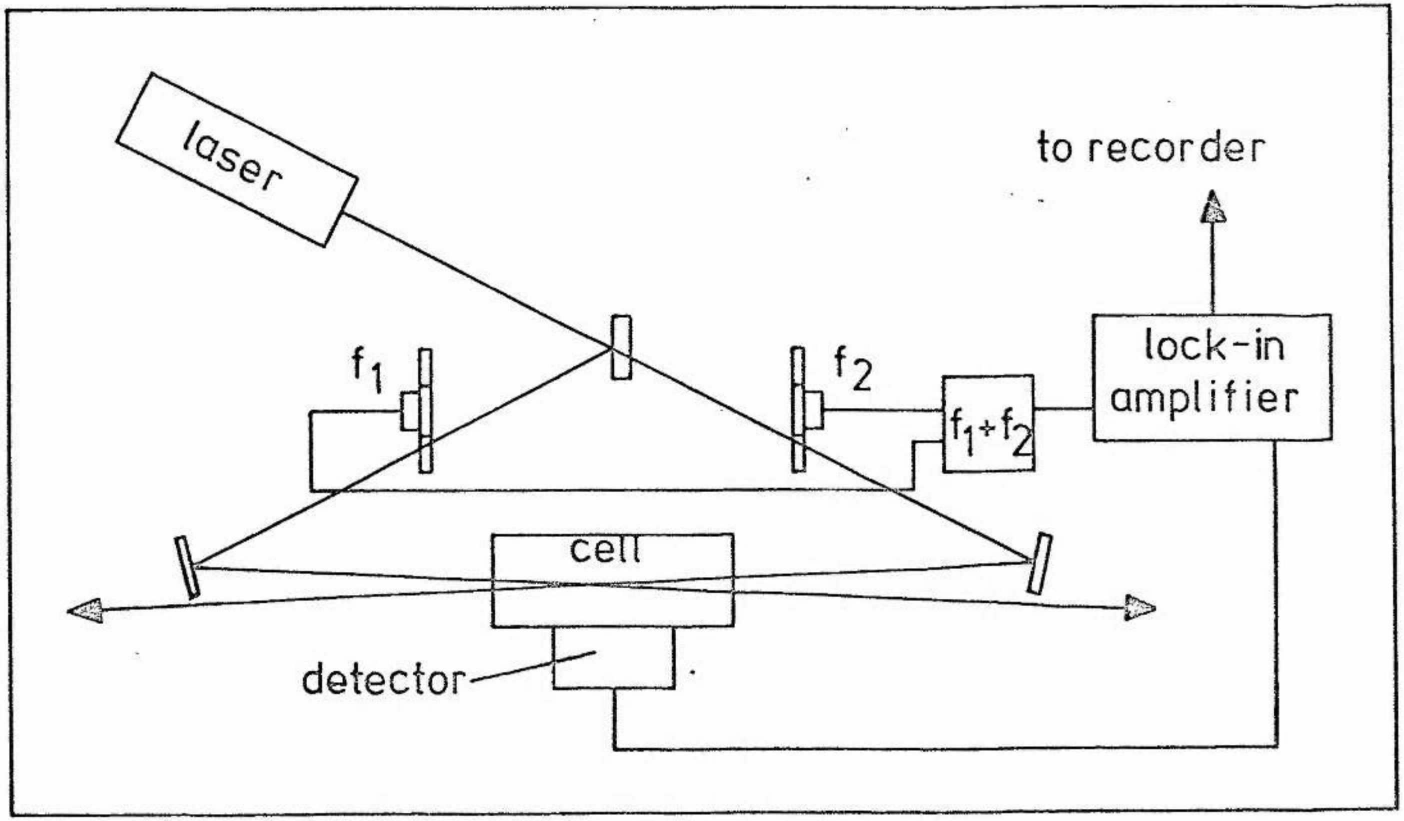

Figure 14. Schematic diagram of set-up of nonlinear fluorescence or ionization spectroscopy. One of the beams is modulated at f_1 and the other at f_2. The ionization or fluorescence signal is observed at $f_1 + f_2$.

CHAPTER VII

A SINGLE FREQUENCY SECOND HARMONIC DYE LASER

Abstract

Fast stabilization techniques for single frequency visible dye lasers are reviewed. Frequency stabilities of 1 part in 10^{11} and intensity stabilities of 1 part in 10^4 are now possible using these techniques.

A prototype single frequency second harmonic dye laser is described. The free running linewidth measured at visible wavelengths was 10MHz and the ultraviolet power was 0.1mW. The laser frequency was stabilized on an external reference cavity resulting in linewidths in the region of 2MHz. Frequency scanning was accomplished by either a tilting etalon method or a piezoelectrically scanned etalon. A tuning range of about 500MHz was achieved. Methods of increasing the single mode UV power, frequency stability and tuning range are proposed. In particular, it is proposed that fast frequency stabilization of the ultraviolet laser can be accomplished by using the same crystal as harmonic generator and cavity length modulator.

VII.1 Introduction

One of the main advantages of a continuous wave laser over a pulsed laser is that ultimately very narrow linewidths can be achieved. The linewidth of a pulsed laser is fundamentally limited by the uncertainty relation $\Delta\omega\Delta t \overset{\sim}{>} 1$ where $\Delta\omega$ is the laser linewidth and Δt is the pulse duration. For a nitrogen pumped dye laser the pulse duration is in the region of 5 nsec and the linewidth is therefore at least 200 MHz. CW dye lasers have been reported with linewidth of less than 1 kHz although 1 MHz is more common in practice. At present the only way of producing tunable UV radiation with linewidths of the order of 1 MHz is by frequency doubling a single frequency CW dye laser. The successful development of tunable single frequency UV radiation is therefore one of the most significant aspects of the CW frequency doubled dye laser. Typical output powers from fundamental single frequency CW dye lasers are 100 mW. This power is limited by the dye laser going multimode at higher pump powers. In a fundamental laser the output is usually coupled through a 4% transmitting mirror indicating that intracavity powers of up to 2.5W should be expected before the laser goes multimode. The UV power generated by a 1.5 cm ADA crystal in a 2.5W laser cavity would be about 2 mW. This power should be adequate to perform a variety of single frequency Doppler-free experiments.

In this chapter some of the methods of producing stabilized single frequency dye lasers are reviewed. The construction of a prototype single frequency UV dye laser is then described and future improvements and possible experiments proposed.

VII.2 Single Frequency Fundamental Dye Lasers

VII.2.1 Frequency Stabilization

Some of the most significant developments in laser spectroscopy in recent years have arisen from the availability of single frequency tunable

CW dye lasers. The ultimate free-running linewidth of a CW dye laser is determined by the length stability of the laser cavity. A change in length of only $\lambda/2$ is enough to move the laser frequency by a free spectral range of the cavity which is usually of the order of several hundred MHz. The cavity length must therefore be stabilized to within a very small fraction of λ if the ultimate linewidth is to be attained. The main factor which determines the linewidth of a CW dye laser is the flowing jet stream, normally present in the cavity. The free-running linewidth of a typical jet stream dye laser is in the region of 10 MHz to 20 MHz. This compares with linewidths of less than 1 MHz for a typical gas laser. In order to reduce the linewidth of a dye laser to that of a typical gas laser a variety of laser stabilizing systems have been developed.

The linewidth of a typical CW dye laser with a single tuning element usually lies between 0.1 nm and 0.01 nm. For a cavity of length 50 cm this means that there are normally somewhere between 30 and 300 modes oscillating in the cavity simultaneously. The linewidth can be greatly reduced by the introduction of a low finesse etalon whose free spectral range is greater than the laser linewidth. Thus an etalon of between 0.1 mm and 1 mm thickness is usually sufficient to reduce the oscillation to less than 5 modes, corresponding to a linewidth of about 3 GHz. If an etalon with a free spectral range of greater than about 6 GHz (<1.5 cm) is also included, this is then usually sufficient to reduce oscillation to single mode.

The dramatic improvement in dye laser frequency stability when servo locking techniques are used has been shown by Hartig and Walther[1] who have locked the laser frequency to a Na resonance line in a fast atomic beam apparatus, Wu, Grove and Ezekiel[2] who have locked the laser to molecular transitions and Barger, Sorem and Hall[3] who have locked the laser to an external reference cavity. Of these methods the most versatile is that of Barger, Sorem and Hall since the reference cavity can be made to scan and so tune the laser frequency. This is of course at the expense of long term frequency stability since thermal drifts in the reference cavity can take place.

A schematic diagram of a servo system of the kind used by Barger, Sorem and Hall is shown in figure 1. Part of the laser beam is directed into an external Fabry-Perot interferometer while the laser intensity is monitored on a photodiode. The intensity of the light falling on the photodiode is adjusted until it is equal to half of the peak intensity of the beam transmitted by the interferometer. The difference signal between the reference channel and the intensity transmitted by the interferometer is amplified, and is then fed through a 3 dB per octave filter, integrator and high voltage amplifier to a pieozoceramic which moves one of the laser cavity mirrors. The resulting change in cavity length changes the laser frequency in such a way as to reduce the difference between reference and interferometer channels. The laser can stabilize on either side of the interferometer fringe depending on whether a positive voltage applied to the laser cavity piezoceramic increases or decreases the laser wavelength. The laser is stabilized half way up a transmission fringe as this gives the highest frequency discrimination. The intensity is monitored so that any intensity fluctuations are not interpreted as frequency shifts, thus mapping intensity fluctuations into frequency fluctuations.

An integrator is used in the servo system so that when the correction signal drives the error signal to zero, the zero crossing voltage will be maintained on the output of the amplifier thus ensuring a stable lock. The 3 dB per octave filter is used to provide high gain at low frequencies while at the same time preventing unduly large phase shifts at the high frequencies. The overall servo gain of the integrator and filter is 9 dB per octave. In more refined systems the correction signal is divided into high and low frequency components by a crossover network. The low frequency (< 1 kHz) corrections are applied to a long excursion piezoelectric driver attached to the output coupling mirror while the high frequency ones are applied to a very fast piezoelectrically driven mirror elsewhere in the dye laser.

With this system a short term (< 20 μsec) frequency stability of better than 50 kHz can be obtained whereas the long term (> 10 sec) frequency stability,referred to the stabilizing cavity,is typically 100 Hz. However the absolute long term frequency stability is limited to about 1.5 MHz min^{-1} due to thermal drift of the reference cavity.

The long term frequency drift of the dye laser can be eliminated by locking the external reference cavity to a He-Ne laser stabilized on either iodine (633 nm) or methane (3.36 μm). The long term frequency stability of an iodine stabilized He-Ne laser is better than 1 part in 10^{11}[4], while for the methane stabilized He-Ne laser it is 1 part in 10^{13}[4]. The dye laser should therefore ultimately be capable of stability of this order. The tunability of the dye laser can be maintained by use of the frequency off-set locking technique described by Barger and Hall[5]. A schematic diagram of a system using the frequency off-set locking technique is shown in figure 3. This technique required two similar reference lasers; one whose frequency is locked to a fixed reference frequency such as the centre of the saturated absorption resonance of a molecule, and a second laser whose frequency can be off-set over a limited range about this fixed frequency, the off-set being monitored by a heterodyne method. The second laser is then used as the local oscillator to which the reference cavity can be locked. In this method the frequency stability of the fixed frequency laser is transferred to the local oscillator which in turn transfers its stability to the reference cavity while at the same time allowing the cavity length to be changed in a controlled manner.

A dye laser which uses this frequency off-set locking technique and incorporates other improvements has been described by Barger, West and English[6]. The improvements that they have effected have been to include an electro-optic modulator in the cavity for very fast frequency stabilization, to use the frequency off-set locking technique for long term stability and to intensity stabilize the dye laser output using a second external electro-optic modulator.

In this dye laser the slow servo control of the cavity length was maintained by a large extension piezo electric driver and fast (> 1 kHz) control was accomplished with an intracavity deuterated KDP crystal. The servo electronics had a unity gain point of 500 kHz with a 9 dB per octave roll-off from d.c. to 50 kHz and 6 dB per octave from 50 kHz to 500 kHz. The error signal was processed by a fast amplifier which split the signal into low, intermediate and high frequency components with cross-overs at 1 kHz and 150 kHz. The low component is amplified and fed to the piezoceramic on the laser's output coupler. The intermediate components were amplified with a ± 150 V operational amplifier and the high frequency component with a high speed ± 15 V operational amplifier. The faster components were applied to opposite electrodes of the K$\overset{*}{\mathrm{D}}$P crystal.

The laser intensity was stabilized by referring the output from a photodiode, which measured the laser intensity, to a stabilized d.c. current source. After being amplified by a fast servo system the error voltage was applied to a low voltage (half wave voltage = 250 V) ADP modulator placed at the dye laser output. The intensity stability was about 1 part in 10^4 for times between 10^{-4} sec and 10 sec.

A methane stabilized He-Ne laser operating at 3.39 μm was used as the frequency reference.The frequency of the local oscillator could be tuned over ± 220 MHz which corresponds to a tuning range of about 2.5 GHz for the visible dye laser. The short term frequency stability of the dye laser was found to be 1 kHz, this increased to about 3 kHz for times of the order of 1 sec but fell to about 300 Hz over the long term (300 sec). The frequency stability should continue to improve over long time scales until the ultimate stability of the methane stabilised laser, about 1 part in 10^{13}, is reached. The drop in stability for integration times around 1 sec was due to noise in the electronics.

Gerhardt and Timmermann[7] have extended the frequency off-set locking technique of stabilizing a dye laser to the use of a lamb dip stabilized He-Ne laser operating at 633 nm as the fixed frequency laser. It is desirable to operate the reference laser in the visible since the reference cavity only has to have a high finesse at one wavelength instead of two as in the case of stabilizing a visible laser by locking to a cavity locked to an infrared methane stabilized laser. However the required frequency shift between the reference laser and the local oscillator is almost the same as the tuning range of the dye laser when both lasers operate in the visible. In the system of Gerhardt and Timmermann[7] a beat frequency of up to 1 GHz could be detected. For frequency tuning ranges larger than this it is necessary to count different modes of the reference cavity. Thus a scan of greater than 1 GHz would be accomplished by scanning the local oscillator to the maximum beat frequency while the reference cavity is locked to it. The reference cavity length is then fixed while the local oscillator frequency is moved back through a free spectral range of the reference cavity. This will only work if the free spectral range is less than the continuous scan range. The lock is then re-established and the scan continued. Using this technique Gerhardt and Timmermann[7] have scanned a rhodamine 6G dye laser through about 3 GHz with a resolution of approximately 100 kHz.

In conclusion, a dye laser can be stabilized to a stability approaching that of gas lasers provided certain precautions are taken. These include a very fast servo system to reduce the noise introduced by a flowing dye jet and fast intensity stabilization to ensure the residual intensity fluctuations are not mapped into frequency shifts. Some rules of thumb in using stabilized dye lasers have been summarized by Hall and Lee[8]. Fast electronic servo circuits of the kind used by Hall and his colleagues at the National Bureau of Standards are described in an appendix.

VII.2.2 Tuning a Single Frequency Dye Laser

Most single frequency dye lasers are frequency narrowed by a broad-band tuning element reducing the laser linewidth to less than 1 nm followed by two low finesse etalons of free spectral range in the region of 300 GHz and 10 GHz. The cavity longitudinal mode spacing is usually about 100-300 MHz. If the laser frequency is changed by a piezoceramically mounted output coupler approximately 50 V is required to scan one cavity mode for a 1" diameter 0.1" thickness PZT ceramic. Thus a scan of about 3 GHz can be expected for an applied voltage of 1 kV if the mode spacing is 150 MHz. In order that this scan can be realized the thick etalon transmission frequency must be changed so that the laser frequency does not hop. The peak transmission of an etalon is changed by changing the separation between the two reflecting surfaces. This can be done either by using a piezoceramic spacer or by tilting the etalon. The accuracy to which the etalon plate separation must be set is determined by the free spectral range of the etalon and the mode spacing of the cavity. The peak of the etalon transmission must be located to better than plus or minus half of the mode spacing. For an etalon of separation ℓ in a cavity of length L oscillating at a frequency ν_o the required length stability is

$$\delta\ell < \pm c\ell/4\nu_o L \tag{1}$$

If the etalons is of 1 cm thickness and the cavity is 1 m in length the length stability of the etalons must be better than ± 1.5 nm. A typical PZT ceramic is extended by about 0.6 nm V^{-1} when the electric field is applied along the same direction as the extension. Thus the voltage must be stable to at least 2.5V over the useful tuning range of the thick etalon. Since the free spectral range of the etalon is 15 GHz it only has to be expanded through about one fifth of a free spectral range for a frequency excursion of 3 GHz. This requires only 100 V and a source stable to within 2.5V over a range of 100 V is easy to obtain.

The piezoelectric expansion of an etalon would therefore appear to be an attractive method of scanning the laser frequency. The disadvantage of a piezoelectrically scanned etalon is that the two plates must be set parallel to better than $\lambda/10$ over the whole area of the plates and this can be difficult when a piezoceramic is used as the spacer. Also the rear surface of each plate must be wedged and antireflection coated so the laser cavity losses are low and to ensure that the back surfaces do not interfere with the etalon effect. These advantages are overcome by using a solid etalon and tilting it within the cavity. A solid etalon can be polished to $\lambda/20$ or better and will maintain this finesse for a long period of time. This, combined with the fact that there are only two surfaces, means that the linear losses of the cavity will be smaller.

The shift in oscillation frequency in tilting an etalon from on axis to an angle θ is given by (see Chapter V)

$$\Delta\nu = \nu_o\theta^2/2 \qquad (2)$$

Any small change in θ of size $\delta\theta$ will give rise to a change in oscillation frequency $\delta(\Delta\nu)$ given by

$$\delta(\Delta\nu) = \nu_o\theta\delta\theta \qquad (3)$$

Now the stability and linearity of a non-servo controlled torque galvanometer is typically 1%. Hence the etalon can be located to a frequency accuracy of about

$$\delta(\Delta\nu) = \nu_o\theta^2 \times 10^{-2} \qquad (4)$$

The total scan range for a given frequency stability $\delta(\Delta\nu)$ is therefore

$$\Delta\nu = 50 \times \delta(\Delta\nu) \qquad (5)$$

on substituting for θ in equation (2). The intermode spacing of a 1 m laser cavity is 150 MHz and the etalon must then be scanned with an accuracy of better than ± 75 MHz. Thus for this cavity equation (5) predicts that a total scan range of up to about 3.8 GHz can be expected with standard scanning galvanometers assuming a linearity of better than 1%. This estimate assumes that the drive electronics are perfectly linear and that the etalon has been accurately centred on zero.

If there is a small zero error in the alignment of the etalon, s, the frequency shift becomes

$$\Delta\nu = \nu_o(\theta + s)^2/2 \qquad (6)$$

The change in frequency shift for a small change in s is given by

$$\delta(\Delta\nu) = \nu_o(\theta + s)\delta s \qquad (7)$$

Assuming that $\theta >> s$ and that the uncertainty in s is approximately equal to s this becomes

$$\delta(\Delta\nu) = \nu_o\theta s \qquad (8)$$

Substituting for θ from equation (2) the accuracy of zeroing the etalon is given by

$$s < \frac{\delta(\Delta\nu)}{(2\Delta\nu\ \nu_o)^{\frac{1}{2}}} \qquad (9)$$

Assuming that the required accuracy of locating the etalon corresponds to $\delta(\Delta\nu)$ = 75 MHz and that a scan of 3.8 GHz is required the zeroing accuracy of the etalon must be better than 40 μrad. This kind of zero setting accuracy should be possible using scanning galvanometers.

It would therefore appear on the basis of these calculations that the scanning of a single frequency dye laser can be accomplished either by piezoelectrically scanning the intracavity etalons or by tilting the etalons. Although most of the single frequency dye lasers reported in the literature are tuned by piezoelectrically scanned etalons, some workers are now using tilting etalon scanning systems. Hall and Lee[8] have reported the scanning of a single frequency dye laser over the range 1.5 - 2.5 GHz using a pair of tilting etalons.

One notable dye laser which uses both tilting etalons and piezoelectrically scanned etalons is a commercial system produced by

Coherent Radiation. In their 599 dye laser the cavity length is varied by tilting an intracavity plate set at Brewster's angle. The cavity oscillation frequency is determined by a three plate birefringent filter, a thin, low finesse etalon which is galvo-driven and a piezo driven thick etalon. The laser frequency is stabilized by using an external reference cavity similar to that used by Barger, Sorem and Hall[3]. The reference cavity length is changed by tilting a Brewster angled plate inside the cavity. The laser frequency is locked to the reference cavity length by feeding a fast error signal to a small mirror mounted on a piezoceramic and a slow error signal to the Brewster angled plate in the laser cavity. The thick etalon is modulated and locked to maximise the laser output intensity ensuring that it is always centred on the maximum of a transmission fringe. When tuning is required the Brewster plate in the reference cavity is tilted and the thin etalon, thick etalon and the Brewster plate in the laser cavity are all ganged. Simultaneously, the cavity length is stabilized on the reference cavity. Using this system a scan of 30 GHz can be obtained.

VII.3 A Single Frequency Second Harmonic Dye Laser

A schematic diagram of a prototype second harmonic single frequency dye laser is shown in figure 3. The basic dye laser cavity was similar to the improved cavity design described in Chapter V. Two etalons were included in the cavity to reduce the oscillation to a single mode.

The thin etalon was a 0.5 mm solid fused silica plate polished flat and parallel to λ/20 over its 25 mm diameter and coated to 30% reflectivity at 590 nm. This etalon was mounted on a torsion galvanometer (General Scanning Inc).

The second thick etalon was air spaced and piezoelectrically scanned. Details of its construction are shown in figure 5. The piezoceramic was PZT-5H supplied by Vernitron Ltd. A 25 mm long and 25 mm diameter cylindrical ceramic was cut back to 10 mm in length. The top and bottom surfaces were machined flat to normal workshop tolerances and then filed at three points around each rim to provide three location points. The location points were then polished by hand until less than a fringe appeared across test plates held against the surfaces. When the etalon was assembled with its own plates the finesse could be adjusted by three screws set above each of the pressure points. The etalon plates were coated to 30% reflectivity at 590 nm on one side and anti-reflection coated on the other. When the etalon was assembled the estimated flatness was about $\lambda/4$ over the area of the plates. A voltage of 800 V was required to scan a free spectral range.

The output coupler was fitted to a 25 mm diameter, 25 mm long piezoceramic. Approximately 50 V was required to scan this mirror through a cavity mode separation.

The laser modes were analysed using a degenerate interferometer. The interferometer mirrors were of 10 cm radius of curvature and separated by 5 cm giving a free spectral range of 1 GHz and a finesse of better than 150. The interferometer bandpass was therefore in the region of 7.5 MHz. The construction and operation of degenerate interferometers for laser mode analysis is described in more detail in appendix C.

In order to reduce pressure fluctuations in the dye flow system a low pass acoustic filter was included in the flow line. This consisted of a large volume vessel (8 litres) which could be pressurised with a pump. As the dye flows into the vessel a volume of air is trapped. The vessel will fill up until the air pressure equals that of the dye flow.

Dye pressures are typically 40-45 psi and so the flow will reach equilibrium when the vessel is about 2/3 full. Since the attenuation of pressure fluctuations depends on the trapped volume of air the filter will be more efficient if this volume can be increased. The volume of air can be increased if the vessel is pressurised while the dye is being pumped. In this system the air volume was increased by a simple stirrup-type pump. The ratio of dye to air volume could be reduced to better than 1:10 and gross pressure fluctuation in the dye flow were virtually eliminated.

The laser was pumped by an argon laser operating on 514.5 nm in the TEM_{oo} mode (Spectra Physics 171). The threshold pump power was about 1W and single mode operation could be maintained up to a pumping power of about 3W. The UV output power was then about 0.1 mW. The dye laser linewidth at visible wavelengths was better than 10 MHz for times of the order of a few seconds. For longer times the dye laser mode tended to drift and eventually hop. The dye laser mode would very often hop to the next cavity mode for short times (< 1 msec) and then hop back to the original cavity mode. This hopping was usually accompanied by mini-bubbles crossing the jet. The bubbles were the main obstacle to reliable single frequency operation in the free-running dye laser and were very difficult to eliminate. Some reduction in the amount of bubbles in the dye flow was obtained by immersing the dye pressure vessel in an ice bath because of the increased viscosity of the ethylene glycol solution at low temperature. This did not eliminate them completely, but further reduction may be possible using ultrasonic techniques[8].

The generated UV power was much less than had been expected on the basis of the intracavity power of the dye laser expected from reports of single frequency dye lasers working only in the visible. The maximum single mode power was independent of which thick etalon was used and appeared to be the same when the thin etalon was changed from 0.5 nm to 1 mm. It is therefore unlikely that the etalons were causing the laser to operate multimode at relatively low powers. Even when the laser was operated as a fundamental dye laser without the second harmonic crystal the maximum single mode output power in the visible was less than 10 mW. A possible explanation for the poor single mode power is poor optical quality of the dye jet. On observing the spots reflected from the jet surface they appeared to be somewhat distorted. The dye laser spots from the front and back surfaces of the jet were displaced by about 10 cm at a distance of 3 m. This jet wedge of about 30 mrad and poor surface quality is probably sufficient to destroy the single mode efficiency and so limit the maximum single frequency power.

VII.4 Single Frequency Stabilisation

Despite the low single mode efficiency it was decided to assess the laser frequency stabilization of the second harmonic laser. The stabilising system is shown schematically in figure 3. While UV was being generated the visible output from the dye laser was split and directed into a photodiode reference channel and through the degenerate interferometer in a manner similar to that used by Barger, Sorem and Hall[3] as described earlier (VII.2.1). The signals from the reference and transmission channels were fed through a fast differencing amplifier. The resulting error signal was fed into a 3 dB per octave filter and integrator followed by a high voltage amplifier and onto a piezoelectric ceramic on the laser output mirror. The electronics were designed at the National Physical Laboratory and are described in detail in the report Qu 28. The circuit diagrams and description are summarised in appendix A.

The stabilising circuits were rather slow having a unity gain bandwidth of less than 1 kHz. This meant that any fast frequency excursion which moved the laser through the bandpass of the reference cavity (< 10 MHz) would make the stabilization circuits loose control. With this circuit the laser could be stabilized to about 2 MHz for periods in the region of 30 sec before jumping out of lock. This situation could undoubtedly be improved by including fast electronic stabilization as has been done previously in connection with visible lasers. In particular the second harmonic crystal could be used as an electro-optic modulator for very fast stabilization. This shall be considered in more detail later (VII.6). Circuits suitable for accomplishing this are described in appendix A

VII.5 Tuning the Single Frequency Laser

Two tuning arrangements were investigated; one using the piezo-electrically scanned thick etalon, the other using a solid thick etalon that could be tilted.

In the former an applied voltage ramp was used to scan both etalon and cavity, with suitable proportional control to keep the modes in step. The laser could only be scanned over about 100-200 MHz with this system; for scanning ranges larger than this the laser hopped many cavity mode spacings. This was found to be due to interference between the back surface and front surface of one of the etalon plates.

The tilting etalon method of tuning the laser was a little more successful. In this case the ramp voltage passed through a square root circuit before going to the tilting galvanometer, the control of the cavity mode tuner being as before. A zero adjust served to centre the etalon along the beam axis perpendicular to the plane of the tilt. In order that the laser cavity length and etalon gang accurately it is necessary to centre the etalon to within at least one cavity mode spacing. This could be done by tilting the etalon using the zero control. As the etalon goes through the zero position the frequency goes through a minimum. This minimum can be located with sufficient accuracy to locate the zero position.

In order that the scan be linear over a broad tuning range the square root circuit must be more accurate than about 1%. The square root circuit described in appendix A is only 1% accurate at the maximum input voltage of 10V and drops to about 10% for voltages less than 1V. This is clearly insufficient to provide a linear scan. An improved version of the square root circuit was constructed using the ratiometer circuit described in appendix A. The ratiometer was designed for low noise, high stability applications and has the capability of better than 0.2% accuracy. However, this accuracy requires careful setting up and only 3% accuracy was achieved during the course of these experiments. The ratiometer takes two signals A and C and divides them to give $B = A/C$. If the output B is fed to the input C then $B = C$. Therefore the output becomes $B = A^{\frac{1}{2}}$. Since the accuracy of the circuit is degraded at small inputs a ramp voltage of up to 10 V was fed to the A input and the output was attenuated before going to the drive amplifier. Using this circuit the dye laser could only be scanned over the region of about 500 MHz before hopping to the next cavity mode. The mode hopping in this case was much more controlled than in the piezoelectrically scanned etalon case, indicating that the scanning was only slightly out of step. The limited scanning range in this case is due to the nonlinearity in the square root electronics. This can only be overcome by careful adjustment.

Although tuning the dye laser met with very limited success, it did illustrate the tolerance required on the electronics and optical quality of the components. Once these difficulties have been overcome a scan of about 3 GHz should be possible.

The single frequency experiments have shown that the problems associated with a second harmonic dye laser are no different from those of a fundamental dye laser. The single frequency problems of the fundamental dye laser will have to be eliminated before the successful operation of a UV dye laser is possible.

VII.6 Proposed Improvements

There are some fairly obvious improvements which can be made to the existing single frequency system such as an improved jet, better scanning electronics and improved optics. These are changes which must be made before the dye laser will operate in a stable manner. The major improvement which is to be discussedin this section is the fast frequency stabilization of the dye laser. The novel feature is that the second harmonic crystal could be used as fast electro-optic modulator for frequency stabilization.

For maximum second harmonic generation the ADA crystal is orientated with the beam propagation direction at 90° to the z-axis and the x- and y-axes at 45° to the beam polarization. If an electric field is applied along the z-axis this is just the arrangement for a transverse electro-optic modulator. For this orientation the extraordinary refractive index is unchanged by application of a field but the ordinary ray refractive index changes by[9]

$$\Delta n = r_{63}\, n_o^{\,3}\, V/2t$$

where V is the voltage applied across the crystal of thickness t, n_o is the ordinary refractive index and r_{63} is the electro-optic constant of ADA. If the effective cavity length changes by $\lambda/2$ the laser frequency will be shifted by a cavity mode separation. The applied voltage required for a $\lambda/2$ length change is thus

$$V_{\frac{1}{2}} = \lambda t / r_{63} \, n_o^3 \, \ell$$

where ℓ is the crystal length. For an ADA crystal of 5 mm thickness and 15 mm in length the halfwave voltage at 600 nm is 6 kV. For a laser of cavity length 1m this corresponds to a frequency shift of 150 MHz. Typical fast frequency excursions correspond to frequency shifts in the region of 10 MHz. A stabilizing voltage of up to ± 200 V is therefore required for fast frequency stabilization.

In Chapter V it was shown that the UV second harmonic intensity was reduced by approximately 1% on application of about 700 V. The ± 200 V stabilization voltage should therefore have little effect on the UV intensity since fluctuations of this order already exist in the laser output.

A circuit with a bandwidth in the region of 1 MHz and capable of supplying up to ± 150 V is described in appendix A. The use of this circuit to stabilize the dye laser frequency should reduce the laser linewidth to less than 1 MHz.

A further improvement in the laser would be possible by the use of an intensity stabilizer. In this case a low voltage electro-optic modulator could be placed between the argon pump beam and the dye laser. By monitoring the visible dye laser power and comparing this with a variable reference current an error signal can be obtained. After going through the standard integrator and 3 dB per octave filters this signal can be amplified and applied to the electro-optic crystal. The applied voltage will then rotate the polarization of the pump beam. This change in polarization is transferred to an intensity change by going through an analyser. The change in pump intensity will therefore maintain the dye laser output power at a constant value.

A suitable modulator is a low voltage ADP modulator. Typically the half-wave voltage of these crystals is 250 V. A high voltage, high frequency circuit is therefore required once more.

A large bandwidth circuit for accomplishing this is given in appendix A. In this circuit the fast and slow signals are applied to opposite sides of the modulator. The bandwidth of the system is greater than 1 MHz and the voltage swing is ± 150 V. The use of this stabilizer should reduce intensity fluctuations to less than 1 part in 10^3.

References

1. W Hartig and H Walther, Appl Phys 1, 171 (1973)
2. F Y Wu, R E Grove and S Ezekiel, Appl Phys Lett 25, 73 (1974)
3. R L Barger, M S Sorem and J L Hall, Appl Phys Lett, 22, 573 (1973)
4. A J Wallard, J Phys E 6, 793 (1973)
5. R L Barger and J L Hall, Appl Phys Lett 22, 196 (1973)
6. R L Barger, J B West and T C English, Appl Phys Lett 27, 31 (1975)
7. H Gerhardt and A Timmermann, Opt Comm 21, 343 (1977)
8. J L Hall and S A Lee, Tunable Lasers and Applications, A Mooradian and T Jaeger (Eds), Springer-Verlag, Berlin (1976)
9. A Yariv, Introduction to Optical Electronics, Holt, Rinehart and Winston, New York (1971)

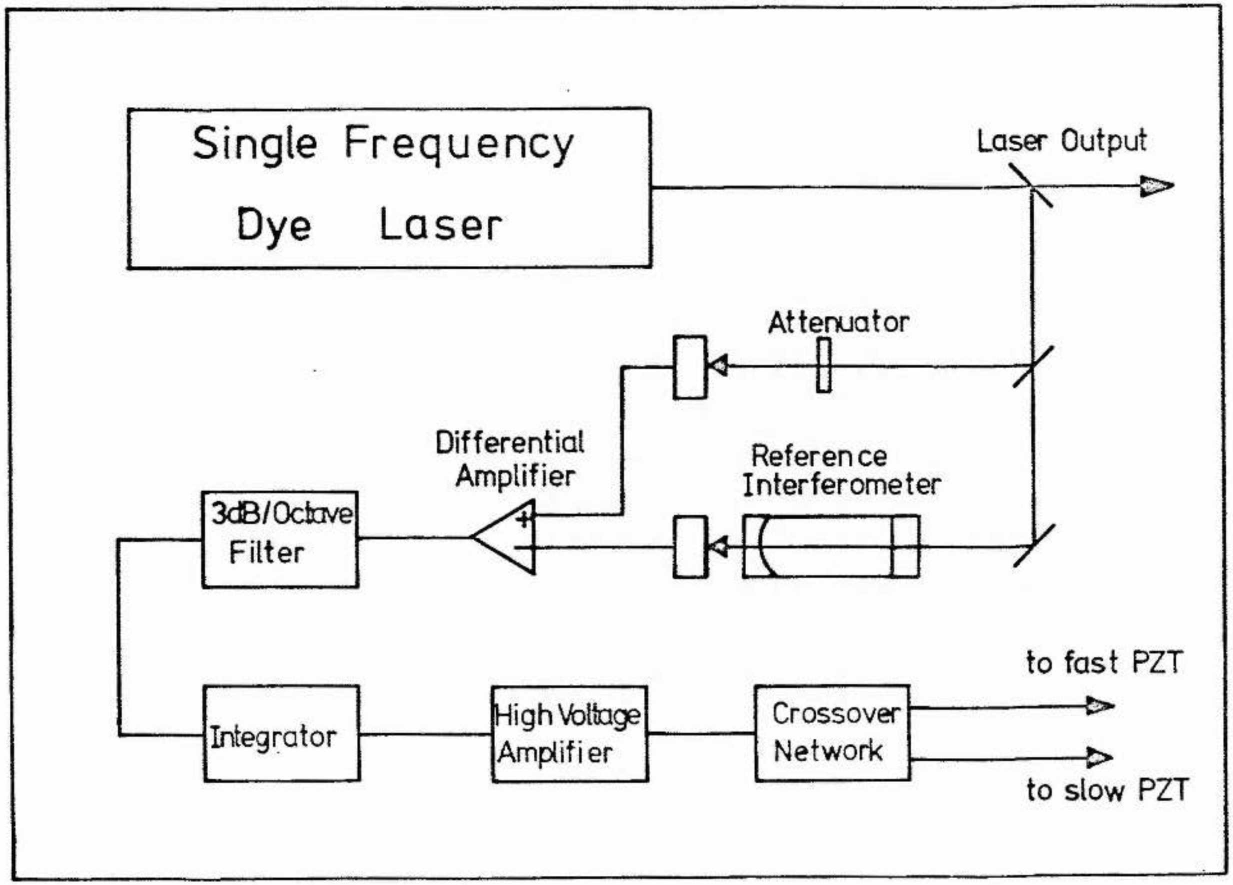

Figure 1. A typical laser frequency stabilizing arrangement.

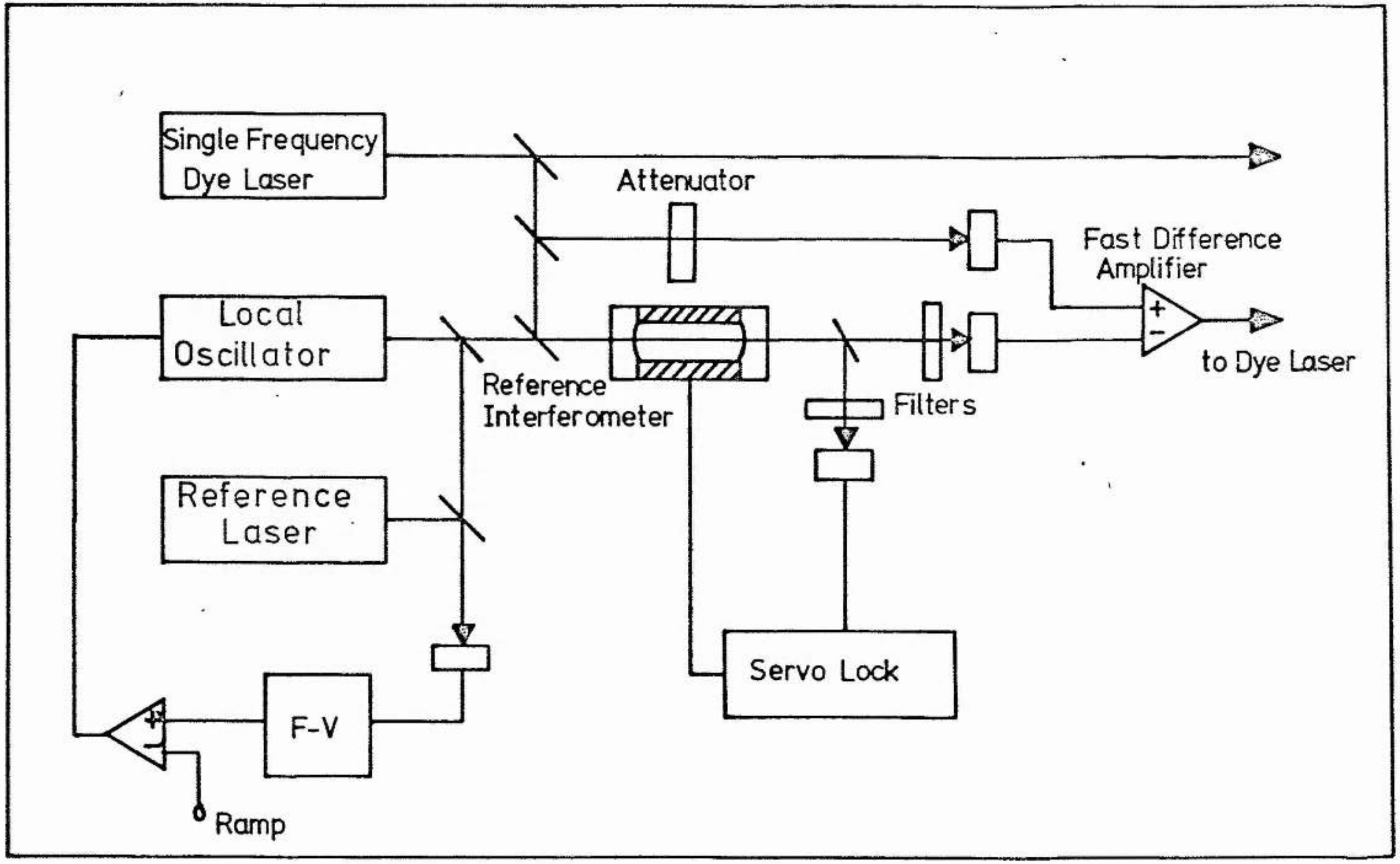

Figure 2. Schematic of typical frequency off-set locked dye laser.

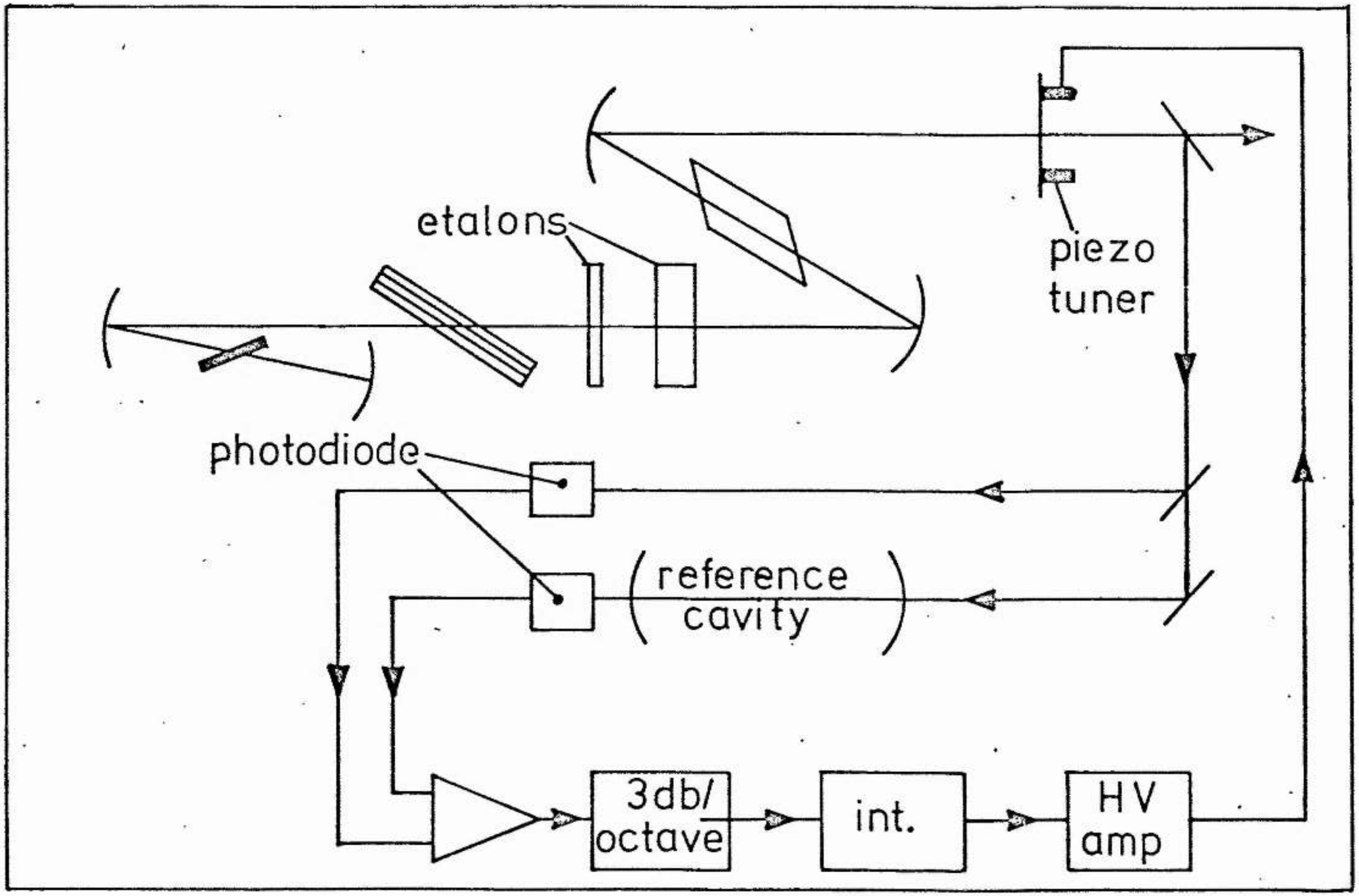

Figure 3. Experimental second harmonic single frequency dye laser stabilized on reference cavity.

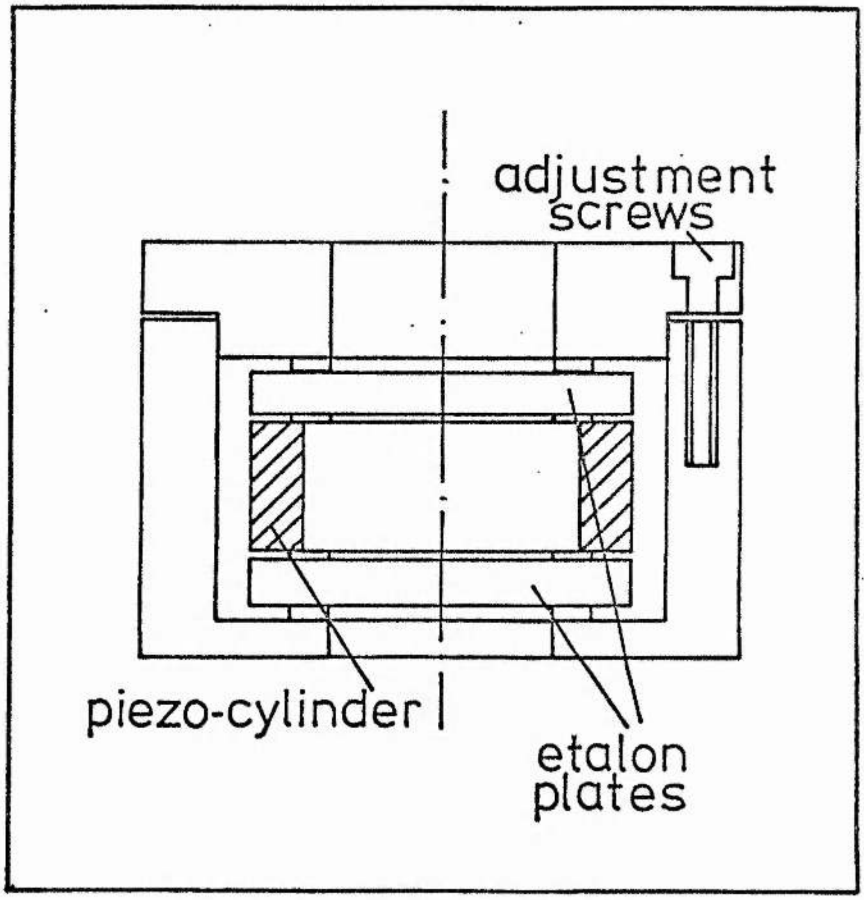

Figure 4. Diagram of a piezoelectrically scanned thick etalon. Drawn approximately to twice the actual size.

Appendix A

SOME SPECIALISED ELECTRONIC CIRCUITS

Abstract

In this appendix some of the specialised electronics which have been extensively used throughout the course of this work are described and briefly discussed. Only the information required for the use of the circuits is given.

Contents

A.1 A 3 Db per Octave Filter and Integrator

This circuit was designed at NPL and details are given in the NPL report Qu 28.

A 3 dB per octave filter and integrator are at the heart of all the stabilizing circuits used in this work. This combination is used since the combined frequency response of 9 dB per octave gain is the maximum roll-off which can be allowed without introducing phase shifts of 180° or more. Although more recent NPL circuits contain double integrators giving a roll-off of 12 dB per octave, they only work if the corner frequency of the first integrator is much less than the unity gain point.

The circuit diagram of the 3 dB per octave filter and integrator are shown in figure 1. Operational amplifiers with dual FET inputs are used for both stages to minimise dc drifts due to changes in input bias currents and voltages. These drifts are of particular importance since they directly affect the stability of the servo system. The filter is provided with a switchable, parallel feedback loop so that when the loop is connected the filter has a flat frequency response of gain 0.5. This greatly reduces the low frequency response of the servo system and allows a loose loop to be established before the high gain filter is switched in. Without two stage locking a slight zero error signal would cause large transient voltages to be developed when the loop is closed. These surges could cause an overshoot in the servo system and prevent locking taking place.

A variable gain control is provided in the servo system by switching the value of input resistance to the integrator from 330Ω to 10 MΩ in roughly equal steps. A 10 kΩ series resistor is included in the output of the integrator to protect the amplifier in the event of an accidental short circuit of the output.

The output voltage from the integrator is monitored on a panel meter to ensure that the saturation of the amplifier output can be easily recognised.

The link G-H is provided to compensate for any phase shifts of component which come before the 3 dB octave filter. In most cases this was just shorted out.

The servo system incorporates a search mode which allows the integrator output to be scanned and set to the required value prior to closing the lock loop. This is accomplished by switching a variable current source to the integrator input while a 470 kΩ feedback resistor is switched in parallel with the 2 μF capacitor. The integrator is then used as an inverting amplifier but the capacitance is left in circuit so that it is charged to the appropriate potential before the lock switch is closed. A zeroing potentiometer is provided to adjust the integrator output while in the search mode.

Because of the very high low frequency gain of the servo system the dc off-sets on the integrator and 3 dB per octave filter must be carefully adjusted. This is done by shorting the input to the filter and adjusting the offset of the filter and then the integrator. Slight adjustments to the off-sets have usually to be made while the system is in operation. This is most conveniently done by adjusting the off-set of the ladder filter at a high gain setting until the integrator output remains steady.

A.2 High Voltage Amplifier

In cases when the integrator output has to be interfaced with a piezoelectric ceramic a high voltage output is required. An amplifier with a unity gain frequency response of up to 1 kHz and maximum output voltage of 900 V is shown in figure 2.

A 1 kV power supply with a maximum current capability of 1 mA is required. The circuit has been designed so that no more than 300 V appears across any transistor or resistor. The signal input is through R_2 which converts the voltage output of the integrator into a current signal. The output voltage as a function in input current is shown in figure 3. The capacitor C_2 across R_2 is used for bandwidth compensation to correct for the loss of high frequency response in the piezoelectric crystal when its impedance approaches the 200 kΩ output impedance of the amplifier. A bias current of −50 μA is provided through R_3 to bring the output to mid-range for zero input through R_2.

A.3 Fast Difference Amplifier

When comparing the laser intensity with the transmission fringe of a reference cavity a fast differencing amplifier is required to give a zero error signal to feed into the laser stabilizing servo system. An amplifier with a bandwidth of 15 MHz is shown in figure 4.

The reference and transmission fringe intensity are monitored on two reverse biased silicon photodiodes connected back-to-back. The difference in photo current is fed directly to an Analogue Devices AD 50J FET input operational amplifier. There is provision for dc off-set and frequency trim in the amplifier feedback loop.

A.4 Fast Laser Frequency Stabilizer

This circuit is based on that designed and developed by J L Hall of the National Bureau of Standards, Boulder, Colorado. It is used in the very fast frequency stabilization of dye lasers. A circuit diagram is shown in figure 5.

The input consists of a variable gain inverting amplifier, the output of which is fed to a 3 dB per octave ladder filter. The output from the ladder filter is then split to provide a fast and slow signal. The fast signal is provided by applying the output from the ladder filter to the non-invert input to a fast high voltage Datel AM 302B amplifier. This operational amplifier provides an output of up to ± 150 V at frequencies up to a few MHz. The output is limited by a voltage clamp. The fast output signal can then be applied either to a fast piezoceramic or to an electro-optic modulator.

The output of the ladder filter is also applied to a variable gain non-inverting amplifier. A slow signal is provided by applying this output to an integrator. The integrator output can then be applied to a high voltage dc amplifier of the type discussed in A.2 and then to a piezoceramic for slow stabilization.

The circuit incorporates an automatic lock facility. A small dc voltage applied to the non-invert input of the integrator allows the integrator output to be scanned in a search mode. When the output voltage from the first amplifier falls to less than a preset value (1V in this case) a fast voltage comparitor is used to throw two MOS switches. During the seach mode the MOS switch in the feedback lock of the non-inverting amplifier is closed and the MOS switch at the input to the integrator is opened. This effectively decouples the integrator while its output is being scanned. When zero error voltage at the input drops sufficiently so that the input voltage to the comparitor is less than 1 V the MOS switches are thrown; the non-intraverting amplifier and the integrator are brought back into circuit and the feedback loop is closed. An LED (not shown in the circuit diagram) indicates whether the circuit is locked.

A.5 Intensity Stabilizer

In this circuit the intensity of the laser output is monitored on a reverse biased silicon photodiode and compared with a constant current source. The resulting error signal can then be fed to any suitable servo system such as those described in sections A.1 and A.4.

A circuit diagram is shown in figure 6. A variable constant current source is provided by applying a FET to the feedback loop of an LM301 operational amplifier. This current is compared with that of a reverse bias silicon photodiode and amplified by a fast difference amplifier used as a current to voltage convertor. The resulting error voltage is then split into two components. The fast component is amplified and applied direct to the electro-optic modulator. The slow signal is passed through a 3 dB per octave ladder filter, amplified, integrated and fed to the electro-optic modulator. The fast and slow signals are applied to opposite sides of the modulator.

A.6 Ratiometer

The ratiometer is a device which has three inputs, A, B and C. The output is equal to $(A-B)/|C|$ and when A and B are each independantly shortened $A/|C|$ and $-B/|C|$ are the outputs. The ratiometer is particularly useful for monitoring a signal A, say and normalising it to some other parameter applied to C.

The circuit diagram is shown in figure 7. The inputs at A, B and C are buffered. The C buffer stage is then connected to a sense amplifier the output of which controls two FETs. These are then used to give inverting or voltage-follower operation to the next stage depending on whether the C input is positive or negative.

The input to the ratiometric circuit requires an ac voltage proportional to A-B. This is obtained by chopping the A and B inputs with parallel/series FETs. The switching is obtained from a multivibrator which runs at about 400 Hz. The chopping on A and B is an antiphase so that the required difference A-B is obtained.

This is then fed to the ratiometric part of the circuit which is just an ac amplifier with an input proportional to A-B and with gain inversely proportional to C.

The output from the ratiometric circuit is a chopped waveform with amplitude proportional to the desired ratio. The output consists of a full-wave demodulator which produced the final dc output. Smoothing of the residual chop components is provided by a large capacitor in the feedback loop of the laser operational amplifier.

The inputs A and B can be between ± 10 V and C between 50 mV and 10 V. The linearity of the circuit should be better than 0.02% under these circumstances. The output has a maximum of ± 10 V which represents 100%. When not in use A or B should be shorted. The time constant of the output state is 100 ms.

A.7 Birefringent Filter Positioner

This circuit controls the orientation of the birefringent tuning element by sensing the position of a potentiometer linked to the filter. The circuit diagram is shown in figure 8. The position of the filter is linked to the setting of VR1. The voltage across the potentiometer is put through a buffer stage. This voltage is then compared with the voltage derived from either a ten turn potentiometer incorporated in the circuit or an external signal of between 0V and 3V. The output from the high gain difference amplifier is fed through the drive circuit for a dc motor. The motor which drives the birefringent filter was a Maxon dc motor supplied by Trident Engineering Ltd. A stabilized 3V supply used for biasing the positioning potentiometers is also shown in figure 8 .

A.8 Temperature Controller

The temperature controller was supplied by Electro Optic Developments and was used to control the temperature of both the ADA and ADP crystals. The temperature could be controlled to within 0.01°C over the range from room temperature to 90°C. The detailed circuit of the controller can be found in the manufacturers handbook but is fairly simple. The controller was modified so that the temperature of the crystals could be scanned by an input ramp voltage.

A schematic diagram of the original control circuit is shown in figure 9. The wiper of RV1 is the set temperature control and was a ten turn digital read out potentiometer. The input voltage to IC1 is set between ± 5 V and the output assumes the same value. The thermistor T and the resistor R are mounted on the oven and provide a potential divider circuit. The voltage from this portion of the circuit is proportional to the temperature of the oven. The outputs from IC1 and IC2 are summed and the resulting error signal is amplified by two operational amplifiers and two power transistors which supply the current to the heater.

The modified circuit is applied between points A and B and is shown in figure 9. This circuit simply allows a voltage to be summed with the voltage across RV1 and so change the crystal temperature. An input voltage of up to 10V is first reduced by a potential divider. A ten position switch allows the sensitivity to be changed from $1^{o}C\ V^{-1}$ to $10^{o}C\ V^{-1}$ in equal stages. The attenuated voltage is put through a buffer stage before being summed with the voltage at RV1. The resulting voltage is amplified and fed to the input of the original balancing circuit.

A.9 Galvanometer Driver

In applications when a galvanometer is used to tilt an etalon in the laser cavity it is necessary to take the square root of the input drive voltage to ensure a linear wavelength scan. A simple circuit capable of taking the square root of an input voltage of up to +150 V is shown in figure 10. The sensitivity of the circuit can be changed by altering the voltage divider at the input. A ganged switch bypasses the square root circuit for direct access to the galvanometer driver.

The power amplifier which drives the galvanometer is shown in figure 11. A current capability of greater than 1A per rail is required from the supply line. A 50 kΩ potentiometer is included to provide damping. This is adjusted to maximise the frequency response of the galvanometer for a given load.

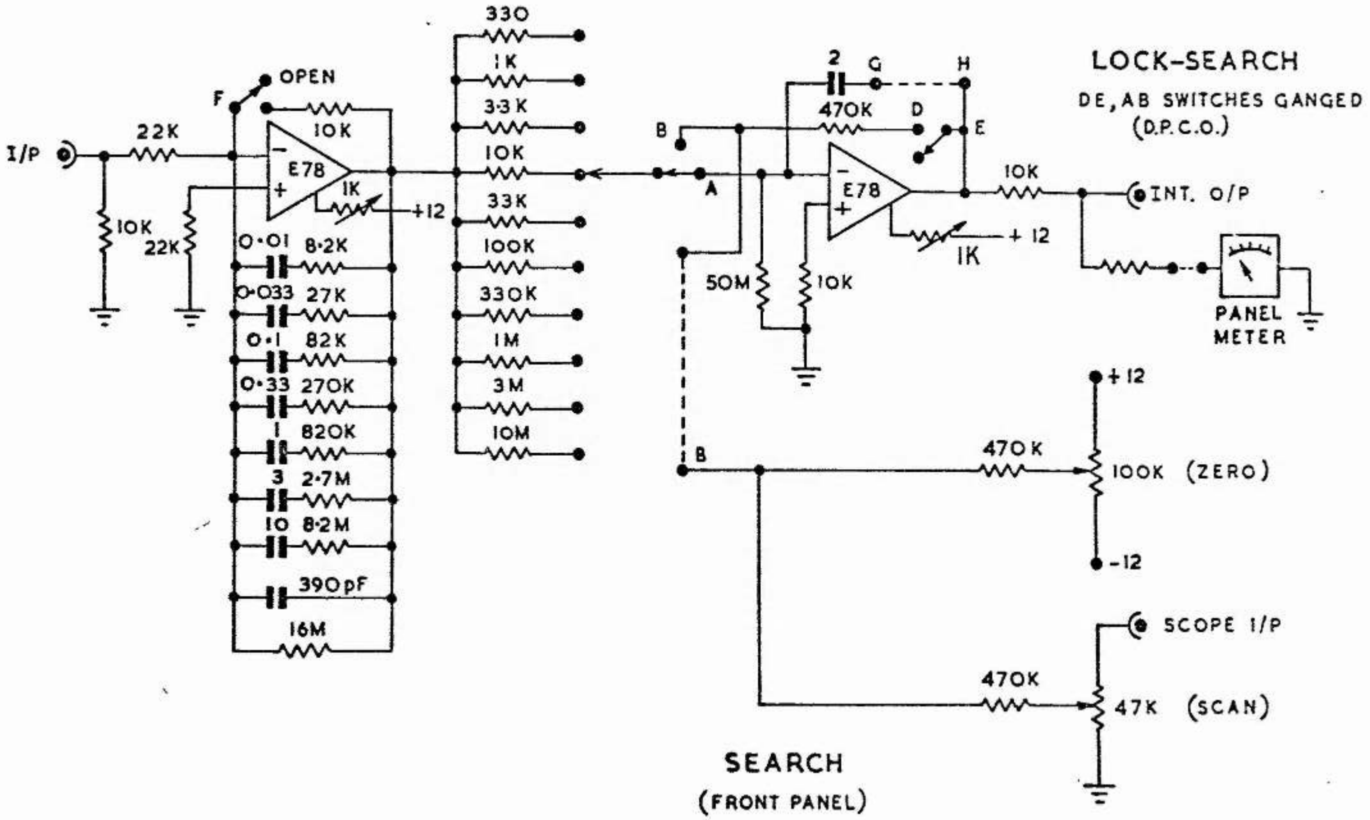

Figure 1. Circuit diagram of 3 dB per octave ladder filter and integrator.

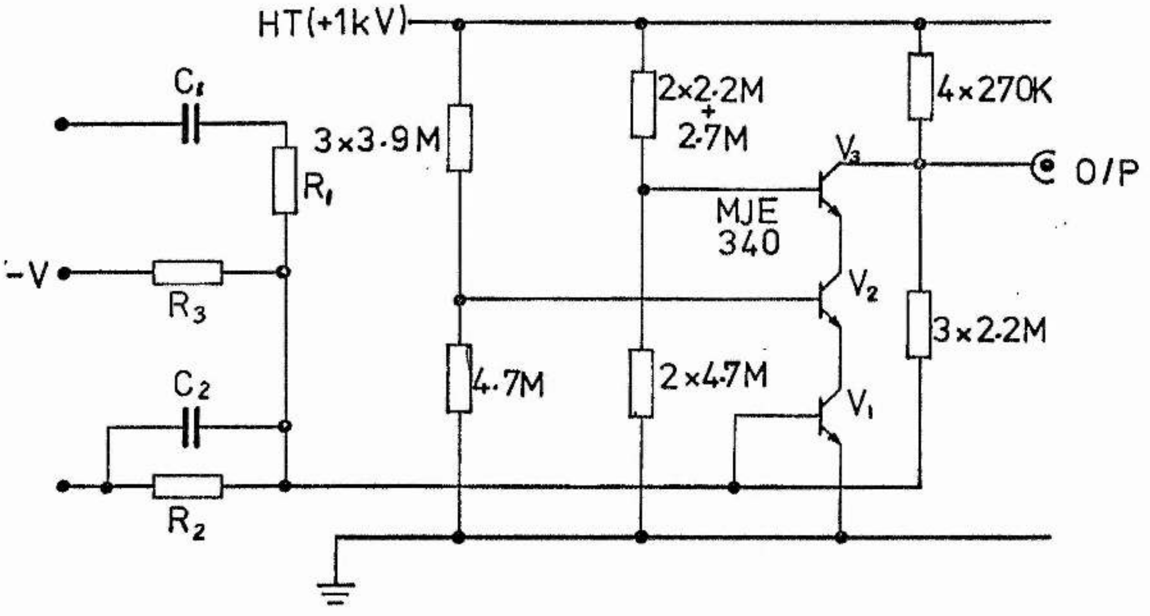

Figure 2. Circuit diagram of high voltage amplifier.

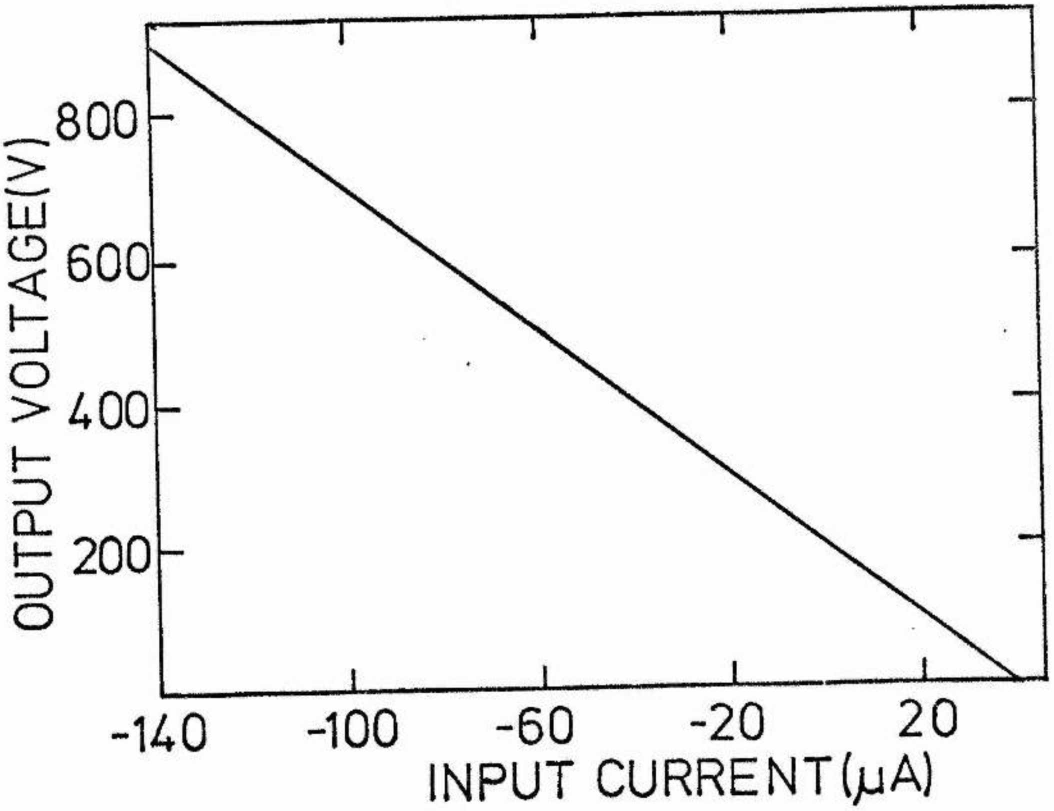

Figure 3. Voltage output of high voltage amplifier as a function of input current.

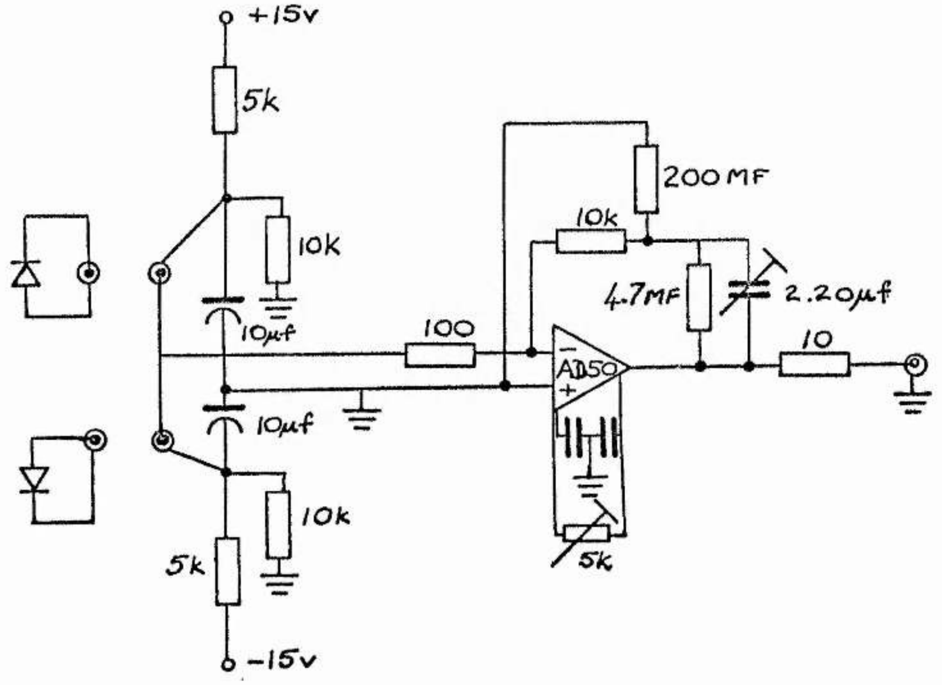

Figure 4. Circuit diagram of fast difference amplifier.

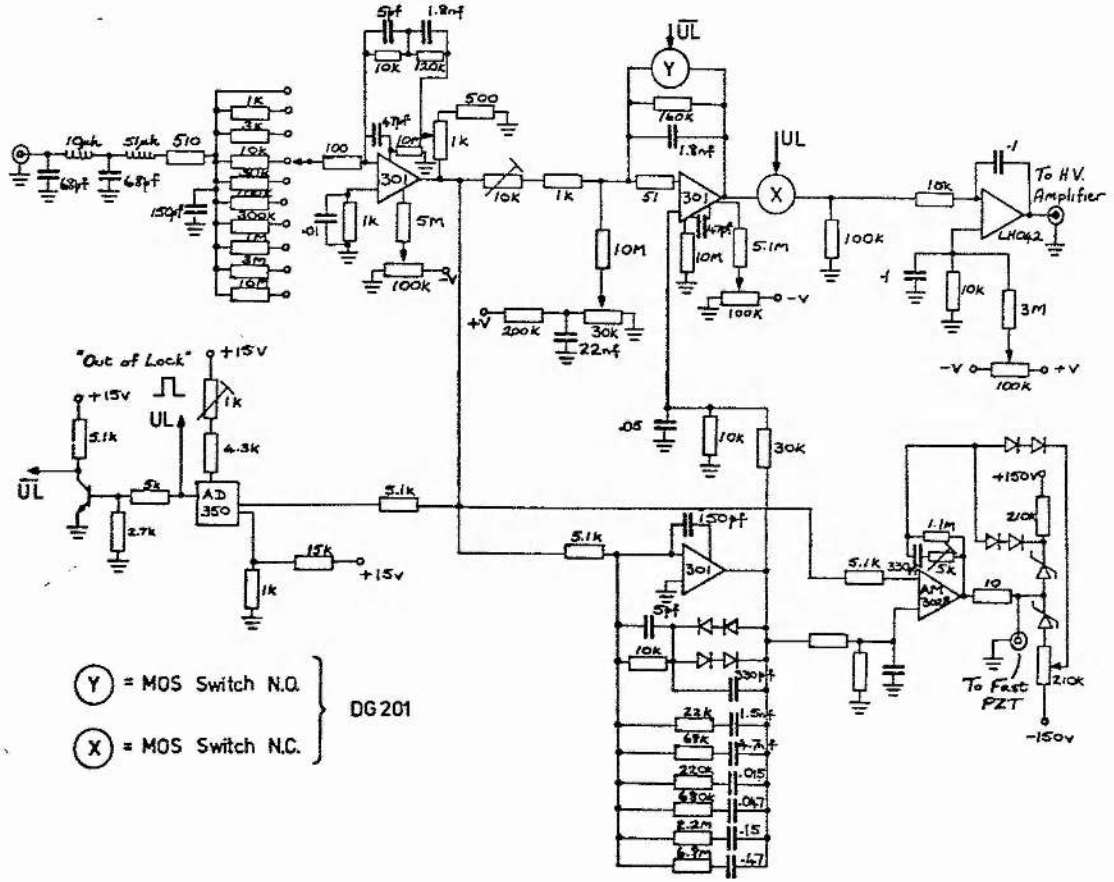

Figure 5. Circuit diagram of fast laser frequency stabilizer.

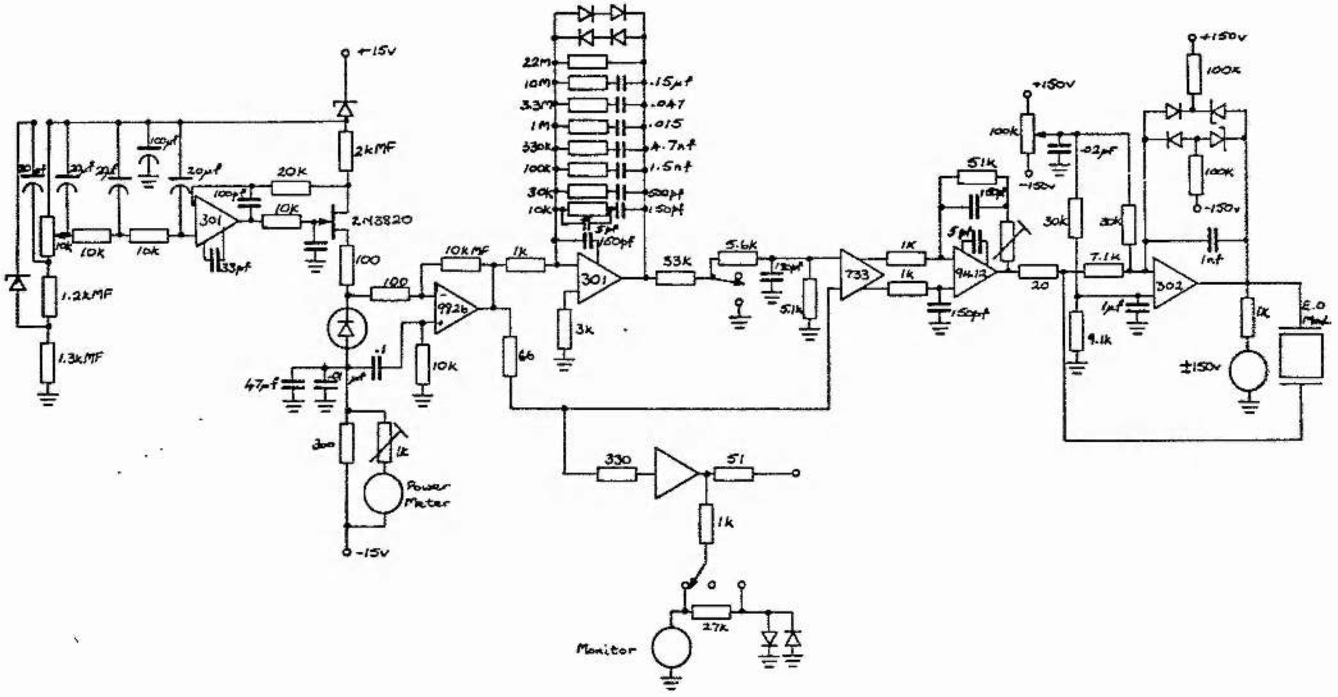

Figure 6. Circuit diagram of fast laser intensity stabilizer.

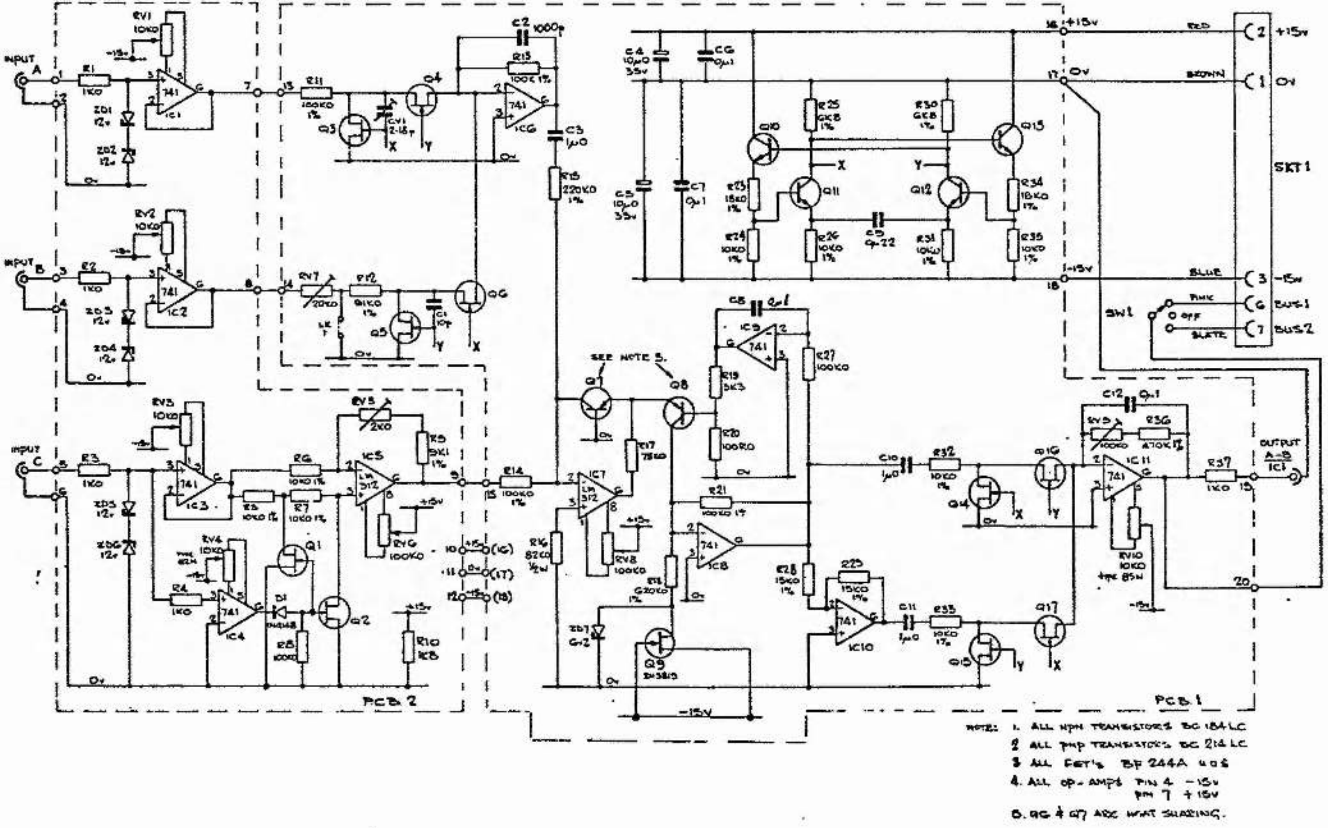

Figure 7. Circuit diagram of the ratiometer.

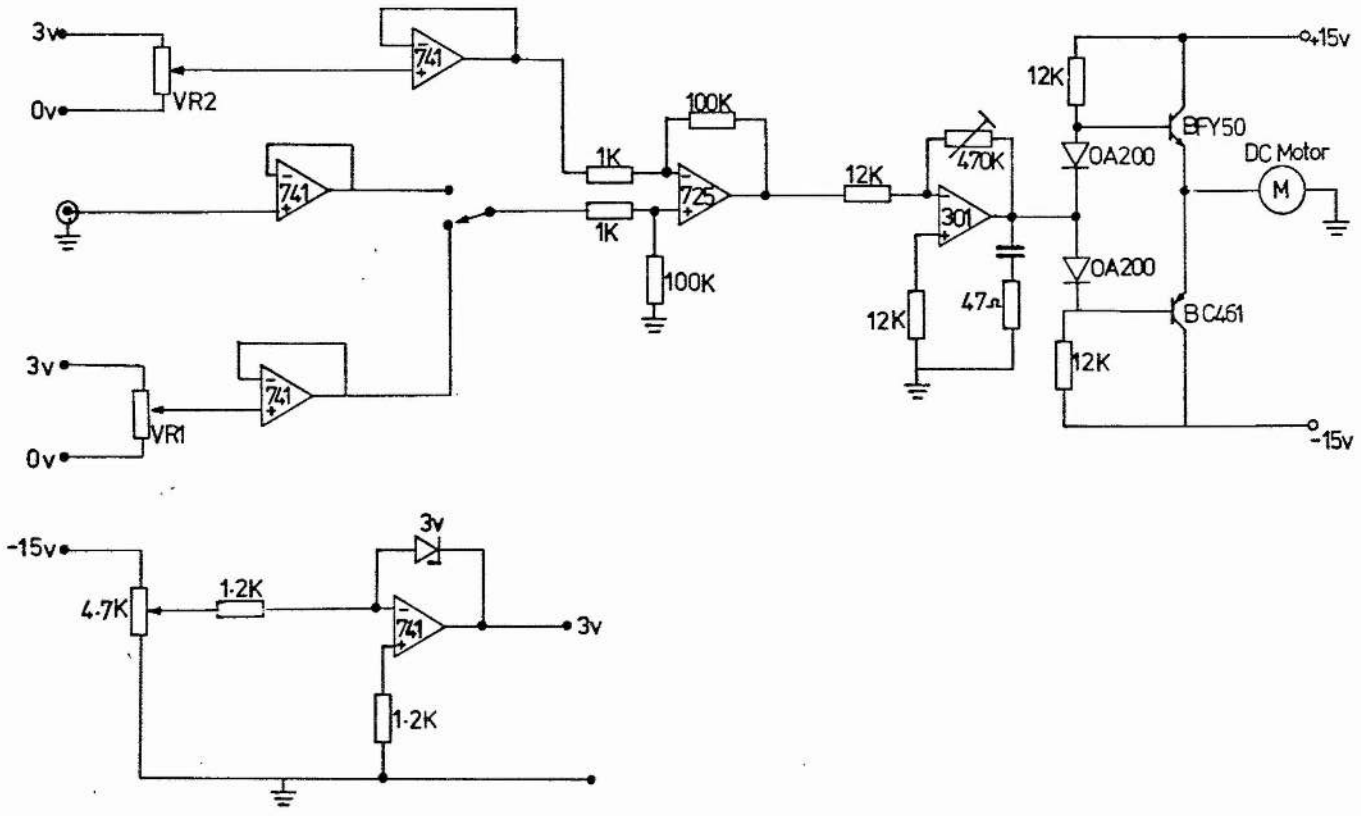

Figure 8. Circuit diagram of birefringent filter positioner.

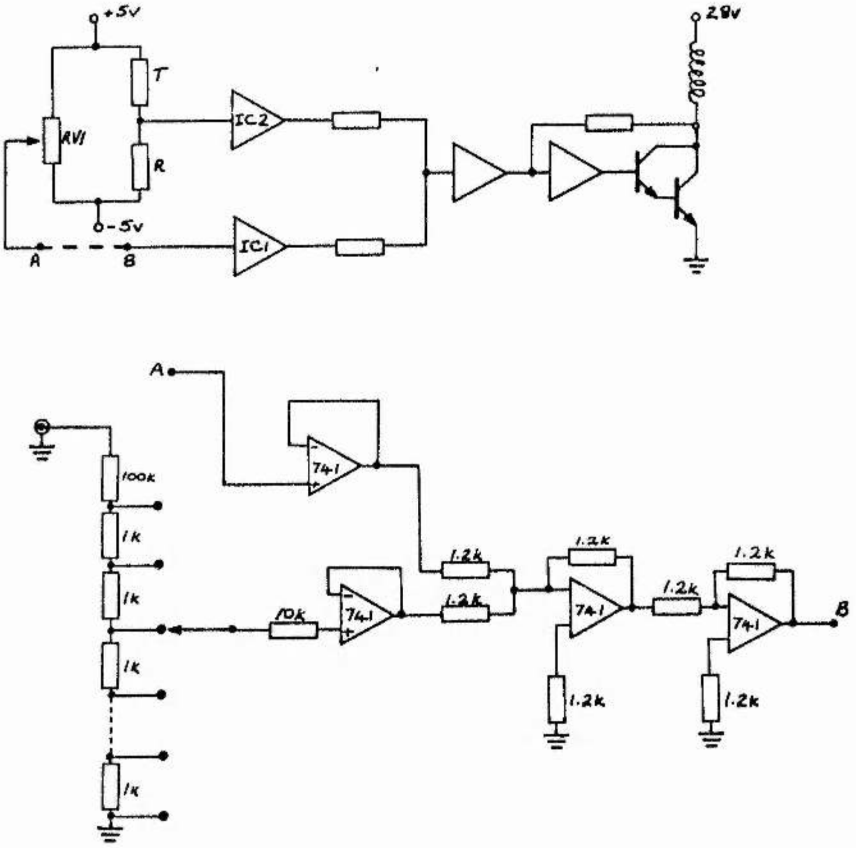

Figure 9. Simplified circuit diagram of the temperature controller. The modified circuit is also shown and is inserted between points A and B.

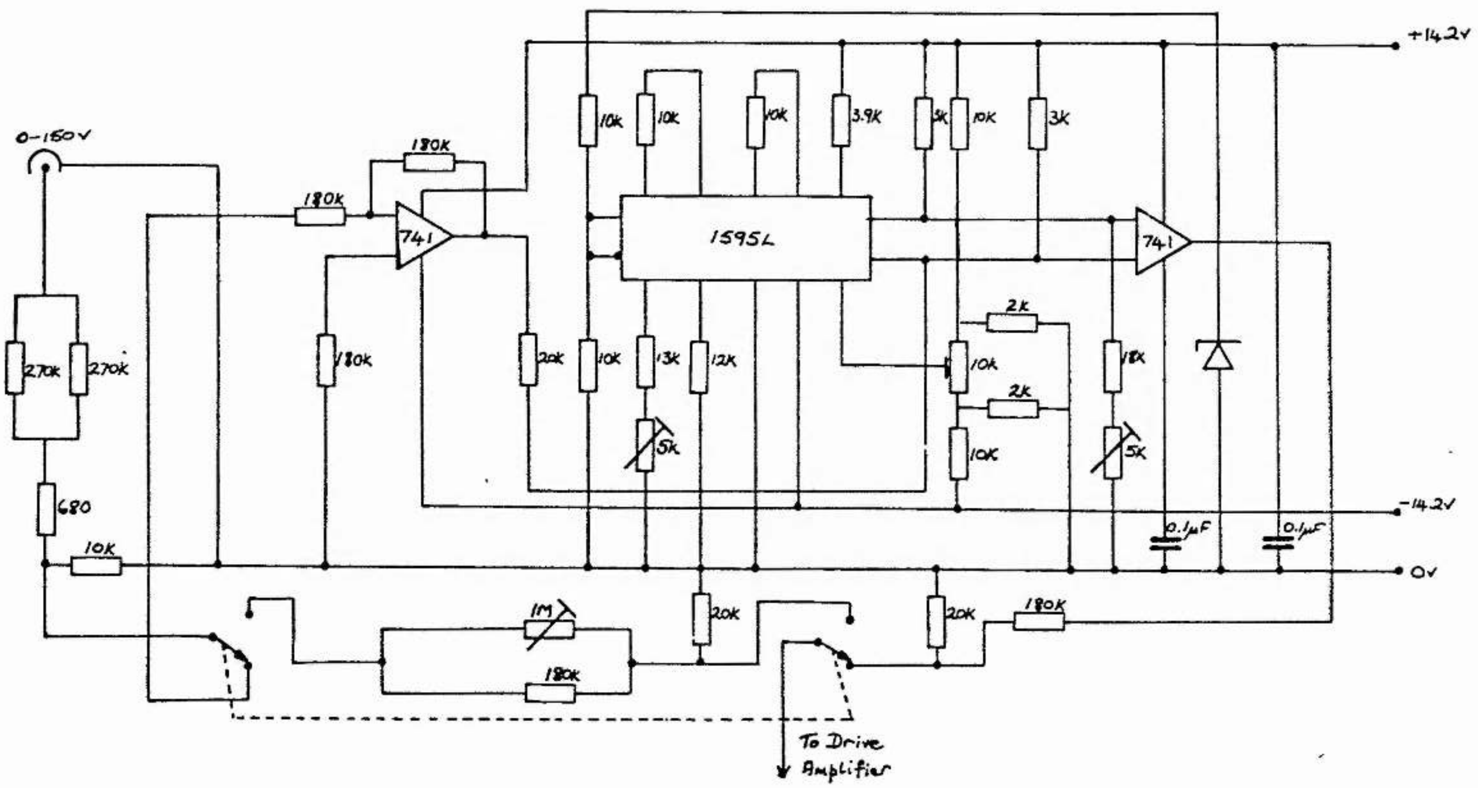

Figure 10. Circuit diagram of the square root amplifier.

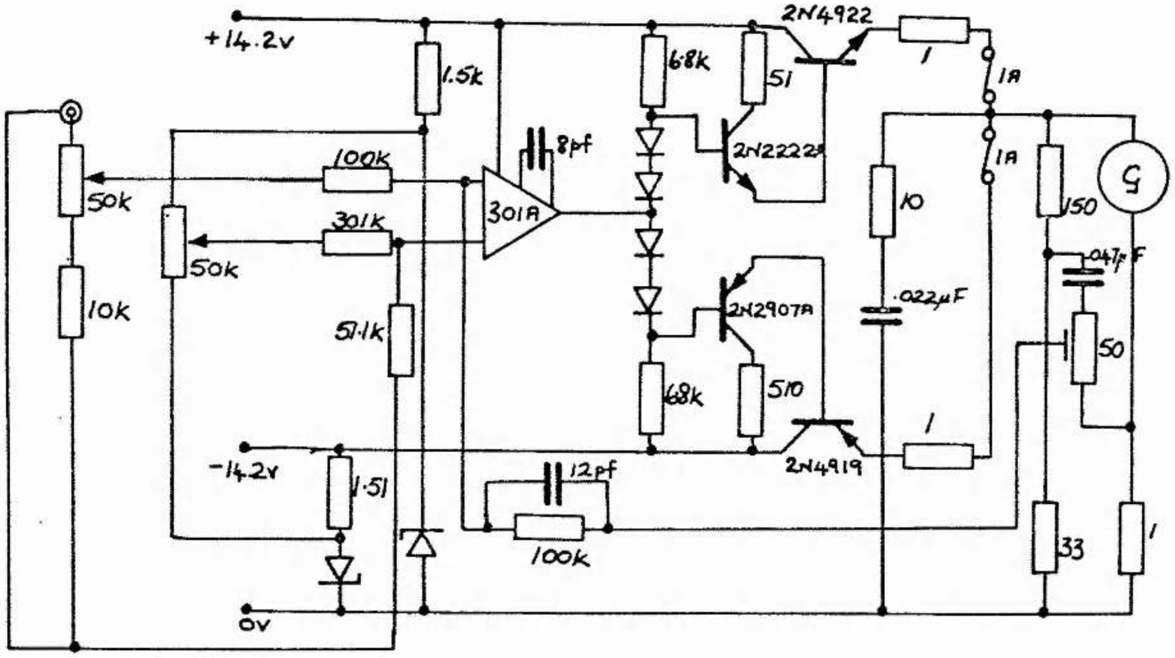

Figure 11. Circuit diagram for the drive amplifier for the torsion galvanometers.

Appendix B

AN ATOMIC WAVELENGTH REFERENCE

In this appendix a device for obtaining optical wavelength references which is simple to use and compact is described. The method is based on the perturbation of a hollow cathode discharge when the dye laser is tuned to an atomic resonance of the vapour contained in the discharge.

In spectroscopic investigations with a tunable dye laser it is important to obtain a frequency reference which is accurate, compact and simple to use. It is also highly desirable that the reference source be fairly dense in reference points so that interpolation can be readily performed. A compact device for use as a frequency standard for most of the visible region of the spectrum is described.

The device is based on a commercial neon hollow cathode lamp of the type used in atomic absorption spectrophotometers. The method relies on the fact that when a laser is directed into the hollow cathode discharge and tuned to an atomic resonance the increased excitation gives rise to an enhancement of the ionization and hence the discharge current. By suitable phase sensitive detection this change in current can be easily monitored.

Most hollow cathode lamps for atomic absorption are filled with neon. Since the emission lines of neon have been used as secondary frequency standards their frequencies are accurately known. Furthermore neon is very dense in atomic lines throughout the visible region and is therefore ideal as a frequency reference.

A schematic diagram of a typical experimental set-up is shown in figure 1. A portion of the output from a continuous-wave dye laser pumped by an argon ion laser is directed into the centre of a hollow-cathode lamp. The laser beam is modulated by a chopper and a discharge current at the modulation frequency is observed by phase sensitive detection. In the course of experiments we have used several discharge lamps and some brands tend to oscillate and mask any signal. For most of the work a Cathodeon hollow cathode lamp has been used. The dye laser was a Coherent Radiation 490 dye laser of linewidth approximately 0.05 nm and was scanned from 570-630 nm. The signal for most of the neon lines was found to be well above the noise level for an incident laser power as small as a few milliwatts. The minimum power required to observe a signal was reduced by about two orders of magnitude when the laser linewidth was reduced to approxmately 3GHz by the inclusion of a 0.5 mm solid fused silica etalon with 30% reflectivity coatings. A typical spectrum of a neon hollow cathode lamp is shown in figure 2. The wavelength of the neon lines are indicated in figure 2.

The discharge current was approximately 5 mA and the signal was measured across a 20 kΩ ballast resistor. A capacitor was used to decouple the d.c. level. The integration time of the phase sensitive detector was 10 msec.

Also shown, in table 1, is a list of NeI lines which it is possible to observe over the range of a Rhodamine 6G dye laser. The data for this table has been extracted from G R Harrison, Wavelength Tables, Wiley, New York.

This method of obtaining an accurate frequency reference has proven to be very easy in use and inexpensive to construct. With the increasing use of lasers for performing atomic absorption spectrophotometry the hollow cathode lamp of the appropriate element could be used to monitor the wavelength of the laser and could further be used to lock the laser frequency to the peak of the atomic absorption.

Table 1 Wavelength of NeI reference lines observable with a Rhodamine 6G laser.

Wavelength (nm)	Wavelength (nm)
629.3766	594.48342
627.6039	593.4458
627.3018	592.2709
626.64950	591.9037
625.8796	591.8899
624.6734	591.3633
622.5742	590.6429
621.72813	590.2792
621.3878	590.2463
620.5787	590.2097
620.2981	589.8406
618.9076	588.18950
617.5291	587.2828
617.4888	587.2149
617.2821	587.0971
616.35939	586.8417
615.0303	585.24878
614.30623	582.8910
614.2508	582.0155
612.8451	581.6645
611.8027	581.1417
609.61630	580.4449
607.43377	580.4098
606.4552	577.0307
604.6158	576.4418
602.9971	576.4063
600.0951	576.0585
599.1675	574.8299
598.7907	571.9225
597.55340	571.8899
597.4628	571.5399
596.6171	578.9817
596.1626	568.4647
	566.2547
	565.6659
	565.6030
	565.2570

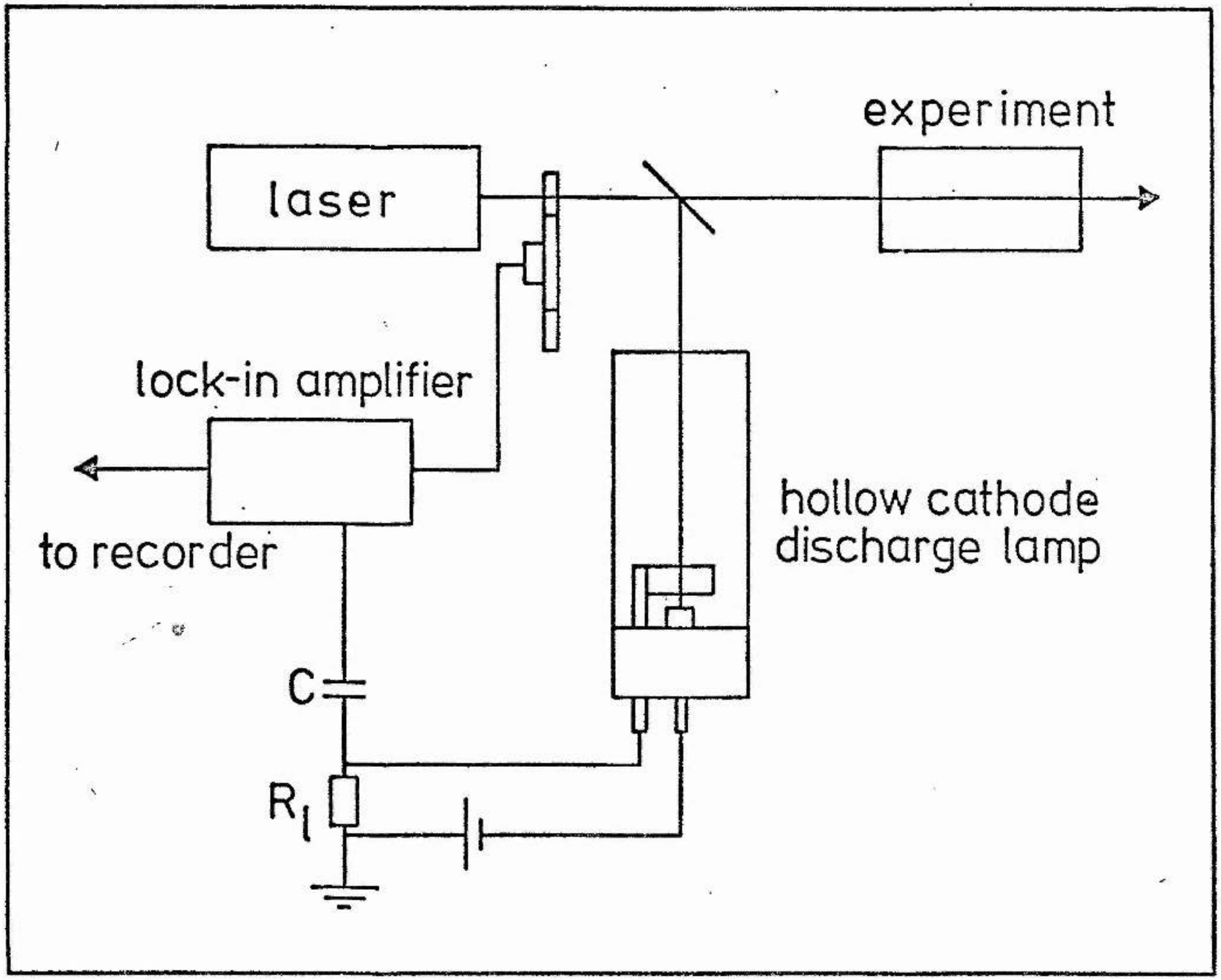

Figure 1. Schematic diagram of the hollow cathode wavelength reference source.

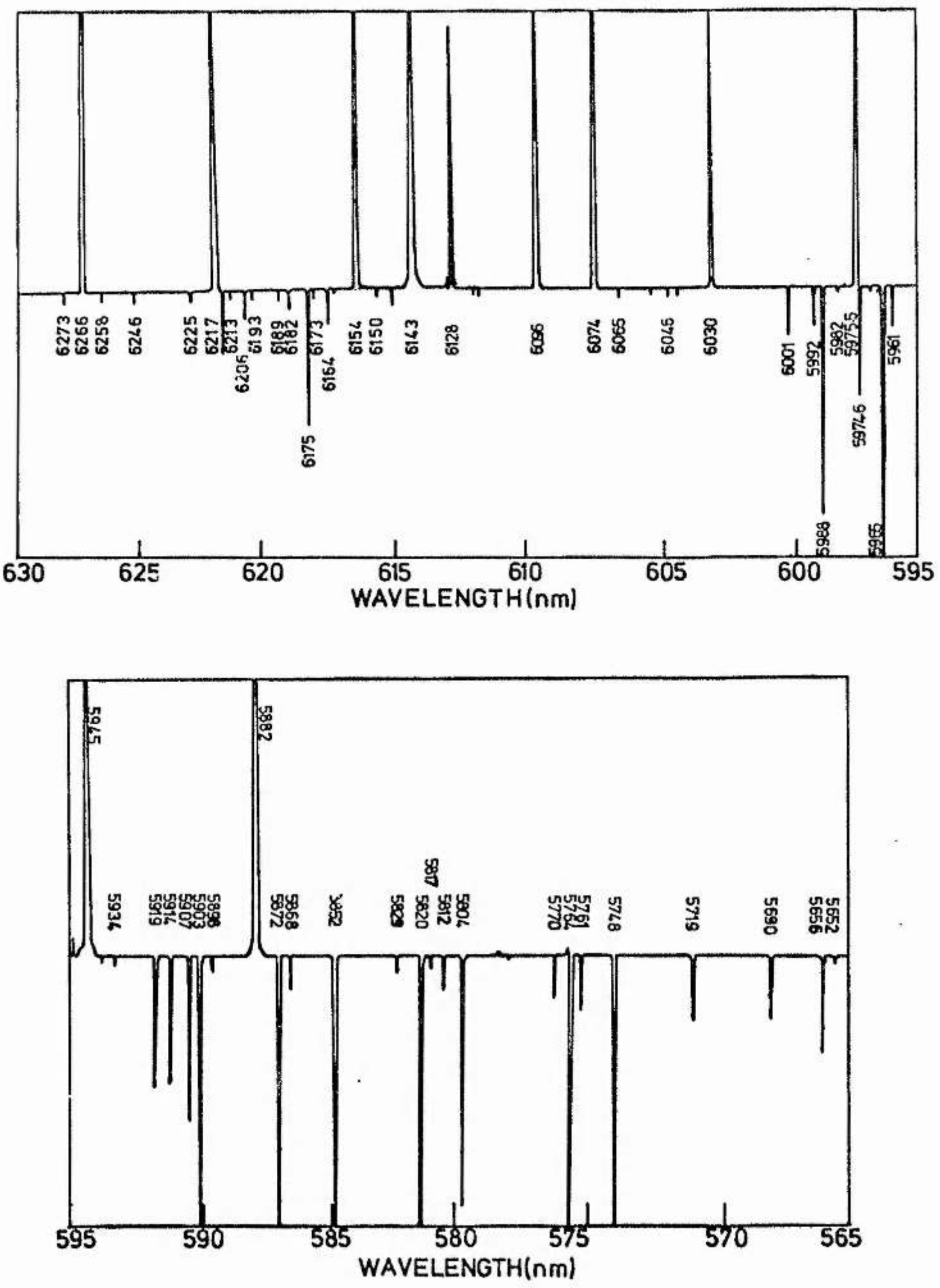

Figure 2. Typical spectra obtained with the perturbation of a hollow-cathode neon lamp by a rhodamine 6G dye laser. The approximate wavelength of the neon lines in Å are also indicated.

Appendix C

LASER FREQUENCY ANALYSERS

C.1 Introduction

The use of spherical mirror interferometers for the frequency analysis of laser radiation has been extensively treated by several authors[1,2,3,4]. In this section we shall review only the results of those analyses where they are particularly relevant to the construction and operation of an interferometer for use in laser mode analysis.

The spherical mirror interferometer is superior to a plane-plane system because of the less severe tolerance on mirror flatness and alignment. This is because a plane-plane system must have a large aperture if the finesse is to be high, in order to avoid diffraction loss. This puts a severe restraint on the flatness of the mirrors since if an interferometer is to have a finesse of E the mirror surfaces must be made flat to at least $\lambda/2E$ over the whole of the aperture and they must also be aligned parallel to this degree of accuracy. In addition, if a narrow bandpass of say 5 MHz is required, for instance to measure the linewidth of a dye laser, then assuming a typical finesse of 50, the free spectral range required is 250 MHz and hence the interferometer length must be 60 cm. In order to avoid excessive diffraction losses and consequent reduction in finesse the mirrors must be flat to $\lambda/100$ over an aperture at least equal to the plate diameter, ie 60 cm! As we shall show the requirements on mirror size and surface quality are severely reduced by use of a spherical system.

Spherical mirror interferometers can be divided into two main categories. The first of these categories is the general spherical system where the mirror radii of curvature and separation can have any desired value. The use of this kind of cavity has been described by Fork et al[2]. This kind of cavity is more useful than a plane-plane system for analysing laser radiation. However it is necessary to match the laser beam to be analysed into the interferometer so that only a single transverse mode of the interferometer is excited. If other transverse modes were excited they would appear as spurious frequencies when analysing the input laser. The mode matching of this kind of interferometer is normally accomplished by use of a suitable lens positioned at a distance from the interferometer which is dependent upon the beam parameters of the radiation to be analysed[2].

The second category of spherical mirror interferometers is the degenerate interferometer. This is a subgroup of the more general interferometers discussed previously. The degenerate interferometers get their name from the fact that groups of the transverse modes of the interferometer have the same oscillation frequency,ie they are frequency degenerate. The best known degenerate interferometer is the confocal interferometer which is formed by two mirrors of equal radii of curvature separated by a distance equal to their common radius of curvature. The degenerate interferometer has the advantages that no mode matching is required, it has good light gathering efficiency and is very easy to use once it has been aligned. The degenerate systems suffer from the disadvantage that the separation of the mirrors is quite critical and as a result the free spectral range is fixed. For all spherical cavities the tolerance on mirror surface quality is greatly reduced since only a small aperture is used. Beam sizes of the order of 0.5 mm are typical in these applications and substrates with surfaces qualities in excess of $\lambda/400$ over this aperture are available. Dielectric mirror coatings with reflectivities in excess of 99.9% present no real problems and the finesse of a spherical mirror interferometer is typically greater than 200 when carefully designed.

C.2 Mode analysis of a spherical mirror interferometer

Consider an optical cavity with spherical mirrors of radii R_1, R_2 and separated by a distance d. The mode pattern which this cavity can sustain are denoted TEM_{mnq} and the frequency associated with each mode is given by[5]

$$\nu_{mnq} = (c/2d)\ \{q + (1/\pi)\ (1 + m + n)\ \cos^{-1} [\,(1 - d/R_1)(1 - d/R_2)\,]^{\frac{1}{2}}\} \qquad (1)$$

Suppose that a monochromatic field of frequency ν_o is incident on this resonator. This field will excite a large number of transverse modes each of which will be resonant when the cavity length satisfies

$$d = (c/2\nu_o)\ \{q + (1/\pi)\ (1 + m + n)\ \cos^{-1} [\,(1 - d/R_1)(1 - d/R_2)\,]^{\frac{1}{2}}\} \qquad (2)$$

In general, therefore, a monochromatic field will be decomposed into a large number of transverse modes each of which will be resonant at a different mirror separation unless mode matching precautions are taken. In the special case of degenerate interferometer the mirror curvatures and separations are chosen to satisfy the equation

$$\cos^{-1} [\,(1 - d/R_1)(1 - d/R_2)\,]^{\frac{1}{2}} = \pi/\ell \qquad (3)$$

where ℓ is an integer. The resonance can be written

$$\nu_o = (c/2\ell d)\ [\,\ell q + 1 + m + n\,] \qquad (4)$$

Since increasing the sum (m + n) by ℓ and decreasing q by one leaves the resonant frequency of the interferometer unchanged, it follows that the interferometer will have ℓ sets of degenerate transverse modes and each of these will be equally separated in frequency.

The best known degenerate interferometer is the confocal interferometer which corresponds to $\ell = 2$. The interferometer's modes can be either even - symmetric corresponding to (m + n) being even, or odd - symmetric corresponding to (m + n) being odd. The even - symmetric resonances fall exactly halfway between the odd-symmetric mode resonances. The free spectral range of a confocal interferometer, when it is illuminated simultaneously in several transverse modes is thus c/4d rather than c/2d.

In general, the free spectral range of an ℓ-fold degenerate interferometer is given by

$$\mathrm{fsr} = c/2\ell d \qquad (5)$$

and the transmittance is

$$I/I_o = [T^2 \sum_{j=1}^{\ell} R^{2(j-1)}/(1 - R^{\ell})^2]\{1 + [4R^{\ell}/(1 - R^{\ell})^2] \sin^2 2\pi\nu\ell d/c\}^{-1} \qquad (6)$$

where T is the transmission of the interferometer mirrors. If we define A to be the sum of absorption and scattering at the mirrors then $(1 - R) = T + A$. If the reflectivity of the mirrors is close to unity the transmittance of the interferometer near to a resonant frequency is given by

$$I/I_o = [\ell(1 + A/T)^2]^{-1}\{1 + [4\pi d/c(1 - R)]^2 (\nu - \nu_o)^2\}^{-1} \qquad (7)$$

The peak transmission on resonance is thus given by

$$I/I_o = [\ell(1 + A/T)^2]^{-1} \qquad (8)$$

This function is plotted in figure 1 for the particular case of a confocal interferometer ($\ell = 2$). Whenever the absorption plus scattering loss becomes comparable to or exceeds the transmission loss at the mirror the net transmission of the interferometer is drastically reduced. It should be noted that very high reflectivities are usually only obtained at the expense of an increased value for (A/T). In applications where high collection efficiency is desirable it may be necessary to make a compromise between finesse and transmission.

The instrumental bandwidth of a degenerate interferometer for R close to unity is given by (7) as

$$\Delta\nu = c(1 - R)/2\pi d \qquad (9)$$

and the resolving power by

$$\nu/\Delta\ \nu = Q = 2\pi d/c(1 - R) \qquad (10)$$

and the finesse by

$$F = \pi/\ell(1 - R) \qquad (11)$$

From the above formulae it can be seen that the instrumental bandwidth and resolving power of a degenerate interferometer are the same as for a general spherical mirror interferometer but that the finesse, free spectral range and peak transmission are reduced by a factor ℓ. The confocal interferometer ($\ell = 2$) has the highest finesse of any degenerate interferometer. (The case of $\ell = 1$ corresponds to a concentric interferometer which cannot adequately be treated in the theory leading to the above equations.)

C.3 Light Gathering Power

One of the major factors in evaluating any spectrometer is its ability to gather light from a source, filter the light and transmit the light to a detector. An important parameter which measures the effective light gathering power of an instrument is known as the étendue and is defined by ΩA where Ω is the solid angle of light collection and A is the area of the entrance pupil of the instrument.

The size of the entrance pupil of the confocal interferometer is usually determined by the spherical aberration of the curved mirrors. Spherical aberration of the mirrors gives rise to a fundamental limit on the amount of mode mismatch that can be tolerated in a mode-degenerate interferometer. The theory of the mode structure of a spherical mirror interferometer is based on the paraxial approximation and large departures from on-axis illumination cannot be adequately treated by this method. The dominant aberration which leads to departures from the theory is spherical aberration.

In a confocal interferometer the path-difference variation caused by spherical aberration for rays entering the interferometer parallel to the axis but displaced from it by a distance ρ can be shown to be

$$\Delta = -\rho^4/d^3. \tag{12}$$

If it is demanded that this path-difference variation be less than the transmission wavelength divided by the finesse the incoming beam must have a radius ρ_s which is less than

$$\rho_s = (d^3\lambda/F)^{\frac{1}{4}}. \tag{13}$$

If the radius of the incoming light is limited to ρ_s the finesse will drop to approximately 70% of the value calculated assuming on-axis illumination[3].

If we assume that the radius of the incoming beam is limited to ρ_s the étendue is given by

$$V_o = [\pi\rho_s{}^2] \; [\pi\rho_s{}^2/r^2] = \pi^2 r\lambda/F \tag{14}$$

It is interesting to compare the étendue of a confocal interferometer with a plane-plane Fabry-Perot interferometer. We define the angle α as the angle which represents the mirror surface figure and alignment accuracy which is required to maintain a finesse F over a plate diameter D. This angle is then given by

$$\alpha = (\lambda/FD) \tag{15}$$

and the étendue of a Fabry-Perot is

$$U_p = \pi D^2 \lambda/4dF = \pi \lambda^3/4dF^2 \alpha \tag{16}$$

where d is the plate separation. The ratio of the étendue of a confocal interferometer to that of a plane Fabry-Perot is given by

$$U_s/U_p = 4rdF^2 \alpha^2/\lambda^2. \tag{17}$$

If we require that the plane Fabry-Perot and the confocal interferometer have the same free spectral range, ie $d = 2r$, we can find a value of r at which the confocal interferometer is superior to the plane Fabry-Perot with regard to étendue. This condition is satisfied when

$$r > (\lambda/\alpha)/2F.$$

If, as an example, a plane Fabry-Perot can be aligned to within $\lambda/100$ per centimetre of its aperture and a finesse of 50 is desired, the étendue of a plane Faby-Perot interferometer is less than that of a confocal interferometer for a mirror spacing of greater than 2 cm. Thus a confocal interferometer should be used when the free spectral range required is less than that for a mirror separation corresponding to 2 cm, if the light gathering efficiency is to be maximised.

C4. Some Practical Confocal Interferometer Designs

As was mentioned in the introduction to this section, the critical adjustment on a confocal interferometer is transferred from the parallelism and alignment in the plane system and mode-matching in the spherical mirror systems, to the separation of the mirrors. In setting up a confocal interferometer there must be a fine adjustment available on the mirror separation. The criticality of this adjustment can be seen by observing equation (2). The departure from the exact confocal condition which can be tolerated without allowing the TEM_{mn} mode to resonate at an observably different mirror spacing from the TEM_{oo} mode is given by

$$|E|_{max} = \pi r/2(1 + m + n)F$$

Thus an interferometer with $r = 5$ cm, $F = 100$ and $(m + n) \simeq 100$ must have its separation set to an accuracy of at least 8 µm. There is little difficulty in obtaining a screw thread sufficiently fine to ensure this kind of resolution but it is clearly highly desirable to have a method of recognising the onset of the confocal condition when making the adjustment.

There are two simple methods of recognising the confocal condition of an interferometer. In the first method a laser beam whose wavelength is within the high reflectivity zone of the mirrors to be adjusted is shone into the interferometer. Interference fringes will be formed in the vicinity of the centre plane of the interferometer. If the beam is large enough several fringes will be seen on looking into the interferometer. If a fine adjustment is made to the separation of the interferometer, say by gently squeezing, so that the separation is made smaller, the fringes will appear to become smaller. If the separation is greater than the confocal separation and the mirrors are squeezed together the fringes will increase in diameter. When the confocal condition has been established the high transmission peaks will fill the whole aperture of the interferometer. This is a very sensitive method of establishing the confocal condition.

In cases when the interferometer is to be used in a scanning mode of operation some means for electronically changing the cavity length will be provided. It is then possible to align the interferometer without looking into the interferometer. This may be important when high power lasers are being used in the alignment in order to protect the eye when a high transmission condition is reached. In this case the adjustment is most easily made by applying the x-ramp from an oscilloscope to a piezoelectric separator while displaying the transmitted light falling on a photodiode on the oscilloscope screen. The sequence of events illustrated in figure 2 is usually encountered. When the interferometer is well away from the confocal condition the mirror separation which will allow each of the TEM_{mn} modes to resonate will be quite different as shown in figure 2(a). As the mirrors are moved closer to the confocal conditions two distinct sets of mode on each scan will be observed (figure 2(b)). These corresponds to the even-symmetric and odd-symmetric sets of modes. When the confocal condition is satisfied the two sets of modes will each have their own resonant separation and each TEM_{mn} mode will lie at one or toher of these separations (figure 2(c)). This adjustment can be made easily and quickly with a very high degree of accuracy.

In the course of this work several confocal interferometers have been constructed. We shall describe in detail only two such interferometers: a 5 cm spacing 1.5 GHz free spectral range and 30 cm spacing 250 MHz free spectral range version.

C.5 The 5 cm Confocal Interferometer

A drawing of the design for this interferometer is shown in figure 3. The mirrors are separated by a piezoceramic cylinder of 1" diameter and 2" length made of PZT-5H and supplied by Vernitron Ltd. The mirrors have a radius of curvature of 5 cm on the front and back surfaces and are therefore of zero optical power. This ensures that if the interferometer is to be used as a very narrowband filter a collimated beam of light will be transmitted without affecting the collimation. The mirror substrates were supplied by IC Optical System, Franklin Road, London and are spherical to $\lambda/20$ over the central 10 mm of their ½" diameter. The multilayer dielectric coatings have a maximum reflectivity of 99.9% at 600 nm and the reflectivity falls to 99.5% at 550 nm and 650 nm. The back surfaces of the mirrors are anti reflection coated to avoid spurious reflections. The coatings were supplied by Ferranti Ltd, Dundee. The entrance lens was of 5 cm focal length and was used to focus an incident collimated beam at the centre of the interferometer. All the light falling within a zone of radius $2\rho_s f/r$ on the lens will pass through the detector aperture of radius ρ_s and be filtered by the instrument. The lens was supplied by Ealing Ltd and the photodiode was a modified Mullard BPX25. In this mode of operation the confocal interferometer can be used as a static filter, tunable filter or scanning spectrum analyser. If the incident beam is not collimated there will be no loss in resolution but there may be a reduction in the amount of light received by the detector. The entire system is mounted on an adjustable mirror mount so that the interferometer can be tilted in the plane of the lens. There is provision made for the fine adjustment to the mirror separation. There is easy access to the mirrors so that they can be replaced by mirrors coated for different spectral regions.

If the detector is removed and a collimated beam is incident on the rear of the system the fringe pattern can be formed in the focal plane of the imput lens. If an observer or camera focused on infinity is placed at the exit the fringes can be readily viewed. This may be useful in analysing the modes of pulsed laser systems.

Figure 4 shows an oscilloscope trace of the interferometer being used as a scanning mode analyser. An He-Ne laser is incident on the interferometer and the scan is provided by the oscilloscope x-ramp. The finesse measured using this system was in excess of 200 and the stability was about 1 $\text{MHz}\,\text{min}^{-1}$.

C.6 The 30 cm Confocal Interferometer

This interferometer is somewhat different in design to the 5 cm interferometer and so it is worth describing. It took the form of a stainless steel rod with a small hole bored along the axis. Because the length of the interferometer is long compared to the mirror diameters some adjustment of the angle of each mirror was necessary. All that is required when aligning the system is that a collimated beam which passes through the centre bore be reflected back along the axis. When this has been achieved for both mirrors the modes can be scanned on anoscilloscope and the confocal separation can be set by adjusting a screw thread and locking with a lock nut. The mirrors used were standard Spectra-Physics high reflectivity dye laser mirrors of 7.75 mm diameter, 30 cm radius of curvature and $\lambda/20$ sphericity on the front surface and plane back surface. The back surface was not anti-reflection coated as it was not parallel to the front surface. The photodiode and piezoceramic are the same as those used in the 5 cm interferometer. As this system stands the only practical use is as a scanning mode analyser. This is because the mirrors are not of zero power and because there is no acceptance lens in front of the system. However, if it were necessary to use the system in any of the other modes described above the modifications could easily be made.

Despite the fact that the design of this interferometer has grown up with several historical accidents it works very well and has a free spectral range of 500 MHz, a finesse in excess of 200 and an instrumental pass-band of less than 2.5 MHz. The narrow bandwidth of the instrument make it ideal for measuring the single mode linewidth of a dye laser.

References

1. P Connes, Revue d'Optique 35, 37(1956)
2. R L Fork, D R Herriott and H Kogelnik, Appl Opt 3, 1471 (1969)
3. M Hercher, Appl Opt 5, 951 (1968)
4. D C Sinclair, Spectra-Physics Laser Technical Bulletin No6, Mountain View, California (1968)
5. H Kogelnik and T Li, Appl Opt 5, 1550 (1966)

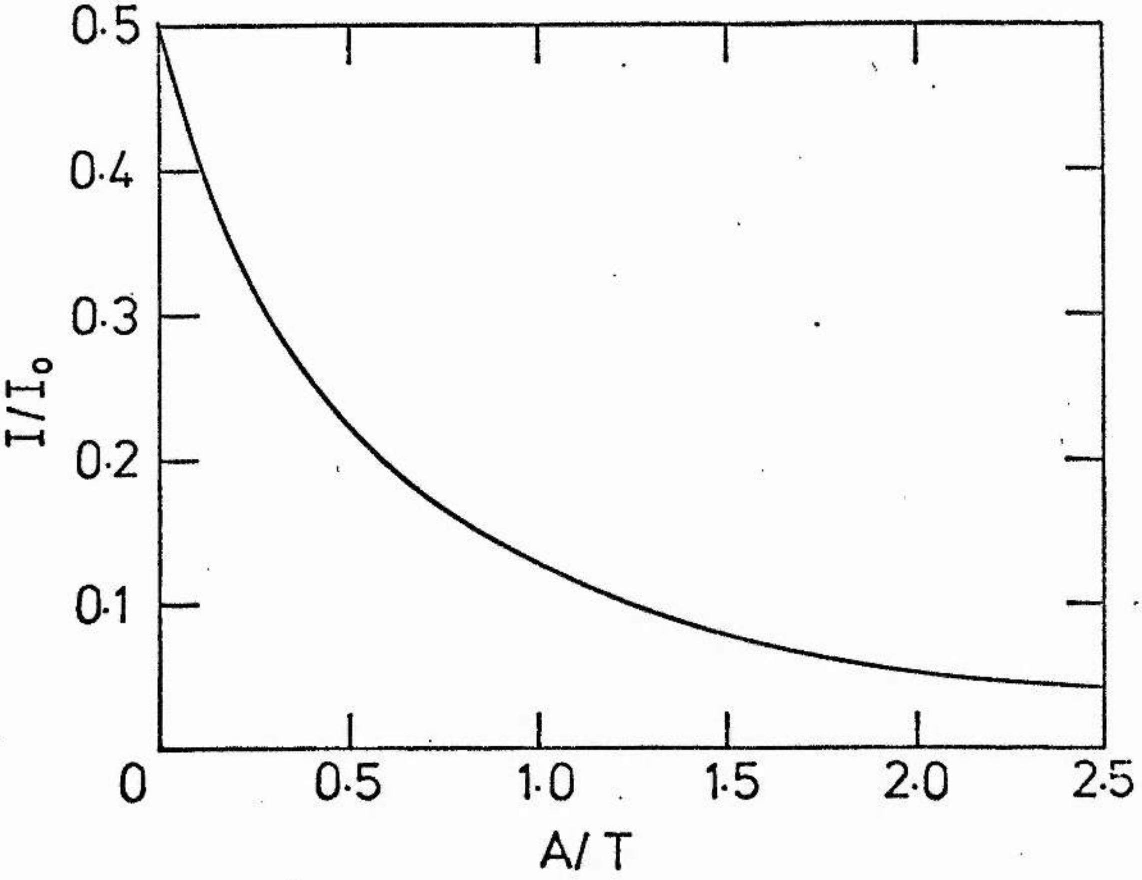

Figure 1. The reduction in peak transmission of a confocal interferometer as the absorption and scattering losses are increased.

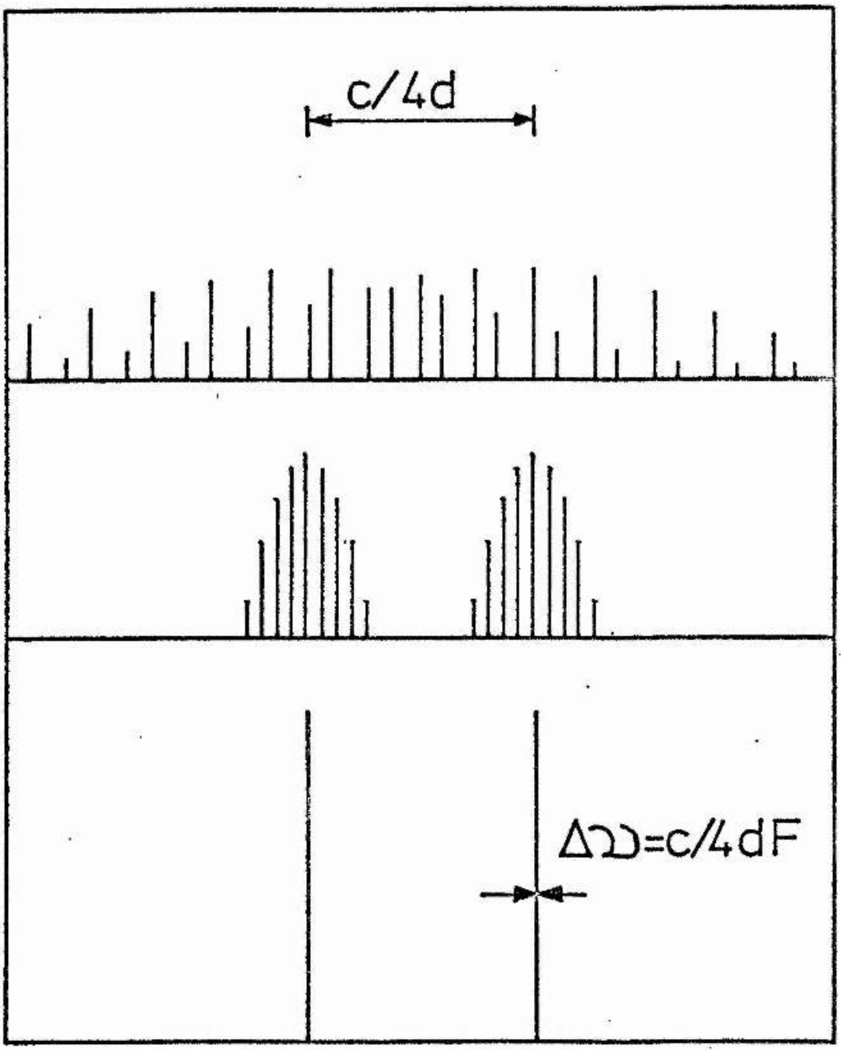

Figure 2. Appearance of the modes of an interferometer in frequency space as the confocal condition is approached; (a) far from the confocal condition, (b) approaching confocal condition, (c) confocal condition.

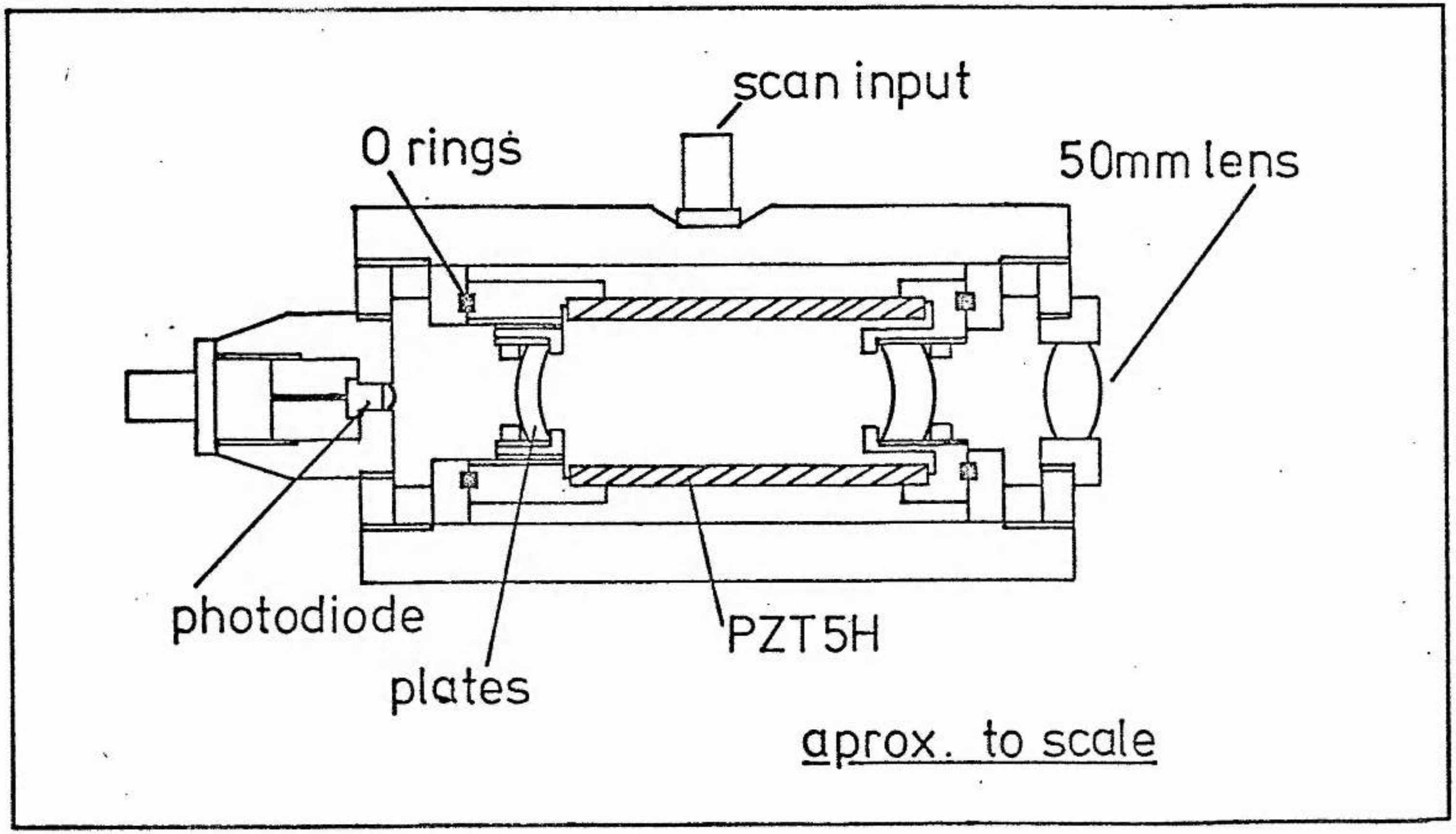

Figure 3. Diagram of the 5 cm confocal interferometer used in this work.

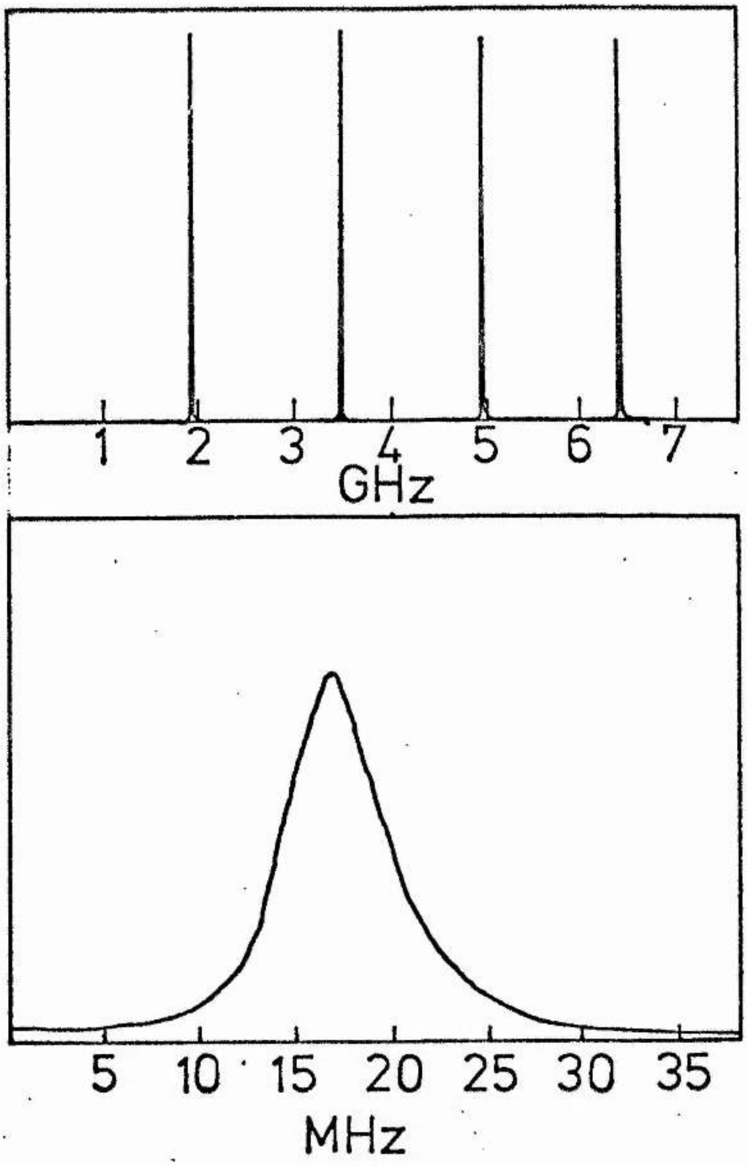

Figure 4. Some oscilloscope traces of the 5 cm confocal interferometer used to analyse the modes of an HeNe laser. The lower trace is a 200x expansion of the upper trace.

Appendix D

ELEMENTS ACCESSIBLE TO A FREQUENCY DOUBLED RHODAMINE 6G DYE LASER

List of Levels Accessible to Frequency Doubled Rhodamine 6G dye laser (i.e. those transitions radiatively coupled to the ground state). From Tables of Spectral-Line Intensities Part I Arranged by Elements. W.F.Meggers, C.H.Corliss, B.F.Scribner. (280nm - 310nm).

Aℓ
Bi
Co
Eu
Gd
Ga
Hf
In
Ir
Fe
Pb
Lu
Mg
Mn
Mo
Ni
Os
Pd
Pt
Re
Rn
Sc
Sr
Sn
Ta
Tr
Tm
Ti
V
W
U
Y
Zn
Zr

	Wavelength	Intensity
Aℓ	3082.16 Å	320
Ba	3071.58 Å	18
Bi	3067.72	3600
CoI	2928.81 Å	1.6
	2987.16 Å	5
	2989.59 Å	36
	3013.60 Å	17
	3044.00 Å	160
	3082.62 Å	34
	3121.42 Å	17
EuI	2878.87 Å	10
	2892.54 Å	20
	2893.03 }Å	14
	2893.83	36
	2908.99 Å	16
	2958.91 Å	3
	3058.98 Å	12
	3106.18 Å	32
	3111.43 Å	95
GdI	3087.05 Å	8
GaI	2874.24 Å	500
HfI	2819.74 Å	22
	2833.28 Å	20
	2860.56 Å	20
	2866.37 Å	240
	2889.62 Å	90
	2940.77 Å	220
	2944.71 Å	18
	2980.81 Å	120
	3016.78 Å	60
	3018.31 Å	110
	3072.88 Å	240

	Wavelength	Intensity
VI	2838.06 Å	4
	2848.77 Å	9
	2855.22 Å	26
	2894.58 Å	8
	2899.60 Å	15
	2903.70 Å	8
	2942.35 Å }	
	2943.20 Å	30
	3043.56 Å	30
	3050.89 Å	22
	3053.65 Å	60
InI	2858.14 Å	3
	3039.36	800
IrI	2823.18 Å	50
	2849.72 Å	280
	2924.79 Å	320
	2951.22 Å	85
FeI	2795.01 Å	2
	2825.69 Å	3
	2835.46 Å	2.5
	2874.17 Å	10
	2912.16 Å	20
	2936.90	80
	2966.90	170
	2983.57	140
	3020.64	280
PbI	2833.06	950
LuI	2903.05	20
	2989.27	120
	3080.11	26
	3171.36	140
MgI	2852.13	6000
MnI	2801.06	480
MoI	3112.12	170
	3132.59	1800

	Wavelength	Intensity
NiI	2984.13	20
	3019.14	28
	3031.87	10
OsI	2806.91	260
	2872.40	16
	2909.06	900
	2929.51	34
	3018.04	460
	3058.66	900
PdI	2763.09	160
PtI	2830.30	140
	2929.79	170
	3064.71	320
ReI	2895.01	44
	2976.29	28
	2992.36	160
	3067.40	160
RuI	2818.36	38
	2874.98	200
	2988.95	150
ScI	2965.86	28
	2974.01	100
	3015.36	180
SrI	2931.83	2
TaI	2836.62	4
	2873.36	32
	2933.55	200
	2940.22	140
	3103.25	75
ThI	3060.44	6
TmI	2914.83	17
	2932.96	8
	2973.22	50
TmI (cont'd)		
	3046.87	?
	3081.12	34
	3131.26	700
	3133.89	220
SnI	2863.33	1000
TiI	2933.55	17
	2942.00	100
	2968.23	2.5
	2970.38	7
WI	2879.39	75
	2911.00	34
UI	3114.54	7
YI	2919.05	18
	2948.40	44
	2974.59	55
	2996.94	16
ZnI	3075.90	26
ZrI	2814.90	70
	2960.87	50
	2985.39	130
	3014.44	10
	3065.21	8